
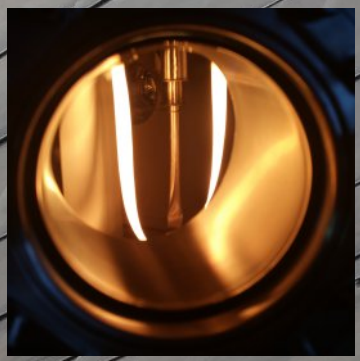
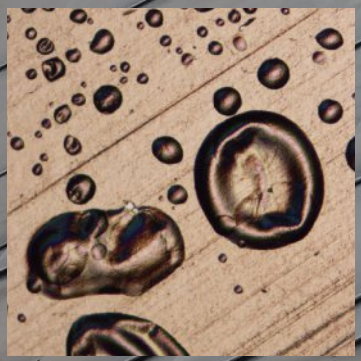
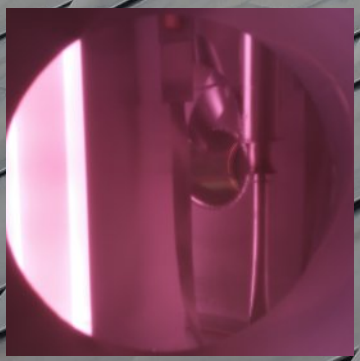

Benedikt J. Peters

Development of a Hydrogen-Selective Vacuum Pump on the Basis of Superpermeation

Development of a Hydrogen-Selective Vacuum Pump on the Basis of Superpermeation

Benedikt J. Peters

B.J. Peters, Development of a Hydrogen-Selective Vacuum Pump on the Basis of Superpermeation, PhD-thesis, Karlsruhe Institute of Technology, Karlsruhe, 2020. doi: 10.5445/IR/1000122305

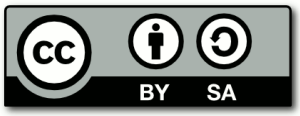

Entwicklung einer auf Superpermeation basierenden, wasserstoffselektiven Vakuumpumpe

Development of a Hydrogen-Selective Vacuum Pump on the Basis of Superpermeation

zur Erlangung des akademischen Grades eines

Doktors der Ingenieurwissenschaften (Dr.-Ing.)

von der KIT-Fakultät für Maschinenbau des
Karlsruher Instituts für Technologie (KIT)
genehmigte

Dissertation

von

Dipl.-Ing. Benedikt Josef Peters

aus Düsseldorf

Tag der mündlichen Prüfung: 18. Mai 2020
Referent: Prof. Dr. Robert Stieglitz
Koreferent: Prof. Dr. Anton Möslang

Kurzfassung

In zukünftigen Fusionskraftwerken wird für den Einsatz des „Direct Internal Recycling“ Konzepts (DIR) die Abtrennung von Wasserstoff aus Gasmischungen bei niedrigem Druck in einem Verfahrensschritt benötigt. Nach dem derzeitigen Stand der Technik ist dies bisher nicht möglich. Der Effekt der Superpermeation ist in der Lage die Anforderungen für diesen Prozess zu erfüllen. Darauf basierend wird in der vorliegenden Arbeit eine Prozesseinheit, die Metallfolienpumpe (MFP), entwickelt.

Um die Bedeutung der dargelegten Entwicklung aufzuzeigen, werden zunächst die Vorteile des DIR herausgearbeitet. Es ist derzeit keine andere Technologie bekannt, die eine solch bedeutende Verbesserung des Brennstoffkreislaufs von zukünftigen Fusionsreaktoren ermöglicht. Die charakteristische Funktionsweise der MFP wird ausgehend von den grundlegenden physikalischen Abläufen erklärt. Die beeinflussenden Materialeigenschaften werden dabei beschrieben und die relevanten Literaturdaten dargestellt. Basierend auf den erläuterten Vorgängen wird ein dimensionsloses Modell abgeleitet, das die dominierenden Prozesse in der Metallfolie, dem Kernelement der MFP, beschreibt. Aus diesem Modell werden die Limitierungen für die möglichen Folienmaterialien abgeleitet. Mit Hilfe der dargestellten Materialeigenschaften wird die dimensionslose Beschreibung in quantifizierte Aussagen für einzelne Materialien umgewandelt. Auf diese Weise wird gezeigt, dass sich die Metalle Niob und Vanadium am besten für Metallfolienpumpen in Fusionskraftwerken eignen. Die Bildung von Wasserstoffbläschen wird als wichtige Materiallimitierung aufgezeigt und begründet.

Im Rahmen dieser Arbeit werden zwei experimentelle Einrichtungen genutzt. Dabei wird eine im Rahmen dieser Arbeiten entworfen, gebaut, in Betrieb genommen und eingesetzt. Die Superpermeation wird erfolgreich mit mehreren Metallfolienmaterialien und Energiequellen für Wasserstoff demonstriert. Diese Energiequellen sind neben der Metallfolie das zweite bedeutende Element einer MFP. Ihr Einsatz ist stark vom gewünschten Saugdruck der Pumpe abhängig. Mehrere Vorhersagen des dimensionslosen Modells werden experimentell nachgewiesen. Basierend auf den experimentellen Ergebnissen wird ein klarer Entwicklungspfad aufgezeigt. Dabei werden die offenen Forschungsfragen und ihr Einfluss diskutiert.

Abstract

Currently, the separation of hydrogen from other gases at low pressures cannot be performed within a single step. A new technology with this capability is needed for the demonstration of Direct Internal Recycling (DIR) for future fusion power plants. The superpermeation effect is able to meet the requirements for this process. A new process unit, the metal foil pump (MFP), is developed on the basis of superpermeation in this work.

In order to demonstrate the importance of the presented development, the advantages of the DIR are quantified at the beginning of this study. No other technology currently offers such a tremendous improvement of the fuel cycle of future fusion reactors. Superpermeability is explained based on the basic physical processes. The relevant material properties are described and corresponding literature data is presented. Based on the explained processes, a dimensionless model that describes the dominant processes in the metal foil, the core element of the MFP, is derived. From this model, the limitations of the possible foil materials are deducted. With the help of the previously given material properties, the dimensionless description is transferred into quantified statements for individual materials. In this way, it is demonstrated that the metals niobium and vanadium are best suited for metal foil pumps in future fusion power plants. The possibility of hydrogen blister formation is discussed and justified as an important material limitation.

Two experimental facilities are used for this work, one of which has been designed, built, commissioned and used within the scope of this work. Superpermeation is successfully demonstrated with several metal foil materials and energy sources for hydrogen. These energy sources are the second important element of an MFP, in addition to the metal foil, and their use is highly dependent on the operation pressure of the unit. Several predictions of the non-dimensional model are experimentally proven. Based on the experimental results, a clear development path is shown. Finally, the open research questions and their influence are discussed.

Schläft ein Lied in allen Dingen,
Die da träumen fort und fort,
Und die Welt hebt an zu singen,
Triffst du nur das Zauberwort.

Joseph von Eichendorff

Table of Contents

Symbols and Abbreviations

Symbols and Constants

Symbol	Description		Unit	
a	Lattice constant		(m)	
A	Area		(m^2)	
B	Magnetic field		(T)	
c	Concentration		(mol/m^3)	
c	Speed of light in vacuum	= 299 792 458	(m/s)	1
c_R	Material-dependent Richardson constant		($A/(cm^2K^2)$)	
C	Conductance		(m^3/s)	
D	Diffusivity		(m^2/s)	
e	Elementary charge	$= 1.602\,176\,634 \cdot 10^{-19}$	(C) or (J/eV)	2
E	Electric field strength		(V/m)	
E_C	Activation energy for dissociative chemisorption		(eV)	
E_D	Activation energy for diffusion		(eV)	
E_S	Energy of dissolution		(eV)	
f	Fugacity		(Pa)	
f^G	Gaussian (normal) distribution function		(−)	
f^M	Maxell-Boltzmann distribution function		(−)	
G_f	Gibbs free energy of formation		(J)	
H_f	Enthalpy of formation		(J)	
i_M	Squared Miller index number		(−)	
i_{te}	Thermionic emission current		(A/cm^2)	
j	Flux		($Pa\ m^3/(m^2\ s)$)	
J	Flow		($Pa\ m^3/s$)	
k	Boltzmann constant	$= 1.380\,649 \cdot 10^{-23}$	(J/K)	2
k_r	Recombination coefficient		($m^4/(mol\ s)$)	
K	Solubility		$\left(mol/\left(m^3\ \sqrt{Pa}\right)\right)$ for H_2	
K_e	Equilibrium constant		(−)	
$K_{e,\mathrm{m}\,a}$	Equilibrium constant between molecular and atomic hydrogen		(−)	
l	Length		(m)	
$\bar{l}$	Mean free path		(m)	
L_c	Characteristic length		(m)	
m	Mass		(kg)	
m_e	Mass of an electron	$= 9.109\,38 \cdot 10^{-31}$	(kg)	3
m_p	Mass of a proton	$= 1.672\,62 \cdot 10^{-27}$	(kg)	3
$\widetilde{M}$	Molar mass		(kg/mol)	
n	Amount of substance		(mol)	
$\dot{n}$	Molar flux		($mol/(m^2\ s)$)	
$\dot{N}$	Molar flow		(mol/s)	

$\dot{N}_{Fus}$	Fusion reaction rate		(mol/s)	
N_A	Avogadro constant	$= 6.022\,140\,76 \cdot 10^{23}$	(1/mol)	2
n_c	Cut-off electron density (in plasma)		($1/m^3$)	
n_e	Electron density (in plasma)		($1/m^3$)	
p	Pressure		(Pa)	
P	Permeability		$\left(\text{mol}/\left(\text{m s}\sqrt{\text{Pa}}\right)\right)$ for H_2	
$\mathbb{R}$	Gas constant	$= 8.314\,462\,618\,153$	(J/(K mol))	4
r	Atom radius		(m)	
S	Pumping speed		(m^3/s)	
S_f	Entropy of formation		(J/K)	
t	Time		(s)	
T	Temperature		(K)	
T_c	Critical temperature for the formation of hydrides		(K)	
$\bar{u}$	Mean molecular speed (scalar)		(m/s)	
W	Permeation number		(−)	
x	Length		(m)	
x_Q	Mole fraction of isotope (in solid)		(−)	
y_Q	Mole fraction of isotopologue (in gas)		(−)	
α_a	Sticking coefficient for atomic hydrogen		(−)	
α_m	Sticking coefficient for molecular hydrogen		(−)	
β	Molecular hydrogen release rate coefficient		($\text{mol}/(\text{m}^5\ \text{s})$)	
β_a	Atomisation coefficient on the surface		(−)	
β_S	Recombination coefficient on the surface		(−)	
γ	Surface to bulk transition rate coefficient of hydrogen		($\text{mol}/(\text{m}^2\ \text{s})$)	
δ	Diffusivity for bulk to surface transition		($\text{mol}/(\text{m}^2\ \text{s})$)	
ε	Surface asymmetry factor		(−)	
ε_0	Electric field constant	$= 8.854\,187\,817\ldots \cdot 10^{-12}$	(A s/(V m))	1
ζ	Relative implantation depth		(−)	
η	Efficiency		(−)	
η_{MFP}	Metal foil pump separation fraction		(−)	
θ	Surface coverage factor		(−)	
λ	Wavelength		(m)	
μ	Conversion factor from pressure to surface flux		($\text{mol}/(\text{Pa s m}^2)$)	
μ_0	Magnetic field constant	$= 4\pi \cdot 10^{-7}$	(N/A^2)	1
$\vec{\xi}$	Velocity (vector)		(m/s)	
π	Pi	$= 3.141\,592\,653\,589\,793\ldots$	(−)	5
ϱ_n	Number density		(mol/m^3)	
${\sigma_{sd}}^2$	Standard deviation of normal distribution		same unit as the deviating quantity	
σ	Surface roughness factor		(−)	
σ_c	Conductivity		(1/(Ω m))	
Φ	Work function		(eV)	
χ	Permeation likelihood or permeation fraction		(−)	
Ω	Capture coefficient		(−)	
ω	Angular frequency		(rad/s)	
#	Number (of particles)		(−)	

Sources for the given values

[1] P.J. Mohr, D.B. Newell, B.N. Taylor, E. Tiesinga, Data and analysis for the CODATA 2017 special fundamental constants adjustment, Metrologia 55 (2018) 125–146. doi: 10.1088/1681-7575/aa99bc

[2] D.B. Newell, F. Cabiati, J. Fischer, K. Fujii, S.G. Karshenboim, H.S. Margolis, E. de Mirandés, P.J. Mohr, F. Nez, K Pachucki, T.J. Quinn, B.N. Taylor, M. Wang, B.M. Wood, Z. Zhang, The CODATA 2017 values of h, e, k, and N_A for the revision of the SI, Metrologia 55 (2018) L13–L16. doi: 10.1088/1681-7575/aa950a

[3] P.W. Atkins, J. de Paula, Physikalische Chemie (in German), 5. Aufl., Wiley-VCH, Weinheim, 2013.

[4] From calculation: $\mathbb{R} = \mathrm{N} \cdot \mathrm{k}$, values from [2]

[5] I.N. Bronstein, K.A. Semendjajew, Taschenbuch der Mathematik (in German), Verlag Harri Deutsch, Thun, 1987.

Indices

Index	Description
$\blacksquare_a$	Atomic hydrogen
$\blacksquare_{abs}$	Absorption
$\blacksquare_{ads}$	Adsorption
$\blacksquare_{des}$	Desorption (from surface to gas)
$\blacksquare_{dsb}$	Desorption (from bulk to surface)
$\blacksquare_{dif}$	Diffusion
$\blacksquare_d$	Downstream side of metal foil (Back)
$\blacksquare_u$	Upstream side of metal foil (Front)
$\blacksquare_f$	Tritium fuelling (stands for “of formation” when used with G, H or S)
$\blacksquare_m$	Molecular hydrogen
$\blacksquare_i$	Implantation point
$\blacksquare_{in}$	Entering
$\blacksquare_{out}$	Leaving
$\blacksquare_o$	Orifice
$\blacksquare_L$	Limit
$\blacksquare_H$	Hydrogen isotope protium
$\blacksquare_D$	Hydrogen isotope deuterium
$\blacksquare_T$	Hydrogen isotope tritium
$\blacksquare_Q$	Hydrogen, all isotopes
$\blacksquare_{Q_2}$	Hydrogen, all isotopologues
$\blacksquare_s$	Suprathermal hydrogen
$\blacksquare_V$	Vanadium
$\blacksquare_{x,y,z}$	Into the *x*-, *y*-, *z*- direction
$\blacksquare^*$	In equilibrium

Abbreviations

Abbreviation	Description
ADP	Atom-driven permeation
DIR	Direct Internal Recycling, a concept for DEMO to minimize the tritium inventory
DSMC	Direct Simulation Monte Carlo, an approach to calculate transitional flow
ECR	Electron cyclotron resonance (plasma)
GDP	Gas-driven permeation
HERMES	Hydrogen Experiment for Research on MEtal foils and Superpermeability
HERMES*plus*	Hydrogen Experiment for Research on MEtal foils and Superpermeability – PLasma Utilization Setup
JET	Joint European Torus, an experimental tokamak in Oxfordshire, UK.
KALPUREX	KArlsruhe Liquid metal based PUmping process for fusion Reactor EXhaust gases
MFP	Metal Foil Pump, name of the pump that is developed in this work.
PEG	Plasma Enhancement Gas, gas that is deliberately added to the fusion torus besides the hydrogen isotopologues
PDP	Plasma-driven permeation
RF	Radio-frequency
TPMC	Test Particle Monte Carlo, an approach to calculate free molecular flow

Vorwort / Preface

In den letzten Jahren wurde ich häufig gefragt, womit ich mich beschäftige. Immer wieder hat es mir Freude gemacht, mein Dissertationsvorhaben zu erläutern. Denn es klingt fast zu gut, um wahr zu sein: Ich entwickle eine Anlage um Wasserstoff aus einem Gemisch abzutrennen, die das Gas auch gegen ein Druckgefälle transportiert und keine bewegten Teile benötigt. Die meisten waren daraufhin recht erstaunt. Trotzdem habe ich nicht übertrieben. Vieles davon habe ich in dieser Arbeit zeigen können. Dabei durfte ich auf viele Vorarbeiten zurückgreifen. Jetzt kann ich meinen kleinen Beitrag zum Stand der Technik leisten und hoffe, damit neuen technischen Möglichkeiten den Weg zu bereiten. Viele haben mich bei meiner Arbeit unterstützt. Diesen fühle ich mich zum Dank verpflichtet.

Zunächst möchte ich meinem Doktorvater, Professor Robert Stieglitz, für die Übernahme des Referats meiner Arbeit danken. Seine Ideen und Denkanstöße haben diese Arbeit sehr bereichert. Für die Übernahme des Koreferats dieser Arbeit möchte ich zudem dem Zweitgutachter, Professor Anton Möslang, danken.

Ganz besonders möchte ich mich bei Herrn Dr. Christian Day für die Aufnahme in seine Arbeitsgruppe am Institut für Technische Physik, die alltägliche Betreuung und die guten Rahmenbedingungen für diese Arbeit bedanken. Von ihm habe ich viel gelernt – fachlich, wie auch menschlich. Der ganzen Vakuumgruppe bin ich ebenfalls zu Dank verpflichtet; ohne ihre Mitarbeit wäre diese Arbeit nicht möglich gewesen. Besonders möchte ich Stefan Hanke für die gute und freundschaftliche Zusammenarbeit im letzten Jahr meiner Arbeit danken. Zudem war es nur durch die Unterstützung meiner Kollegen Peter Pfeil, Hartmut Stump und Jürgen Jung sowie Jürgen Weinhold, Martin Jäger und Thomas Johann möglich, eine funktionstüchtige Anlage zu bauen. Ralf Müller möchte ich für seine technischen Zeichnungen und Volker Hauer für seine hilfreichen praktischen Hilfestellungen danken. Meinen Mitdoktorranden Yannick Hörstensmeyer und Cyra Neugebauer möchte ich für den inhaltlichen Austausch danken, der mich vielseitig bereichert hat.

Ohne die Arbeit von vielen Studenten, die im Bereich der Superpermeation eine Abschlussarbeit geschrieben haben, wäre diese Arbeit ebenfalls nicht möglich gewesen. Deshalb danke ich Yannick Kathage, Daniel Bitter, Maximilian Schlereth, Jonas Heimpel, Daniel Rau, Oliver Linder, Yannick Ille und Daniel Fischer.

Außerhalb meiner Arbeitsgruppe haben auch weitere Kollegen vom KIT mir geholfen. Besonders danken möchte ich Marco Langer für die Aufnahme der XRD Scans und Dr. Annette Heinzel und Dr. Alfons Weisenburger für die Folienbeschichtungen.

Experienced colleagues in the research community have freely shared their knowledge and ideas. I would like to express my gratitude to Professor Livshits, his research group and especially to Dr Andrei Busnyuk. In addition, I would like to thank Dr Walter Shmayda.

Besonders danken möchte ich auch meiner Familie, sie hat mich immer unterstützt und war ein Fels in der Brandung für mich. Das gilt insbesondere für meine Frau Sonja, die sicher die meiste Last während teilweise schwierigen Zeiten von meinen Schultern genommen hat.

Bonn, im Oktober 2019

Benedikt J. Peters

1 Fusion and its fuel cycle

1.1 Fusion as an energy source

Nuclear fusion, the merging of two light nuclei into a heavier one, is the major origin of the energy known today. Most other sources obtain their energy from fusion.[1] Fusion is the energy source of the sun. The sun emits electromagnetic radiation, which provides the energy for all life on earth. This makes biomass grow, which is turned into coal, oil and gas after conversion processes. This light drives the winds and powers the water cycle. Even heavy elements, which fission in nuclear power plants, were created by fusion during supernova explosions [1]. Many of these energy sources are technologically harnessed, but fusion has not yet been used to produce electricity.

One of the big endeavours of science has been to harvest fusion energy directly. A false claim by the Argentine dictator Juan Peron in 1951 to have built a fusion nuclear power plant simultaneously sparked research on the peaceful use of fusion in Russia and the USA [2]. The progress made since then is huge, but more knowledge and more technology are still needed. In addition to the potential to solve the problem of energy supply for centuries, it also drives the development of technology. It is not known where else this technology is put into use, but it certainly allows for the solving of other problems.

The source of energy for fusion is the binding energy between protons and neutrons within an atomic nucleus. This binding energy exists due to the extremely short-range "strong interaction", one of the four fundamental forces. The binding energy per nucleon for most isotopes known today is shown in Figure 1.1. Only a small number of isotopes are stable. These tend to be the ones close to the upper curve, which are the isotopes with the highest binding energy at each number of nucleons. The most stable nucleus is iron-56. Any nuclear reaction that results in a higher average binding energy will release energy. This can either be nuclear fusion, for elements with fewer nuclei than iron-56, or nuclear fission for heavier isotopes.

The lightest and thus most interesting element for fusion is hydrogen. There are seven known hydrogen isotopes. Four of them decay with half-lives below 10^{-21} s, and are thus irrelevant for most purposes. The other three are relevant for fusion. Protium (^{1}H) is the simplest atom, containing just one proton and electron. Deuterium (^{2}D or ^{2}H) additionally holds a neutron. Both are stable and occur in nature. Tritium (^{3}T or ^{3}H) holds a second neutron and is radioactive. It decays with a half-life of 12.33 years in a β^-- decay to ^{3}He, emitting an electron with up to 18.5743 keV [3].

[1] The exceptions are probably only sources that are driven by gravity, such as tidal power generation.

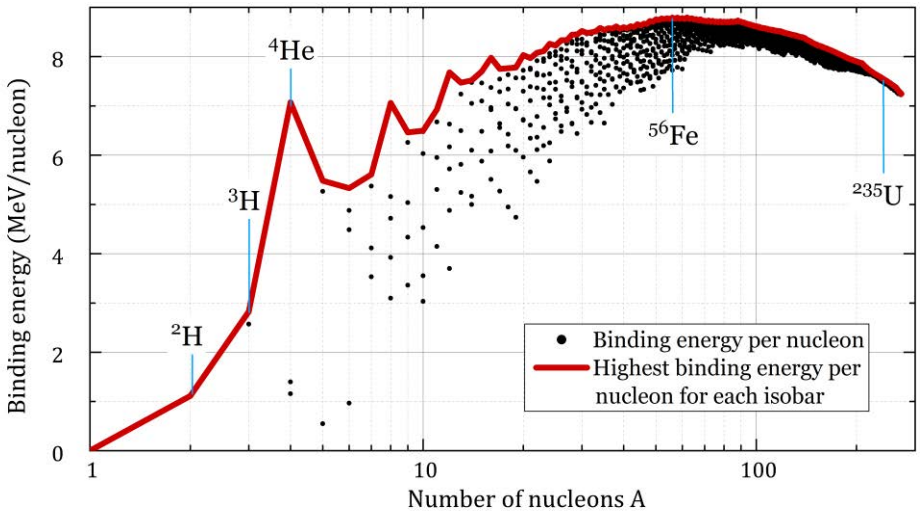

Figure 1.1: Binding energy per nucleon for most isotopes and the highest value for each isobar (all isotopes with the same number of nucleons). Data from [4].

Different nuclei repel each other due to their positive charge. In order to overcome these forces to reach fusion, they need to have very high kinetic energy. The likelihood of merging can be described by a cross-section. Due to the relatively high fusion cross-section at reasonable interaction energies, the most promising fusion reaction for the operation in a fusion reactor is

$$ {}_{1}^{3}\mathrm{T} + {}_{1}^{2}\mathrm{D} \rightarrow \mathrm{n} + {}_{2}^{4}\mathrm{He} + 17.6\ \mathrm{MeV}. \tag{1.1} $$

This is often abbreviated as $\mathrm{T(d,n)\alpha}$ in nuclear physics [5].

In Figure 1.2, the fusion cross-sections for some fusion reactions are plotted. These cross-sections are given for interactions with exactly these centre-of-mass energies. If a reaction rate is the desired outcome, the velocity distribution of all interacting particles has to be taken into account. This distribution is in thermal equilibrium for thermonuclear fusion. As this is also important in another context, it is described at the beginning of Chapter 3.

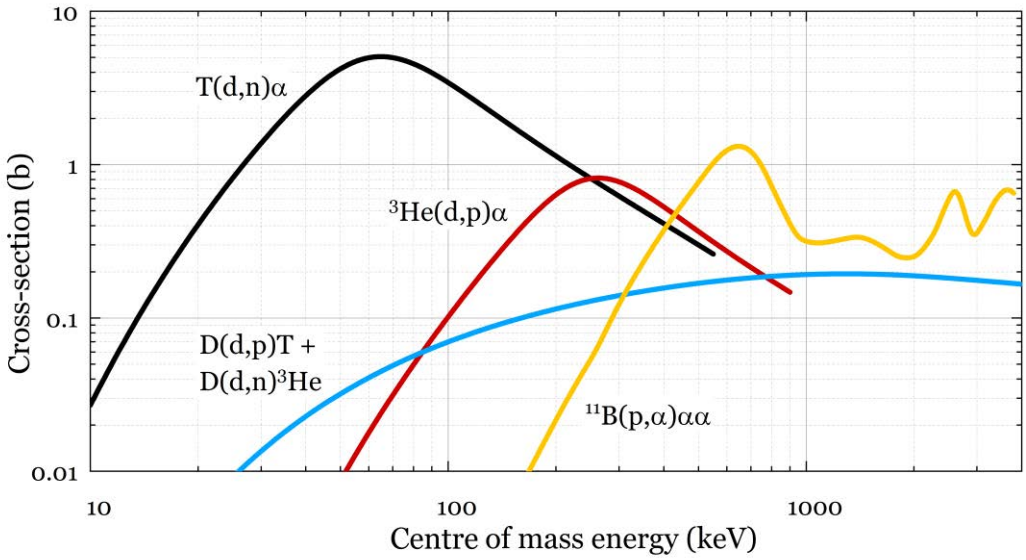

Figure 1.2: Selected fusion cross-sections over the centre-of-mass energy of the reaction. Data for the first three reactions from [6]; data for the $^{11}\mathrm{B(p,\alpha)\alpha\alpha}$ reaction from [7].
The unit of the *y*-axis is called barn: $1\ \mathrm{b} = 10^{-28}\ \mathrm{m}^2$.

The energy needed for fusion is orders of magnitude higher than the binding energy between electrons and their nuclei (e.g. $13.6\ \mathrm{eV}$ for $\mathrm{T} \rightarrow \mathrm{T}^+ + \mathrm{e}^-$ [8]). This means that thermonuclear fusion can only occur in plasma, which is a state of matter with a high degree of ionization. Such a plasma cannot be contained in a solid container, as it would rapidly distribute its energy, decreasing its temperature and vaporizing the container wall. As the plasma consists of free charge carriers, it can be manipulated by (electro-)magnetic fields. Two different magnetic configurations are potential candidates for a fusion power plant in the future. In Figure 1.3, these two concepts are shown schematically. The magnetic field coils are shown in blue and the resulting closed magnetic field lines, along which the charged plasma particles travel, are shown in orange. The "tokamak", displayed in a), is a Russian invention and is currently more developed than the "stellarator", shown in b). In contrast to the stellarator, the design of the magnet coils is much simpler in the tokamak, but it is inherently a pulsed machine and cannot be operated continuously. The phase between the plasma pulses of a tokamak is called dwell time. It is necessary to re-establish the state of the magnetic system for the next pulse.

Figure 1.3 a) shows a previously unmentioned element. The "blanket" is a crucial concept for the realization of fusion energy. While the deuterium needed for fusion is abundantly accessible in natural water [9], tritium is a scarce resource. While there might be enough tritium available to start up a fusion reactor, there is certainly not enough to continuously burn externally supplied tritium in a fusion machine with considerable energy output. Thus, the tritium must be produced in a fusion reactor. This can be done via the nuclear reaction [10]

$$^6_3\mathrm{Li} + \mathrm{n} \rightarrow {}^4_2\mathrm{He} + {}^3_1\mathrm{T} + 4.8\ \mathrm{MeV}. \tag{1.2}$$

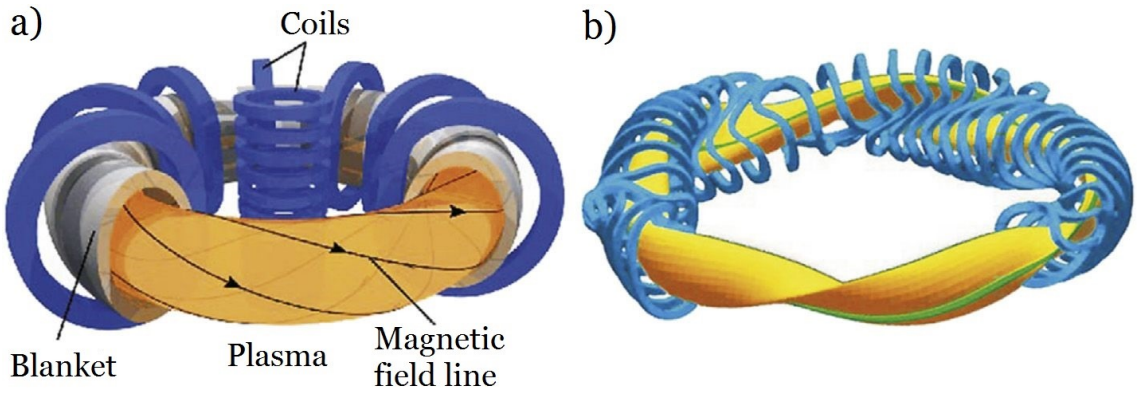

Figure 1.3: Schematics of magnetically confined plasmas in a) tokamaks and b) stellarator configurations, from [11].

In order to produce at least the same amount of tritium as is burned, it attempts to utilize most of the neutrons by surrounding the plasma with a so-called breeding blanket. To avoid each neutron that does not undergo reaction (1.2) decreasing the amount of tritium in the system, neutron multipliers are added. These are materials that undergo a $(n, 2n)$ reaction. In current blanket developments, either beryllium or lead is planned for use as a neutron multiplier [12]. The second function of the breeding blanket is similarly important for a fusion power plant. This is the removal of the majority of the heat from the reactor. This thermal energy has to be utilized for the production of electric energy [12].

Another piece of technology that has proven crucial for fusion machines is a divertor. This fulfils two tasks. First, it allows for removing gas from the torus, so it is the connection point for the vacuum pumps. Second, it is important for obtaining a clean fusion plasma. Energetic particles escaping the fusion plasma hit the vessel wall and release particles from it. These particles of wall material can then enter the fusion plasma and contaminate it. To prevent this, the magnetic field of the fusion machine is adapted so that the energetic particles are guided away from the core of the plasma and collide with divertor plates provided for this purpose. Figure 1.4 shows a photograph of the torus of the tokamak JET. On the right-hand side, a photograph of plasma operation can be seen. The core of the plasma itself is translucent, but wherever impurities have entered the plasma, it glows. This is particularly the case in the divertor area at the bottom of the torus.

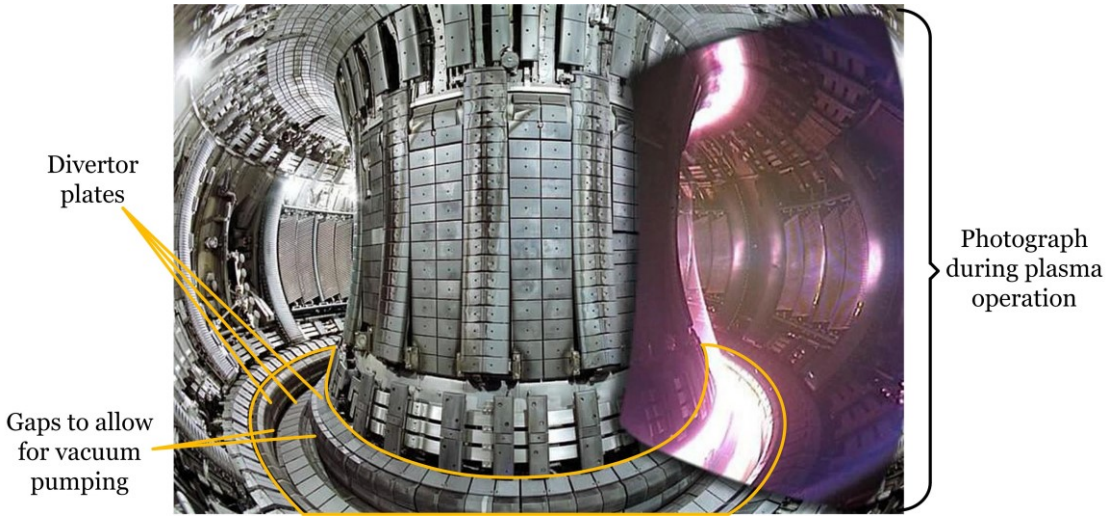

Figure 1.4: Collage of photographs of the tokamak JET. The divertor region is outlined in yellow, adapted from [13].

While quite several stellarators and tokamaks are used for experimental purposes, only a few machines have previously been operated with tritium. The main purpose of the setups without the heavy hydrogen isotopes is the study of the plasma physics, which is a big research field on its own. The next experiment that is planned to be operated with deuterium and tritium is ITER, a tokamak, which is currently under construction in southern France. ITER will also have an experimental focus and will neither breed a enough tritium for operation nor produce electricity for the electrical grid.

The first fusion power plant is likely to be built as a tokamak, in a consecutive step to ITER. This demonstration power plant, called DEMO, has the aim of being tritium self-sufficient and delivering energy to the electrical grid [14]. There are currently various DEMO designs being developed in different countries. China [15], Japan [16], South Korea [17], Russia [18] and Europe [19] are each working on their own designs. The USA is considering an approach with an additional facility, which is to be operated between ITER and DEMO [20]. The presented work is part of the European design.

1.2 Fusion fuel cycle

A fusion power plant will consist of many different parts that need to work together. The system of interest here is the fuel cycle. This describes all process units for the supply and handling of the fuel of a fusion reactor. The main reason for the existence of a fuel cycle is that much more gas must be fed to the torus than is consumed by the reaction. The need for the replenishment of burned fuel and the need to remove the produced helium are easiest to comprehend, but many more functions have to be fulfilled. Dependent on the plasma scenario, gases other than deuterium and tritium are introduced in the torus chamber. As it is impossible to remove species from the torus selectively, the gas mixture is pumped out. At the very least,

the scarce resource tritium needs to be fed back to the plasma after processing. This closes the loop and explains the term “fuel cycle”. This processing path, from torus exhaust to reinjection, is called the “inner fuel cycle”. The term “outer fuel cycle” is used for the other systems that handle tritium, such as the breeding blanket.

The current design of the inner fuel cycle of EU-DEMO is shown in Figure 1.5. What was previously described as a single cycle is in fact a multi-loop concept. This design is based on the Direct Internal Recycling (DIR) concept [21]. This concept tries to minimize the tritium inventory through smart fuel cycle architecture and is based on simple principles. In order to decrease the total tritium inventory, any system that handles large amounts of tritium should process these very quickly. In contrast, a system with smaller tritium content is allowed to have a longer residence time. This gives rise to the three-loop fuel cycle design. The DIR loop is intended to handle most of the hydrogen in the torus exhaust. In order to be able to do this, performing only the minimum treatment necessary is planned. Therefore, the only function is to separate most of the unburned hydrogen species from the torus exhaust. Helium and other impurities remain in the exhaust stream and must be separated in the inner loop. As the tritium content is still considerably high, the processing times should be reasonably quick. To ease the demand on the systems in the inner loop, the intention is not to separate all the hydrogen isotopes from each other but simply to re-establish the desired deuterium to tritium ratio, e.g. a 1:1 D:T mixture that can be used for fuelling. If trace amounts of tritium are handled, the time of treatment has a minor importance for the tritium inventory. These systems can be found in the outer loop.

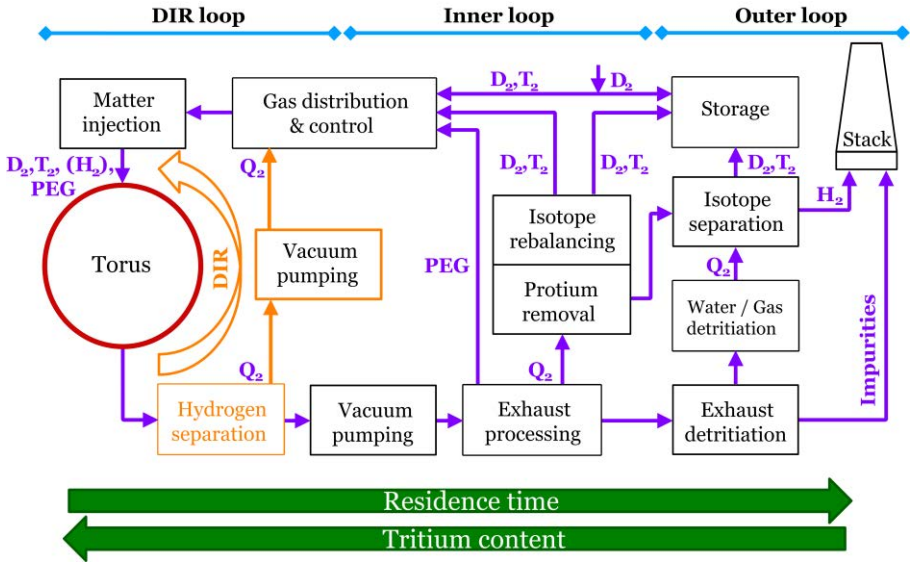

Figure 1.5: Scheme of the inner fuel cycle of EU-DEMO with Direct Internal Recycling (DIR). PEG = Plasma enhancement gas, Q_2 = Isotopologues of hydrogen

The previous explanations describe the demand of the process units in the fuel cycle architecture, but not which technology is used. This is a deliberate step to fulfil the systems engineering approach demanded by the European roadmap towards fusion energy [22, 14]. For each of the process units, several technologies can often be selected. Much more detail is obviously needed if these choices are to be explained. In the following, the technology choices for vacuum pumping and the DIR are stated.

The currently favoured technology solution [23] for the DIR loop is given by the "KArlsruhe Liquid metal based PUmping process for fusion Reactor EXhaust gases" (KALPUREX) [24]. As stated in the name, this process suggests a solution for the torus vacuum pumping systems based on a liquid metal [25]. ITER is planned to use a cryosorption pump as a high vacuum pump [26] and a cryoviscous screw compressor [27] as a fore vacuum pump. These do not only result in a high and dynamic load on the cryogenic plant, but also have a high tritium inventory [28]. Both drawbacks are eliminated by KALPUREX. A mercury diffusion pump was selected as a well-known, tritium compatible and proven high vacuum pump [29, 30]. As backing pump, a liquid ring pump has been suggested. While this pump type is also well-known and reliable, it is normally not operated with a tritium-compatible fluid [31]. As mercury is known to be perfectly tritium-compatible [32] and is already used in the system, it has been chosen as the operating fluid. Although for this pump commercial products are readily available, the circumstances of operation are new. The situation for the third pump in KALPUREX is exactly the opposite. This third pump is called "metal foil pump" (MFP) and is based on the effect of superpermeability. While the fundamental physics principle has been investigated, no technical solutions are available. Moving towards the realization of such a pump is thus the starting point for this thesis.

The basic idea of the multi-loop design of the fuel cycle has been explained previously, but the impact has not been quantified. This is done in the following. The process layout and the variables used are detailed in Figure 1.6. The process units from the inner and outer loop are combined as "tritium plant" in the figure.

The fusion reaction rate $\dot{N}_{Fus}$ directly depends on the flow of tritium fuelling $\dot{N}_f$, the fuelling efficiency η_f and the burnup fraction f_b. For the steady state,

$$\frac{\dot{N}_{Fus}}{\dot{N}_f} = \eta_f f_b, \tag{1.3}$$

describes this relationship. As the tritium burnup fraction and the fuelling efficiency always appear together in this context, their product is referred to as the tritium conversion rate in the following; in other words, the tritium conversion rate is the ratio between the tritium burned and the tritium being put into the torus.

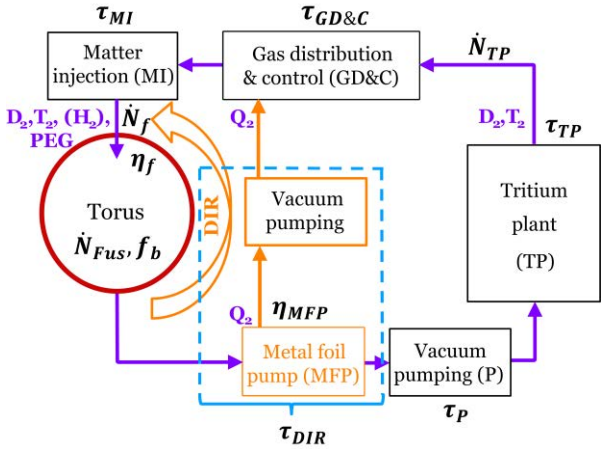

Figure 1.6: Simplified scheme of the EU-DEMO fusion fuel cycle to evaluate the effect of the DIR. τ = characteristic time of a process (unit).

In the case of a fuel cycle without DIR, the amount of tritium fuelling is equal to the tritium stream coming from the tritium plant $\dot{N}_{TP}$. In a fuel cycle containing a DIR, this is reduced by the ratio

$$\frac{\dot{N}_{TP}}{\dot{N}_f} = 1 - \eta_{MFP}(1 - \eta_f f_b), \tag{1.4}$$

where η_{MFP} is the fraction of tritium that is separated in the metal foil pump. It contributes to the tritium stream of the DIR $\dot{n}_{DIR}$.

Figure 1.7 a) shows the tritium stream reduction relative to a fuel cycle without a DIR. Two cases are displayed. The case “high conversion rate” exaggerates the values for the fuelling efficiency ($\eta_f = 1$) and the burnup fraction ($f_b = 0.05$). The other case “low conversion rate” underrates the fuelling efficiency ($\eta_f = 0.1$) and the burnup fraction ($f_b = 0.001$). By using this wide span of values, it is justified to assume that the achievable operational point lies within the displayed bounds.

The term fuelling efficiency is used quite differently in literature. Here, the ratio between the tritium input stream into the torus and the tritium arriving in the plasma core is meant. In the process treatment of this work, possible tritium losses or inefficiencies between the input stream of the matter injection system and the tritium stream entering the torus are neglected. It is noteworthy that the plasma physics demands a certain tritium density in the scrape-off layer (SOL) of the fusion plasma. This can only be fulfilled by a fraction of tritium that passes through the torus without entering the plasma core. Hence, the upper achievable limit for the fuelling efficiency is less than unity.

It can be seen that the DIR has a tremendous impact on the amount of tritium that needs to be supplied by the tritium plant. It can also be seen that the reduction of the necessary tritium stream is only weakly dependant on the conversion rate.

Another way to express this improvement is to identify the factor by which the implementation rate would need to be improved to achieve the same effect.

In a plant without DIR, the conversion rate determines the tritium flow needed; see equation (1.3). The flow from the tritium plant $\dot{N}_{TP}$ is the same as the fuelling rate $\dot{N}_f$. In a plant with DIR, these two flows differ. For this case, equation (1.3) can be altered to express the flow from the tritium plant, yielding

$$\frac{\dot{N}_{Fus}}{\dot{N}_{TP}} = \frac{1}{1-\eta_{MFP}(1-\eta_f f_b)}\,\eta_f f_b. \tag{1.5}$$

The difference between equations (1.3) and (1.5) is the pre-factor of the conversion rate on the right side of the equation. This "improvement factor" of the conversion rate is plotted in Figure 1.7 b) against the separation fraction of the metal foil pump. Although even small separation fractions of the metal foil pump improve the conversion rate, the biggest influence can be seen for high separation fractions. The current design point foresees a separation fraction of 0.8.

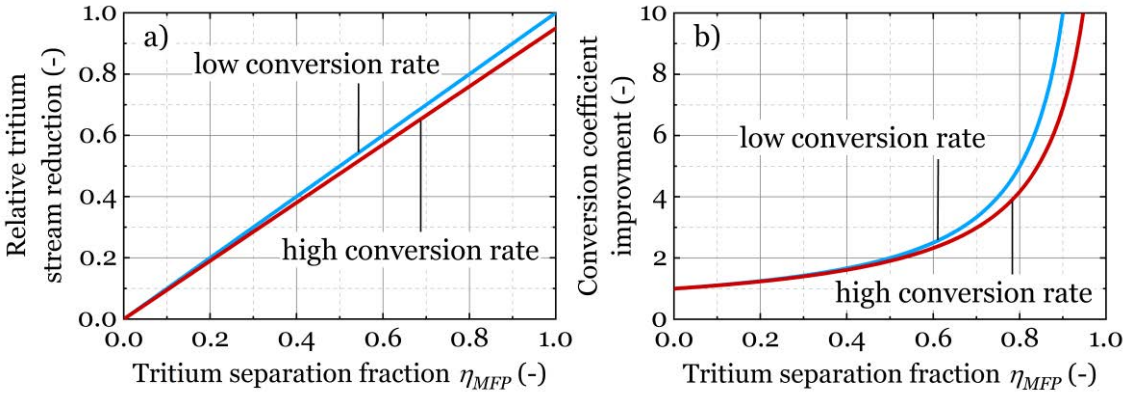

Figure 1.7: Relative improvements of the DIR concept. On the *x*-axis, the MFP separation efficiency is shown. a) Relative tritium stream reduction between the cases without and with DIR; b) Improvement of the tritium conversion rate from the point of the tritium plant. The values are the ratios between the cases without and with DIR.

The previous figures considered the decrease of the tritium flow that needs to be supplied by the tritium plant. The DIR has another advantageous effect: it decreases the mean processing time. This can be seen as an evaluation of the fuel cycle from the perspective of the torus. The mean processing time τ_{FC} gives the average time that is needed by a tritium atom between leaving and re-entering the torus. For a fuel cycle loop without a DIR, it is the sum of the mean residence times τ_i of all process units along the tritium process stream, and is given by:

$$\tau_{FC} = \tau_{MI} + \tau_{GD\&C} + \tau_P + \tau_{TP}. \tag{1.6}$$

Even for a fuel cycle with a DIR, the mean residence times of the matter injection systems τ_{MI} and the gas distribution and control system $\tau_{GD\&C}$ will be fully part of the mean processing time, as every tritium atom has to pass through it. In contrast, the mean residence times of the pumping system τ_P and the residence time in the tritium plant τ_{TP} will only be partially included:

$$\tau_{FC,DIR} = \eta_{MFP}\,\tau_{DIR} + (1 - \eta_{MFP})\,(\tau_P + \tau_{TP}) + \tau_{GD\&C} + \tau_{MI}. \tag{1.7}$$

The separation fraction of the metal foil pump η_{MFP} determines how much the mean residence time of the DIR cycle τ_{DIR} and the mean residence time of the pumping system τ_P and the tritium plant τ_{TP} impact the processing time. It is likely that the mean residence time in the tritium plant will dominate the processing time; it is expected to be in the order of hours [33]. In contrast to this, the mean residence time in the DIR loop is expected to be in the order of seconds. For a separation fraction of 0.8, the mean processing time from the torus exhaust to the gas distribution and control unit is also decreased by nearly 80 %.

Abdou et al. [33] presented results of a simulation from a required start-up inventory of a fusion fuel cycle. Details of the calculation can be found in [34]. In Figure 1.8, some results of this study, obtained by simulation, are plotted. Although the numbers are only valid for the system chosen, it gives an impression of the influence of the tritium conversion rate and the mean processing time on the start-up inventory needed. The start-up inventory of the fusion reactor decreases reciprocally with an increasing tritium conversion rate. The mean processing time also affects the slope of the curve, but mainly shifts it towards higher start-up inventories for longer processing times.

The data in the original source only states values for start-up inventories up to 50 kg. A reciprocal fit function has been used to extend this range to higher values, to allow the depiction of the following demonstration of the DIR capabilities shown in Figure 1.8. One could imagine achieving a tritium conversion rate of 0.5 % and a mean processing time of around 24 h, as was demonstrated in the US facility TSTR [35]. Without the DIR, the start-up inventory would drastically exceed 50 kg (point ① in Figure 1.8). For the envisioned separation efficiency of 80 %, the improvement of the tritium conversion rate is around four. Therefore, the tritium conversion rate is increased to 2 % ②. If the mean processing time of the matter injection and the gas distribution and control is below 1.5 h, the total mean processing time would be decreased to a value below 6 h ③. This results in a start-up inventory of around 15 kg. Two conclusions can be drawn from this example. First, the DIR decreases the operational and start-up inventory drastically and is thus very beneficial in the quest for tritium self-sufficiency and better safety, due to minimized tritium inventory. Second, the whole fuel cycle design has to be

optimized, as the one assumed by Abdou et al. [34] will result in tritium inventories that are too high to be reasonable for DEMO.

The previous descriptions and the example clearly show that the Direct Internal Recycling (DIR) concept allows for a tremendous improvement in the fuel cycle design of future machines. It is unlikely that any other physics or technology advancement has a similarly high impact on the sizing of the fuel cycle. Today, the big disadvantage of this technology is that its technical readiness level is still low. This provides the design driver for the presented research.

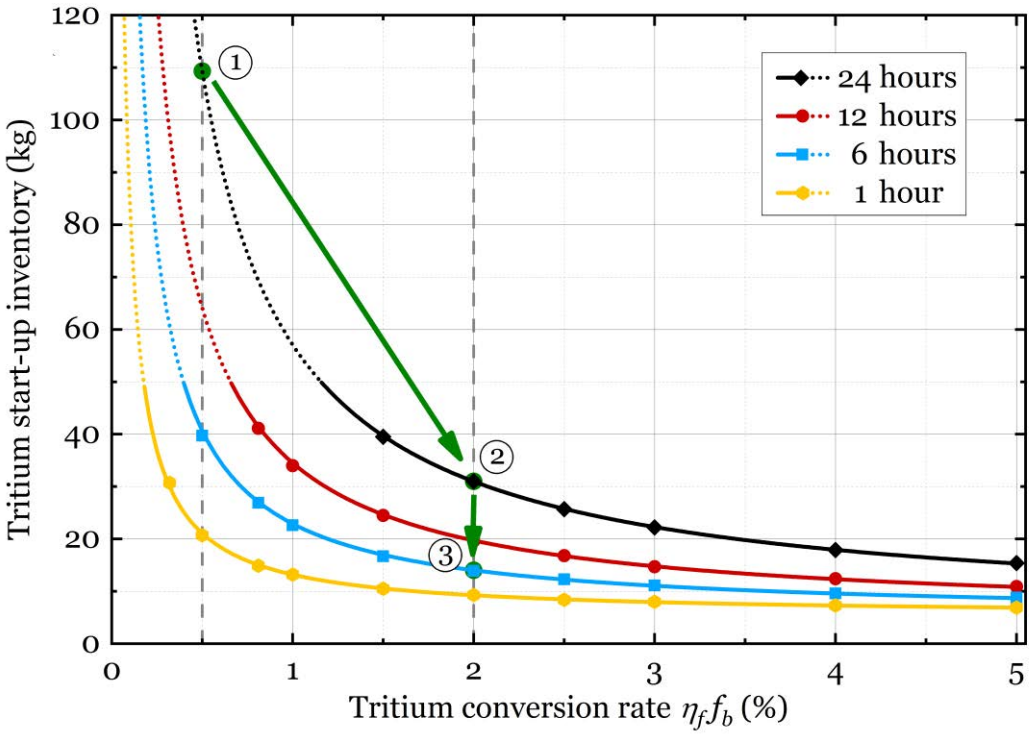

Figure 1.8: Simulation data of a necessary tritium start-up inventory vs. tritium conversion rate for different mean processing times. Simulation results from [33]. The published data only provides data for inventories below 50 kg; a reciprocal fit function is used to extend the graph to higher values. The numbered states show the decrease in inventory due to the DIR in the example described.

1.3 Objective of work

This work aims towards the implementation of Direct Internal Recycling (DIR) based on a metal foil pump (MFP) for future fusion devices.

Many aspects that support this aim are laid out in this thesis. The focus is certainly tailored towards the development path of a metal foil pump. Nevertheless, this is not the sole focus considered in this work. For example, the advantages of the DIR are quantified for the first time, providing a powerful motivation for the implementation of DIR (1.2 Fusion fuel cycle). Another example is the quantification of the concentration of each hydrogen isotopologue in a gas stream leaving an MFP (3.3.3 Release from metal surfaces), which is certainly important for the modelling of the fuel cycle.

For the development of a metal foil pump, the most relevant physics aspects of superpermeability are described. This allows for deriving a model description of superpermeability, which is employed to analyse the processes occurring. Once the requirements are known, the metal foil pump can be tailored to the intended area of use. The description of the limits of superpermeability is also part of this work. Experiments in the dedicated setup HERMES and the model are used for this. They are carried out to quantify the achievable flow rates through an MFP and to identify the technical challenges of such a pump. While working with the HERMES installation, its fundamental limitations became clear. An improved facility, HERMES*plus*, has been developed and commissioned to overcome these restrictions and to enable the use of superpermeability at higher pressures than ever before.

1.4 Structure of work

This doctoral thesis follows the stated objectives. The structure of this work aims to underline this.

In Chapter 1, “Fusion and its fuel cycle”, an introduction to the field and the necessary basic information is given. A special emphasis is put on the fusion fuel cycle, which can be greatly benefited by implementing a DIR loop. This improvement is quantified for the first time in literature.

Chapter 2, “Superpermeability”, explains the effect that is to be used in a metal foil pump (MFP). This chapter provides definitions of the most relevant terms and summarizes the current stage of knowledge.

The “Description of relevant processes” in Chapter 3 highlights separately the occurring physics steps for superpermeability. The relevant material properties from the literature are collected and displayed, along with the theory. This allows the skilled reader to follow the work in the remaining chapters and put the results into context.

Based on the different processes, a “Model description of superpermeability” is developed in Chapter 4. The non-dimensional description allows the differentiation of the governing mass transport limitations in each condition. By applying the model, the performances of different metal foil pumps are given. This resolves the disagreement in the literature on the best material choice for an MFP.

In Chapter 5, “Experimental installations HERMES and HERMES*plus*”, the setups and the incorporated devices are described. In this chapter, the analytical methods used to obtain the experimental results are explained. This also allows for expressing the uncertainty of the measurements.

The previous description of the facilities and measurement methods allows for concentration on the experimental results in Chapter 6, “Superpermeation proof in practice”. An example measurement for each of the setups, HERMES and HERMES*plus*, is presented, followed by several parameter variations. In this chapter, the surface change of metal foils is also documented, as well as information on material aspects of superpermeability.

Chapter 7 is used to provide an outlook for the next possible steps in this field of research. In Chapter 8 the work is summarized.

2 Superpermeability

The effect of "superpermeation[1]" requires a volume of low-pressure hydrogen gas with an energy source that is confined by a metal foil. Depending on the pressure, a plasma source or an incandescent filament can supply the required energy. Superpermeation means that hydrogen is transported through the metal foil in a particular manner. Livshits, the creator of the term "superpermeability", describes it as follows:

> *"Superpermeability, as we understand it, implies that the permeability of a membrane of usual thickness nears its conceivable limit: the permeability of an opening of the same area"* [36].

The term had been coined much earlier, but in a more technical manner:

> *"a penetration probability x ≈ 0.1-1 comparable to the value of x for an aperture in a thin wall can be achieved in real systems. In this letter we refer to this effect as 'superpermeability.'"* [37] [2]

This description can be fulfilled if most of the hydrogen in the upstream volume obtains energy from the described source and if the volume on the other side of the metal foil is constantly evacuated. If the downstream volume is not constantly pumped, the hydrogen will accumulate and cause the pressure to rise. This increase can continue to create much higher pressures than in the upstream chamber. In this case the permeation probability can drastically decrease. As the basis for this pumping still lies in the very same effect as in the previous descriptions, it is necessary to define superpermeation anew:

> *Superpermeation is a physical effect that causes the transport of hydrogen through metal by the combination of an energy source and an energetic surface barrier on the metal foil surface. It is caused by assisted dissociation of hydrogen, which promotes entering the metal bulk.*

This already dives into the explanation of the effect, which will be discussed more thoroughly in the next subchapter.

[1] In the remainder of this thesis, *superpermeation* is used to refer to the described process, while *superpermeability* or *superpermeable* refers to the corresponding property of a system.
[2] In the remainder of this thesis, the Greek letter χ is used to describe the variable x. It is then referred to as "permeation probability".

2.1 Principal physics of superpermeability

To understand superpermeability, it is first necessary to be aware of the processes involved in the classical permeation of hydrogen. In Figure 2.1, these are shown schematically. The figure displays the process from left to right. Hydrogen atoms are shown as small blue dots; the metal lattice of the metal foil is shown with ordered grey circles. The hydrogen molecule first needs to come close to the metal surface (1). Due to the interaction with the metal, it is able to split up into atomic form and adsorb on the metal surface (2). From this surface site, it can be absorbed into the metal lattice (3). Within the metal, it travels by moving from one interstitial site to the next (4). At some point, this will cause the atom to come to the opposite surface (5). By recombining with another surface atom, it can desorb on the back surface of the membrane (6). Hence, permeation requires a clean metal surface to which hydrogen can bind. If hydrogen permeation is to be prevented, the metal surface is often coated by a protection layer. In vacuum technology, for instance, a protective oxide layer is produced by a so-called “air bake” process [38].

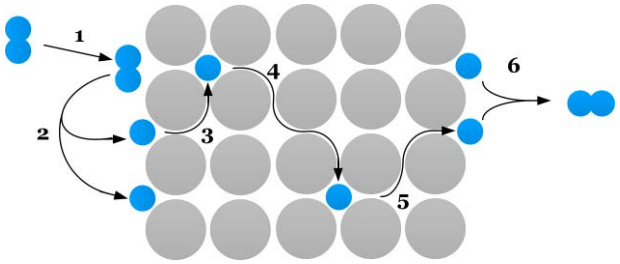

Figure 2.1: Schematic representation of permeation of hydrogen (blue) through a metal (grey).

Superpermeability uses such a protection layer (red circles) to inhibit the process to one direction and, hence, to pump, as illustrated in Figure 2.2. Before meeting the metal membrane, the hydrogen molecule is dissociated by an external source, displayed here by the yellow flash (2). Thus, it does not need a clean metal surface to enter the metal lattice (3). As soon as the atomic hydrogen has entered the metal, however, it cannot return to the surface (3a) and must penetrate the foil through the process explained above (4–6).

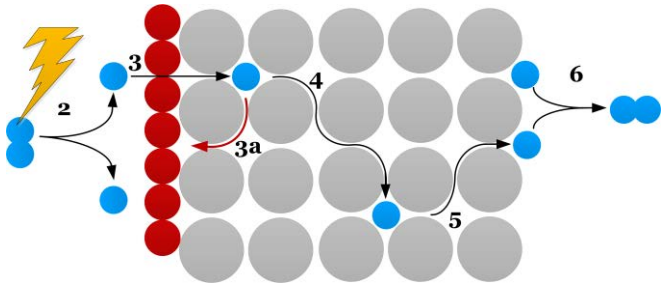

Figure 2.2: Schematic representation of superpermeability of hydrogen (blue) through a metal (grey).

The previous explanation provides an idea about superpermeability. Nevertheless, this description does not cover all aspects of superpermeability, as it simplifies the processes.

In the aforementioned example, atomic hydrogen is the species that approaches the metal foil surface. This is not the only form of hydrogen that can enter the metal foil through a surface barrier: all species that carry enough energy can do so. A reaction enthalpy, as in the case of atomic hydrogen, is one example of this. Another possibility is a high kinetic energy for accelerated molecules or ions [39]. All these forms of hydrogen can be utilized and are summarized as "suprathermal hydrogen" in the following.

A second simplification that was made in the previous description concerns the protection layer. In the schematic description, it is a perfect, monoatomic layer on one side of the membrane, but it is nearly impossible to attain such a condition on large surface areas. The different approaches for coping with this are described in the following.

2.2 Present stage of knowledge

The first account of superpermeability dates to the year 1938. Günterschultze et al. observed deuterium ions passing through an iron plate [40]. Back then, the term "superpermeability" had not yet been coined, but the comments in the paper describe the effect quite precisely. In a report from 1961, the increase of hydrogen permeation through thin metal foils by applying a glow discharge close to the metal foil is also likely to have been caused by superpermeability [41]. In 1963, Young published the design of a pump based on superpermeability [42]. The explanation of the working principle in this publication is different from superpermeation, but the design suggestion and the operation parameters allow the claim that this pump operates with this effect. From these examples, one can see that superpermeability has been studied independently in a variety of locations for a long time. The research from the different places is only weakly interlinked. This can be attributed mainly to two reasons. First, the subject of superpermeability has not had a common, well-established term until more recently. Without such a specific term, it is difficult to find other related publications. Second, most of the research was carried out during the Cold War, and research was published either in English or in Russian. Although some of the relevant Russian journals have been translated into English, the translation is often mediocre at best.[3] This second factor only began to play a role once different groups, mainly in Russia and Germany, followed this topic for extended periods.

In Russia, A.I. Livshits has worked on the topic of superpermeability for many years. Many of the important milestones in the field have been published by him. He is still working in the field and, since the 1970s, has been based at the Bonch-Bruevich St. Petersburg State University of Telecommunications in Russia. Over the years, he has collaborated with M. Bacal and her group at the Laboratoire de Physique et Technologie des Plasmas at the Ecole Polytechnique in Palaiseau, France, and Y. Hatano and K. Watanabe at the Hydrogen Isotope Research Center in Toyama, Japan. Livshits' motivation to enter this field of research was

[3] Statement by A.I. Livshits on the English translations of some of his papers (in an email to the author on 07.11.2016).

already aimed at the development of a hydrogen vacuum pump. Most of his publications focus on the different physical correlations and effects.

In the 1980s, intensive research was carried out by F. Waelbroeck and his group at the Institut für Plasmaphysik at the nuclear research centre in Jülich, Germany. Their interest was sparked by an uncommon outgassing behaviour by the stainless steel-walled tokamak TEXTOR [43]. The group collaborated with other institutes of the nuclear research centre and had W. Shmayda as a visiting researcher for several stays. Research in this field was discontinued in Jülich when the carbonization of the tokamak wall became common practice [44]. Based on the ideas of Waelbroeck, the research in this field was continued at the Institute for Aerospace Studies at the University of Toronto until the early 1990s.

Superpermeability has been demonstrated with various metals, such as palladium [45–47], iron [48, 49], molybdenum [50], nickel [37, 51], vanadium [52] and niobium [53, 54]. It has also been demonstrated with composite metal foils. These membranes consist of a foil made from one base material with a thin metal coating on one or both sides. The tested composites are copper-AISI 1008 mild steel [55], copper-iron, iron-palladium, copper-iron-palladium and palladium-copper (the base metal is underlined) [56]. While the application of cover layers has proven to be one way of altering the surface conditions, this is also possible through non-metal cover layers [57]. In these cases, not a macroscopic layer is formed, but one with a thickness in the order of one monolayer. To be more accurate, these non-metal layers are often necessary for superpermeability. While most of the studies with pure metals have relied on "natural" surface layers, these can also be introduced by adding O_2, H_2O [58], H_2S, C_6H_6 or C_2H_2 [36] to the upstream gas mixture. While these surface layers can be introduced from the gas phase, they can also be sustained from dissolved non-metals in the bulk [52].

The two research groups that worked for an extended period in the field favour different metal foils for the construction of a pump. While Waelbroeck's group favours iron or coated iron membranes, Livshits favours the group 5 metals niobium or vanadium with non-metal surface layers. Although these materials display significantly different properties, these choices have never been rated.

As energy sources for the hydrogen, incandescent filaments [59, 60], glow-discharges [41, 51], accelerated hydrogen beams [61–63], inductively coupled RF discharges [64, 46], electron cyclotron resonance (ECR) plasma [65] and a multicusp plasma setup [66], as well as thermal plasmas of fusion devices [67, 68], have been used. All designs for a pump based on superpermeability suggest and employ incandescent filaments.

While many experiments have been performed with protium and deuterium, one setup has additionally operated successfully with tritium [69]. The excellent separation capability between hydrogen and other gases has been proven multiple times [70, 60].

Most experimental papers also describe the underlying processes, but some dedicated theory publications attempt to provide more holistic explanations [71–74, 36]. For some of the mathematical descriptions, no analytic solution is known. This is true for some steady state permeation regimes, as well as for the transient behaviour. Thus, numerical tools need to be used. For the plasma-wall interaction of tokamaks, similar processes must be considered. This

gave rise to the development of specialized computer codes, which can also be employed for superpermeability calculations (e.g. PERM [75] and PERI [76, 77]).

While the processes behind superpermeability play an important role for metallic first walls of fusion devices, the deployment as a hydrogen-selective pump has also previously been suggested [62]. Even the operation conditions for such a pump for ITER have been evaluated [78], although this proposal has not been continued further. Additional investigations have also revealed a major drawback of all proposed metal foil pump designs: the use of incandescent filaments is only reasonable below a certain operation pressure [79].

While many challenges in the field of superpermeability have already been addressed, some important questions remain unanswered. The advantages and disadvantages of the different metal foil materials need to be evaluated in order to be able to provide a reasonable recommendation for a DEMO pump. This is especially important given that the main research groups in the field disagree on this matter, and all their ideas should be considered. In view on the operation limitations of incandescent filaments as suprathermal hydrogen sources, an alternative needs to be found to cover the complete expected operation regime for DEMO.

2.3 Steps in the superpermeation process

In the exemplary description of superpermeability, all steps are described for a single atom in a consecutive manner. For a pump working on this principle, the view on a single atom is much too narrow. During such a process, many steps are occurring for many different atoms at the same time. This will lead to the interplay of the different steps. Nevertheless, the aforementioned description includes all the important processes.

To be able to separate the occurring processes, they are shown schematically in Figure 2.3. These are:

① Production of suprathermal hydrogen,

② Transport from the suprathermal hydrogen source to the metal foil,

③ Upstream surface processes on the metal foil: ad-, ab- and desorption,

④ Diffusion and trapping in the bulk,

⑤ Downstream surface processes on the metal foil: ad-, ab- and desorption.

In the following chapter, the different steps are highlighted individually. ① and ② can be found in sections 3.1 and 3.2. As the physics behind the processes in ③ and ⑤ are the same, they are discussed in 3.3.1 together. Step ④ is discussed in 3.3.2. Some considerations for the isotopologue composition, which forms in process ⑤, are given in 3.3.3. In Chapter 4, all steps concerning the metal foil are combined in a model. In Chapter 5 the experimental facilities are described, while in Chapter 6 the experimental work is presented.

Describing these process steps requires the combination of several research fields. These include plasma physics, vacuum technology, material- and surface science. Breaking down the superpermeation process into individual steps and understanding the physical basis for each of them is thus important in order to describe their interplay successfully. It can be seen as the main cornerstone for the successful development of a metal foil pump.

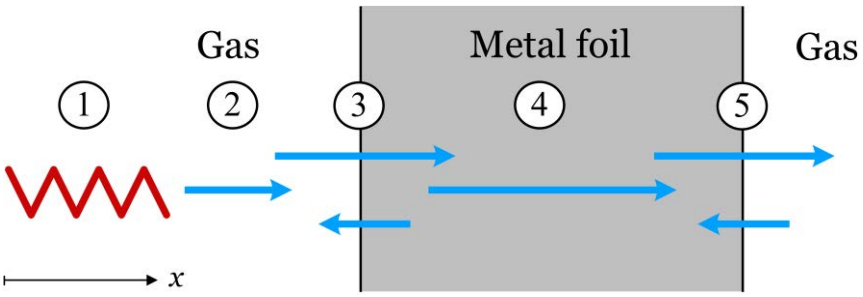

Figure 2.3: The relevant process steps for superpermeability.

3 Description of relevant processes

Many processes under investigation can be easily understood for a single atom or molecule, but in order to derive macroscopic effects, the collective behaviour must be described. Most of the following explanations are based on the kinetic theory of gases [80]. The collective behaviour of gases is commonly treated in statistical physics by distribution functions. These functions describe the number of particles that are in a given state, e.g. at a given position $\vec{x}$ and with a given velocity $\vec{\xi}$ at a certain point in time *t*. The term "particle" is used here to summarize atoms and molecules.

A Gaussian distribution of velocities describes the characteristic properties of a system in global equilibrium (see equation (0.1) in the appendix). This Gaussian distribution with the standard deviation ${\sigma_{sd}}^2$ of,

$${\sigma_{sd}}^2 = \sqrt{\frac{\mathrm{k}\,T}{m}}, \tag{3.1}$$

is called the Maxwell-Boltzmann distribution f^M. T is the temperature of the gas in [K], k is Boltzmann's constant and m is the mass of the particle. It is given in one dimension by

$$f^M(m,T,\xi_x) = \sqrt{\frac{m}{2\,\pi\,\mathrm{k}\,T}}\exp\left\{-\frac{m\,{\xi_x}^2}{2\,\mathrm{k}\,T}\right\}. \tag{3.2}$$

If it is assumed that the distributions of the three possible directions in space are independent and isotropic, the distributions can be multiplied to yield

$$f^M\left(m,T,\vec{\xi}\right) = \left(\frac{m}{2\,\pi\,\mathrm{k}\,T}\right)^{3/2}\exp\left\{-\frac{m\,\vec{\xi}^2}{2\,\mathrm{k}\,T}\right\}. \tag{3.3}$$

If not, the velocity $\vec{\xi}$ as a vector is needed, but the speed u, which is a scalar, can be derived with:

$$u = \left|\vec{\xi}\right| = \sqrt{{\xi_x}^2 + {\xi_y}^2 + {\xi_z}^2}, \tag{3.4}$$

to give

$$f^M(m,T,u) = 4\,\pi\,u^2\left(\frac{m}{2\,\pi\,\mathrm{k}\,T}\right)^{3/2}\exp\left\{-\frac{m\,u^2}{2\,\mathrm{k}\,T}\right\}. \tag{3.5}$$

Quite an interesting observation can be made. Even when multiple types of particles with different masses are present and interact, the velocity of each type can be described with the given equations. As the different species also interact with each other, one may ask which physical quantity distributes between the two species. The answer becomes clear if the Maxwell-Boltzmann distribution is rewritten as an energy distribution. This gives:

$$f^M(T,E) = \sqrt{\frac{4\,E}{\pi\,\mathrm{k}^3\,T^3}}\exp\left\{-\frac{E}{\mathrm{k}\,T}\right\}. \tag{3.6}$$

This description of the distribution does not contain the mass anymore. Even if particles with different masses are present and interact, one global energy distribution, which can be described by equation (3.6), will be the equilibrium case. Therefore, the Maxwell-Boltzmann distribution is actually an energy distribution. There is no clear physical explanation for why this is the case and there is not another property, such as the momentum, that distributes evenly.

This distribution is quite important for the work in this thesis because many processes, which will be described later, are thermally activated. A description of a rate constant, such as the recombination coefficient k_r, of the form

$$k_r = k_{\mathrm{r},0}\exp\left\{-\frac{E}{\mathrm{k}\,T}\right\}, \tag{3.7}$$

will be found to be valid for processes such as diffusivity and solubility. The exponential term defines a probability that the particles contain at least a certain amount of energy E. The factor k_0 can be seen as an "attempt frequency" – the frequency with which a certain reaction could occur if the particle had sufficient energy. The characteristic energy E in a thermally activated process can be easily determined by plotting the temperature dependence in logarithmic form (Arrhenius plot).

A brief introduction to the energy distribution of particles in thermal equilibrium has been given. This behaviour is the basis of most processes in superpermeation and is thus described in the introduction of this chapter. The different steps that occur during superpermeation are highlighted individually in the following.

3.1 Particle transport in vacuum

The previously given basic equations can be used to derive some of the important properties to describe the transport of particles in vacuum.

One of these important properties is the mean molecular speed $\bar{u}$ of particles. This can be obtained by integrating the product of the speeds with their corresponding probability density over all speeds [81]. If the velocities are discrete values, one could understand this as the sum of all speeds multiplied by their corresponding probability:

$$\bar{u} = \int_0^\infty u\,f^M(m,T,u)\,du = \sqrt{\frac{8\,\mathrm{k}\,T}{\pi\,m}}. \tag{3.8}$$

The full integration can be found in equations (0.2) to (0.5) in the appendix.

Another value that must be determined for later calculations is the flux of particles hitting or crossing a surface from one side. Assuming that this surface lies in a plane orthogonal to the *x*-axis, one can use equation (3.2) for the calculation. For this calculation, one wants to know how many particles hit the plane from one side, so we take all particles with a positive velocity

in the *x*-direction into account. To obtain a molar flux $\dot{n}$, the probability density has to be multiplied by a number density ϱ_n of the gas [81]. Thus, the equation is

$$\dot{n}_x = \int_0^\infty \varrho_n \, f^M(m, T, \xi_x) \, d\xi_x = \varrho_n \sqrt{\frac{\mathrm{k}\, T}{2\,\pi\, m}} = \varrho_n \frac{\bar{u}}{4}. \tag{3.9}$$

The full integration can be found in equation (0.6) in the appendix. Instead of a number density, the pressure can also be used to express this flux. As this expression will be used frequently, the gas- and temperature-dependent variable μ is introduced, which combines all factors for a direct conversion from pressure to surface flux:

$$\dot{n}_x = \varrho_n \frac{\bar{u}}{4} = \frac{p}{\mathbb{R}\, T} \frac{\bar{u}}{4} = \frac{1}{\mathrm{N_A}\sqrt{2\,\pi\, m\, \mathrm{k}\, T}} p = \mu\, p, \tag{3.10}$$

where $\mathrm{N_A}$ is the Avogadro number and $\mathbb{R}$ the universal gas constant. This molar flux can be easily transferred into a volumetric flux j given by:

$$j = \dot{n}\, \mathbb{R}\, T. \tag{3.11}$$

Equation (3.10) can be rephrased to yield a volumetric, or pV-flow, a common measure for a flow of a substance in vacuum technology. This gives:

$$J = A \frac{\bar{u}}{4} p. \tag{3.12}$$

This pV-flow can be transformed easily into a volumetric flow by using

$$S = \frac{J}{p}. \tag{3.13}$$

A volumetric flow that is compressed by a vacuum pump is commonly called pumping speed and is indicated by the letter S. For a channel or geometry between a gas source and a vacuum pump, the term conductance, indicated by a C, is used to describe how well gas can move through the geometry. In this case, the pressure difference Δp between the two sides of the channel is important. This changes the equation only slightly to:

$$C = \frac{j}{\Delta p}. \tag{3.14}$$

While the Maxwell-Boltzmann distribution is time-independent, as it describes an equilibrium case, this is not the case for all distribution functions. A description of the distribution of particles will contain information on the position $\vec{x}$ and the velocity $\vec{\xi}$ (or momentum in some descriptions) of each particle at a given time. The difference between one distribution and the distribution after an infinitesimal time step is influenced by three factors: first, the change in position due to the velocity; second, the change in velocity due to an external force; and third, changes due to collisions. This is described in the Boltzmann equation [82]

$$\frac{\partial f\left(\vec{x},\vec{\xi},t\right)}{\partial t} + \vec{\xi} \frac{\partial f\left(\vec{x},\vec{\xi},t\right)}{\partial \vec{x}} + F \frac{\partial f\left(\vec{x},\vec{\xi},t\right)}{\partial \vec{\xi}} = \left(\frac{\partial f\left(\vec{x},\vec{\xi},t\right)}{\partial t}\right)_{coll}. \tag{3.15}$$

In the classical description of the collision term, only two-particle interactions are considered. This is in any case the most probable collision term, as the likelihood of two particles interacting is always higher than for three or more particles. Only for special cases – for example, where reactions can occur during a three-particle interaction – do they need to be considered. If the density of particles in a certain volume is very low, one can neglect the collision term, as the likelihood of two particles coming within interaction distance is miniscule. To determine the relevance of the collision term, the Knudsen number is used. It can be used to transfer equation (3.15) into to a dimensionless form [83]. The dimensionless Knudsen number is defined by

$$Kn = \frac{\bar{l}}{L_c}. \tag{3.16}$$

It consists of the mean free path $\bar{l}$ that a particle travels before it collides with another one and the characteristic length L_c that describes the dimension of the sourrounding vessel. The mean free path for a certain temperature T and pressure p can be calculated by

$$\bar{l} = \frac{\mathrm{k}\,T}{\sqrt{2}\pi D^2 p}. \tag{3.17}$$

The diameter of the collision cross-section D of the particles can be determined in various ways. A common approach is the calculation of the collision cross-section from the gas viscosity at low densities. To obtain the cross-section diameter for different temperatures, the Sutherland correction is often used:

$$D(T) = D_\infty \sqrt{1 + \frac{T_S}{T}}. \tag{3.18}$$

This equation considers the fact that at high temperatures the cross-section diameter D_∞ appears smaller than at lower temperatures. The correction term T_S is the temperature at which the effective particle diameter appears to be twice as big as at high temperatures. Due to the slower particle speeds at lower temperatures, the attractive force between the particles increasingly affects the paths travelled.

If the mean free path is much smaller than the dimensions of the vessel that contains them, the collisions between particles dominate the process. In these cases, the Knudsen number is very small. This is the most common regime in everyday life; it is called viscous regime and can be described through the classic approaches of fluid mechanics. For the description of these processes, the gas–surface interaction is often neglected and the speed of the fluid close to a wall is assumed to be zero. The other extreme, marked by very big Knudsen numbers, describes the free molecular regime. In this case, the surface interaction is very important and is the only interaction of the particles. In between these two regimes, the so-called transitional flow can be found. It is the region around a Knudsen number of one, so the interaction between different particles and the interaction with the wall are equally likely. Sometimes a fourth regime is also used, which is called the “slip-flow” regime. It lies between the transitional and continuum flow and treats the surface interaction with a slip-flow coefficient. The different flow regimes can be determined with corresponding Knudsen numbers, shown in Figure 3.1.

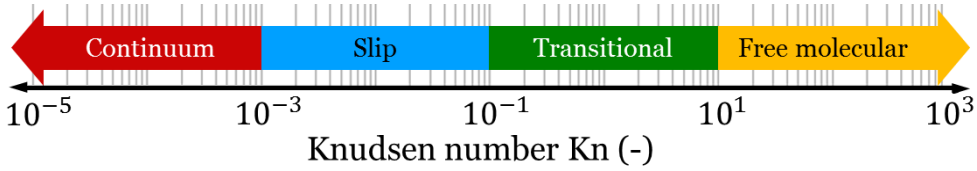

Figure 3.1: The different flow regimes and the Knudsen numbers in which they apply, according to [84].

Obviously, the boundaries between these regimes are not rigid but aim to describe the validity of a certain approach to describing a vacuum flow.

To illustrate this relationship, the flow rate through a long rectangular channel is calculated using different approaches and is depicted in Figure 3.2. On the lower *x*-axis and on the left *y*-axis, a dimensionless description is given. On the top *x*-axis and the right *y*-axis, this is transferred to one special case: hydrogen (protium) at $298\,\mathrm{K}$ passes through a channel with a rectangular opening of $5 \times 50\,\mathrm{mm}$ and a length of $75\,\mathrm{cm}$. The corresponding pressure for hydrogen at $298\,\mathrm{K}$ is calculated via the collision cross-section, with $D_\infty = 2.3 \cdot 10^{-10}\,\mathrm{m}$ and the Sutherland correction of $T_S = 110\,\mathrm{K}$, as given in [85]; also see Table 11 in the appendix.

On the *x*-axis, the Knudsen number is given; on the *y*-axis, the flow rate through the channel is given. The mathematical description that best meets the reality is marked by “kinetic”. This case solves the Boltzmann equation (3.15) with a kinetic description of the collision term called the BGK Model, which is the most common approach for isothermal use cases [87]. Calculating this case is achieved by the Direct Simulation Monte Carlo Method (DSMC), which is computationally very demanding and is thus mainly used for calculations in the transition regime. At very small Knudsen numbers, the continuum description is normally used; it is based on the Navier-Stokes equation, with a boundary condition of a speed of zero at all walls. For higher Knudsen numbers this description fails, as it underestimates the actual flow. To improve the hydrodynamic calculation, a slip parameter can be introduced, which greatly improves the flow calculation for higher Knudsen numbers. For very high Knudsen numbers, the free molecular description gives a good estimation of flow. For simple geometries, empirical equations are given in the literature, but for cases that are more complicated, the Test Particle Monte Carlo (TPMC) method is used.

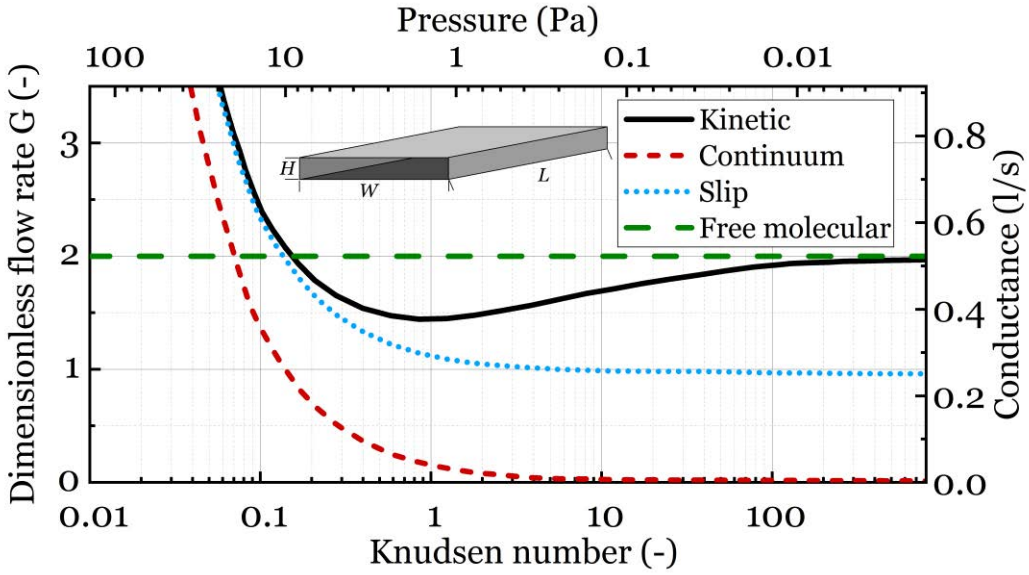

Figure 3.2: Calculated flow of gas through a rectangular, long channel with a height-to-width ratio of 1: 10. The "kinetic" curve is closest to the actual flow; the other models are shown to display their limitations. The bottom *x*-axis and the left *y*-axis are always valid for this geometry. The top *x*-axis and the right *y*-axis are calculated for H_2 at 298 K and a channel with $H = 5$, $W = 50$, $L = 750$ mm. The flow calculations are shown in [86].

The TPMC calculates the paths of the different particles individually. From the entrance opening, the particles are released with a certain velocity distribution. The speed of release corresponds to the Maxwell-Boltzmann distribution of a chosen temperature. The particles travel in straight lines until they hit a surface. There they are adsorbed and released, with the surface temperature and a certain release angle. In most calculations, a fully random release angle is assumed. A large number of particles has to be simulated to obtain sufficient statistics to achieve a good result. As no particle interaction is considered, the calculation of each particle is independent of the others and the calculation can be parallelized. The test volume must be fully enclosed by boundaries, with either reflection conditions for walls or release conditions for openings. The most common entrance condition is that particles enter as described and leave the system when they cross this opening in the outward direction. This allows the creation of the ratio between the number of entering particles $\#_{in}$ and the number of particles that leave through the entrance opening $\#_{out}$:

$$\Omega = \frac{\#_{out}}{\#_{in}}. \tag{3.19}$$

This ratio Ω is called the capture coefficient or Ho-factor, after [88]. This factor allows determining the conductance or effective pumping speed in relation to the entrance area of the element in question by extending equation (3.13):

$$C = A\frac{\bar{u}}{4}\Omega. \tag{3.20}$$

The previously given explanations on vacuum flows are crucial for the metal foil pump for two reasons. First, it is planned to install the MFP in proximity with the DEMO torus. This

means that it will have to operate at similar pressures as found in the divertor. Obviously, the pressure must always be lower than this, as a pressure difference will drive the gas flow; compare equation (3.13). Second, the processes within the metal foil pump will be dominated by the vacuum conditions. This is especially true for the production and transport of the suprathermal hydrogen, which will be discussed in the following.

3.2 Production of suprathermal hydrogen

For the absorption of hydrogen gas into a metal lattice, the molecule must split up as it dissolves into metals in atomic form. For the reaction from hydrogen molecule to atomic hydrogen, the reaction enthalpy has to be provided, which in this case is equal to the binding energy. For a hydrogen (protium) molecule, this is $2.26\,\mathrm{eV}$ per atom[1] (for each of the six hydrogen isotopologues, this is between 2.24 and $2.30\,\mathrm{eV}$ [8]). This energy must be provided for superpermeability. Dependent on the operating conditions, various devices converting incoming hydrogen to suprathermal hydrogen can be used. As the envisioned operation will be directly connected to the exhaust region of the DEMO torus, the operation pressure needs to be in the same range. The intended divertor pressure of DEMO is not yet known, and nor is the conductance between torus and pump. Thus, a solution for the complete expected pressure range has to be provided.

The demanded operation pressures for DEMO are shown in the upper part of Figure 3.3. As described earlier, DEMO is expected to be a tokamak and therefore a pulsed machine. The main gas load has to be pumped via the divertor during the pulses. The expected pressure regime therefore depends strongly on the plasma scenario and the chosen divertor solution. For the classical ITER-style divertor in the DEMO configuration, together with an H-mode high-density plasma, the currently expected pressure range is between 10 Pa (burn) and 2 mPa (dwell) [89], in which the dwell time denotes the time for re-establishing the magnetic system and the plant for the next plasma pulse. However, more stable plasma scenarios are currently being explored as alternative and more advanced divertor solutions, where alternative magnetic configurations may be chosen in DEMO. Therefore, the task for this work is to demonstrate that suprathermal hydrogen sources that can cover a wide pressure range can be used for the demonstration of superpermeability, namely between $100\,\mathrm{Pa}$ and $5 \cdot 10^{-4}\,\mathrm{Pa}$. While it is certainly desirable that the metal foil pump continues to pump during the dwell time, as this accelerates the pressure decrease, it is not necessary. The main function of the metal foil pump is the separation of hydrogen. As the amount of gas pumped during the dwell time is orders of magnitude smaller than during the pulse, this load can easily be taken by the tritium plant.

In the lower part of Figure 3.3, the operating pressures of the different suprathermal hydrogen sources in the presented work are displayed. One important reason for the selection of these sources is the coverage of the whole operation pressure range. Others relate to the previous demonstration in the literature or the scalability.

[1] From [90]: 52.103 ± 0.003 kcal/mol at 298 K converted to 2.26 eV/atom or 218.3 kJ/mol.

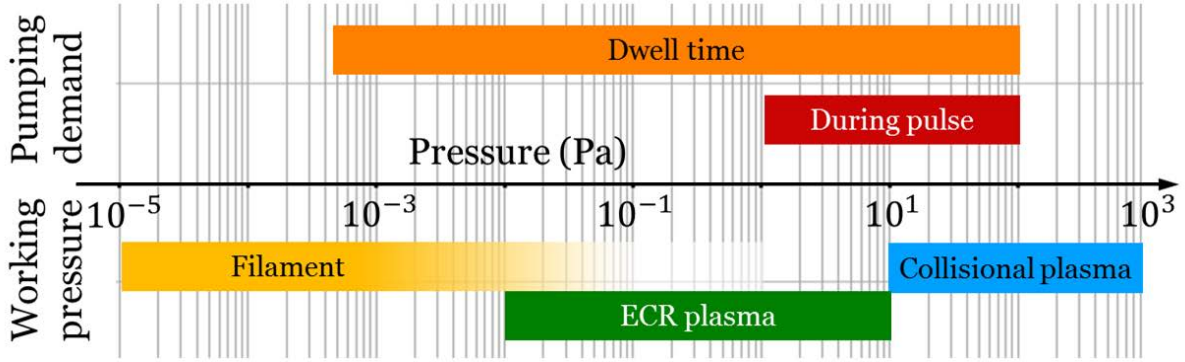

Figure 3.3: Likely pressures at which vacuum pumping of the torus are required in DEMO and working pressures of selected atomic hydrogen sources for a metal foil pump. Working pressure for filament from [79], for ECR plasma from [91] and for collisional plasma from [92].

In the following, the different approaches are highlighted. The collisional and ECR plasma sources are treated together as "cold plasma source", as they share common physics.

3.2.1 Production by a hot filament

The most straightforward approach for supplying this energy is by splitting the molecule. A common way to do this is using an incandescent filament. This has been used for many experiments on superpermeability [79, 93, 94].

The physics of the atomization is surprisingly simple. Three main steps govern its behaviour:

Dissociative adsorption of hydrogen molecules on the metal surface,

Thermal desorption of atomic hydrogen,

Recombination of hydrogen atoms on the surface and release as molecules.

The pressure and the temperature of the surrounding gas determine the hydrogen flux onto any surface. A hydrogen molecule impinging on a filament surface has material-dependent likelihood α_{m} to be adsorbed. For clean metal surfaces, this is temperature-independent; some relevant values are shown in Table 1.

Table 1: Relevant material properties for hot filament atomic hydrogen sources. Sticking coefficient of molecular hydrogen on clean metal surfaces from [95], melting temperatures at STP from [96] and thermionic emission temperatures calculated with data from [97]; see (0.8) and Table 13 in the appendix.

		W	Pt	Nb	Ta	Mo	Thoriated W
Sticking coefficient α_m	$(-)$	0.3	0.24	0.2	0.2		f(p, T) $\ll$ 0.2
Melting temperature	(K)	3683	2045	2741	3269	2890	
Temperature for thermionic emission of 1 $\mathrm{A/cm^2}$	(K)	2400	2849	2166	2195	2218	1673

The surface-specific volumetric flow of atomic hydrogen S_a/A coming from an incandescent filament for the two extreme cases is given by

$$\frac{S_a}{A} = \sqrt{\frac{2\,\mathbb{R}\,T_g}{\pi\,\tilde{M}}} \cdot \begin{cases} \alpha_m, & p \ll p^* \\ \beta_a(T_f, p), & p \gg p^* \end{cases}. \tag{3.21}$$

Two temperatures are included in this equation. The (average) gas temperature T_g is used in the square root term. This part describes the volumetric flux of gas impinging on the filament. For pressures significantly higher than the transition pressure p^*, the filament temperature T_f is needed to describe the likelihood of atomization. The validity of each of the two functions is only given at pressures that considerably differ from the transition pressure.

If the atomic release of hydrogen is much faster than the recombination, the adsorption governs the production, and equation (3.21) for the case $p \ll p^*$ is applicable. The release of atomic hydrogen in the case of equilibrium between dissociation and recombination is given in equation (3.21) for the case of $p \gg p^*$. The atomization likelihood β_a is a function of the filament temperature and of the pressure. In equilibrium, the atomization rate and the recombination rate will be the same, which can be described by

$$\beta_a\,\mu_{Q_2} p_{Q_2} = \frac{1}{2}\beta_S\,\mu_Q\,p_Q. \tag{3.22}$$

The recombination coefficient for hydrogen atom recombination upon surface contact β_S typically has a similar value as the sticking coefficient α_m [79]. If the thermal equilibrium constant $K_{e,m\,a}$ between the atomic and molecular hydrogen is defined by

$$K_{e,m\,a} = \frac{p_{Q_2}}{p_{Q}{}^2}, \tag{3.23}$$

the last two equations, together with the substitution of the recombination coefficient, can be combined to give

$$\beta_a = \frac{1}{2}\frac{\mu_Q}{\mu_{Q_2}}\alpha_m\sqrt{\frac{K_{e,\mathrm{m}\,a}}{p}} \tag{3.24}$$

for small fractions of atomic hydrogen. Taking information from the literature on the equilibrium constant for protium [79], the equation can be expressed as:

$$\beta_a = 80.65\;\alpha_m \frac{\left(T_f/[\mathrm{K}]\right)^{0.61}}{\sqrt{p/[\mathrm{Pa}]}} \exp\left\{\frac{-218.3\ [\mathrm{kJ/mol}]}{\mathbb{R}\,T_f}\right\}. \tag{3.25}$$

A few features of this relationship already give a hint to the underlying processes. The exponential part of the equation is typically for thermally activated processes, as it describes which fraction of particles has the shown or a higher energy. The energy (-218.3 kJ/mol) used in this equation is the binding energy of each atom in the hydrogen molecule. The square root dependency of the pressure indicates that the likelihood of having two neighbouring atoms on the metal surface plays a role. This is certainly important for the recombination of atoms to a molecule. This dependency is explained in more detail in section 3.3.1.

The pressure p^* is simply the intersection point of the two functions. It is given by

$$p^* = \left(80.65\,\left(T_f/[\mathrm{K}]\right)^{0.61}\exp\left\{\frac{-218.3\ [\mathrm{kJ/mol}]}{\mathbb{R}\,T_f}\right\}\right)^2 \mathrm{Pa}. \tag{3.26}$$

These described equations fit very well with the experimental observations as shown in [79]. The atomization speed of such a filament over the gas pressure is displayed in Figure 3.4. One can clearly see the constant atomization speed for low pressures and the decreasing atomization speed for high pressures.

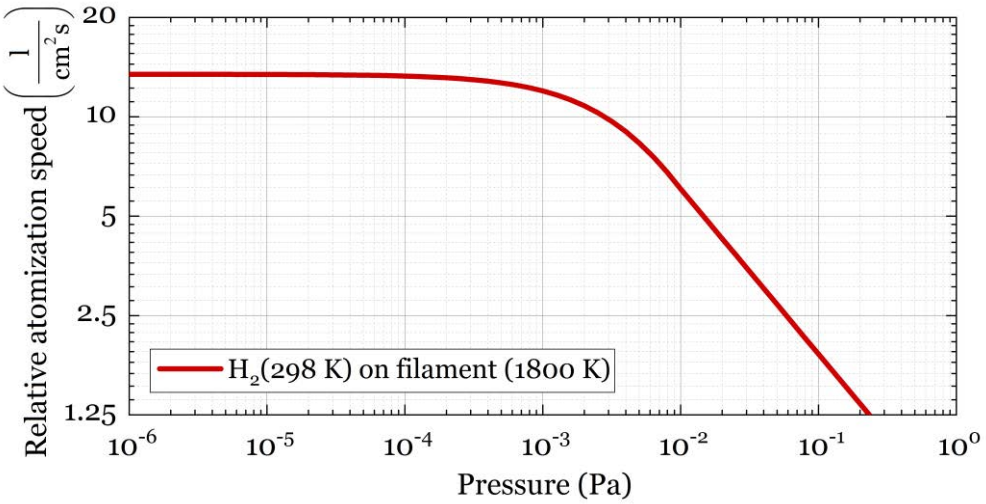

Figure 3.4: Relative atomization speed per filament surface area of incident hydrogen at a temperature of 298 K for a filament at 1800 K, according to [79].

Equations (3.21) and (3.26) show that a higher temperature of the filament is favourable for an extended operation regime. Obviously, the temperature of the filament is limited. This is not only determined by the melting temperature of the material, but also by its vapour pressure. If the filament is operated at too high temperatures, it thermally sputters itself onto the surrounding surfaces. As a short distance between the suprathermal hydrogen source and the superpermeable metal foil is desired, this will cause the formation of a metal layer on the superpermeable membrane. This can degrade its performance. Another limiting factor for this process is the thermionic emission of electrons. Depending on their work function Φ, hot metals emit electrons. Although these electrons can aid the production of suprathermal hydrogen, this inhibits the production of atomic hydrogen. This is the reason why the sticking coefficient of molecular hydrogen on thoriated tungsten, which is specially designed to have a low work function, is not a simple value, but a function of temperature and pressure. Some example values for the thermionic emission are given in Table 1. This does not exclude thoriated tungsten from being used, but it is unclear how efficient the production of suprathermal hydrogen is. This is the reason why thoriated tungsten is not investigated further in this work.

From the point of the melting temperature and the sticking coefficient, a filament made from tungsten is superior. This has also been used in multiple studies [59, 60, 98]. Another possible route is to make the metal foil and filament compatible, so that even if the

superpermeable membrane is covered by the filament material, it does not cause a problem. This is especially true for the materials V, Nb and Ta, which are all in group 5 of the periodic table and have very similar chemical properties. This is used for example in [69].

The successful operation of a filament demands a clean filament surface. Especially trace amounts of oxygen passivate the surface of group 5 metals. This effectively hinders the use as a filament, which can become a problem if the vapour pressure of water is significant in the operation regime. A filament in operation has a very high capture coefficient for water molecules. While the hydrogen in this molecule can be released by the above described principles, there is no release mechanism for the oxygen. The oxygen will preferably be located on the surface and will hinder the effective operation. The use of the filament at very high temperatures (~ 2300 K) can mitigate this problem partially by increasing the diffusion of the oxygen into the bulk, but the sputtering of the filament material sets a limit to this practice. One must supply a release mechanism for the oxygen if a successful operation is desired. This can be done by dissolving carbon in the metal. To do this, the filament is previously heated in a methane atmosphere. The methane will stick to the surface and the hydrogen can be released by the aforementioned processes. If carbon and oxygen are both present, they can be released in the form of carbon monoxide (CO) or carbon dioxide (CO_2). This process will only work as long as carbon is still present in the filament.

In summary, the filament is a reliable atomic hydrogen source for low pressures but has its limitations at higher pressures. This is obvious if one considers the fact that the interaction of different gas particles in the free molecular regime is extremely unlikely. This is the reason why only surface reactions are viable to produce suprathermal hydrogen at low pressures. This is also the reason why this method does not have a limiting lower pressure. For higher pressures, gas phase reactions can also be taken into account.

3.2.2 Production by a cold plasma source

The most straightforward way to supply energy evenly to a gas phase is via an electric field that acts upon charge carriers in the bulk. There is always a small number of free electrons in a gas phase due to natural radioactivity or cosmic radiation, which can act as an initial energy recipient. A static electric field would accelerate the electrons towards an anode, which would get lost upon contact, thus a changing electric field – or, in other terms, electromagnetic radiation – is used. In the right conditions, the electrons gather enough energy to ionize neutrals upon collision and thus create more free electrons. A gas with a high rate of ionization is called plasma. For the production of suprathermal hydrogen, many collisions with electrons are needed. In order to produce a high amount of suprathermal hydrogen, a high concentration of electrons is thus desirable. Unfortunately, there is a limit to the number of electrons, as they make the plasma more conductive, which will result in a reflection instead of absorption of the electromagnetic wave. This "cut-off" density n_c can be calculated by [91]:

$$n_c = \frac{{\omega_0}^2 \varepsilon_0 \mathrm{m_e}}{\mathrm{e}^2}. \tag{3.27}$$

It is dependent on the angular excitation frequency ω_0 and several constants. These are the vacuum permittivity ε_0, the mass $\mathrm{m_e}$ and the charge e of an electron. This equation shows that a

higher frequency is more desirable for obtaining a high electron density. For the experimental work, a frequency of $2.45\,\mathrm{GHz}$ has been chosen, which corresponds to a cut-off density of $7.5 \cdot 10^{16}\,\mathrm{m}^{-3}$. While in theory the cut-off density is a hard boundary, in reality it can be slightly exceeded, as the theory predicting the cut-off density assumes a collisionless plasma, which is obviously not physically given.

Both the ionization reactions and the creation of hydrogen radicals are two-body interactions. The reverse reaction, the recombination, must be a three-body interaction in order to fulfil both energy and momentum conservation. At the pressures intended for the metal foil pump, practically no three-body interaction occurs in the gas phase, and all recombination reactions only happen on the surrounding surfaces.

While the electric field exhibits a force on ions and electrons alike, it mainly accelerates electrons, as they are around 1,800 times lighter than the lightest ion (a proton). The distribution of energy to ions is suppressed, as the large difference in mass also prevents the dissipation of kinetic energy from electron to ion or neutral, due to the conservation of momentum. This causes an energy distribution between all particles in the plasma that cannot be described by a Maxwell-Boltzmann distribution. Thus, it is called “non-thermal” or “cold” plasma. These plasmas are characterized by a low temperature of ions and neutrals T_i, while the electron temperature T_e is high, so $T_e/T_i \gg 1$.

Although the collisions between electrons and background gas do not allow the transfer of much energy, they are nevertheless crucial for the plasma processes. An electron that is accelerated in one direction during the first half period of an electromagnetic wave will be decelerated in the second half period when the field has reversed. To transfer the energy of the electrons in an efficient manner, they need to distribute the energy before the electric field reverses. If the collision frequency is much smaller than that of the electro-magnetic wave, the particle will gain the maximum energy but will not distribute it to others. If the collision frequency is much higher than that of the electro-magnetic wave, it will not gain enough energy before a collision to ionize neutrals, and the plasma will extinguish. Ideally, the frequency of collisions should be the same frequency as the electro-magnetic wave. The gas specie and the operation pressure determine the collision frequency. This type of plasma is called “collisional plasma”. The main problem for the use of a collisional plasma source is the question of scaling. As soon as the conditions for plasma are given, it will ignite and then shield the RF-wave. Energy can only be absorbed up to the cut-off density and additional power will be reflected. To overcome this limitation, a scalable collisional plasma source called “DuoPlasmaline” is used in the experimental part of this work. This plasma source has been developed at the University of Stuttgart and uses the reflection of the RF-wave for the generation of a large plasma surface [99, 100].

A schematic setup of such a DuoPlasmaline is shown in Figure 3.5. The basic idea of this concept mimics a coaxial waveguide. The RF-wave is fed into a waveguide that consists of a central copper rod (inner coax) and a short cylindrical metal housing (outer coax). In between these two is a dielectric window, e.g. a ceramic tube and a volume, which is cooled by dry, atmospheric air. The dielectric tube goes through a vacuum chamber in which the right conditions for a plasma are established. The outer coax only extends for a few centimetres into

the vacuum chamber. At the end of the short metal housing, the RF-wave will enter the chamber. If no plasma has been ignited yet, the RF-power will do so. The plasma will consume a part of the power, but as it is conducting, the coaxial line is prolonged and the plasma can ignite along the plasma line.

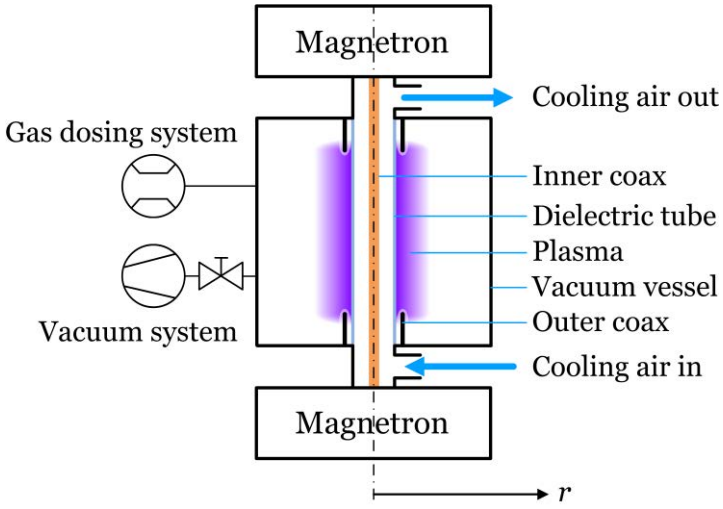

Figure 3.5: Schematic representation of a DuoPlasmaline in a vacuum chamber. The *r*-axis is the same as in Figure 3.6.

It is possible to construct a plasma line with only one magnetron or another RF source, but this restricts its use. The RF power will decrease with increasing distance from the source. If the RF power is not completely dissipated at the end of this plasma line, it will be reflected. This will interfere with the forward power, causing destructive interference resulting in an inhomogeneous plasma. Only exactly matched lengths of these antenna-like plasma lines are possible.

The DuoPlasmaline, a plasma source that is fed from both sides, can have variable lengths and exhibits a more homogenous and stable plasma operation. The plasma distribution along the DuoPlasmaline in the axial direction is relatively homogenous if sufficient RF-power is applied. The distribution of the electric field and the electron density along the radial axis is displayed in Figure 3.6. The small picture at the top provides the coordinates for the *r*-axis in Figure 3.6 a) and b).

The electric field E generated by the DuoPlasmaline is shown in Figure 3.6 a). Just from the geometry, one would expect a reciprocal decrease with distance. While this explains the general decrease, other effects also play a role. As some of the energy is converted in the plasma to kinetic energy, and subsequent to the formation of ions, the electric field has to decrease more than in the ideal case. If the electromagnetic wave passes an interface between two materials with different permittivity, a jump in the electric field is observed. This is most easily seen in the dielectric. However, this effect also plays an important role for the two peaks in the electric field within the plasma. The permittivity of the plasma changes with the electron density and shows a minimum at the critical electron density n_c. These minima in the permittivity result in the two distinct peaks in the electric field. The electron density for this case is displayed in solid

red for the pressure p_2 in Figure 3.6 b). The peaks of the electric field line up with the critical electron densities. Electrons are produced in the gas phase due to particle interactions. Electrons can recombine on the surfaces, so their density decreases towards both sides. Additionally, the electron density distribution is shown for two other gas pressures. The plasma extends further into the vacuum chamber for lower gas pressures.

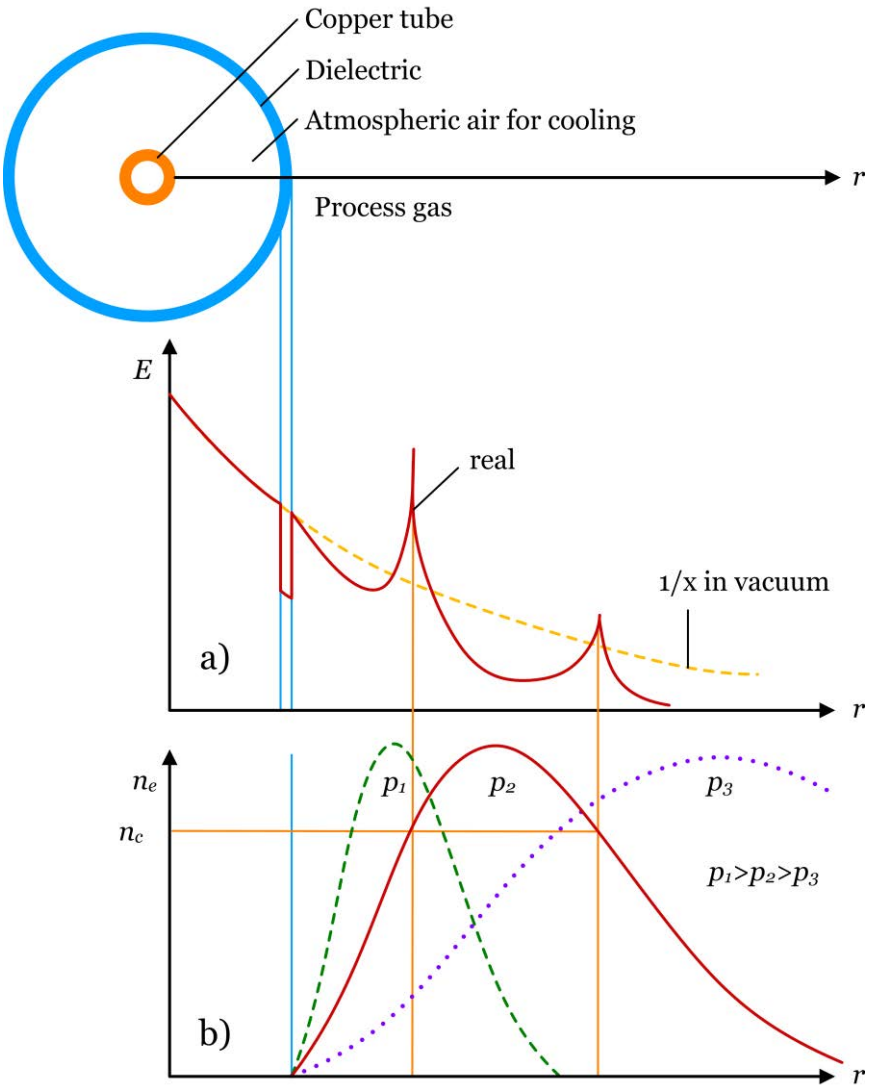

Figure 3.6: Schematic representation of a) the electric field E in a plasma line in a radial direction, and b) the corresponding electron density n_e with the cut-off density n_c, as well as the electron density n_e at higher p_1 (green) and lower p_3 (violet) gas pressure.

If the pressure in the setup is too low to sustain a collisional plasma, an electron cyclotron plasma (ECR) is still able to operate. The basic idea for this kind of plasma source is that electrons are forced on helical paths in a static magnetic field B. If the angular frequency of these gyrations ω_e is the same as that of the electromagnetic wave ω_0, its energy constantly

increases. This concept is shown for different ratios of the two described frequencies in Figure 3.7. The graph shows the kinetic energy of electrons for four magnetic fields. These fields cause a certain angular frequency. The four different cases are labelled by the ratio between the gyration angular frequency and the exiting wave, in this case $\omega_0 = 2\pi \cdot 2.45 \cdot \mathrm{GHz}$. The closer the ratio matches unity, the longer the periods of acceleration, which causes higher kinetic energies. In the case of the resonant case, a constant energy increase can be observed.

The electron frequency can be calculated by [91]:

$$\omega_e = \frac{\mathrm{e}\, B}{\mathrm{m_e}}. \tag{3.28}$$

In order to obtain an electron cyclotron resonance plasma with an RF-excitation of 2.45 GHz, a magnetic field of 87.5 mT is needed. Such a field is easily attainable with a permanent magnet. To obtain an ECR plasma, it is not necessary to have a homogenous magnetic field. If a permanent magnet with a higher surface field than this value is placed in the reaction chamber, its field decreases with the distance. Along the field line with the necessary resonance field, ECR heating occurs.

In contrast with the collisional plasma source, the distribution of energy should not occur within one period. In this case, the electrons are not able to gather sufficient energy. Instead, they should have time to gather energy before they collide. It can be seen as ideal if the RF-frequency is two to four magnitudes higher than the collision frequency. This corresponds to a pressure range of roughly $10^{-2} - 1$ Pa. Due to the lower interaction rate of electrons and ions, the ion temperature in an ECR plasma is also lower in comparison to a collisional plasma.

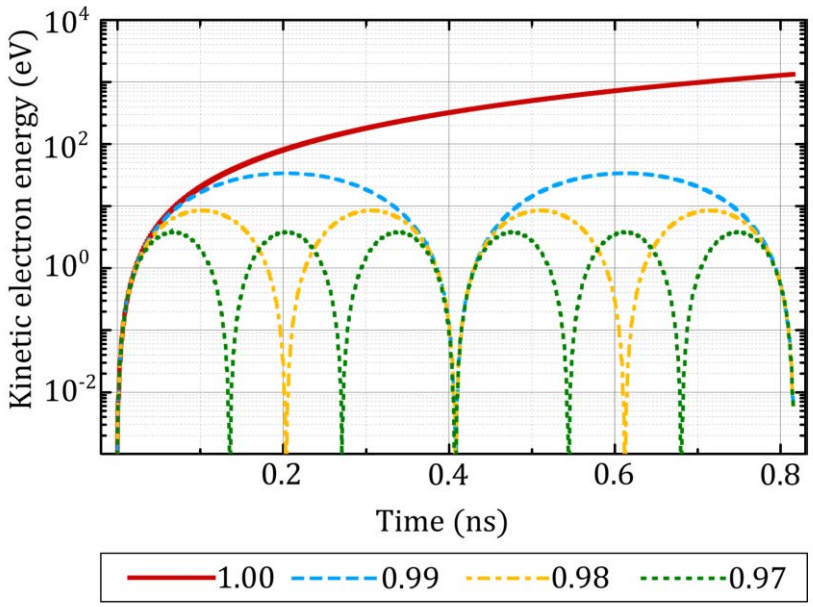

Figure 3.7: Kinetic energy of an electron in a collisionless ECR plasma for different ratios of ω_e/ω_0 using $\omega_0 = 2\pi \cdot 2.45 \cdot \mathrm{GHz}$ and $E_0 = 3000\ \mathrm{V/m}$ (typical value of the electric field strength in a microwave-excited plasma [101]). In the case $\omega_e/\omega_0 = 1$, the electron's kinetic energy is constantly increasing.

3.3 Metal hydrogen interaction

While the transport of hydrogen as a molecule, ion or radical will follow the classical vacuum physics described in section 3.1, the hydrogen–metal interactions still need to be described.

3.3.1 Sorption processes on the metal surface

A relationship between the hydrogen concentration within a metal c_H and its surrounding partial pressure of hydrogen has already been established by Sieverts, in the early 20th century [102]. The suggested equation,

$$c_H = K\sqrt{p}, \tag{3.29}$$

must therefore already contain some information on the sorption process. The constant K is called solubility or Sieverts' constant, and is dependent on the metal and the temperature of the process. Following the ideas of Wang [103], one can assume a number of hydrogen adsorption sites on a metal surface that is in the order of surface atoms, and a surface occupation of up to one complete monolayer. One can introduce a fractional surface coverage factor θ with a value between zero and one. For the dissociative chemisorption of a two-atomic molecule, such as hydrogen, the adsorbed flux $\dot{n}_{ads}$ can be described by:

$$\dot{n}_{ads} = 2\,\alpha_m\,(1-\theta)^2\,\mu\,p, \tag{3.30}$$

already incorporating equation (3.10). $(1-\theta)^2$ gives the probability of having two neighbouring, vacant adsorption sites. The factor of two accounts for the two atoms per molecule. The probability factor α_m describes the likelihood of adsorption per surface interaction for molecular hydrogen. This equation is illustrated in step A in Figure 3.8. The different processes in this figure are explained first, followed by a paragraph on the energy diagram at the top.

The opposite reaction, the desorption flux $\dot{n}_{des}$, will have its own probability, represented with the factor δ, so the flux will be

$$\dot{n}_{des} = 2\,\delta\,\theta^2. \tag{3.31}$$

This process is shown as step B in Figure 3.8.

In equilibrium, adsorption and desorption will be the same and the surface coverage can thus be described by

$$\theta = \frac{1}{1+\sqrt{\delta/(\alpha_m\,\mu\,p)}}. \tag{3.32}$$

This takes the processes from and to the gas and the adsorbed state into account, but not yet the absorbed state. The absorption is also dependent on the surface coverage, so we can assume

$$\dot{n}_{abs} = \gamma\,\theta\,, \tag{3.33}$$

where γ denotes a probability factor (step C in Figure 3.8). In addition to the free sites on the surface and another probability factor β, the reverse process will be dependent on the hydrogen concentration c close to the surface (step D in Figure 3.8). So we assume

$$\dot{n}_{dsb} = \beta(1-\theta)\, c\,. \tag{3.34}$$

The different process steps of the model are illustrated schematically in Figure 3.8. To give some meaning to the activation energies of the different process steps, a potential energy diagram for hydrogen from gas to metal is shown. By definition, hydrogen has a potential energy (or reaction enthalpy) of zero in its molecular form. This is the reason why the energy diagram starts on the left side at the value zero. Towards the right, first the surface between gas and metal and then the bulk metal is shown. A hydrogen molecule that approaches the metal surface first has to dissociate, which requires energy [108]. This is the first energy barrier E_C for this process. For clean metals, this is a very small activation barrier, as the *d*-orbital electrons of the metal catalyse this dissociation [104]. Small amounts of adsorbed non-metals already successfully shield this catalysing effect and drastically increase this energy barrier [109]. This is especially noteworthy, as a non-metal surface monolayer has proven to be energetically favourable for many metals [110]. At ambient conditions, oxide or carbide layers that are much thicker than a monolayer often form on the surface. Upon heating, the non-metals dissolve in the bulk, except for the stable monolayer [111]. At position 1, a local minimum can be found. The binding energy between the hydrogen atom and metal causes this minimum, while the metal lattice is not distorted, which requires some energy for most metals. At this point, process E in Figure 3.8 should be mentioned separately. The atomic hydrogen is already dissociated and therefore is not hindered by an energetic barrier. It therefore easily adsorbs on the metal surface with a sticking probability that is in the range of a clean metal surface. From the surface state, the adsorbed hydrogen can enter the subsurface and, subsequently, the bulk of the metal.

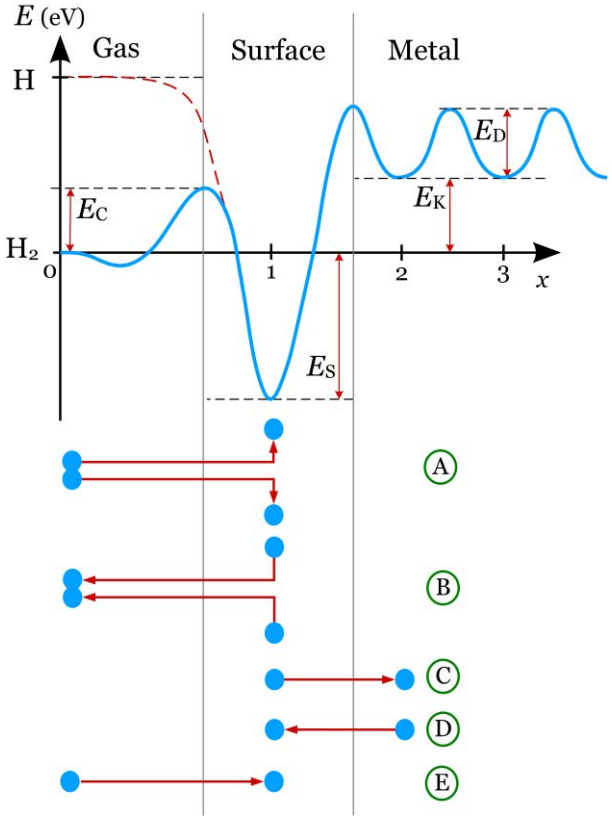

Figure 3.8: Simplified potential energy diagram of metal surface for hydrogen and relevant process steps for superpermeability.

According to Pick and Sonnenberg [104], the different rate constants $(\alpha, \beta, \gamma, \delta)$ are thermally activated and can thus be described in the same form as equation (3.7).

The previously described concept is based on various assumptions. To prove its value, one can demonstrate its consistency with experimentally proven relationships. This is done by taking the four described processes and their mathematical descriptions (3.30), (3.31), (3.32) and (3.34) into account. For the local equilibrium ($\dot{n}_{ads} = \dot{n}_{des}$ and $\dot{n}_{abs} = \dot{n}_{dsb}$), one gets for the surface concentration c the following relationship:

$$c = \frac{\gamma}{\beta} \sqrt{\frac{\alpha_m \mu}{\delta}} \sqrt{p}. \tag{3.35}$$

If the process probabilities are combined to one temperature-dependent factor and are compared with equation (3.29), one obtains an expression for the Sieverts' constant:

$$K = \frac{\gamma}{\beta} \sqrt{\frac{\alpha_m \mu}{\delta}}. \tag{3.36}$$

This provides an explanation of how the solubility can be understood in terms of the surface processes.

In a metal foil pump, the different processes described in (3.30) to (3.34) take place. Figure 3.9 displays these and the corresponding hydrogen fluxes. Additionally, it shows the diffusion flux, which will be discussed in the next subchapter. For a mathematical description of an MFP, all of these must be considered. Most of these fluxes describe the various surface processes. Luckily these can be simplified to express a resulting flux through the surface. The derivation of this surface flux is given in the following.

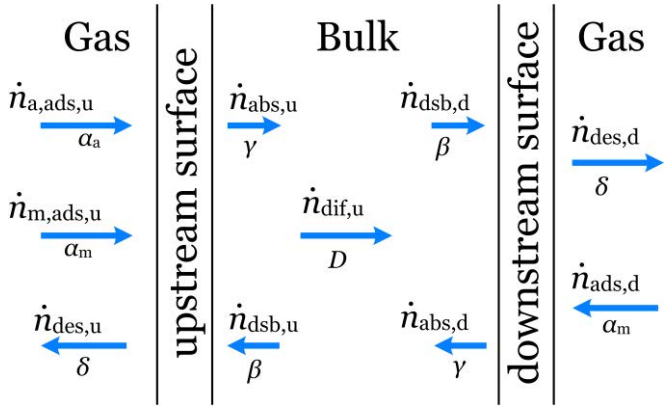

Figure 3.9: Schematic representation of the processes on a gas metal surface. The arrow describes the direction of each process; the name of the correspondent flux is given above, and the correspondent rate constant is below the arrow.

Although the derivation that results in equation (3.36) shows consistency with previous findings, the model introduces four probability factors ($\alpha_m, \beta, \gamma, \delta$) that are hard to measure, as they are closely interconnected. Waelbroeck and others in the field avoid this problem by combining three of the probability factors. He describes the desorbing hydrogen flux as

$$\dot{n}_{des} = 2\,\sigma\,k_r c^2. \tag{3.37}$$

The factor k_r is referred to as the surface recombination factor. However, not just one factor was introduced; there was also a second one. σ is the surface roughness factor, which describes how much the real surface is larger than an ideal flat one.

For the assumption that the surface coverage is small, and the absorption and desorption between surface and subsurface layer are approximately the same, Andrew [56] shows that

$$k_r = \delta\frac{\beta^2}{\gamma^2}, \tag{3.38}$$

can be deduced from equation (3.31). For an equilibrium condition, Sieverts' law (3.29) and (3.37) can be combined to give

$$\dot{n}_{in} = 2\,\sigma\,k_r K^2 p. \tag{3.39}$$

The factor $2\,\sigma\,k_r K^2$ is often used in Waelbroeck's and connected publications as a single factor and not split into its individual components. It is referred to as the "surface limited permeation rate constant" [56]. Equation (3.36) shows that the solubility can be expressed in terms of the sorption probability factors, yielding in combination with equation (3.38) a simple relationship between surface recombination factor and solubility:

$$k_r = \frac{\alpha_m\,\mu}{K^2}. \tag{3.40}$$

Therefore, equation (3.39) can also be written in the form

$$\dot{n}_{in} = 2\,\sigma\,\alpha_m\,\mu\,p. \tag{3.41}$$

This is equation (3.30), with the assumption of low surface coverage.

The previously given model description of the surface processes is based on the model by Pick and Sonnenberg [104]. Baskes [105] has developed a model that additionally incorporates some direct gas-to-bulk metal transitions. Although it includes more effects, some important conclusions drawn are incorrect. This was shown by Richards in [106], who included additional gas-to-bulk metal interactions to the previously named models. This rendered the results of Baskes incorrect. Richards concluded that the model of Pick and Sonnenberg is *"generally adequate"* but discouraged using the model by Baskes [106]. This is also confirmed by Pisarev and Ogorodnikova, who compared all three approaches and found that only the model by Pick and Sonnenberg describes the well-known Sieverts behaviour for the commonly assumed desorption process (desorption by recombination of chemisorbed hydrogen atoms) [107].

As superpermeability is an effect that can only take place if the metal foil is in its surface-limited regime, the energy barrier on metal surfaces is tremendously important. This energy barrier can be described in various ways. Often this is done via the recombination coefficient k_r. This is probably reasoned given the fact that this value can be measured via the desorption flux; compare equation (3.37). This does not allow a very good comparison between materials, as the solubility has a strong effect on this value; see equation (3.40). This is the reason why the literature values shown in Figure 3.10 have been transformed into a sticking coefficient.

The sticking coefficient can be conceived as the likelihood of an impinging hydrogen molecule being adsorbed on the metal surface. In combination with the solubility, it also describes the desorption flux out of a metal foil for a given hydrogen subsurface concentration. Figure 3.10 shows the sticking coefficient over the inverse temperature. It can be seen that the sticking probability is also a temperature-activated process, as the reported values form a straight line in this graph. An attempt has been made to find extreme cases of the sticking coefficient for each of the materials; the area in between these extreme cases is shaded. The highest sticking coefficient, with a value close to one, is reported for high-purity palladium in direct contact with a cleaning discharge plasma [112]. The lower values of the sticking coefficient are taken from [113], with about 20 % non-metals (mainly sulphur) on the surface. As palladium is known to not be prone to surface poisoning, it is not surprising that this material has the highest of the reported sticking coefficients. The values for nickel are the extreme cases published in a collection of literature values in [51]. The results for iron are published in [114] and are

obtained from the investigation of several foils. The measurements yielding higher sticking coefficients have about 10 % surface coverage of non-metals, while the lower ones have about 40 %. This observation once again confirms the sensitivity of the sticking coefficient towards non-metals on the surface. The values for niobium are obtained from a dedicated study that relates the sticking coefficient of hydrogen on niobium with a given oxygen content in the bulk [115]. A clear relationship between the bulk concentration and the surface concentration of oxygen can be seen. The highest sticking coefficients are found for low oxygen contents, 0.03 % in this case, and the lowest sticking coefficients are reported for a bulk oxygen concentration of 1.53 %. As the sticking coefficients show different temperature behaviour in different temperature ranges, the reported data is fitted within the relevant temperature ranges. The medium sticking coefficient data in Figure 3.10 is reported for a bulk oxygen content of 0.13 %. The values shown in Figure 3.10 can be found in Table 14 in the appendix.

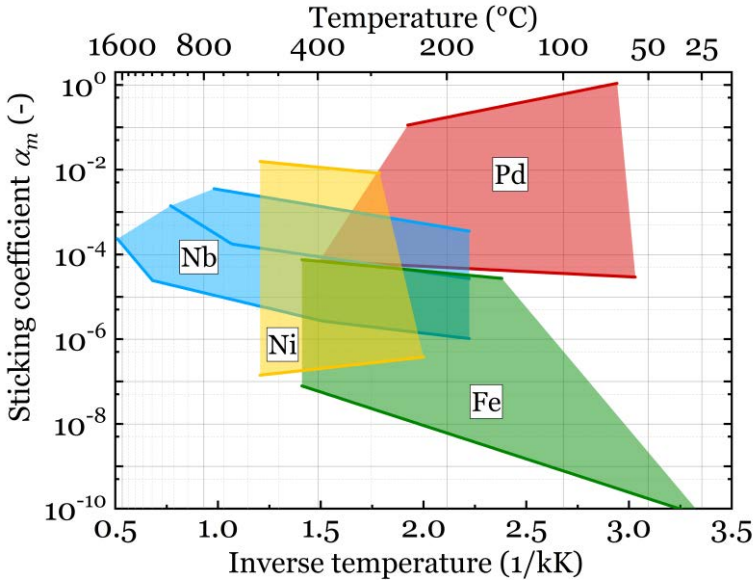

Figure 3.10: Reported sticking coefficients of selected metals from the literature. The colour-shaded areas denote the range between extreme high and low values.

The study that has been used for the niobium values also has an additional implication. If the diffusivity of the non-metal from the bulk to the surface is large enough, the non-metal monolayer can replenish itself, even if it is subject to significant sputtering. This is shown for niobium, which is virtually resistant to sputtering if no carbon but only oxygen is dissolved in the metal foil. This is explained by niobium carbide impeding the oxygen exchange between surface and bulk [116, 117].

In this subchapter, the most important correlations for hydrogen sorption on clean and non-metal-covered metal surfaces are described and the literature data for selected metals is collected and compared. This is used in the non-dimensional model in section 4.1 to elaborate the feasibility for applying these metals in an MFP. To be able to perform this comparison, the bulk properties also have to be taken into account. These are described in the next section.

3.3.2 Transport within a material bulk

An atom can dissolve in two ways in a metal lattice: either it can substitute a host atom, or it is dissolved between the lattice atoms as interstitial. A substituent can only move within the lattice if vacancies are present. In most cases, the movement in the bulk is much easier for interstitials, as many places to move to are available. Thus, the activation energies for interstitial diffusion are considerably lower. Hydrogen always dissolves as interstitial in metals and can be quite mobile.

Dependent on the structure of the host lattice, various interstitial sites are available. The relevant metals have either a body-centred-cubic (bcc) lattice (V, Nb, Ta, Fe for $T < 910$ °C and $T > 1402$ °C) or a face-centred-cubic (fcc) lattice (Ni, Pd, Fe for 910 °C $< T < 1402$ °C). As shown in Figure 3.11, there are many interstitial sites in each unit cell. In the fcc lattice, there are four octahedral (one fully enclosed and 12 that are also reaching into three neighbouring unit cells) and eight tetrahedral sites. In the bcc lattice, there are four octahedral and 12 tetrahedral sites.

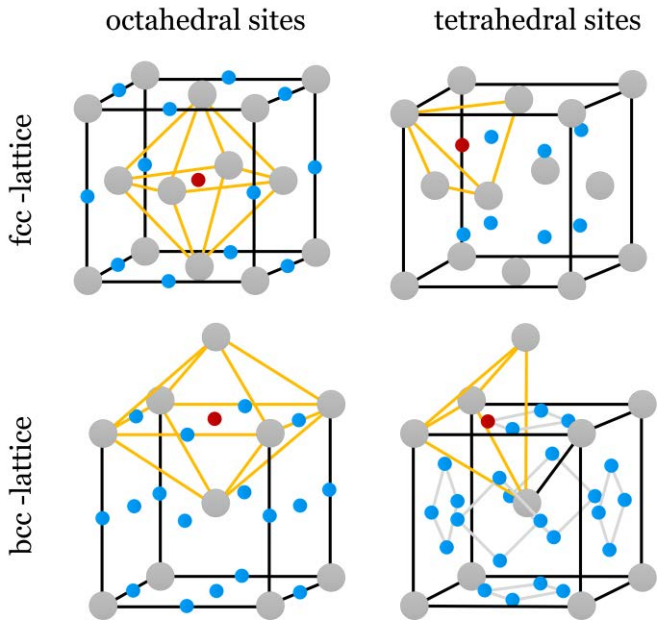

Figure 3.11: Interstitial sites in the bcc and fcc lattice. One octahedron and one tetrahedron are shown with orange boundaries, each with the interstitial site marked in red. The lattice atoms are shown in grey, and the other interstitials in blue. The tetrahedral sites in the bcc lattice on each cubic surface are connected with light grey lines.

The theory of diffusion of hydrogen in metals assumes localized hydrogen nuclei that move from one interstitial site to the next. At low temperatures, the tunnelling from one site to the next is the dominating transport process. This holds especially true for bcc metals, which have a smaller distance between interstitial sites. At higher temperatures (T>300 K), this can be neglected [118] and a thermally activated hopping can be assumed.

In fcc metals hydrogen preferably occupies the octahedral (O-) sites whereas in bcc metals the tetrahedral (T-) sites are occupied. This statement holds for low hydrogen concentrations. It can be understood by geometric considerations of the size of these sites. For the radius r of a metal atom, the biggest sphere that can fit into these interstitial sites has a radius of $0.414\,r$ for an O- and $0.225\,r$ for a T-site in the fcc lattice. Whereas in the bcc lattice the sphere fitting into the O-site only has a radius of $0.115\,r$ and for the T- site of $0.291\,r$. These numbers are also shown in Table 2. The closest distance between two bcc tetrahedral sides is roughly half as long as between two fcc octahedral sites for the metals of interest [119]. In most cases, this leads to lower activation energies and higher values for the diffusion coefficient (at relevant temperatures).

Table 2: Size and number of interstitial sites in metal lattices.

Crystal structure	Interstitial site	Size of site	Maximum (theoretical) composition
bcc	O	0.414	MeH
	T	0.225	MeH_2
fcc	O	0.115	MeH_3
	T	0.291	MeH_6

For some metals, this rule of occupational site also holds true for higher hydrogen concentrations, but for the group 5 metals, this is not true. As an example, this is discussed for vanadium. At low concentrations, the hydrogen in vanadium still occupies the T-sites (α-phase), but at higher concentrations, it moves to O-sites [120]. This causes an elongation of the unit cell of about 10%, making it first monoclinic (β-phase) and, for even higher hydrogen concentrations, body-centred tetragonal (ε-phase). It is believed that the elongation of the unit cell favours the occupation of the O-sites [121].

The β-phase of vanadium is called a hydride; it can be found in the phase diagram of vanadium and hydrogen (Figure 3.12). Hydrides can be classified by their binding character. Three major classes can be identified: ionic, metallic and covalent hydrides. For hydrides of just one element and hydrogen, the binding character can be shown in a periodic table of elements, as shown in Figure 0.1 in the appendix. The hydrides of interest in this work all have a metallic character. The periodic table only names the hydrides with stoichiometric composition, but many metals also show non-stoichiometric hydrogen contents. They are often also referred to as hydrides. The hydrogen is, as previously described, in interstitial solid solution. The structures of these hydrides are fundamentally similar to the corresponding metals. Properties such as the electrical conductivity are also often preserved, but the brittleness is often increased [122].

The behaviour of the different hydrogen isotopes within the metal is similar but not identical, as can be seen in Figure 3.12. This phase diagram shows the thermodynamically stable phases and phase compositions of the hydrogen isotopes in vanadium. It can be seen that above a temperature of ~ 200°C, the β-phase is not stable for any isotope and concentration, and the hydrogen stays in the T-sites (α-phase) for all isotopes [123].

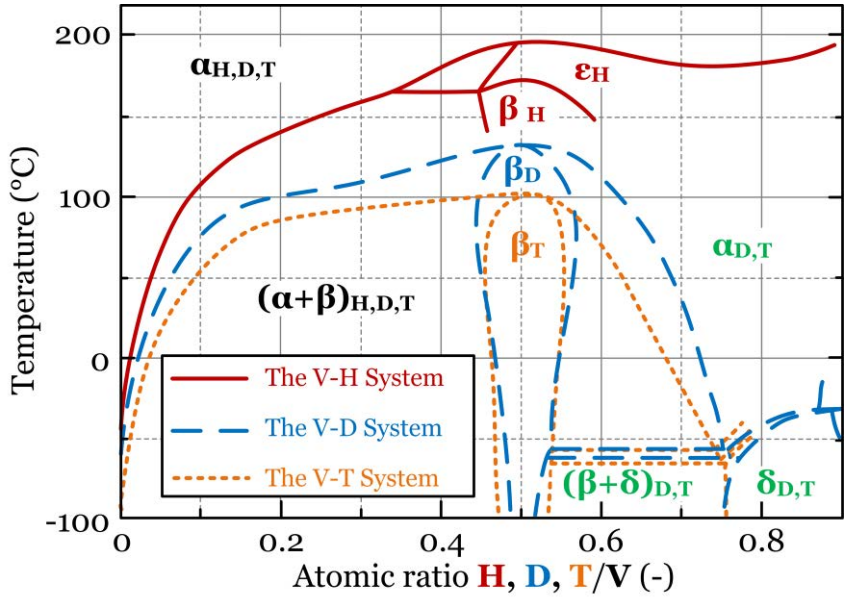

Figure 3.12: Vanadium-hydrogen phase diagram for the three different hydrogen isotopes. Phase information from [124, 125, 8].

The increased brittleness is the main reason why hydride formation in a metal foil pump and in membrane applications is undesirable. This can cause material failure, as described in [126–128]. The common practice to avoid hydride formation is to heat the considered metal to a temperature at which no phase change occurs. This "critical temperature" is shown in Table 3 for selected metals. Another reason for the avoidance of the β-phase for an MFP is the lower diffusion coefficient of hydrogen in the hydride [129].

Table 3: Critical temperatures for the formation of (protium) hydrides in selected metals, from [130].

	V	Nb	Ta	Pd
T_c (°C)	170	171	10	298

While the hydride formation is one cause of embrittlement, a high hydrogen concentration itself can also cause embrittlement, as it pins dislocations. For the group 5 metals, the temperature increase also decreases the solubility of hydrogen in the metal and is thus additionally beneficial. For an insight into this behaviour, it is beneficial to consider the energy diagrams of hydrogen in metals. One of these is shown in Figure 3.8. This diagram is generic and does not aim towards a special metal. In Figure 3.13, potential energy diagrams of three metals are shown. The energy of dissolution from gas to bulk site has the value E_S. It can be a positive value for an endothermic solution reaction, as displayed for iron, or negative, as shown for palladium or vanadium. The energy required for diffusion E_D is always positive, as it is the difference between a local minimum in the bulk and the height of the energy barrier for the diffusion step to the next interstitial site.

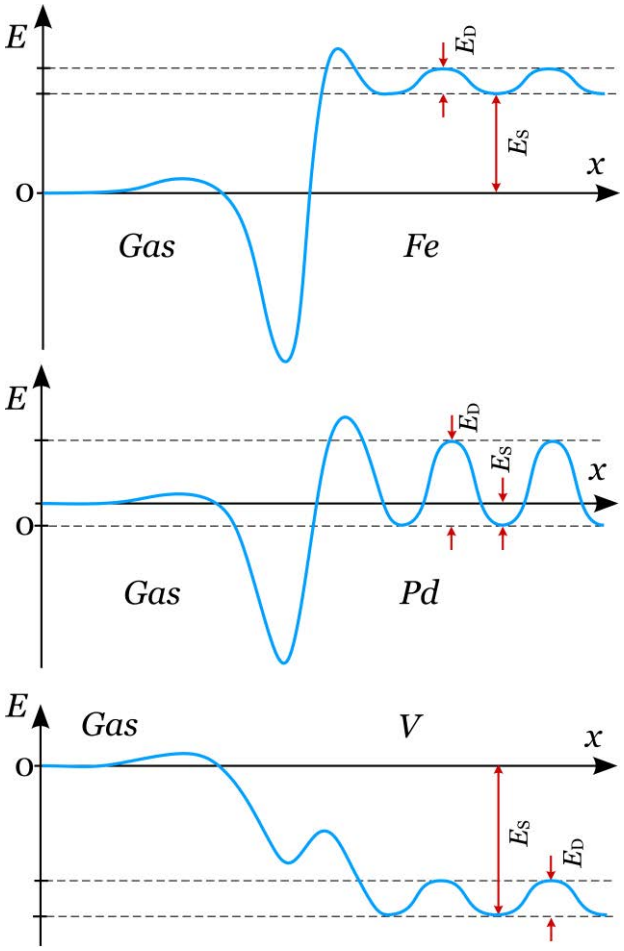

Figure 3.13: Potential energy diagrams of hydrogen in gaseous state and in interstitial solution in the metals iron (Fe), palladium (Pd) and vanadium (V).

As described in equation (3.7), the solubility K and diffusivity D can be described in the forms

$$K = K_0 \exp\left\{-\frac{E_S}{\mathrm{k}\,T}\right\}, \tag{3.42}$$

and

$$D = D_0 \exp\left\{-\frac{E_D}{\mathrm{k}\,T}\right\}. \tag{3.43}$$

The pre-exponents K_0 and D_0 are sometimes called frequency factors, as they can be understood as attempt frequencies of the solution or diffusion process.

In Figure 3.14, the diffusivity of hydrogen in a number of metals is shown at different temperatures. The activation energy of diffusion is always positive, so the diffusivity always increases with rising temperature. The bcc metals (V, Nb, Ta, and Fe) have a higher diffusivity than the displayed fcc metals (Pd, Cu, and Ni) at low and moderate temperatures. They also have lower activation energy of diffusion, which can be seen by the flatter gradient of the diffusivity in the graph.

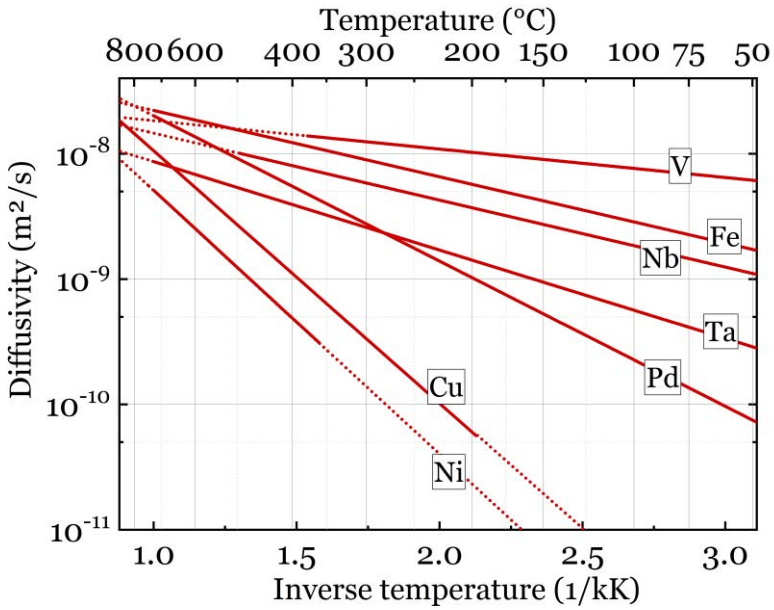

Figure 3.14: Diffusivity of hydrogen (protium) in some metals. The plotted functions are given in the appendix in Table 15 and the corresponding sources are shown in Table 16.

While the diffusivity of the group 5 metals and iron is quite similar, the solubility is very different. In Figure 3.15, the solubility for the same metals and temperature range as in the last graph is shown. Again, the slopes of the curves provide an important insight. All curves with a decreasing value for increasing temperature have a negative heat of solution. Hence, the dissolution process is exothermic. As it is energetically favourable for hydrogen to be dissolved, it is not surprising that the solubility is highest for these metals.

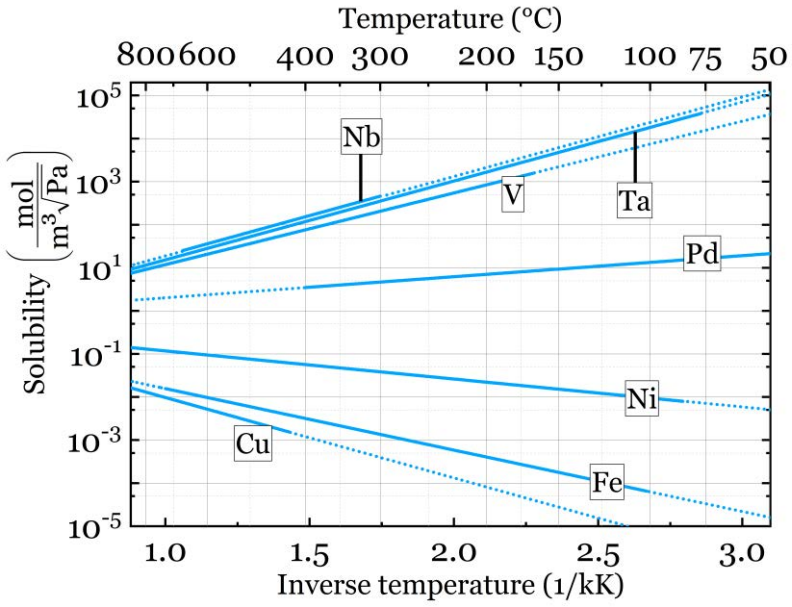

Figure 3.15: Solubility of hydrogen (protium) in some metals. The plotted functions are given in the appendix in Table 15 and the corresponding sources are shown in Table 16.

The permeability, being the product of diffusivity and solubility, is shown in Figure 3.16. While for copper, nickel and iron it is obvious that the slope of their permeability is the same as for diffusivity and solubility, it is not obvious for the other displayed metals. The group 5 metals have the same trend as the solubility, because the heat of solution is greater than the activation energy of diffusion. In contrast, in palladium the activation energy of diffusion is greater than the heat of solution (see Figure 3.13). Thus, the permeability increases with temperature

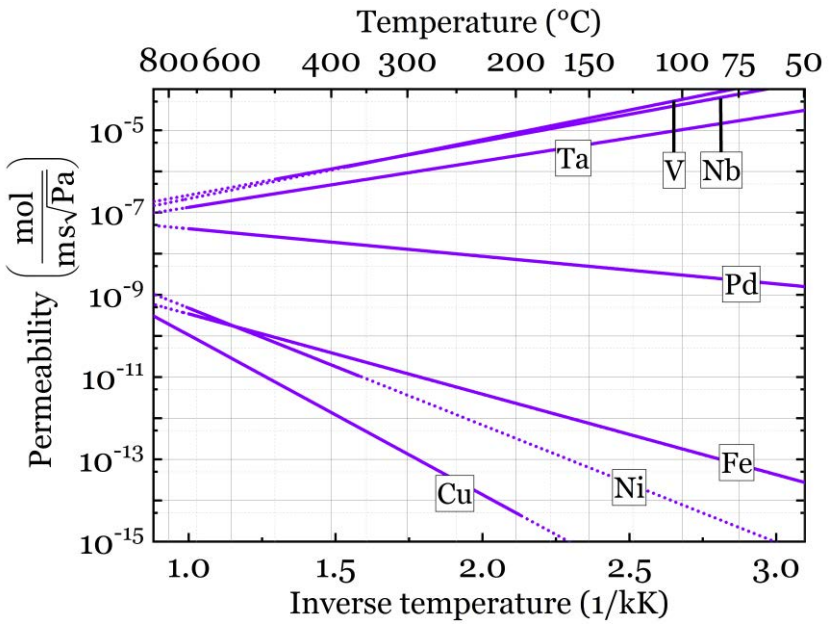

Figure 3.16: Permeability of hydrogen (protium) in some metals, evaluated by averaging literature data from multiple sources.

Literature data for the diffusivity, solubility and permeability should not be seen as exact values; literature data often exhibits a large spread. There are multiple reasons for this, an important one certainly being the tested sample itself. Both grain size in the sample and the surface state affect these measurements. Wherever several sources for a value are found in the literature, averaged data has been used. The idea for this approach is taken from [131]. The data from the previous graphs, as well as data for all three hydrogen isotopes, can be found in Table 15 in the appendix.

Helium permeability

For the application of a metal foil pump for the Direct Internal Recycling of a fusion fuel cycle, the separation capability of hydrogen from other gases is of foremost importance. The upper limit of gases permeating through a membrane is given by the permeability. One component that has to be separated is helium, but not many sources that describe the permeability of helium through metals can be found. In one source, a measurement of the permeability of helium through tantalum [132] is described. As the group 5 metals behave similarly in terms of permeability of hydrogen, it is assumed that they behave similarly for helium as well. Kershner [132] determines the permeability of helium in tantalum to be

$$P_{He\ in\ Ta} = 5.57 \cdot 10^{-12} \exp\left\{-\frac{4.23\ \text{eV}}{\text{k}\,T}\right\} \left[\frac{\text{mol m}}{\text{s m}^2\ \text{Pa}}\right]. \tag{3.44}$$

As helium is a monoatomic gas, the permeability does not have a square root dependency on the pressure, but a linear one. The diffusivity has the same unit for both gases, so the discrepancy is caused by the solubility. If one considers the desorption process from the metal surface into the gas phase, the reason for this difference can be uncovered. Hydrogen dissolves atomically in metals. In order to leave the metal, the hydrogen atoms need to recombine to a H_2 molecule on the surface. The likelihood of a hydrogen atom on the surface having a neighbouring hydrogen atom is a quadratic function of the hydrogen concentration, only in this case the molecule can form and be released into the gas phase. Thus, the reverse process, the adsorption, has the inverse relationship: a square root dependency. In contrast, helium always stays in atomic form. Therefore, the relationship between the gas pressure and the dissolved helium concentration is linear. This explains why the unit for the permeability is different for helium than for hydrogen.

To be able to compare the permeability between hydrogen and helium an example calculation can be performed. A permeated gas flux through a tantalum foil with a thickness of 0.1 mm at a temperature of 900 K and a partial pressure difference of 100 Pa is calculated for hydrogen and helium, and yields:

$$j_{He} = 3.34 \cdot 10^{-30} \left[\frac{\text{mol}}{\text{s m}^2}\right], \tag{3.45}$$

$$j_{H_2} = 1.77 \cdot 10^{-2} \left[\frac{\text{mol}}{\text{s m}^2}\right]. \tag{3.46}$$

This is more than 27 orders of magnitude difference. This difference is so enormous that the permeation of helium can be neglected for technical purposes. Possible leaks in the manufacturing of the module will thus have a much higher influence on the separation factor than the permeability. As the permeability of hydrogen decreases with increasing temperature and the permeability of helium increases with temperature, the difference will become much smaller for higher temperatures, but even at 2000 K there are still more than 12 orders of magnitude difference. The main contribution to this difference is due to the low solubility of helium in tantalum [132].

3.3.3 Release from metal surfaces

There is a square root dependency between the partial pressure and the hydrogen concentration in equilibrium; compare equation (3.29). While it is easy to determine the partial pressure if only one isotope is present, it is more complicated if a second isotope is present. Many sources in literature use the partial pressure of the single-isotope molecule (H_2, D_2, T_2) that is put into a system as the relevant pressure to determine the hydrogen concentration (e.g. [133]). This is a mistake. The Sieverts' relationship describes an equilibrium case. This is the reason why only equilibrium partial pressures need to be used. Using the partial pressures of the single-isotope molecules neglects the fact that in equilibrium the mixed-isotope molecules (HD, HT, DT) also form, and accordingly decrease the partial pressures of the single-isotope molecules. To obtain the total hydrogen concentration in a metal, one must use

$$c_H + c_D + c_T = \left(K_H\sqrt{y^*_{H_2}} + K_D\sqrt{y^*_{D_2}} + K_T\sqrt{y^*_{T_2}}\right)\sqrt{p_{tot}}\,, \tag{3.47}$$

with $y^*_{Q_2}$ being the equilibrium molar isotopologue fractions and p_{tot} the total pressure [134].

This relationship can be used not only to determine the concentration of the isotopes in the metal from the partial pressures, but also to determine the composition of the hydrogen flux leaving the metal. During operation, hydrogen leaves the metal foil of an MFP to both the up- and the downstream sides. The determination of this composition is highly relevant for the integration of a metal foil pump into the fuel cycle. Some process steps that could use gases processed by the metal foil pump, e.g. cryodestillation or a thermal diffusion membrane, are dependent on the isotopologue composition and not the isotope composition.

For the chemical equilibrium reaction

$$a \cdot A + b \cdot B \rightleftharpoons c \cdot C + d \cdot D, \tag{3.48}$$

the equilibrium constant K_e is defined as the ratio between the product of the fugacities f of the products and the product of the fugacities f of the educts

$$K_e = \frac{{f_C}^c \cdot {f_D}^d}{{f_A}^a \cdot {f_B}^b}. \tag{3.49}$$

For an ideal gas, as assumed for hydrogen mixtures at the considered pressures, the partial pressures can be used instead of the fugacities.

There are six reactions between the isotopologues:

i) $\mathrm{H_2 + D_2 \rightleftharpoons 2\,HD}$,
ii) $\mathrm{H_2 + T_2 \rightleftharpoons 2\,HT}$,
iii) $\mathrm{D_2 + T_2 \rightleftharpoons 2\,DT}$,
iv) $\mathrm{H_2 + DT \rightleftharpoons HD + HT}$,
v) $\mathrm{D_2 + HT \rightleftharpoons HD + DT}$,
vi) $\mathrm{T_2 + HD \rightleftharpoons HT + DT}$. (3.50)

To describe the equilibrium, only three of them have to be treated, because of linear dependency of the six equations. If the Roman number in front of the reaction is used as a subscript of the corresponding equilibrium constant, one can formulate the equilibrium constants as:

$$\begin{aligned} K_{e,HD} &= K_{e,\mathrm{i}} = K_{e,\mathrm{iv}} \cdot K_{e,\mathrm{v}}, \\ K_{e,HT} &= K_{e,\mathrm{ii}} = K_{e,\mathrm{iv}} \cdot K_{e,\mathrm{vi}}, \\ K_{e,DT} &= K_{e,\mathrm{iii}} = K_{e,\mathrm{v}} \cdot K_{e,\mathrm{vi}}. \end{aligned} \tag{3.51}$$

The equilibrium constants are temperature-dependent. For very high temperatures, the constants are equal to the statistical combination of the isotopologues, which is expressed by an equilibrium constant of

$$\lim_{T\to\infty} K_{e,HD} = \lim_{T\to\infty} K_{e,HT} = \lim_{T\to\infty} K_{e,DT} = 4. \tag{3.52}$$

For lower temperatures, this can be described by

$$K_{e,HD} = \exp\left\{\frac{-2\Delta G_{f,HD}}{\mathbb{R}\,T}\right\}, \tag{3.53}$$

with $\Delta G_{f,HD}$ as Gibbs free energy of formation for the reaction (3.50 i). This can be applied by analogy to the reactions (3.50 ii) and (3.50 iii). The Gibbs energy can be described by

$$\Delta G_f = \Delta H_f - T\,\Delta S_f. \tag{3.54}$$

Assuming the enthalpy H and the entropy S to be temperature-independent, equation (3.53) can be separated into a temperature-independent and a temperature-dependent part:

$$K_{e,HD} = \exp\left\{\frac{2\Delta S_{f,HD}}{\mathbb{R}}\right\} \exp\left\{\frac{-2\Delta H_{f,HD}}{\mathbb{R}\,T}\right\}. \tag{3.55}$$

The two temperature-independent terms are bundled as constants in the following as

$$K_{e,HD} = K_{e,0,HD} \exp\left\{\frac{C_{h,HD}}{T}\right\}. \tag{3.56}$$

The assumption of a temperature-independent enthalpy and entropy is the reason why a description with fixed values of $K_{e,0}$ and C_h is only valid for a certain temperature range. While thermodynamic data can be found in the literature for H_2, D_2 and HD [4, 135], values for tritium and tritiated species are hard to find. Nevertheless, two sources provide values for the equilibrium constants. Neither of these are measured, but are instead calculated by partition functions.

The earliest source was published by Jones, who had already calculated several thermodynamic properties of hydrogen isotopologues by partition functions in the late 1940s [136, 137]. In addition, he later experimentally determined several values for the equilibrium constants, which are in very good agreement with his predictions [138].

In the 1970s, Pyper and Souers reviewed the previous data and fitted the equilibrium constants to the reported literature values [139]. To extend the predictions, they also used the partition function method to calculate the equilibrium constants at even lower temperatures (below 50 K) [140]. The results are in good agreement with the values of Jones (within 1 %). In [141], the same results as in [140] are shown, but more detail concerning an explanation of the method is given.

The previously named sources only provide data fits in the range below 300 K. At 300 K, the chemical equilibrium constants are still considerably smaller than the high temperature value of four. This is the reason why the data from Jones [137] is used to determine fit functions. They span the temperature range 50 (25 for K_{DT}) to 2500 K. A fit over the whole temperature range is quite inaccurate. This is the reason why the fit has been made for $250 - 1250$ K. For higher temperatures than 1250 K, the equilibrium constant is practically four. Concerning temperatures between 50 and 250 K, a second fit has been elaborated. For this, the data points calculated by Souers are used, as they focus on the low temperature range. The data points used for both fits, as well as the resulting fit functions, are displayed in Figure 3.17. The different values for the fitting functions for all hydrogen isotopologues over the temperature range of $4.2 - 1250$ K can be found in the appendix in Table 17.

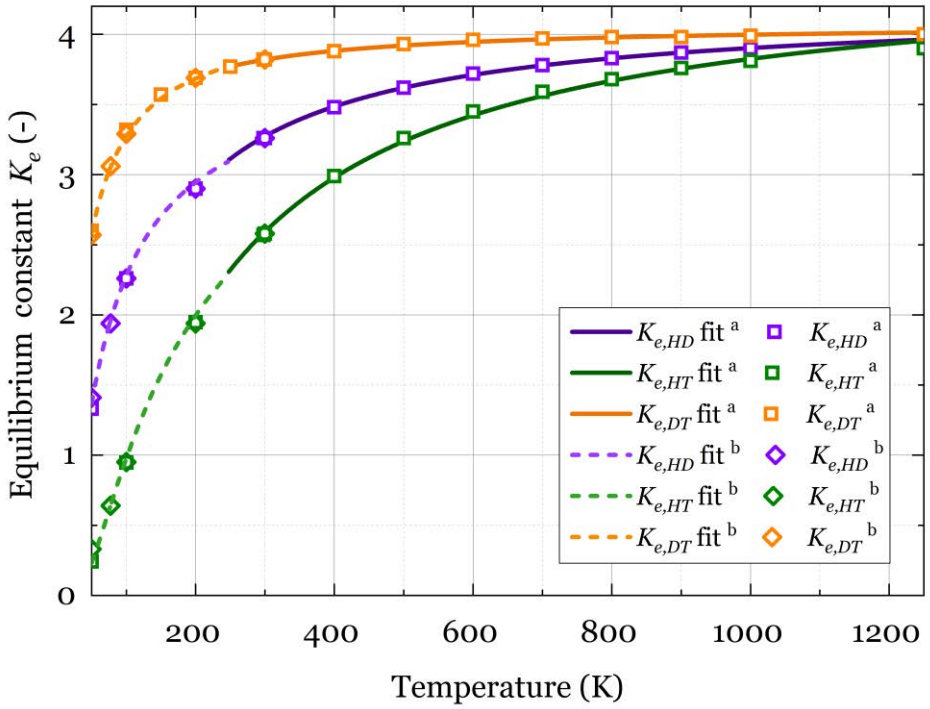

Figure 3.17: Equilibrium constant fit functions extracted from data of [a] [137] and [b] [141]. The symbols show the calculated equilibrium constants of the two sources. The lines give the fit functions in their interval of relevance.

To calculate the equilibrium fraction of the isotopologues, it is irrelevant which isotopologues are mixed to form the equilibrium concentration. The only information necessary is the atomic isotope fraction of a mixture or a solid solution x_Q. The amount of each isotope in a mixture will stay constant during the equilibrium reaction, so mass conservation holds:

$$x_H = 0.5\, y_{HD} + 0.5\, y_{HT} + y_{H_2}, \tag{3.57}$$

$$x_D = 0.5\, y_{HD} + 0.5\, y_{DT} + y_{D_2}, \tag{3.58}$$

$$x_T = 0.5\, y_{HT} + 0.5\, y_{DT} + y_{T_2}. \tag{3.59}$$

y_{Q_2} is the molar isotopologue fraction. Together with the three equations defining the equilibrium constants,

$$K_{e,HD} = \frac{{y_{HD}}^2}{y_{H_2} \cdot y_{D_2}}, \tag{3.60}$$

$$K_{e,HT} = \frac{{y_{HT}}^2}{y_{H_2} \cdot y_{T_2}}, \tag{3.61}$$

$$K_{e,DT} = \frac{{y_{DT}}^2}{y_{D_2} \cdot y_{T_2}}, \tag{3.62}$$

the six equations (3.57) to (3.62) form a system of equations with six unknowns, which contains enough information to determine the equilibrium fractions for each isotopologue. If the isotope composition is known as well as the temperature, one can calculate the equilibrium constants, as shown in the previous chapter. Since, there is no analytical solution to this problem, a numerical approach is chosen.

To demonstrate the relevance of using the temperature-dependent equilibrium constants to determine the isotopologue composition and not just the statistical case, one exemplary result for a mixture with equal amounts of the three isotopes is shown in Figure 3.18. It shows the molar equilibrium fractions of the six isotopologues over the temperature range for a mixture with equal amounts of each isotope. One can clearly see the change of composition over temperature. The fractions of the single-isotope molecules (H_2, D_2, T_2) decrease for increasing temperature and approach the statistical case, which is $1/9 = 0.\overline{1}$. The amount of H_2 is higher than the other two; D_2 occurs least often. The fractions of the two-isotope molecules also approach their statistical value of $2/9 = 0.\overline{2}$ for high temperatures but they do not have the same slope. While the compositions of HT and HD increase with temperature, the amount of DT decreases slightly. The fractions of these three follow the same order as the corresponding equilibrium constants; see Figure 3.17. A small discontinuity in the graph can be seen at 250 K, which can be attributed to the switching of the fitting functions. It can be concluded that the deviation from the statistical case is quite significant, even at temperatures that are considerably higher than ambient temperature and therefore need to be taken into account for fuel cycle studies.

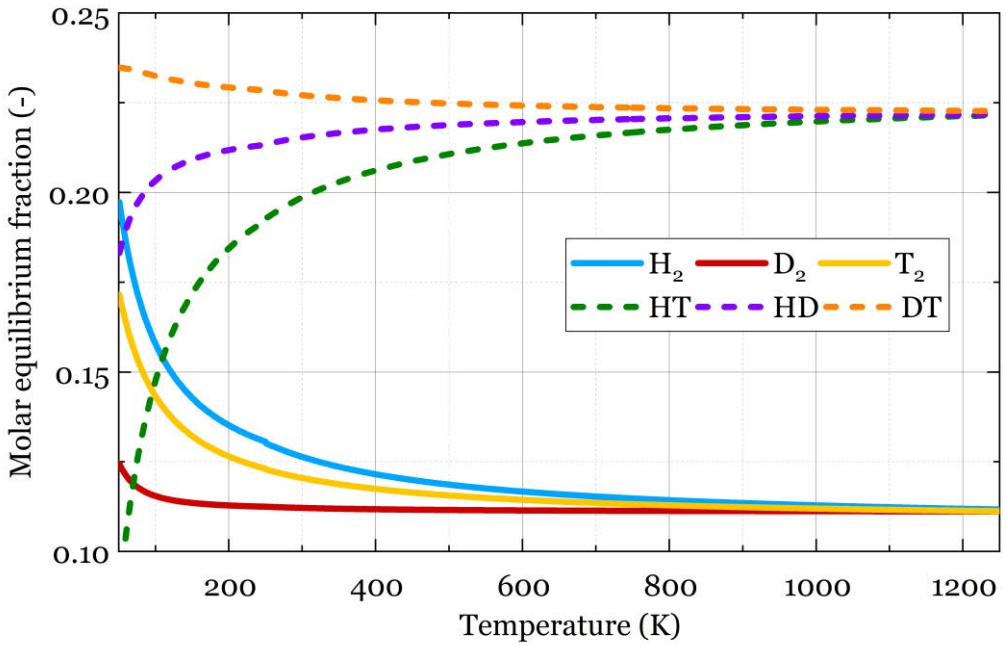

Figure 3.18: Molar equilibrium fraction of the six hydrogen isotopologues for an equal amount of each isotope in the mixture in the temperature range $50-1250$ K. The previously described fit functions are used.

4 Model description of superpermeability

The status of the research as presented in the literature provides a plethora of descriptions for the processes involved in superpermeability. Most of these models can satisfactorily describe the observed phenomena and capture the same physics. Nevertheless, the conclusions drawn from these models differ, and these differences are explained subsequently. Instead of developing a completely new description to provide an answer, there is an attempt to unify the different approaches. To make a comparison viable, a dimensionless description is often highly beneficial. An attempt is made to develop such a model in a rigorous form from scratch, in order to demonstrate the underlying assumptions. After this development, the model is used to characterize the occurring processes. The literature data from the previous chapter is then merged with the model to predict the maximum flux of a metal foil pump. Subsequently, a second model is developed that allows for the prediction of the performance of the HERMES*plus* setup.

4.1 Non-dimensional model to quantify mass transport through foils

A simple physical model is used as a basis for the derivations. In various publications, Ogorodnikova [142–144] develops a model for steady state diffusion of implanted hydrogen through metals, which is adopted here for superpermeable metal foils. This approach was originally used to model metal walls of fusion devices, as they see a high flux of atomic hydrogen. Very similar approaches have also been used in [145–147]. The model is one-dimensional. As the foil is very thin in comparison to its other dimensions, simplifying the description to one dimension is justified, as a movement parallel to the membrane statistically cancels out. Ogorodnikova's model assumes the up- and downstream surfaces of the metal foil to be the same. As this is not necessarily the case for metal foil pumps, the description is altered accordingly.

The model assumes steady state conditions and a foil with a constant thickness x_d. A flux of hydrogen j_i is implanted at a certain position in the membrane x_i. The hydrogen diffuses towards the metal surfaces at which they are released. In Figure 4.1, a schematic concentration distribution in the metal foil is depicted. The concentration gradient is dependent on the diffusivity D and the release on the surface recombination coefficient k_r. The surface roughness σ is also included, as it increases the actual surface of release.

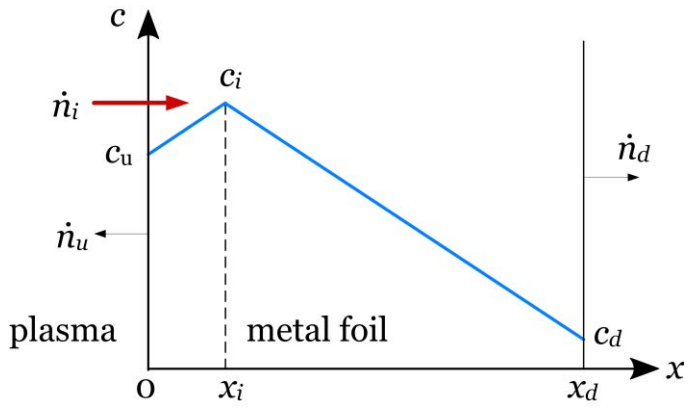

Figure 4.1: Steady state concentration profile of hydrogen in a metal foil. The metal foil with a thickness of x_d is subject to hydrogen implantation from the upstream/plasma side, which is shown left of the foil.

The mass conservation in steady state gives

$$\dot{n}_i = \dot{n}_u + \dot{n}_d \tag{4.1}$$

as boundary information. Both sides of the implantation depth are treated the same way. The surface release flux can be calculated by equation (3.37), which has to be the same as the diffusion flux from the implantation point to the surface. Therefore, the upstream release flux is given by

$$\dot{n}_u = 2\sigma_u k_{ru}\, {c_u}^2 = \frac{D}{x_i}(c_i - c_u), \tag{4.2}$$

and the downstream release flux is

$$\dot{n}_d = 2\sigma_d k_{rd}\, {c_d}^2 = \frac{D}{x_d - x_i}(c_i - c_d). \tag{4.3}$$

With the input information on implanted flux $\dot{n}_i$, surface roughness σ, recombination coefficients k_r, foil thickness x_d, implantation depth x_i and the diffusion coefficient D, the other five unknowns $(c_u, c_i, c_d, \dot{n}_u, \dot{n}_d)$ can be determined with these five equations. For further investigations, the model is transferred to a dimensionless form.

4.1.1 Determination of non-dimensional parameters for superpermeability

The most-needed information in the equations (4.1), (4.2) and (4.3) is the permeating flux $\dot{n}_d$. It can be represented as a function of the necessary input information:

$$\dot{n}_d = f(\dot{n}_i, \sigma_u k_{ru}, \sigma_d k_{rd}, D, x_i, x_d\,). \tag{4.4}$$

The concentrations and flux of upstream release are outcomes of these system-defining properties and thus are outcomes that do not need to be included in this description.

The Buckingham theorem states that the difference between the number of independent variables and the number of their primary dimensions will yield the number of meaningful dimensionless numbers that describe a system [148]. The seven variables in equation (4.4) hold three primary dimensions shown in Table 4, and should thus provide four dimensionless quantities.

Table 4: Dimension matrix (units) of the permeation model.

	$\dot{n}_d$	$\dot{n}_i$	$\sigma_u k_{ru}$	$\sigma_d k_{rd}$	D	x_i	x_d		
l	-2	-2	4	4	2	1	1	(m)	Length
t	-1	-1	-1	-1	-1	0	0	(s)	Time
n	1	1	-1	-1	0	0	0	(mol)	Amount of substance

Multiple combinations of four dimensionless numbers match this model. For many of these possible numbers and combinations, it is hard to identify what they represent from a physics point of view. In order to understand the underlying physics, the dimensional numbers have to be chosen accordingly. In this model, the following four dimensionless (π-) numbers are identified:

$$\chi = \frac{\dot{n}_d}{\dot{n}_i} \qquad \chi \in (0,1), \tag{4.5}$$

$$\varepsilon = \frac{\sigma_u k_{ru}}{\sigma_d k_{rd}} \qquad \varepsilon \in (0,\infty), \tag{4.6}$$

$$\zeta = \frac{x_i}{x_d} \qquad \zeta \in (0,1), \tag{4.7}$$

$$W = \sqrt{2\sigma_u k_{ru}}\frac{x_d}{D}\sqrt{\dot{n}_i} \qquad W \in (0,\infty). \tag{4.8}$$

The number χ is the permeation probability that corresponds to that used by Livshits to define superpermeability [37]. It can be interpreted as the non-dimensional expression of the permeation flux.

The ε is the asymmetry factor of the up- and downstream surface and expresses the relationship of the up- and downstream surface barriers. If this factor becomes unity, the recombination rates up- and downstream are the same: the surfaces are “symmetric”. Values below one give an indication of a lower downstream energy barrier or a higher downstream release rate for a given hydrogen subsurface concentration. Values above one will favour an upstream release.

The ζ factor gives a relative implantation depth. For the case of low energy hydrogen, this factor will be very small and can even be assumed to be zero, as the hydrogen just crosses the surface barrier, but is not implanted any deeper into the bulk. For other cases, such as for experiments with accelerated hydrogen beams, this factor can become much more relevant.

The W-number is first introduced by Waelbroeck et al. in various publications, e.g. [149–151, 74]. It is called the permeation number and gives a relationship between the upstream surface properties and the diffusion through the metal foil. While [152] also uses a W-

number in his description, it is different to that of Waelbroeck. Nevertheless, many of his conclusions are reasonable and are comparable to the development presented in the following. One important piece of information has not been used in any of the treatments using this or a similar dimensionless model. This is the direct connection between the surface recombination coefficient and the solubility. Using equation (3.40), one can rephrase the W-number from equation (4.8) to

$$W = \sqrt{2\sigma_u \alpha_{m,u} \mu}\, \frac{x_d}{DK} \sqrt{\dot{n}_i}. \tag{4.9}$$

While this change does not seem to be significant at this point, its great relevance will be revealed in the conclusions drawn from this model. In a similar fashion, equation (4.6) can be rephrased to yield:

$$\varepsilon = \frac{\sigma_u \alpha_{m,u}}{\sigma_d \alpha_{m,d}}. \tag{4.10}$$

A non-zero gas pressure $p_{g,u/d}$ in the up- or downstream chamber will cause an additional incoming hydrogen flux to the membrane $\dot{n}_{g,u/d}$. This can be quantified to be

$$\dot{n}_{g,u/d} = 2\ \sigma\ \alpha_{m,u/d}\ \mu\ p_{g,u/d}. \tag{4.11}$$

In the described model, one assumes perfect vacuum on both sides of the metal foil. This is a valid assumption if the implanted flux $\dot{n}_i$ is considerably larger than the flux $\dot{n}_{g,u/d}$ entering the metal from the gas phase,

$$\dot{n}_{g,u/d} \ll \dot{n}_i. \tag{4.12}$$

To apply the non-dimensional model, a generic description of the occurring processes is needed. Therefore, equations (4.2) and (4.3) are inserted in equation (4.1). Further use is made of the dimensionless numbers (equations (4.5) – (4.7)), leading to:

$$\chi^2 + \frac{2}{W}\sqrt{\varepsilon\, \chi^3} + \left(\frac{1+\varepsilon}{W^2} - 2\zeta\right)\chi - \frac{2\zeta}{W}\sqrt{\varepsilon\, \chi} + \zeta^2 - \frac{1}{W^2} = 0. \tag{4.13}$$

This equation fully incorporates the described processes and is thus the cornerstone for the application of the model.

4.1.2 Solutions to the non-dimensional model

The non-dimensional expression for the permeating flux is the permeation probability, and thus it is desirable to provide a direct expression of this value. Unfortunately, equation (4.13) cannot be solved analytically to obtain the permeation probability. Two options to solve this problem can be identified and successfully applied.

First, the equation can be solved numerically. In this work the program Mathematica 10 is used. The numerical results require cross-checking, as some trials of using this approach give significantly deviating results for some parameter combinations. These deviating results are obtained especially in the region close to $W \sim 1/\zeta$.

Second, an analytical expression for the permeation number W as a function of the three other parameters has been derived. The equation,

$$W = \frac{\sqrt{1-\chi}-\sqrt{\varepsilon\,\chi}}{\chi-\zeta}, \tag{4.14}$$

can thus be used to find the permeation probability iteratively or to create plots. Obviously, only cases with an existing solution give a reasonable result. While there is a solution for all values of ε and ζ within the given bounds of equations (4.6) and (4.7), this is not the case for the permeation probability. The upper and lower bound of χ has to be found. As this requires some insight into the occurring processes, the relationships for these values are derived in the next chapter (equations (4.20) and (4.21)).

While the first approach to finding a solution to the non-dimensional model is mainly used to find a single value for the permeation likelihood, the second approach is the method of choice for generating the plots in the following subchapters.

4.1.3 Sensitivity study of non-dimensional parameters

The non-dimensional approach allows for probing the behaviour of implanted hydrogen permeation without the use of material data. To do this, the results of equation (4.13) are calculated for several values of ε and ζ over a wide range of permeation numbers. Figure 4.2 shows the results. Both the permeation number on the *x*-axis and the permeation likelihood on the *y*-axis are shown logarithmically. In the graph, four different sets of surface asymmetry with three implantation depth values are shown over a wide range of permeation numbers. All graphs exhibit a similar shape. For low and high permeation numbers, the permeation likelihood tends towards a constant value. These are connected by continuous functions that approach the constant values asymptotically. To understand the occurring processes in these three regimes, it is helpful examine the concentrations in the metal foil in a dimensionless form.

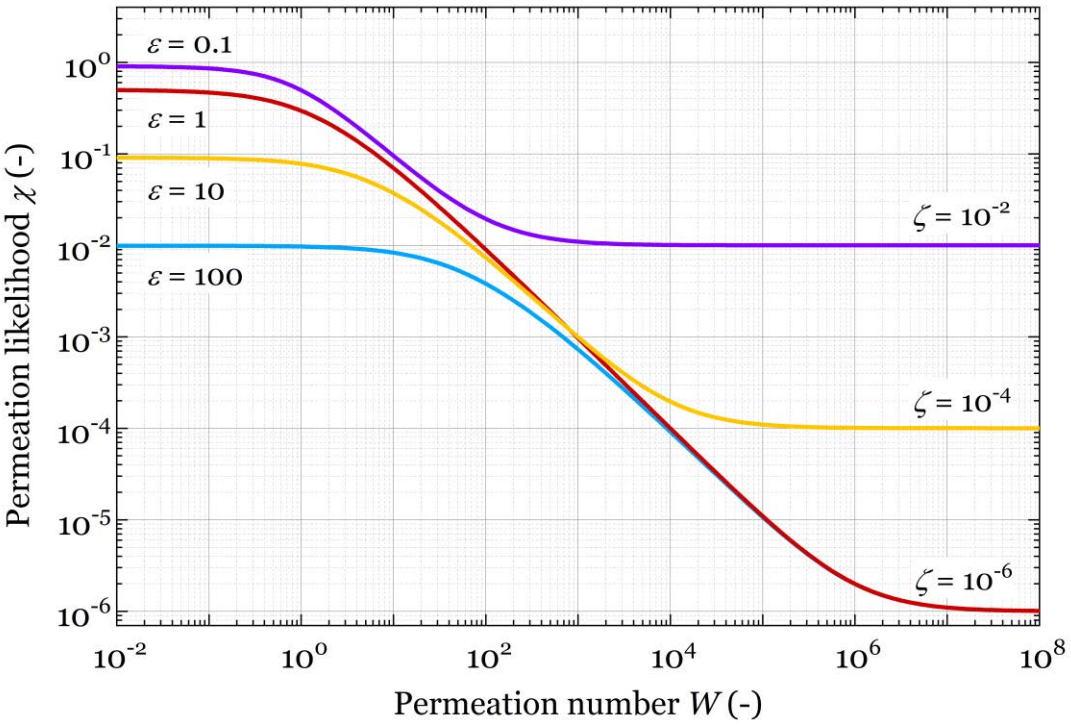

Figure 4.2: Logarithmic representation of the permeation likelihood χ vs. the permeation number W for different asymmetry factors ε and implantation depths ζ.

To derive the concentrations in non-dimensional form, the equations (4.1) to (4.3) can be utilized, in combination with the four dimensionless numbers (4.5) to (4.7) and (4.9). The concentrations can be made dimensionless by a common factor. They are given by:

$$c_u \sqrt{\frac{2\,\sigma_u\,\alpha_{m,u}\mu}{\dot{n}_i K^2}} = \sqrt{1-\chi}, \tag{4.15}$$

$$c_d \sqrt{\frac{2\,\sigma_u\,\alpha_{m,u}\mu}{\dot{n}_i K^2}} = \sqrt{\chi\varepsilon}, \tag{4.16}$$

and

$$c_i \sqrt{\frac{2\,\sigma_u\,\alpha_{m,u}\mu}{\dot{n}_i K^2}} = W\zeta + \sqrt{1-\chi}. \tag{4.17}$$

In Figure 4.3, these concentrations are plotted for one constellation of surface parameters of equal up- and downstream surfaces ($\varepsilon = 1$) and an implantation depth of $\zeta = 10^{-6}$. Three regimes are clearly visible. Two boundaries are defined in the following to separate these regimes. For low permeation numbers, the concentrations on the implantation point and on the two surfaces become the same. This shows that diffusion cannot be the limiting step. It represents the surface-limited regime, which occurs at permeation numbers that are much smaller than the surface asymmetry. This ε-boundary is given by

$$W = \varepsilon. \tag{4.18}$$

The other extreme can be found for permeation numbers much higher than the inverse implantation depth. As the concentrations are very different, this case is entirely diffusion-limited. The boundary can be described by

$$W = 1/\zeta. \tag{4.19}$$

In between these two limiting domains, the upstream concentration c_u and the implantation concentration c_i are practically the same. As the change from one regime to another one transitions gradually, this is only valid for cases far from the boundary values. Between the implantation point and the upstream surface, the hydrogen transport is surface-limited. As the concentration between the implantation point and the downstream surface are very different, there is a diffusion limitation on this side. The intermediate regime ($\varepsilon < W < 1/\zeta$) is thus surface-limited to the side closer to the implantation point (upstream for cases with $\zeta < 0.5$) and diffusion-limited towards the other side (downstream for cases with $\zeta < 0.5$).

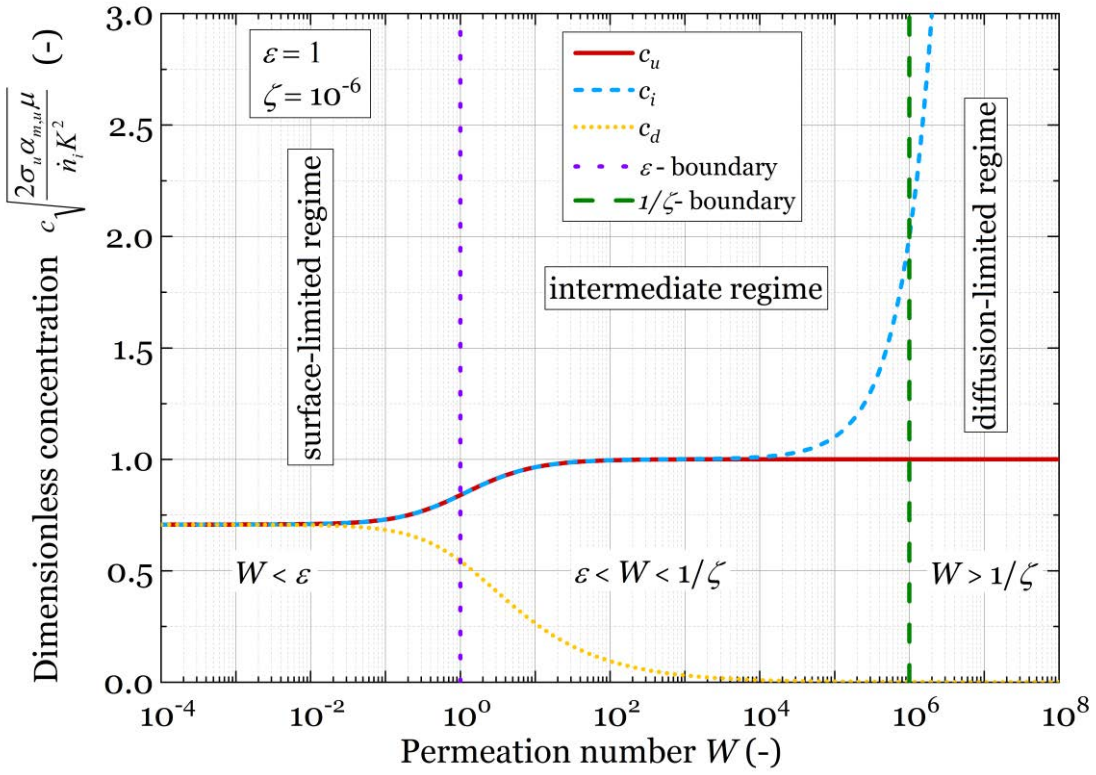

Figure 4.3: Dimensionless concentrations in the metal foil at different locations for different permeation numbers.

With the knowledge of the operational regimes and their meaning, it is possible to find the upper and lower bond of the permeation likelihood χ. These can always be found at the extreme cases of the permeation number W, as all values in between also yield intermediate permeation likelihoods.

As previously shown, small permeation numbers mark a fully surface-limited hydrogen release. The hydrogen release is directly proportional to the recombination coefficient k_r; see equation (3.37). Therefore, the permeation likelihood is given by the downstream recombination coefficient $k_{r,d}$ divided by the sum of the two recombination coefficients. As the ratio between the recombination coefficients is described by the surface asymmetry ε, it can also be used to express this permeation likelihood:

$$\lim_{W\to 0} \chi = \frac{k_{r,d}}{k_{r,d}+k_{r,u}} = \frac{1}{1+\varepsilon}. \tag{4.20}$$

The other extreme, the diffusion-limited case, is marked by high permeation numbers. As shown in equation (4.2), a diffusion flux is caused by a concentration difference over a distance. The relating parameter, the diffusivity D, is constant throughout the metal foil and therefore does not influence the permeation likelihood for this case. For high permeation numbers, the hydrogen concentration at the implantation point is much higher than on the two surfaces. Therefore, the main influencing factor is the inverse distance between the implantation point and each of the two surfaces ($\frac{1}{x_d-x_i}$ and $\frac{1}{x_i}$). To obtain the permeation likelihood, once again these governing parameters have to be set into a relationship. This is done by dividing the inverse distance of diffusion for the downstream release by the sum of the inverse distances for the up- and the downstream release:

$$\lim_{W\to \infty} \chi = \frac{\frac{1}{x_d-x_i}}{\frac{1}{x_d-x_i}+\frac{1}{x_i}} = \frac{x_i}{x_d} = \zeta. \tag{4.21}$$

This equals the relative implantation depth ζ, which therefore also gives the second limiting case for the permeation likelihood.

These limiting cases show the upper and lower bounds of the permeation likelihood. The relationships shown can be used to find the possible input parameters for the analytical solution of the non-dimensional model; compare section 4.1.2.

The description of the concentrations in the metal foil can be used not only for the derivation of the limiting cases of the permeation likelihood, but also to derive a relationship for the hydrogen inventory in the metal foil. This is determined by the foil area A, the foil thickness x_d and the volumetrically averaged concentration $\bar{c}$. In dimensionless form, this concentration is given by

$$\bar{c}\sqrt{\frac{2\,\sigma_u\,\alpha_{m,u}\mu}{\dot{n}_i K^2}} = \frac{1}{2}\left(\sqrt{1-\chi}\,(1+\zeta) + \sqrt{\chi\varepsilon}(1-\zeta) + W\zeta\right). \tag{4.22}$$

In Figure 4.4 the dimensionless average hydrogen concentration in a metal foil is plotted over the permeation number for the same cases, as previously shown in Figure 4.2.

Three regimes can be clearly identified. For low permeation numbers ($W < \varepsilon$), the dimensionless concentration tends to be a constant value. This information is a bit misleading, but it can be explained if the common factor of the dimensionless concentrations is taken into account. This factor has been obtained by the de-dimensioning of the concentration and can be written in the form:

$$\sqrt{\frac{2\,\sigma_u\,\alpha_{m,u}\mu}{\dot{n}_i K^2}} = \sqrt{\frac{2\,\sigma_u\,k_{r,u}}{\dot{n}_i}}. \tag{4.23}$$

It includes the upstream surface properties σ_u and $k_{r,u}$ and the implanted hydrogen flux $\dot{n}_i$.

Instead of stating that the average concentration in the metal foil in the surface-limited regime is constant, one has to state that it is directly proportional to this factor. Hence, the surface-limited behaviour can be considered as a normalization variable to make the concentrations dimensionless. To be precise, the factor uses the properties on the upstream surface. If the surface asymmetry is strongly in favour of an upstream surface release ($\varepsilon \gg 1$), the average concentration is dominated by the upstream surface release and the dimensionless average concentration yields a value close to one. This relationship also explains the lower values for smaller numbers of surface asymmetry. The more hydrogen leaves the metal foil through the downstream surface area, the lower the dimensionless, average hydrogen concentration $\bar{c}$.

The other extreme of this figure is simpler to explain. In the fully diffusion-limited regime ($W > 1/\zeta$), the average concentration becomes much higher than in the surface-limited regime, as the concentration at the implantation point c_i increases, while the dimensionless surface concentrations stay the same, as can be seen in Figure 4.3.

For the region between the described cases, no general conclusion can be drawn, as this depends on both the implantation depth and the surface asymmetry. All four graphs in Figure 4.4 show a saddle point or local minima in this region. This can be best understood if the previous Figure 4.3 is consulted once again. It shows the dimensionless concentrations at the three positions of implantation point, up- and downstream surface. As these three concentrations have been used to derive the equation for the average concentration, they explain the resulting curve. The plotted case of symmetric surfaces ($\varepsilon = 1$) and an implantation depth of $\zeta = 10^{-6}$ in Figure 4.3 is also shown in Figure 4.4 in red. At low permeation numbers, the three concentrations are the same and are independent of the permeation number. Therefore, it is clear that the average concentration also exhibits the same features. At higher permeation numbers, when the intermediate regime between the surface- and the diffusion-limitation is entered, implantation point concentration and the front surface concentration increase, but the downstream surface concentration drops even more. This results in a decrease of the average concentration. When the permeation number approaches the $1/\zeta$–limit, the implantation point concentration strongly increases, while the other two concentrations remain constant. This also results in an increase of the average concentration. This explains the general trend in this intermediate region. The average concentration minimum or saddle point is close to 0.5. Low implantation depths close to zero are the reason for this value. In these cases, the dimensionless concentration on the upstream surface (and implantation point) has the (dimensionless) value of one, while the downstream concentration is practically zero (compare Figure 4.3). The linear decrease of the concentration between implantation point and downstream concentration therefore causes this average dimensionless concentration of 0.5.

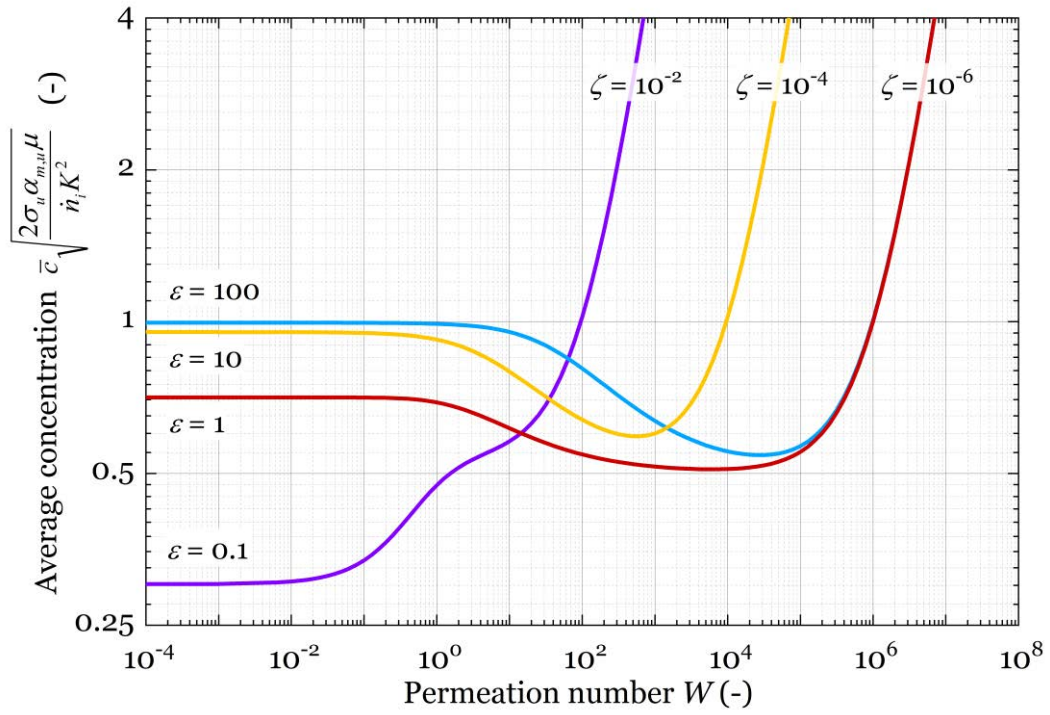

Figure 4.4: Average concentrations for the previously shown cases for different permeation numbers. The concentrations are depicted for the same cases as in Figure 4.2.

4.1.4 Predictive superpermeable performance of a metal foil pump

Probably the most important information that can be derived from this model is the maximum permeation flux in the regime of superpermeability. For this calculation, we assume symmetric surfaces up- and downstream ($\varepsilon = 1$) and a relative implantation depth of 10^{-6}. Symmetric surfaces can be seen as realistically achievable with all materials and the implantation depth plays only a minor role for superpermeation if the implantation depth is much smaller than 0.5. The value of $\zeta = 10^{-6}$ was chosen to allow for easy comparisons with the previous examples. While the results change with the surface asymmetry, the maximum flux by improving the asymmetry is twice the value given in this calculation. The implantation depth has hardly any influence, as the surface-limited regime is considered in this calculation.

Joining the definition of the molar permeation flux,

$$\dot{n}_p = \dot{n}_i \chi, \tag{4.24}$$

with the definition of the permeation number (equation (4.9)), yields:

$$W = \sqrt{2\,\sigma_u \alpha_{m,u} \mu}\,\frac{x_d}{D\,K}\sqrt{\frac{\dot{n}_p}{\chi}}. \tag{4.25}$$

For superpermeability, it is necessary to be in the surface-limited regime. Thus, the criterion for the maximum permeation flux is the ε-boundary (equation (4.18)) – in this case $W = \varepsilon = 1$. Adding this information, using equation (3.11) to convert the molar permeation flux $\dot{n}_p$ to the volumetric permeation flux j_p and rearranging the equation, the maximum volumetric permeation flux $j_{p,max}$ can be calculated:

$$j_{p,max} = \frac{(D\,K)^2 \chi\, \mathbb{R}\, T}{2\, \sigma_u\, \alpha_{m,u}\, \mu\, {x_d}^2}. \tag{4.26}$$

In the fully surface-limited regime, the permeation likelihood is $\chi = 0.5$, compare equation (4.20). At the ε-boundary this value is already slightly smaller, as this boundary marks the transition towards the one-side diffusion-limited case, which has much smaller permeation likelihoods than the surface-limited regime in this example. Its value can be found by numerically solving equation (4.13) for the desired set of variables. In this case, it yields:

$$\chi(W = \varepsilon = 1,\ \zeta = 10^{-6}) = 0.3. \tag{4.27}$$

To be able to compare different materials, a metal foil thickness of $0.1\,\mathrm{mm}$ with a smooth surface ($\sigma_u = 1$) is assumed. Sticking coefficients α_m (compare section 3.3.1) and permeabilities P (compare section 3.3.2) for different materials taken from literature are then used to obtain Figure 4.5.

In Figure 4.5, the maximum superpermeation flux for metal foils with the different materials nickel, iron, palladium and niobium over the inverse foil temperature is shown. For each material, the spread related to the literature data of the sticking coefficients is indicated by a coloured area. It should be noted that the ordinate is displayed in logarithmic form and spans 18 orders of magnitude. The metals iron and nickel have much lower maximum fluxes and their ranges partly overlap. Nickel is more temperature-sensitive, which is indicated by a steeper gradient in the graph. The values of niobium and palladium are at least two orders of magnitude higher. Their temperature dependence is inverse: a lower temperature allows a higher flux. This is an obvious observation if one regards the quadratic dependence on the permeability; see equation (4.26).

This relationship clearly shows that niobium – as a representative of the group 5 metals – or palladium is much better suited for a high superpermeation flux, as is desired for an MFP for fusion. The choice of iron as an ideal MFP material for high permeation fluxes, as suggested by Waelbroeck, can thus be discarded.

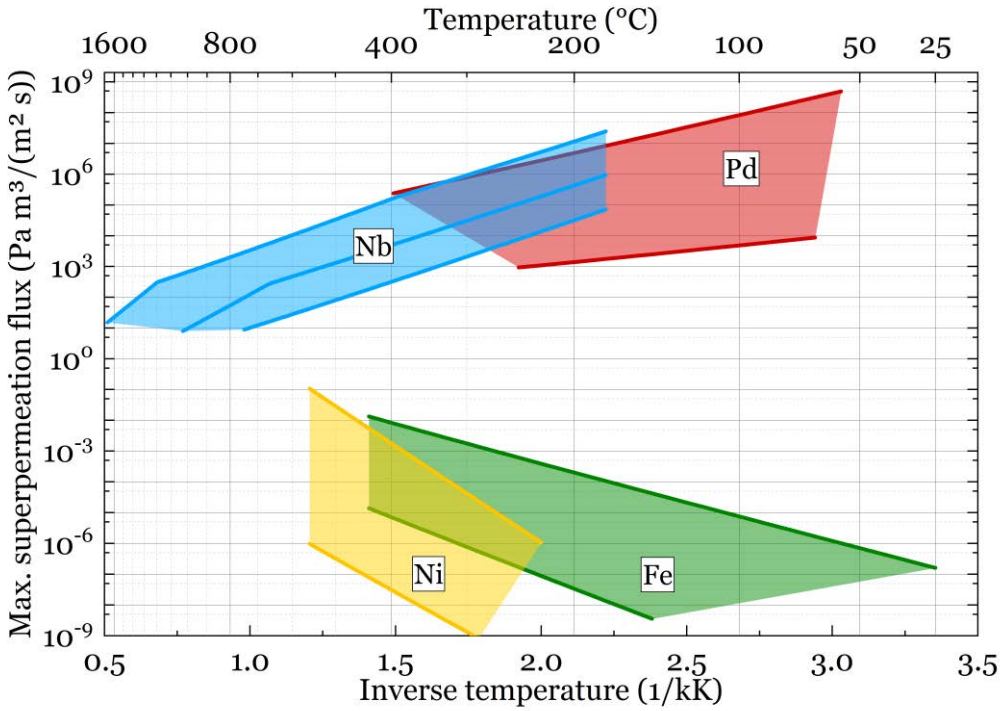

Figure 4.5: Maximum superpermeation hydrogen flux leaving a metal foil on the downstream side for low implantation depths and symmetric surface conditions, according to the previously derived model. Calculated with sticking coefficients from Figure 3.10 and permeabilities from Figure 3.16.

While Figure 4.5 gives a clear answer to the question of which materials allow high superpermeation fluxes, the results should be used with care. The result is obtained based on a non-dimensional model, so all restrictions of this model also apply to these results. The model assumes perfect vacuum on both sides of the metal foil. While the effect of the gas might be negligible for low gas pressures and low sticking coefficients, this certainly becomes increasingly more important for higher pressures and higher sticking coefficients. In the model, any hydrogen concentration in the bulk is feasible. In reality, there is a limit to the hydrogen content of a solid. To test the validity of the predicted maximum fluxes, the highest hydrogen concentration that can be evaluated by this model is analysed.

While some materials can tolerate high hydrogen concentrations, others cannot. The hydrogen solubility is one figure of merit of this property for metals. Sieverts' law allows for calculating a pressure at which the internal hydrogen concentration equals this pressure. In other terms, this "internal" pressure defines the potential for the hydrogen to be released. If the hydrogen concentration becomes too high, the hydrogen can form internal blisters [74]. To compare the results for different materials, this "internal" – or "Sieverts' equivalent" – pressure is used in the following. The highest internal hydrogen concentration always exists at the implantation point. Therefore, the equation for the concentration at this point should be used.

An expression for the permeating flux can be derived by transposing equation (4.25). It is given as a function of the permeation number:

$$j_p = \left(\frac{W\ D\ K}{x_d}\right)^2 \frac{\chi\ \mathbb{R}\ T}{2\ \sigma_u \alpha_{m,u} \mu}. \tag{4.28}$$

The equation for the internal hydrogen pressure as a function of the permeation number can be created by inserting the equation for Sieverts' law (3.29) and the permeating flux, equation (4.28), into the equation for the dimensionless concentration at the implantation point (4.17). Together with the definition of the permeation number (4.9) this gives:

$$p_i = \frac{\dot{n}_\iota}{2\ \sigma_u\ \alpha_{m,u}\ \mu} \left(W\zeta + \sqrt{1-\chi}\right)^2. \tag{4.29}$$

To be able to compare results, an example calculation is performed. The input parameters are chosen to be the same as in the previous graph: the foils are considered to have a thickness of $0.1\,\mathrm{mm}$, with symmetric surface properties ($\varepsilon = 1$) and a relative implantation depth of 10^{-6}. The permeability data is taken from Table 15 and the molecular sticking coefficient from the literature (Table 14 in the appendix). For niobium, the relations No. (8.12) and (8.13) are used, for palladium relation No. (8.10) and for iron relation No. (8.20) is assumed.

Figure 4.6 displays the results of this example calculation. The graph shows a relationship between the internal hydrogen pressures corresponding to the maximum hydrogen concentration and various permeation fluxes. The materials niobium, palladium and iron are compared at three different temperatures in a double logarithmic plot.

The maximum internal hydrogen pressure rises continuously with the permeation flux. For all three materials, the internal hydrogen pressure is lowest for the highest temperature due to a higher diffusivity. The difference between the internal hydrogen pressures at the same permeation flux is much bigger between $300\,\mathrm{K}$ and $600\,\mathrm{K}$, in comparison to the difference between $600\,\mathrm{K}$ and $900\,\mathrm{K}$. For a given temperature and permeation flux, the internal hydrogen pressure is lowest for niobium and highest for iron. Even at the lowest displayed permeation flux, the internal hydrogen pressure at $300\,\mathrm{K}$ in iron is above 10^7 Pa. This certainly causes the formation of blisters in the metal foil. Therefore, these fluxes are prohibitively high. It is difficult to estimate at what internal hydrogen pressure the formation of blisters can be expected; this certainly depends on numerous factors, such as the up- and downstream pressures and the materials used. As it is safe to assume that blistering will not be an issue for hydrogen pressures at or below the operation pressure of the MFP, the expected operation regimes in DEMO are shown highlighted. The red shading corresponds to the range of operation pressures during the plasma burn, which will coincide with high permeation fluxes. The yellow shading highlights the pressures during the dwell phase, in which much smaller hydrogen fluxes are expected. Metals with an endotherm solution process (Fe, Ni) will certainly be more prone to blister formation, as the internal hydrogen distribution will be more inhomogeneous. In these metals, hydrogen can be found primarily at dislocations and grain boundaries allowing for recombination and correspondingly to blister formation. The internal pressures, not only for iron, but also for palladium and niobium will limit the maximum superpermeation flux for temperatures below a certain value. The maximum fluxes predicted by Figure 4.5 are only valid if blistering is not an issue.

The internal hydrogen pressure in niobium is lower than in palladium at the same temperature for high fluxes. This shows that it is capable of handling higher permeation fluxes without blistering. It is therefore regarded as the most suitable material for a high flux metal foil pump from the materials compared.

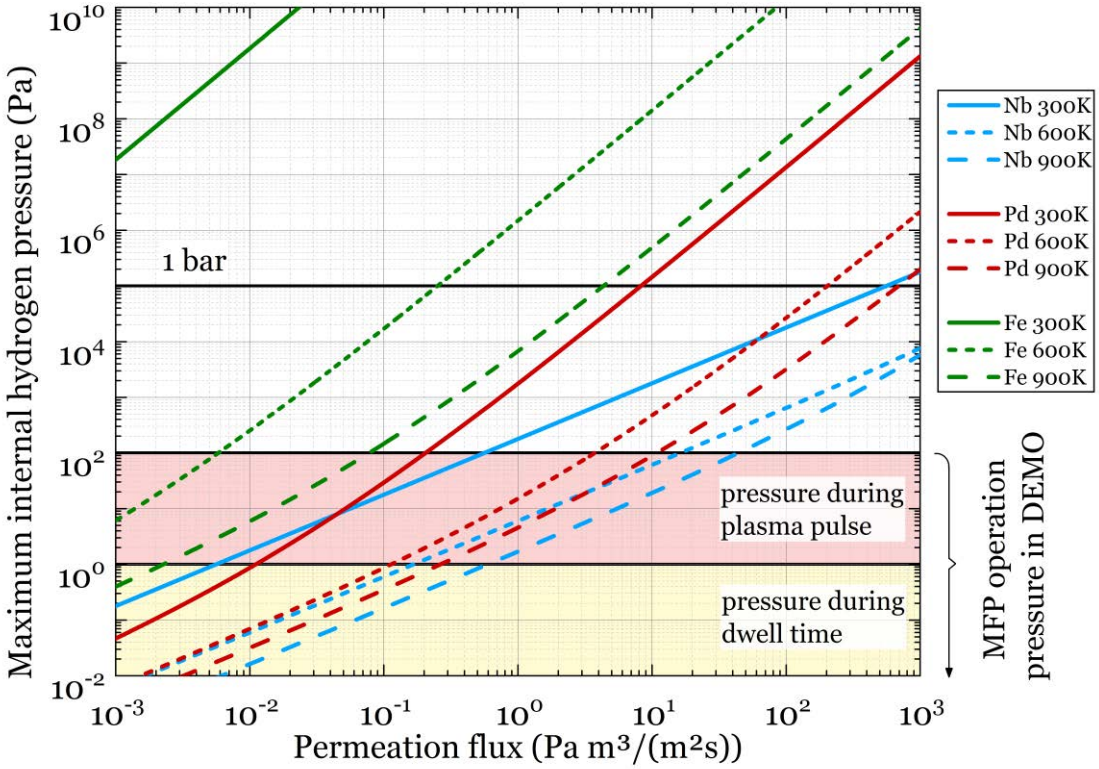

Figure 4.6: Hydrogen concentration at implantation depth is presented as an internal hydrogen pressure for different permeation fluxes at three temperatures for niobium, palladium and iron. For reference, the likely operation pressures of DEMO and of 1 bar are marked.

Several conclusions can be drawn from this study. It has been demonstrated that only materials with good hydrogen solubility are capable of handling high permeating fluxes in the surface-limited regime. This excludes the use of iron as a foil material in future fusion devices. Moreover, even for high-solubility materials, blistering can become an issue if they are used at low temperatures. It has been identified that a higher operation temperature decreases the internal hydrogen pressure, regardless of the temperature-dependence of the solubility.

4.2 Predictive performance of the HERMES*plus* setup

The previously described non-dimensional model has been developed to explain the basic behaviour of superpermeability. It allows for predicting the performance limits of a metal foil and relates the different physical processes. Unfortunately, it is not capable of predicting the performance of the experimental setups. To be able to use the non-dimensional model for performance predictions or assessments, the suprathermal hydrogen flux to the metal foil has to be known. This value is very hard to measure or precisely predict. Therefore, another approach is used to confirm the theoretical description of the metal foil behaviour.

In Chapter 5, the experimental setups are introduced, along with the measurement procedure and how results can be derived from them. The method in section 5.3.2 measures the permeated hydrogen flow through a metal foil pump with constant conditions. To have constant pressures, the downstream chamber needs to be constantly pumped. If this pumping is switched off, the downstream pressure increases. Certain values in this pressure rise are used in the method described in 5.3.3 to be able to determine more properties of the metal foil. Detailed information on these methods is given in the respective sections.

In the following, the pressure rise is predicted based on a few input variables. These values originate from three sources. The metal foil surface A and the downstream chamber volume V are given by the experimental setup. The hydrogen solubility $K(T)$ of the metal foil is taken from the literature. The permeated flow $J_{d,0}$, the corresponding downstream pressure $p_{d,0}$ at the initial stage of the pressure rise, and the properties of the up- and downstream surface $\sigma_u \alpha_{m,u}$ and $\sigma_d \alpha_{m,d}$ can be determined experimentally with the previously mentioned methods.

The prediction is based on the assumption of equilibrium conditions and surface-limited mass transport. The relevant variables are named in Figure 4.7. As the conditions on the upstream side are unchanged in the course of the experiment, a constant absorption flow $J_{abs,u}$ is assumed. The flows are treated in volumetric form; wherever needed, equation (3.11) is used to transpose a molecular flow to a volumetric one.

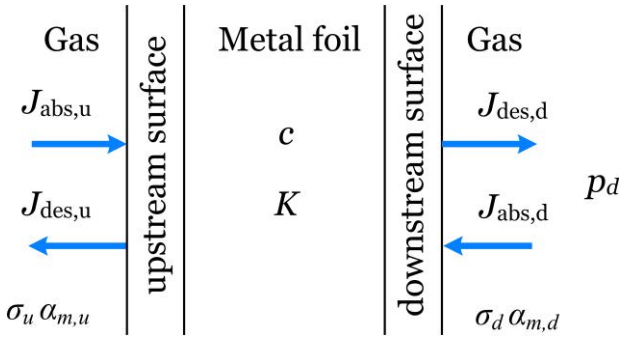

Figure 4.7: Schematic representation of the processes that are taken into account for the prediction of the pressure rise during the compression experiment.

The resulting downstream hydrogen flow J_d is given by the difference between the absorption $J_{abs,d}$ and desorption flux $J_{des,d}$:

$$J_d = J_{des,d} - J_{abs,d}. \tag{4.30}$$

The absorbed flow can be determined with the known values of the downstream pressure, the sticking coefficient and the foil area, as shown in equation (3.41):

$$J_{abs,d} = A\ \mathbb{R}\ T\ \mu\ \sigma_d \alpha_{m,d}\ p_d. \tag{4.31}$$

The desorbed flow is determined by the permeation probability χ multiplied by all input flows, which is equation (4.5) with more than one incoming hydrogen flow:

$$J_{des,d} = \left(J_{abs,u} + J_{abs,d}\right) \chi. \tag{4.32}$$

This flow can also be used to obtain information on the hydrogen concentration by combining equation (3.37) and (3.40) to get:

$$J_{des,d} = A\ \mathbb{R}\ T\ \mu\ \frac{\sigma_d \alpha_{m,d}}{K^2} c^2. \tag{4.33}$$

The pressure increase in the downstream volume can be obtained by using the ideal gas law:

$$\dot{p} = \frac{J_d}{\mathrm{V}}. \tag{4.34}$$

One assumption for this prediction is that the membrane is in the surface-limited regime, which corresponds to low permeation numbers. In this region, the hydrogen release is determined by the surfaces. Therefore, the equations (4.10) and (4.20) are valid and can be combined to give:

$$\chi = \frac{1}{1+\sigma_u \alpha_{m,u}/\sigma_d \alpha_{m,d}}. \tag{4.35}$$

This value can be calculated from the results of the compression method, compare subsection 5.3.3. The constant upstream absorption flux can be obtained by combining equations (4.30), (4.31) and (4.32) to give:

$$J_{abs,u} = \frac{1}{\chi}\left(J_{d,0} + (1-\chi) A\ \mathbb{R}\ T\ \mu\ \sigma_d \alpha_{m,d}\ p_{d,0}\right). \tag{4.36}$$

The temporal pressure evolution can be calculated stepwise by,

$$p_{d,\mathrm{t}=i+1} = p_{d,\mathrm{t}=\,i} + \dot{p}_{t=i}(t_{t=i+1} - t_{t=i}). \tag{4.37}$$

The pressure increase for each step can be calculated by combining the equations (4.30), (4.31), (4.32) and (4.34) to get,

$$\dot{p} = \frac{1}{V}\left(\chi\, J_{abs,u} - (1-\chi) A\ \mathbb{R}\ T\ \mu\ \sigma_d \alpha_{m,d}\ p_d\right). \tag{4.38}$$

To be able to understand the pressure increase better, it is helpful to calculate the hydrogen concentration in the foil. It can be obtained by combining equations (4.31), (4.32) and (4.33) to give:

$$c = \sqrt{\chi K^2 \left(\frac{J_{abs,u}}{A \mathbb{R} T \mu \sigma_d \alpha_{m,d}} + p_d \right)}. \tag{4.39}$$

The concentration can be seen as the driving force for the hydrogen release. The corresponding pressure $p_{c,equiv}$ can be calculated by using Sieverts' law (equation (3.40)) to yield:

$$p_{c,equiv} = \chi \left(\frac{J_{abs,u}}{A \mathbb{R} T \mu \sigma_d \alpha_{m,d}} + p_d \right). \tag{4.40}$$

In Figure 4.8 an example calculation with the prediction of a pressure rise is shown. The input parameters to the calculation are shown in the caption.

The prediction starts with the point in time where the pumping is stopped. In this case, the downstream pressure equals zero. The initial hydrogen concentration in the metal foil has the equivalent of 3.13 Pa. The pressure difference between this pressure and the downstream pressure drives the net downstream release flux. This causes the downstream pressure to increase. The hydrogen in the downstream chamber can be reabsorbed on the surface. This additional input stream to the foil also increases the pressure representing the hydrogen concentration. However, it does not increase linearly, but to a lesser extent, due to the quadratic dependence of the desorption flux on the concentration. The driving force for desorption decreases and the downstream pressure asymptotically approaches a resulting pressure. This simple model allows for predicting the pressures in a compression experiment and thus enables the cross-check between experimental results and this prediction.

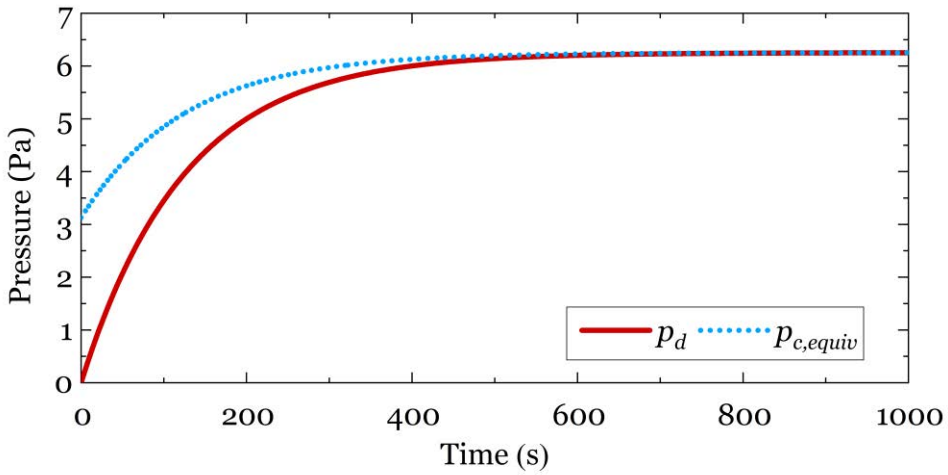

Figure 4.8: Example of a calculated pressure rise for equal surfaces with a sticking coefficient of $2 \cdot 10^{-5}$ at a temperature of 700 °C, an absorbed upstream flux of $j_{abs,u} = 0.1$ Pa $m^3/(m^2\ s)$ and a volume-area ratio of 1 m^3/m^2 (downstream volume to metal foil area). The pressure equivalent of the dissolved hydrogen concentration is also given.

It should be considered that this model does not depend on the diffusivity or the solubility of the metal foil material if the hydrogen concentration is represented as a pressure. Only if the actual concentration is to be determined is the solubility needed. The sticking coefficients are the only material information that is included in the model. This is only possible due to the assumption of an instantaneous equilibrium at each point in time. Certainly, this is not valid in reality. The two main factors that will lead to a deviation of this are the diffusivity and the solubility. For materials like group 5 metals or iron, the time for diffusion will probably be of only minor importance, due to their high diffusivities. The high solubility of group 5 metals will be more likely to cause a more significant delay, as it will take time for the internal hydrogen inventory to build up. Both effects will only slow down the process, so this model will always predict a quicker process than will occur in an experiment. The maximum downstream pressure will nevertheless be the same.

5 Experimental installations HERMES and HERMES*plus*

The experimental element of the presented work has been performed with the two experimental setups HERMES and HERMES*plus*. HERMES, the "Hydrogen Experiment for Research on MEtal foils and Superpermeability", was designed in 2013 and is the starting point for both the experimental investigations on superpermeation at KIT and this thesis. It has been adapted to increase the operation range and improve operability during the presented work. As HERMES has been found to have some fundamental limitations, HERMES*plus*, the "Hydrogen Experiment for Research on MEtal foils and Superpermeability – PLasma Utilization Setup", has been designed, constructed and commissioned as part of the presented work. Many parts of HERMES, especially pressure sensors and vacuum pumps, have been reused in HERMES*plus*.

5.1 Functional facility description

In the following, the two setups are described. As many subsystems are used in both installations, their description is kept brief in the sections regarding the facilities. They are given universal names that show which parts have been reused. More details on the different subsystems are given in "5.2 Measurement devices and infrastructure". The piping and instrumentation diagrams (P&ID) of both setups can be found in the appendix, Figure 0.3 and Figure 0.4.

5.1.1 HERMES

As shown in the schematic layout in Figure 5.1, HERMES consists of two vacuum chambers separated by a metal foil. Gas for operation is supplied by a mass flow controller (FIR1), and is injected into the plasma chamber of the Tectra GenII ECR plasma source. The gas or plasma will enter the upstream vacuum chamber through the open grid (85 holes ∅ 2 mm) of the plasma source. This upstream chamber is pumped by two turbo molecular pumps. The turbomolecular pump P2 (180 l/s for N_2) is directly connected to the chamber. P1 (67 l/s for N_2) is pumping the rear part of the plasma source, and is also connected via a low conductance to the upstream chamber. Both turbo pumps use a common scroll pump (P4) for backing. The metal foil (∅ ~98 mm) is heated by a radiation heater to temperatures up to 600 °C. The downstream chamber is evacuated by the turbo molecular pump P3 (60 l/s), backed by the diaphragm pump P5 (3 m^3/h). A gate valve is able to disconnect the downstream chamber from the pumps (V5). Various pressure gauges are attached to each chamber to provide exact readings. The metal foils used have a thickness of 100 µm and are mounted in an opening with 70 mm diameter (active foil area) between the two chambers. The volume of the downstream chamber is around 1.5 l.

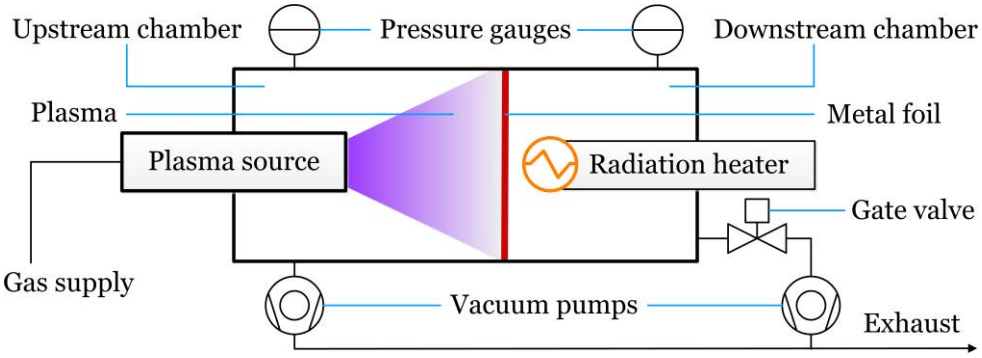

Figure 5.1: Schematic layout of HERMES.

A CAD drawing of the main chambers of the HERMES setup, including the plasma source and the radiation heater, is shown in Figure 5.2.

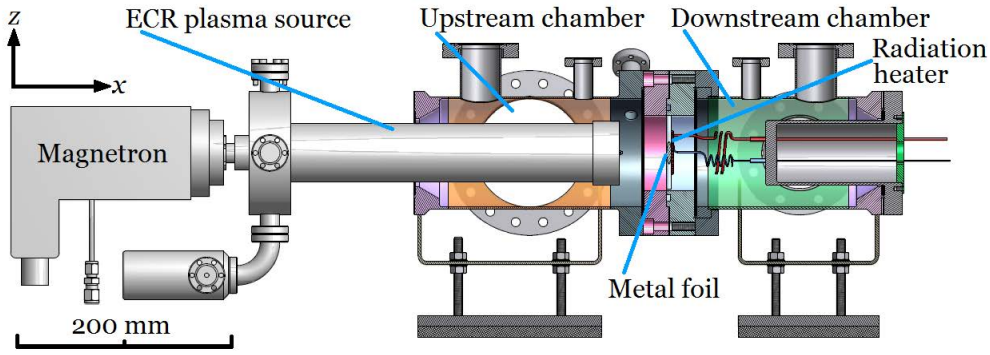

Figure 5.2: CAD model of the HERMES setup without auxiliary systems.

In Figure 5.3, a photograph of the setup can be seen. Due to space restrictions, this photograph was taken from the other side, so the flow of hydrogen is not from left to right, as in all other diagrams of this work, but from right to left. As in most vacuum setups, the main chamber is hardly visible, as the chambers are covered in heating ribbons and insulation in order to be able to perform a bake-out. The attached auxiliary systems are similar in size to the actual measurement chambers. The downstream chamber is hidden behind the large gate valve V5.

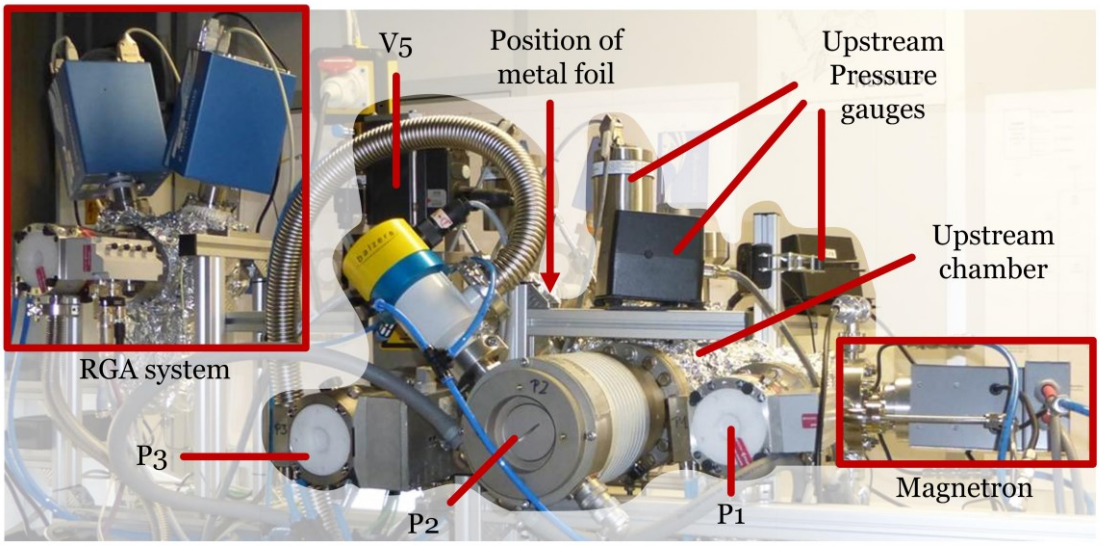

Figure 5.3: Photo of the HERMES facility. In contrast to all the other figures, the upstream chamber is on the right side and the downstream chamber on the left. Due to the auxiliary systems and the insulation for the bake-out, the main chambers are hardly visible. The downstream chamber is positioned behind the large gate valve V5. The metal foil is located between the chambers. The arrow points towards the approximate position.

The suprathermal hydrogen is supplied via the Tectra Gen2 plasma source. Additional information on the design of the plasma source can be found in [153], and a diagram of the source is shown in Figure 5.4. A magnetron supplies microwaves ($f = 2.45$ GHz), which enter the vacuum chamber through an alumina window. They are transported in a coaxial waveguide with a central tungsten rod. The coaxial line is constantly evacuated by a turbomolecular pump. At the end of the coaxial line, the microwaves enter an alumina cup, which is the plasma chamber. The gas is supplied through a capillary into this cup. A set of magnets in a quadrupole configuration supply the necessary magnetic field for the ECR condition. Cooling water flowing in an annular gap surrounding the waveguide and plasma chamber avoids the overheating of the magnets. Two grids in front of the cup allow the adjustment of the plasma potential (anode grid) and focus of the ion beam (cathode grid). The plasma-induced ion current between a metal ring in front of the grids and the ground allows for monitoring the plasma.

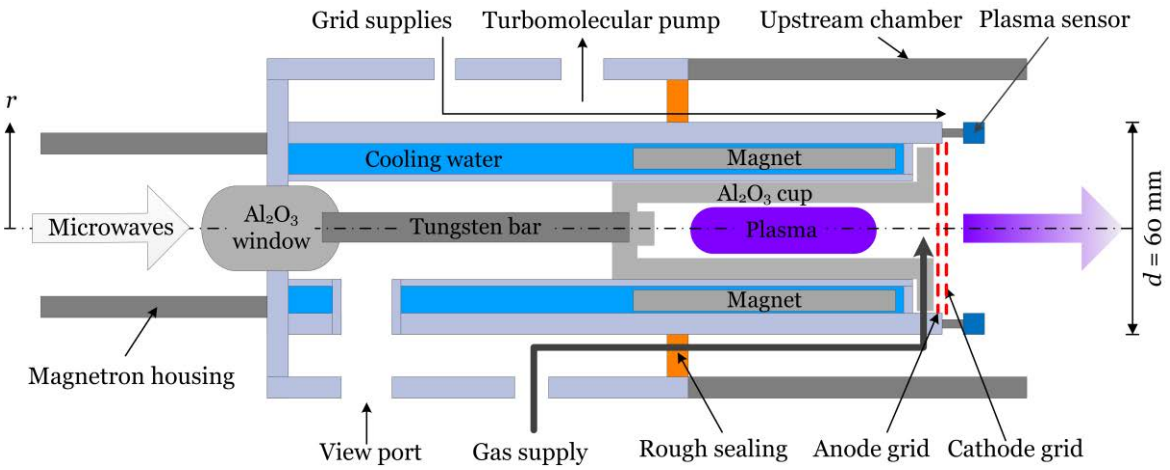

Figure 5.4: Scheme of the Tectra Gen2 ECR plasma source in HERMES.

In the course of the experiments, it became evident that HERMES has some fundamental limitations. First, the operational temperature of the foil is limited. At high temperatures, a radiation heater can sputter itself onto the surrounding surfaces. This is the case for materials with a significant vapour pressure. The radiation heater used in HERMES has a stainless steel skin. The chromium in the alloy in particular will have this effect and thus limits the upper operation temperature. While the heater is specified to be used for temperatures up to 800 °C, this results in a foil temperature of around 600 °C when the downstream pressure is low. When the downstream pressure increases, the heat conductance of the gas causes the foil temperature to decrease to a value of less than 500 °C. Second, the plasma source causes several problems, the most important of these being unreliable plasma ignition behaviour and the contamination of the metal foils with molybdenum. The anode and cathode grids are manufactured from this material. The molybdenum could be found on a metal foil during a surface analysis via Auger electron spectroscopy (AES).

5.1.2 HERMES*plus*

The limitations of HERMES have given rise to the design and setup of HERMES*plus*. One of these issues is the limited heating of the metal foil. This is the reason why resistive heating has been chosen for HERMES*plus*. For this, a current is sent through the metal foil, and the electrical resistivity causes the conversion of electric to thermal energy through ohmic heating. It seems very unpractical to realize the heating of a flat metal foil via this path. A more suitable design is the use of a metal foil wound to a cylinder. This way, the current passes along the tube. This process also causes a much more even temperature distribution. The flat metal foil in HERMES is cooled along the whole circumference by the contact with a massive metal flange. The tubular design has only a small contact area. Even this influence can be decreased by separately heating the connection area, as done in this setup. The temperature is also equilibrated by two additional effects. First, the inner surface of the membrane faces itself. It can distribute heat via radiative heating. Second, the temperature-dependent resistance of the metal is beneficial. The resistivity of the chosen material increases with temperature. If the metal foil is heated asymmetrically by an external source, its resistivity increases, which decreases the current passing through it. This in turn decreases the resistive heating. At the same time, the current on the other side will increase and cause more heating.

In Figure 5.5, a photo of the metal foil module that has been custom made for this setup is shown. On the right side, the tubular metal foil is highlighted. Its diameter is 10 mm and the length is around 100 mm. The lower end is sealed shut. Unconventionally, the foil-tube has three current leads. The middle and the right lead are used for the heating of the membrane, while the left and the middle lead are used to control the temperature of the joint between the metal foil and connection tube. A ceramic ring provides electric isolation between the connecting tube and the vacuum chamber. Two tungsten-rhenium (type-A) thermocouples run through the tubing. One is attached to the foil-tube junction, and the second one runs down to the lower seal of the metal foil. This temperature measurement is used to verify the measurement of a two-colour pyrometer (TI15). It is mounted on top of the facility in front of a borosilicate window, facing along the connection tube into the niobium cylinder. The connection flange has sealing surfaces to both sides. The visible right one is connected to the upstream chamber, while the left side is connected to the downstream volume.

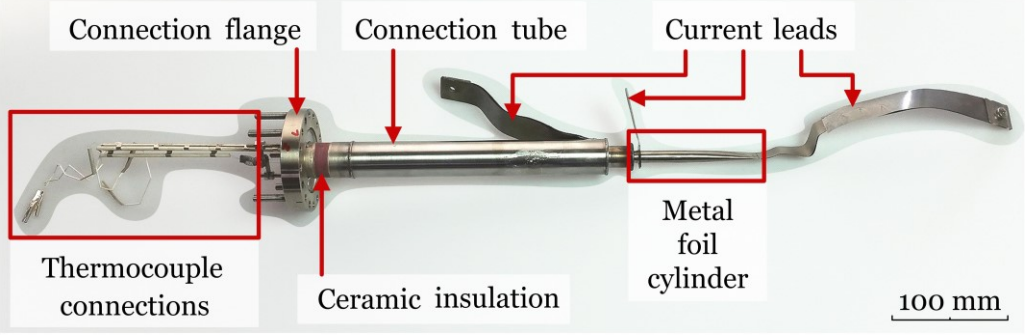

Figure 5.5: Photo of the metal foil module of HERMES*plus*. The module is mounted with the depicted right side facing down.

The metal foil module is mounted in a cylindrical vacuum vessel. In Figure 5.6, a CAD drawing of the vessel is shown on the left. Along the central axis of the vessel, the ceramic tube of the DuoPlasmaline is positioned. On the upper and lower sides of the vacuum vessel, a waveguide is positioned, which feeds microwaves to the plasma source. This waveguide is also used to provide cooling air. At the bottom flange of the vacuum vessel, most of the auxiliary systems are placed. One of these is the gas feed that is connected here. The gas flow is regulated by two parallel-connected mass flow controllers, which cover the ranges $0 - 10\,\mathrm{sccm}$ (FIC1) and $0 - 100\,\mathrm{sccm}$ (FIC2). Behind a manual corner valve to regulate the conductance, the turbomolecular pump P3 ($60\ \mathrm{l/s}$) is connected. Additional items on the lower flange, which are not shown in the CAD, are a burst disc (opening pressure $300\,\mathrm{mbar} \pm 10\,\%$ above ambient pressure) and the pressure gauges PI07 (up to 133 kPa), PI08 (up to 1.33 kPa) and PI02 ($6.67 \cdot 10^{-2} - 101\,\mathrm{kPa}$). The fourth pressure gauge of the upstream chamber, P1 (up to 2.67 Pa), is located on the top flange, as it has to be mounted in an upright position.

The top flange is used to accommodate the metal foil module. It can be seen on the right side of the CAD drawing. The foil itself is depicted in orange in the CAD drawing. On the right of Figure 5.6, a photograph of the top flange is shown, with most of the top flange components in place before assembly of the vacuum chamber. To the right of the metal foil module, two high current feedthroughs for the resistive heating can be seen. The third current feed will be connected from the bottom flange and is shown in the CAD drawing. Two additional high current feedthroughs to the left of the membrane are used for the connection of the filament. This is made of tantalum foil, with the dimensions $0.1 \times 10 \times 300\,\mathrm{mm}$. For better resistance against surface oxidation, the carbon content in the tantalum is increased. To avoid contamination of the ceramic tube by the filament, a molybdenum shielding plate is placed in between the two.

As a plasma source, a DuoPlasmaline by Muegge GmbH is chosen. The vacuum chamber connection is custom made for this setup, while all parts not in direct contact with the vacuum chamber are standard parts, consisting of rectangular aluminium waveguides, connected to two $2\,\mathrm{kW},\ 2.45\,\mathrm{GHz}$ magnetrons and their power supplies. The DuoPlasmaline is a collisional plasma source, chosen for three reasons. First, it is able to operate at higher pressures than an ECR source. This is very important, as one aim of this work is to demonstrate that there are technical solutions for plasma sources at all desired operation pressures. Second, the electron temperature is much lower than in ECR plasma. This is beneficial for the stability of the non-metallic surface layer. Third, the DuoPlasmaline is easily scalable to higher lengths and has a large plasma surface, which is necessary for utilization in future MFPs.

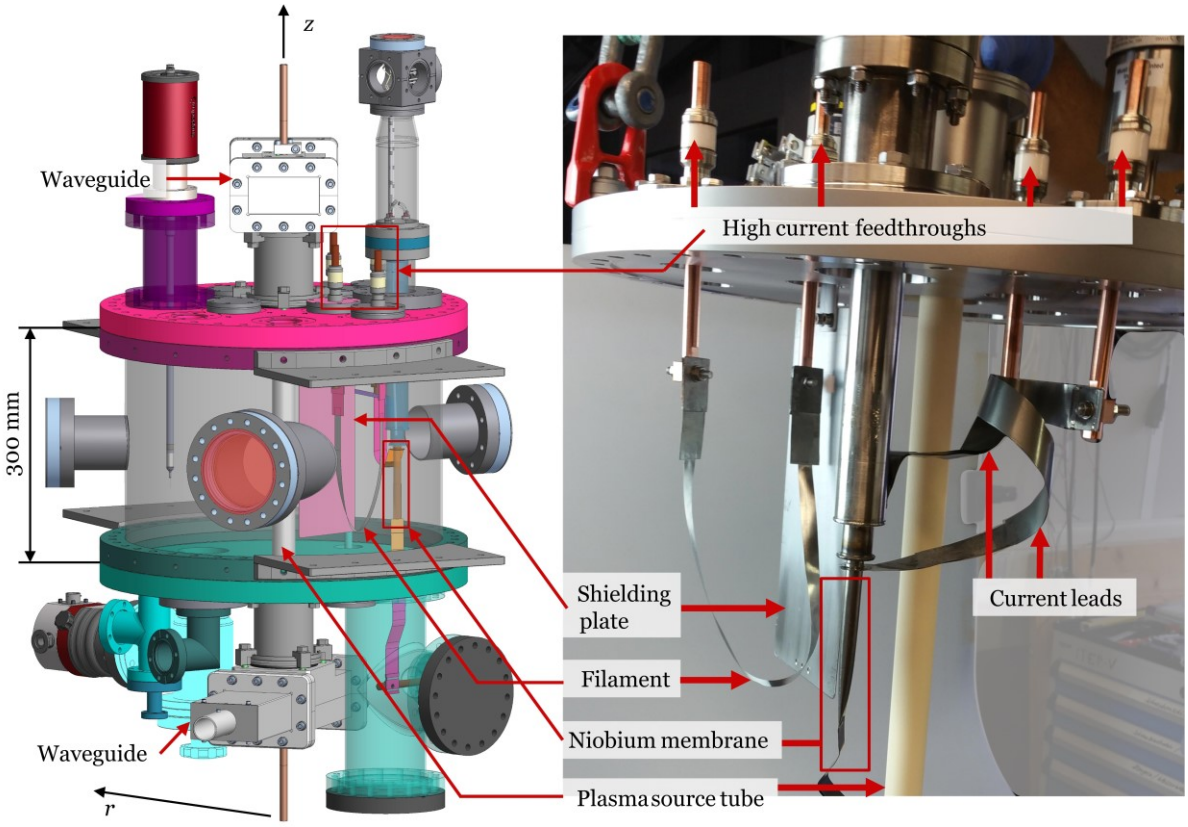

Figure 5.6: Left: CAD drawing of the HERMES*plus* main vacuum chamber. Right: Photograph of the fully mounted top flange of HERMES*plus*.

Figure 5.7 shows a photograph of the assembled facility. The upstream chamber, which is shown in the previous figure, can be seen as the central element in the picture. Several subsystems are outlined and labelled.

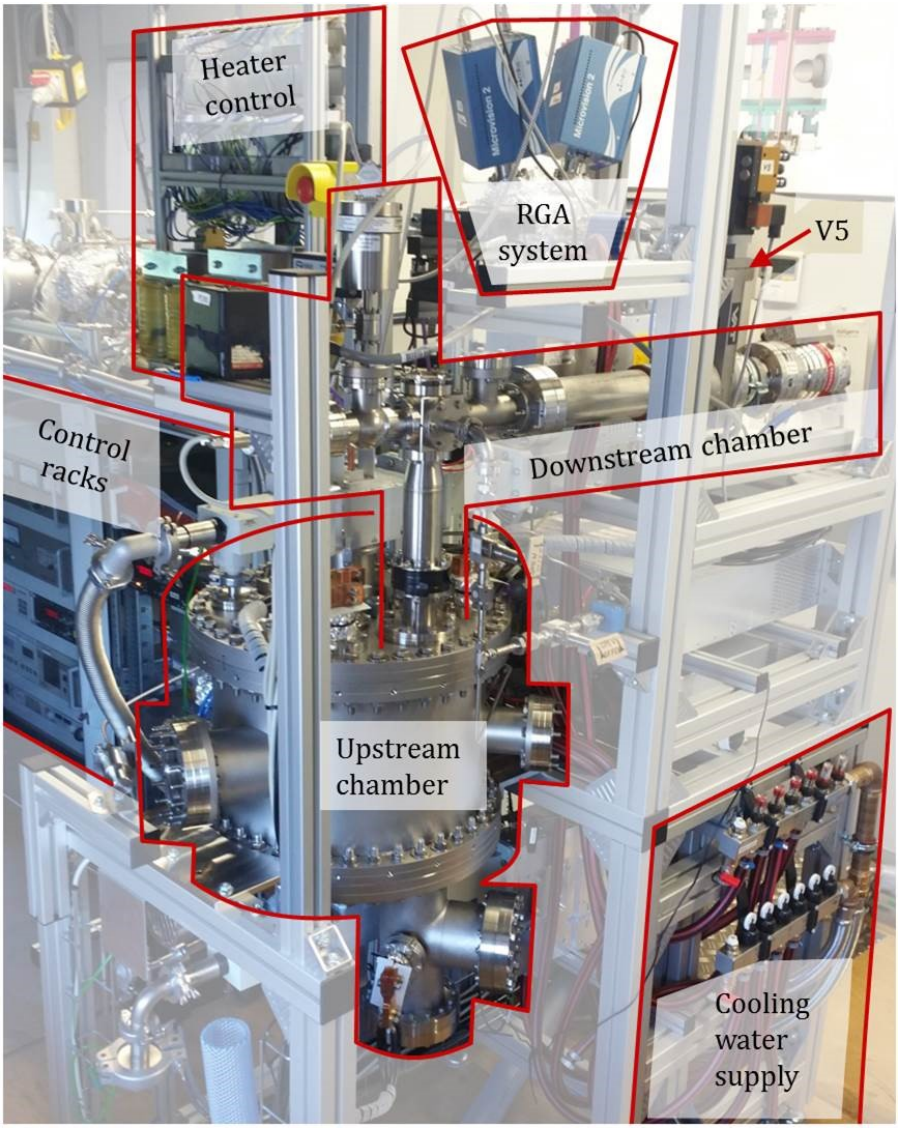

Figure 5.7: Photograph of the HERMES*plus* setup within its rack. Some features are highlighted and labelled.

Summarizing the description of the two facilities, Table 5 provides an overview of the metal foils and gases used in the different experiments.

Table 5: Experimental conditions and analytical methods used in the two setups.

	HERMES	HERMES*plus*
Foil materials	V, Fe, Cu-Fe	Nb
Foil thickness	0.1 mm	0.1 mm
Gases	H_2, D_2, He	H_2
Suprathermal hydrogen source	ECR	Collisional, filament

5.2 Measurement devices and infrastructure

The two facilities have a number of sensors and actuators. They are controlled by a WinCC program that is run on a Siemens SIMATIC S7 unit. For data acquisition, a Delphin Technology ProfiMessage unit is used. In the following, the different elements are outlined. Particular attention is paid to those used to collect the information presented in Chapter 6 "Superpermeation proof in practice", which includes the experimental results. A compilation of these sensors is provided in Table 6. The uncertainty of the measurement devices is discussed in subchapter 5.4

The measurement devices used for the evaluation of the data gained in HERMES and HERMES*plus* are mainly pressure gauges or temperature sensors.

Most temperature sensors in these setups are thermocouples. This type of temperature sensor is well established in industry and is based on the temperature-dependent voltage, which establishes when different metals are brought into contact. In the facilities, type-K thermocouples are mainly used (TI01-TI11). These consist of two nickel-rich alloys and can be used in the range between $-200\,℃$ and $1370\,℃$ [154]. In the setups, fibreglass-insulated thermocouples are used when in ambient air and as cladded thermocouple within the vacuum chamber. For high temperature operation, they have a very limited lifetime. Therefore, two type-A thermocouples are used in the metal foil module of HERMES*plus* (TI12, TI13). Type-A thermocouples have been developed for high temperature use of up to $2300\,℃$ [154]. They consist of two different tungsten-rhenium alloys. In the metal foil module, they are used as bare wires with local ceramic insulations. As the uncertainty of the type-A thermocouples is only specified for temperatures above $1000\,℃$, their reading is only used to verify the measurement of the installed two-colour pyrometer (TI15). This system measures the intensity of emitted light at two wavelengths. By setting these intensities into a relationship, it is possible to measure the temperature with a very low influence of the surface emissivity. In HERMES*plus*, a Metis M322 by Sensortherm is used. Its measurement range spans from $500\,℃$ to $1800\,℃$ with an uncertainty of $0.3\,\%$ of the reading in ℃ plus $2\,K$.

For the operation of the two facilities, the pressure must be measured from ambient condition down to a value that is more than ten orders of magnitude smaller. This wide span cannot be measured precisely with only one method. Pressure is defined as force per surface area. The preferred method for such a measurement is therefore to measure this directly by an induced deformation of a membrane. This is the measurement principle of the MKS Baratrons used. The membrane is part of a capacitor, and its value changes with pressure. The capacitor is part of a resonant LC-circuit, and the frequency shifts with pressure. High accuracy versions, as used in this work, need to be temperature-stabilized, as the thermal expansion of the membrane influences the measurement. The transducers PI01 and PI03 are thermally stabilized at $45\,℃$ [155], and the transducers PI07, PI08 and PI09 at $40\,℃$ [156].

Measurements of pressures below the operation range of Baratrons are carried out with cold cathode gauges (PI02, PI04). Instead of measuring the force per surface area, as in the capacitor method, the gas is ionized and a current is measured that is proportional to the particle density. The ionization is achieved by electron impact upon background particles. To achieve

sufficient ionization, the design of the electromagnetic fields causes the electrons to travel long paths before being absorbed by the anode. This also limits the response time of these gauges. The reading of a cold cathode needs to be converted to a pressure by gas-dependent relationships [157]. The pressure gauges used, which have a cold cathode arrangement, also have a second measuring principle installed. This allows them to cover a wider operating range. The second sensing element is based on the pressure-dependent thermal conductivity of a gas. This "Pirani"-type element has a linear dependence between thermal conductivity and pressure in a wide operating regime, so a single factor can be used to convert the reading to the pressure for each measured gas [157].

Table 6: List of most relevant measurement devices in the HERMES and HERMES*plus* setup.

Name	Device	Manufacturer	Model
PI01	Capacitive barometer	MKS	Baratron Type 627D
PI02	Combined Pirani and cold cathode barometer	MKS	DualMag Type 972B
PI03	Capacitive barometer	MKS	Baratron Type 627D
PI04	Combined Pirani and cold cathode barometer	MKS	DualMag Type 972B
PI05	(Active) Pirani barometer	Edwards	APG-M-NW16
PI06	(Active) Pirani barometer	Edwards	APG-M-NW16
PI07	Capacitive barometer	MKS	Baratron 390 HA-01000
PI08	Capacitive barometer	MKS	Baratron 390 HA-00010
PI09	Capacitive barometer	MKS	Baratron 390 HA-00010
PI10	Hot cathode barometer	MKS	Micro-Ion Type 354
TI06	Type-K thermocouple	TC	
TI07	Type-K thermocouple	TC	
TI12	Type-A thermocouple	Mevodena	Bare W5Re-W20Re
TI13	Type-A thermocouple	Mevodena	Bare W5Re-W20Re
TI15	Pyrometer	Sensortherm	Metis M322
RGA A	Quadrupole mass spectrometer	MKS	MicroVision 2, 1-6 amu
RGA B	Quadrupole mass spectrometer	MKS	MicroVision 2, 1-300 amu

The sensor data is recorded via the specialized readout system ProfiMessage by Delphin Technology AG. The value of the pressure gauges and the pyrometer (TI15) is supplied via a $0-10\,\mathrm{V}$ analogue output, which is recorded via a 24-bit A/D converter in the ProfiMessage. This corresponds to a readout accuracy of $0.01\,\%$ of the measurement range. The only exception is the readout of PI07, which is not recorded via this route. The A/C conversion of this signal is only 9 bit. This signal is not used in any calculation and is required for the operation of the facility. The temperature signals of the thermocouples are directly connected to the ProfiMessage systems, with a measurement accuracy of $\pm 0.1\,\%$ of the upper range value.

In addition to the listed gauges, the two facilities also employ a number of actuators. The different pumps and a side channel blower are listed in Table 7, with their nominal pumping speeds. In Table 8, identification of the other actuators is given.

Table 7: List of used vacuum pumps in the HERMES and HERMES*plus* setup.

Name	Device	Manufacturer	Model	Pumping speed
P1	Turbo molecular pump	Pfeiffer	HiPace 80, CF-DN 63	67 l/s for N_2
P2	Turbo molecular pump	Balzers	TPU 180H, CF-DN 100	180 l/s for N_2
P3	Turbo molecular pump	Pfeiffer	TMU 071 P, CF-DN 63	60 l/s for N_2
P4	Scroll pump	Edwards	nXDS 10i (nXDS 6i for some measurements)	12.7 m^3/h (6.3 m^3/h)
P5	Diaphragm pump	Vacuubrand	MD4	3 m^3/h
P6	Turbo molecular pump	Pfeiffer	HiPace 80 CF-DN 63	67 l/s for N_2
P7	Side channel blower	Elektror	SD42	2.8 m^3/min
P8	Scroll pump	Edwards	nXDS 10 iR	12.7 m^3/h

Table 8: List of most relevant actuators in the HERMES and HERMES*plus* setup (without pumps).

Name	Device	Manufacturer	Model
FIC1	Mass flow controller	MKS	MF1C01311CMAVO, 0-10 sccm
FIC2	Mass flow controller	MKS	2259CC-00100SV, 0-100 sccm
PS1	ECR plasma source	Tectra	Gen 2, 2.45 GHz
PS2	Collisional plasma source	Mügge	DuoPlasmaline 2 × 2 kW, 2.45 GHz
H5	Radiation heater	KIT/PCE Power control	Custom/GEN 60-12.5
C1	Continuous flow chiller	Huber	Unichiller 006-MPC
C2	Continuous flow chiller	Aermec	ANL 020
HV6	Manual valve	Swagelok	
HV7	Manual valve	Swagelok	
HV9	Manual valve	Swagelok	
V4	Piezoelectric valve	Pfeiffer	EVL 016 PC
V5	Gate valve	VAT	CF-DN 63
W1	Thyristor-controlled trafo	Ulmer/Jumo	5 kVA, custom winding
W2	Thyristor-controlled trafo	Ulmer/Jumo	1 kVA, custom winding
W3	Thyristor-controlled trafo	Ulmer/Jumo	4 kVA, custom winding

5.3 Analytical methods

For the investigation of permeation through metal foils, different methods have been used. The method that can be used in each case is mainly determined by the capability of the experimental setup.

The different methods to determine the hydrogen flow through the metal foil can be used for the different permeation measurements. Classical permeation, with a gas pressure difference as a driving force, is called gas-driven permeation (GDP) in the following. If one of the plasma sources is used to cause (super-) permeation, it is called plasma-driven permeation (PDP). In HERMES, this is an ECR plasma, while in HERMESplus this is a collisional plasma. In HERMESplus, the incandescent filament can also be used to enable superpermeability. As the filament mainly produces hydrogen radicals, it is called atom-driven permeation (ADP).

5.3.1 Pressure rise method

The pressure rise method is the most simple and straightforward method of detecting and analysing the flow of hydrogen through a metal foil. This method is used in the HERMES setup.

For a measurement, constant conditions first have to be established while pumping the downstream chamber with P3. The connection between up- and downstream chamber is closed (V4). The temperature of the metal foil (TI06) can be adjusted via regulation of the heating power of H5. The temperature of the heater is monitored by TI07. The pressure in the upstream chamber can be controlled by the gas feed (FIC1) and the speed of the turbo molecular pumps that are connected to the upstream chamber (P1 and P2). For plasma-driven permeation experiments, the plasma source is switched on and magnetron power and grid voltages are adjusted. After reaching a steady state, the downstream pumping is stopped by closing the gate valve V5. The pressure rise in the downstream chamber can be monitored by the various pressure gauges (PI03, PI04 and PI09).

The pressure rise in the downstream chamber $\dot{p_d}$ is proportional to the permeating flow $\dot{n}$. The ideal gas law can be rearranged to describe this relationship:

$$\dot{n} = \frac{\dot{p_d} V_d}{\mathbb{R} T_{av,d}}. \tag{5.1}$$

Unfortunately, the pressure rise itself influences this method in various ways. To calculate the permeated flow, the average downstream gas temperature $T_{av,d}$ has to be known. This changes quite considerably during the course of this experiment. When the pressure rises, the thermal conductivity of the gas also increases, which shifts the foil temperature and the average gas temperature in the downstream chamber. A different membrane temperature also changes the permeating flow. The increased downstream pressure also increases the gas-driven permeation from the downstream to the upstream side. This latter effect is highly important for PDP experiments. For GDP it is of minor importance, as the pressure in the downstream chamber is still about three orders of magnitude lower than in the upstream chamber for all experiments performed.

Although this method suffers from the previously mentioned drawbacks, it is the easiest to realize and allows good comparisons between different measurements.

5.3.2 Flux method

To avoid the influence of the changing downstream pressure in the experiment, the HERMES*plus* setup was designed to measure the permeating flow in a different way. This method is based on the constant pumping speed of high vacuum pumps in the free molecular regime. Equation (3.13) can be rearranged to give:

$$j = \frac{p_d \cdot S_{eff}}{\mathrm{A}}. \tag{5.2}$$

The flux of hydrogen j is therefore determined by the downstream pressure p_d, the effective pumping speed S_{eff}, the metal foil area A and the temperature of the pumped gas T ($S = f(T)$). It is important to note that the temperature is not the average downstream gas temperature, but the temperature of the gas that is pumped. As the surfaces close to the pumping duct in the HERMES*plus* experiment are all at ambient temperature, this temperature needs to be used in this calculation. The effective pumping speed S_{eff} is given by

$$S_{eff} = \left(\frac{1}{C} + \frac{1}{S}\right)^{-1}, \tag{5.3}$$

which consists of the pumping speed S of the connected vacuum pump and the conductance of the piping C. The conductance is dominated by a small orifice that has been chosen to obtain a certain value for the effective pumping speed.

Using the previously derived equation,

$$C = A_o \frac{\bar{u}}{4} \Omega, \tag{3.20}$$

to calculate the conductance of the orifice, the area of the hole A_o and the mean molecular speed can be calculated, but the capture coefficient Ω still needs to be defined. For this, the empirical equation,

$$\Omega = 1 + \frac{{L_C}^2}{4} - \frac{L_C}{4}\sqrt{4 + {L_C}^2} - \frac{\left(\left(8 - {L_C}^2\right)\sqrt{4 + {L_C}^2} + {L_C}^3 - 16\right)^2}{72\, L_C\sqrt{4 + {L_C}^2} - 288\, ln\left(L_C + \sqrt{4 + {L_C}^2}\right) + 288 \ln 2}, \tag{5.4}$$

with the characteristic length

$$L_C = \frac{l_o}{r_o}, \tag{5.5}$$

has been deployed. The length of the tube is given by l_o and the radius of the hole is termed r_o. The equation is well established in vacuum technology and is valid in the free molecular regime for tubes of any length [158].

The experiments in this thesis have been performed with a circular orifice with a diameter of 4.3 mm, which is precision-drilled into a copper disk with a thickness of 2.1 mm. This gives a conductance C for hydrogen H_2 of 4.35 l/s at 25 °C. In combination with the low pressure pumping speed of the turbo molecular pump, which is specified by the manufacturer as 48 l/s for H_2 gas [159], this gives an effective pumping speed of 3.99 l/s.

The measurement itself is even more straightforward than that of the pressure rise method. When stable conditions are established, the downstream pressure is directly proportional to the permeated flow. It can be calculated with equation (5.2).

While this measurement type is only valid if the vacuum flow through the orifice is in the free molecular regime and the pumping speed of the turbo molecular pump is constant in the operated pressure regime, these conditions can be arranged accordingly by the right design of the equipment. As this measurement is based on steady state conditions, the influencing parameters can be studied independently.

5.3.3 Compression method

The compression method can be seen as a combination of the two previously described methods. It allows for evaluating more than just the total permeating flow. This method relies on constant surface properties, as well as a constant flow of suprathermal hydrogen incident on the upstream surface of the metal foil. A measurement using the compression method begins with a measurement of permeating gas via the flux method.

To derive the relationships for the compression method, one must start with the equations describing the flux method. While the downstream chamber is pumped, the total amount of permeating gas is measured. It is composed of the flow caused by the suprathermal hydrogen J_s (PDP/ADP) and the flow of gas-driven permeation (GDP) under the initial conditions $J_{m,0}$:

$$J_s + J_{m,0} = p_0 \cdot S_{eff}. \tag{5.6}$$

This gas-driven permeation can be described by

$$J_{m,0} = \frac{1}{2} A\, \mathbb{R}\, T\, \mu\, \sigma\, \alpha_m\, (p_u - p_0), \tag{5.7}$$

which uses equation (3.10) to determine the hydrogen flux onto the membrane surface $A\,\sigma$. The flow absorbed into the foil is determined by the sticking coefficient α_m. The permeation likelihood is assumed to be one half for equal surface barriers on the up- and downstream side in the surface-limited regime. As this process takes place on both sides of the membrane, the opposing flow, caused by the downstream pressure at this point in time p_0, is substracted.

By closing a valve in front of the downstream vacuum pump (in HERMES*plus*: V5), the pressure rises in the downstream chamber. In Figure 5.8, this is displayed schematically.

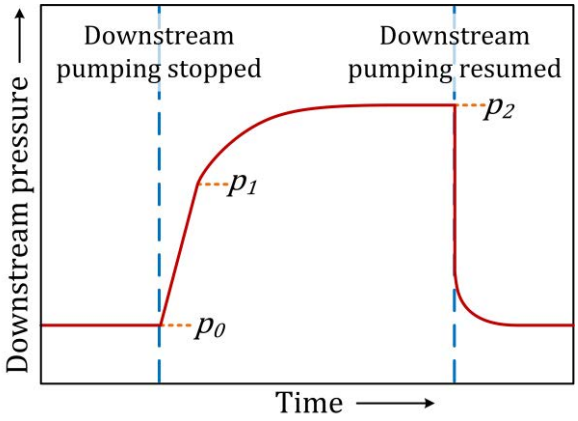

Figure 5.8: Scheme of the downstream pressure curve over time during a compression experiment.

After some time, a constant pressure p_2 is reached. At this stage, the flow due to suprathermal hydrogen equals the reverse GDP flow:

$$J_s = J_{m,2}. \tag{5.8}$$

In combination with (5.7), this gives

$$J_s = \frac{1}{2} A\, \mathbb{R}\, T\, \sigma\, \mu\, \alpha_m\, (p_2 - p_u). \tag{5.9}$$

Combining the equations (5.6), (5.7) and (5.9), one obtains

$$J_s = p_0 \cdot S_{eff}\, \frac{(p_2 - p_u)}{(p_2 - p_0)}. \tag{5.10}$$

The corresponding molecular hydrogen flow in the initial stage of this experiment is therefore

$$J_{m,0} = p_0 \cdot S_{eff}\, \frac{(p_u - p_0)}{(p_2 - p_0)}. \tag{5.11}$$

As the gas-driven permeation into both directions of the foil is part of this experiment, some information on the surface asymmetry of the metal foil can also be gained.

When the hydrogen flows are balanced by the downstream surface of the foil, it becomes clear that the hydrogen release into the gas phase minus the absorption is the permeated flow. This can be described by:

$$J_{des,d} - J_{abs,d} = A\, \mathbb{R}\, T\, \sigma_d k_{r,d} {c_0}^2 - A\, \mathbb{R}\, T\, \sigma_d \alpha_{m,d}\, \mu\, p_0 = p_0 \cdot S_{eff}. \tag{5.12}$$

When the pumping is stopped, a linear pressure increase in the downstream chamber can be observed. For small downstream volumes, the pressure at which the hydrogen concentration in the metal foil is in equilibrium with the downstream pressure (equation (3.29)) is reached quickly. Under the assumption that the hydrogen concentration in the metal foil stays roughly the same in this short amount of time, this equilibrium pressure is p_1. Equation (5.12) can be altered to give

$$A\, \sigma_d k_{r,d} K^2 p_1 - A\, \sigma_d \alpha_{m,d}\, \mu\, p_0 = \frac{p_0 \cdot S_{eff}}{\mathbb{R}\, T}. \tag{5.13}$$

Together with equation (3.40), one can rearrange the equation to obtain a direct expression of the downstream surface properties:

$$\sigma_d \alpha_{m,d} = \frac{S_{eff}}{A\,\mu\,\mathbb{R}\,T}\,\frac{p_0}{(p_1 - p_0)}. \tag{5.14}$$

Similarly, this approach can be used for the upstream surface properties. While the absorbed flow of hydrogen remains constant throughout the experiment, the desorbing flow will become the same when the concentration in the foil is in equilibrium with p_2. In the beginning of the experiment, the absorbed flow is given by

$$J_{abs,u} = J_{des,u} + p_0 \cdot S_{eff} = A\,\mathbb{R}\,T\,\sigma_u\,k_{r,u}{c_0}^2 + p_0 \cdot S_{eff}, \tag{5.15}$$

and when p_2 is reached in the downstream chamber, it is given by

$$J_{abs,u} = A\,\mathbb{R}\,T\,\sigma_u k_{r,u}{c_2}^2 = A\,\mathbb{R}\,T\,\sigma_u\,k_{r,u}K^2 p_2. \tag{5.16}$$

These two equations can be combined to express the upstream surface properties as

$$\sigma_u \alpha_{m,u} = \frac{S_{eff}}{A\,\mu\,\mathbb{R}\,T}\,\frac{p_0}{(p_2 - p_1)}. \tag{5.17}$$

The surface asymmetry can be calculated by combining (5.14) and (5.17) to give

$$\varepsilon = \frac{\sigma_u k_{ru}}{\sigma_d k_{rd}} = \frac{\sigma_u \alpha_{m,u}}{\sigma_d \alpha_{m,d}} = \frac{(p_1 - p_0)}{(p_2 - p_1)}. \tag{5.18}$$

This method is based on the “flux method”. Therefore, the initial flow determination is restricted to the conditions in the previous section 5.3.2. The compression after that initial measurement allows for separating the flow caused by PDP/ADP and by GDP in relation to this initial measurement. The assumption that needs to be fulfilled for the compression method is a constant suprathermal hydrogen flux on the upstream surface, as well as constant metal foil parameters. The measurements incorporating the transition pressure p_1 should be seen as an approximation and are based on the assumption of near constant hydrogen concentration in the metal foil during the initial time of compression. The difficulty of an exact determination of p_1 adds another factor of uncertainty. Nevertheless, these measurements allow the obtaining of a value for the surface symmetry.

5.4 Measurement accuracies and error estimate

The measurement accuracy is dependent on several influencing factors. These are the uncertainties of the sensing element(s), their readout system and possible uncertainties of the measurement method.

HERMES has been designed to measure via the pressure rise method. The pressure value measured during an experiment is determined with the uncertainty of the pressure transducers and of the data acquisition system. As high accuracy pressure transducers (PI01, PI03, PI08 and PI09) are used for these measurements, the uncertainties for these measurements are 0.25 % or lower for all cases. As the resulting error bars in the results in Chapter 6 would be thinner than the lines in the graphs (Figure 6.1, Figure 6.5, Figure 6.6, Figure 6.7, Figure 6.11, Figure 6.12, Figure 6.13), they are not displayed. In contrast to these very accurate pressure measurements, the permeating flows can only be determined with a high uncertainty. This is due to the measurement method. The biggest influence factor for this is the average gas temperature in the downstream chamber. As can be seen in equation (5.1), it is directly related to the molar flow. The average temperature cannot be measured directly but can only be estimated. In the downstream chamber, two temperature sensors are present. One of these is pressed to the middle of the metal foil, and the other one is fixed to the radiation heater. Their measurements give only values that are representative for a small surface fraction of the downstream chamber. Most surfaces belong to the housing of the chamber, to flanges and to the tubing for the connection of the pressure sensors. There are several temperature sensors connected to the outside of the vacuum chamber. Their temperature will be lower than the temperature on the inner surfaces, as the heating comes from the radiation heater within the chamber. Therefore, their readings cannot be used. Considering the huge influence of this variation, a span of values is given for every permeating flow.

Another uncertainty in measurements in HERMES is the metal foil temperature. In the results, a single temperature is given. This is the value measured by the thermocouple pressed to the foil. This temperature is certainly not uniform over the whole surface. The connected stainless steel flange conductively cools the outer diameter. For a low downstream pressure, the heating will occur mainly via radiation. At higher pressures, the gas conduction and convection will also influence the temperature.

As the measurement method is the highest source of uncertainty for the determination of permeating flows in HERMES and the corresponding experiments are hardly repeatable, these results are only compared qualitatively. This is the reason why a span of results is given for the different average gas temperatures as a measure of uncertainty for the permeating gas flows in HERMES in the following chapter.

In contrast to this, the design of HERMES*plus* aims to determine permeating flows that are more accurate. The most important step for this is a change in the measuring method(s).

The evaluation of the uncertainty of the results is performed according to the “guide to the expression of uncertainty in measurement” [160]. This applies to the uncertainties in both the measurement values (according to 4.3.7 of [160]) and the derived values (according to 5.1.2

of [160]). The uncertainties of the different sensors are taken from the data sheets supplied by the manufacturers and are summarized in Table 9.

Table 9: Given manufacturer data on the uncertainty of measurement of the devices shown.

Name	Model	Uncertainty	Source
PI01	Baratron Type 627D	0.25 % of reading	[155]
PI02	DualMag Type 972B	$5 \cdot 10^{-8}$ ... 10^{-3} Torr: $\pm$ 30 % of reading 10^{-3} ... 100 Torr: $\pm$ 5 % of reading 100 ... 760 Torr: $\pm$ 25 % of reading	[161]
PI03	Baratron Type 627D	0.25% of reading	[155]
PI04	DualMag Type 972B	$5 \cdot 10^{-8}$ ... 10^{-3} Torr: $\pm$ 30 % of reading 10^{-3} ... 100 Torr: $\pm$ 5 % of reading 100 ... 760 Torr: $\pm$ 25 % of reading	[161]
PI07	Baratron 390 HA-01000	0.08 % of reading	[156]
PI08	Baratron 390 HA-00010	0.08 % of reading	[156]
PI09	Baratron 390 HA-00010	0.08 % of reading	[156]
TI06	Type-K thermocouple	Below 2 K for used temperature range	[154]
TI07	Type-K thermocouple	Below 3 K for used temperature range	[154]
TI12	Type-A thermocouple	1 % of reading	[154]
TI13	Type-A thermocouple	1 % of reading	[154]
TI15	Metis M322	0.3 % of reading in °C + 2 K	[162]

One uncertainty connected to the flux method is the calculation of the conductance through the orifice. The equation used is taken from the literature [158]. The uncertainty of this equation is determined to be smaller than 0.1% in [163]. In [164, 165], good agreement is confirmed with modern calculations. As this uncertainty is much lower than the uncertainty of the input values, it is neglected. The determination of uncertainty can be easily reproduced with the provided data for most values. This is not the case for the effective pumping speed. The necessary information to derive the standard deviation for this value is given in the appendix; see "Additional information on the measurement accuracy". The uncertainties for all measurements of HERMES*plus* are given in the form of error bars in the following chapter. These present an uncertainty of one standard deviation.

6 Superpermeation proof in practice

The different experiments and findings in HERMES and HERMESplus are described below. In the following two subchapters, an example measurement for each of the experimental setups is explained in detail. This allows for comprehending how the results are gained. In the subsequent subchapter (6.3), the various findings from superpermeation experiments are explained. Other results that have been obtained by other measurement methods are shown in subchapter 6.4. Improvements for further experiments and setups are elaborated in 6.6. All these results are used to draw conclusions for the use of an MFP in future fusion power plants in 6.7.

6.1 Experimental demonstration of superpermeation in HERMES

The measurements taken in HERMES are all performed by means of the pressure rise method. In Figure 6.1, the relevant data of such a measurement is shown. Before the measurement, constant conditions are established in the upstream chamber, while the downstream chamber is evacuated. In this case, a deuterium flow of 8 sccm is introduced to the upstream chamber. P2 is switched off and P1 is kept running. The magnetron is set to full power, the anode grid operates at 1.7 kV and the downstream pressure detected is below 10^{-2} Pa. The measurement is initiated by closing V5; the pressure in the downstream chamber increases immediately. After 25 s, it reaches 6 Pa. This equals the pressure in the upstream chamber. The metal foil temperature decreases in the first five minutes of the measurement, from 416 ℃ to 316 ℃. After these five minutes, the temperature of the membrane and the upstream pressure remains constant, while the downstream pressure linearly increases up to 390 Pa over the next two hours, until the experiment is stopped. The uncertainty in the pressure measurements is 0.08 % and less than 2 K for the temperature.

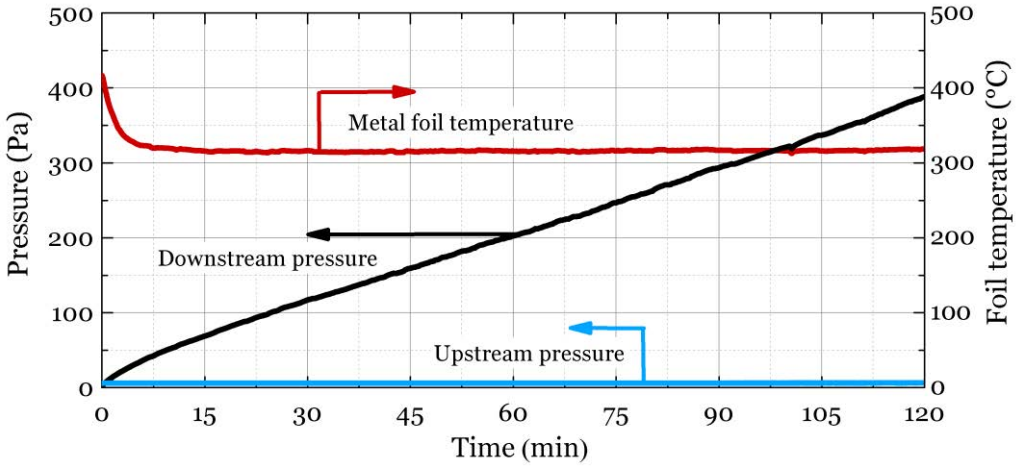

Figure 6.1: Pressure rise due to plasma-driven permeation of D_2 through a 0.1 mm-thick vanadium foil in HERMES. The downstream pressure (PI09) exceeds the upstream pressure (PI08) after 25 s.

The compression ratio between up- and downstream pressure is 65 at the end of the experiment. The average rate of pressure increase in the experiment is revealed to be $5 \cdot 10^{-2}$ Pa/s. If one assumes the average downstream gas temperature to be 150 °C, this corresponds to a pumped deuterium flow of $2.7 \cdot 10^{-2}$ Pa $m^3/(m^2\,s)$ ($3.5 \cdot 10^{-2}$ Pa $m^3/(m^2\,s)$ for 50 °C, and $2.0 \cdot 10^{-2}$ Pa $m^3/(m^2\,s)$ for 300 °C). The flow can be calculated with equation (5.1).

There is a simple explanation for the initial temperature decrease and the slightly different pressure slope in the first few minutes of the experiment. At the beginning of the experiment, the pressure in the downstream chamber is low, and heat conduction and convection by gas is negligible. At this pressure, the temperature of the gas is therefore the average temperature of all the surfaces in the downstream chamber. In Figure 6.2, a CAD model of the HERMES downstream chamber is shown. The surface of the radiation heater is small compared to the other surfaces of the vacuum chamber.

When the pressure rises in the downstream chamber, the heat transfer by the gas is not negligible anymore and the average gas temperature is no longer the same as the surface-averaged temperature, but instead increases due to inter-particle interaction. This can be also illustrated by the Knudsen number. At the beginning of the experiment, the Knudsen number has a value higher than 25. It is thus in the free molecular regime. When the pressure increases the Knudsen number drops to a value below 10^{-3}, which is in the continuum regime. In this regime, the increased heat conduction and convection cools the metal foil and causes its temperature to drop. This also results in a slight change of the pressure slope in the course of the experiment.

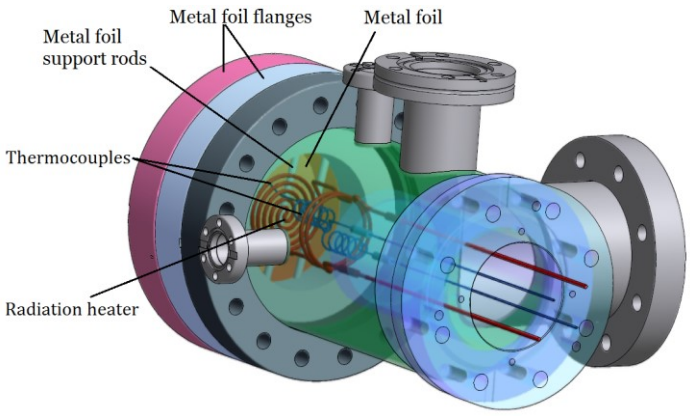

Figure 6.2: CAD model of the HERMES downstream chamber. The metal foil (orange) is sealed between the two metal foil flanges (pink and light blue). Support rods on the downstream metal foil flange (light blue) avoid excessive stress on the foil for the case of high upstream pressure. The foil is heated by the spirally wound radiation heater (red). Two type-K thermocouples (blue) are pressed against the foil and the heater.

The rapid pressure increase to values higher than the upstream pressure is a clear sign of superpermeation. While it is impossible to extract numbers on the incoming suprathermal hydrogen flux and the sticking coefficient of the metal foil, a number of conclusions can still be drawn. The metal foil is clearly in the surface-limited regime, otherwise superpermeation cannot occur. As the pressure increase is linear, the maximum compression pressure will be much higher than 400 Pa. This proves that an ECR plasma source in combination with a vanadium membrane is well suited for superpermeation.

6.2 Experimental demonstration of superpermeation in HERMES*plus*

The measurements in HERMES*plus* are conducted via the flux and the compression method. Every compression measurement starts with a flux measurement. In Figure 6.3, the relevant data for an atom-driven permeation (ADP) experiment via both methods is shown. At the beginning, constant measurement conditions are established. The niobium foil temperature is set to 700 ℃ by regulating the resistive heating. An upstream pressure of $6.3 \cdot 10^{-2}$ Pa is set by varying the gas flow of FIC1 and FIC2 while pumping is active. The filament is heated up to around 1800 ℃ to act as an atomic hydrogen source. The downstream part is isolated from the upstream chamber and is constantly pumped through the orifice. The resulting downstream pressure exhibits $3.7 \cdot 10^{-2}$ Pa. Multiplying this value with the effective pumping speed gives the flow through the membrane: $1.48 \cdot 10^{-4}$ Pa m^3/s. To make this result comparable with the results in HERMES, the flux is obtained by dividing the flow by the membrane area, which gives $4.92 \cdot 10^{-2}$ Pa $\mathrm{m}^3/(\mathrm{m}^2\ \mathrm{s})$. This and the following results are also displayed in Table 10 to provide a better overview.

To begin the compression experiment, the downstream pumping is discontinued by closing the gate valve V5. Immediately, the downstream pressure rises, and exceeds the upstream pressure within two seconds. This higher downstream pressure is a clear sign of superpermeation and is impossible to achieve with classical permeation. While the pressure rise is initially linear, it asymptotically approaches the value of 7.75 Pa. This value in combination with the upstream pressure can be used to distinguish between the flow caused by classical permeation and that by superpermeation for the initially determined flux. Using the equations given in 5.3.3, the flux caused by the suprathermal hydrogen is calculated to be $4.90 \cdot 10^{-2}$ Pa $\mathrm{m}^3/(\mathrm{m}^2\ \mathrm{s})$, which is 99.66 % of the permeated flow. The pressure in Figure 6.3 is plotted logarithmically in order to be able to show the whole pressure regime.

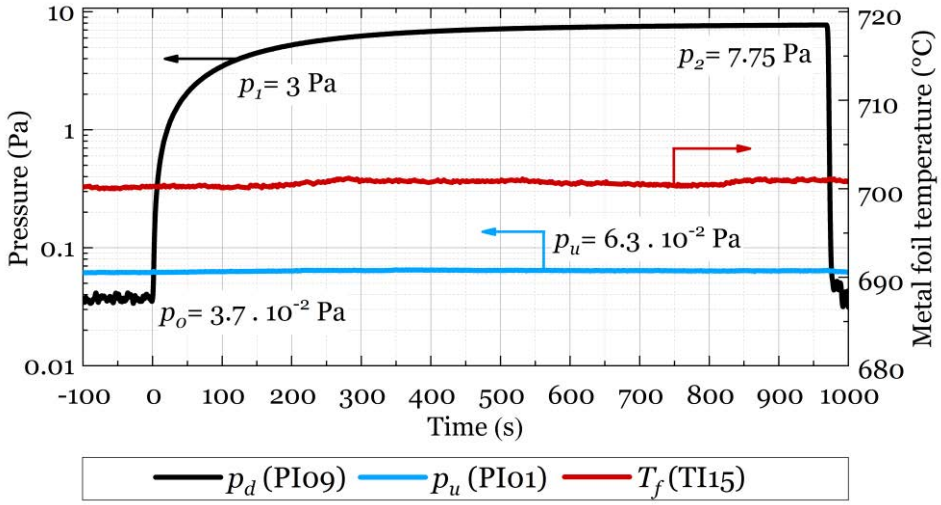

Figure 6.3: Pressure rise due to atom-driven permeation of H_2 through the niobium foil in HERMES*plus*. The downstream pressure exceeds the upstream pressure within 2 s.

In a linear plot, it is easier to distinguish between the initially linear pressure rise and the flattening of the rise. This point is found to be at a pressure p_1 of 3 Pa. This value is then used to calculate the sticking coefficients and the surface asymmetry. ε is found to be 0.62, with an upstream value of $\sigma_u \alpha_{m,u} = 1.3 \cdot 10^{-5}$ and a downstream value of $\sigma_d \alpha_{m,d} = 2.0 \cdot 10^{-5}$. This is a slightly favourable surface asymmetry. One explanation for this asymmetry lies in surface poisoning by non-metals such as water or carbon monoxide, present in bigger quantities in the large upstream chamber.

Table 10: Results of the example measurement from HERMES*plus*.

	Value	Unit	Relative
J_{tot}	$1.48 \cdot 10^{-4}$	(Pa m³/s)	
j_{tot}	$4.92 \cdot 10^{-2}$	(Pa m³/(s m²))	
j_{ADP}	$4.90 \cdot 10^{-2}$	(Pa m³/(s m²))	99.66 % of j_{tot}
j_{GDP}	$1.66 \cdot 10^{-4}$	(Pa m³/(s m²))	0.34 % of j_{tot}
$\sigma_u \alpha_{m,u}$	$1.3 \cdot 10^{-5}$	(–)	$\varepsilon = 0.62$
$\sigma_d \alpha_{m,d}$	$2.0 \cdot 10^{-5}$	(–)	

In section 4.2, a model predicting the pressure rise in a compression experiment is developed. In Figure 6.4, the measured downstream pressure rise, as well as the predicted values, are plotted. All input parameters are given by the previously shown results or the experimental setup, and no fitting parameter is used. One should keep in mind that the determination of the surface properties is not very precise, as described in section 5.3.3.

The general shape of the pressure development and the maximum compression pressure of the prediction match the actual measurement quite well. Nevertheless, the pressure rise is predicted to be faster than the experimental observation. The model assumes instantaneous equilibrium at all times. However, this does not correspond to reality. Therefore, the measured pressure evolution is delayed compared to the prediction.

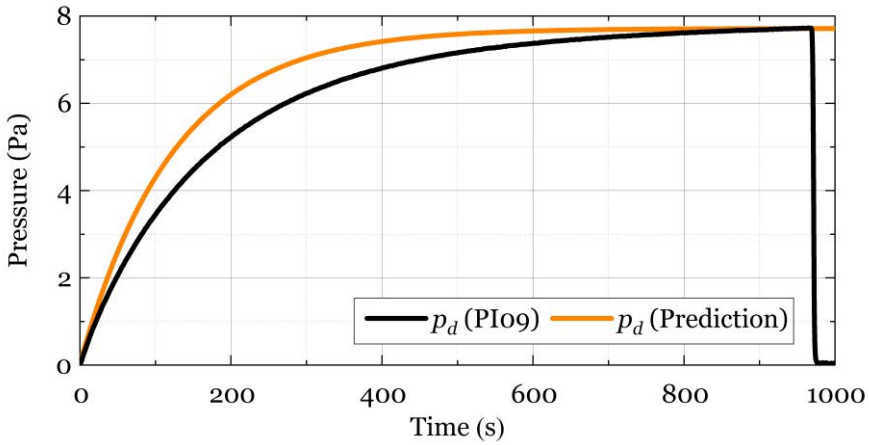

Figure 6.4: Comparison of measured and calculated downstream pressure evolution in the HERMES*plus* facility by means of the compression method.

An advantage of this model is that one additional piece of information can be obtained. This is the absorbed upstream flux, which in this experiment is $0.08\ \mathrm{Pa\ m^3/(m^2\ s)}$.

As in the previously shown measurement in HERMES, this measurement in HERMES*plus* provides a clear indication for superpermeation, as the downstream pressure quickly rises to a value higher than the upstream one. It demonstrates that ADP causes the vast majority of the flow. The sticking coefficients are determined to be slightly in favour of downstream release. With the information gained from the measurement, the pressure rise can be predicted. The model underestimates the time needed to reach a certain pressure, which can be attributed to the neglect of the solubility and diffusivity in the metal foil. Nevertheless, the model predicts the maximum pressure reliably. This is especially noteworthy as only small changes in the sticking coefficient predict significantly different pressures. This confirms that the model reliably predicts the steady state pressure for compression. It also suggests that the method to determine the sticking coefficients is trustworthy.

6.3 Analysis of the impact of process parameters on superpermeability

HERMES was constructed and successfully commissioned in 2013. This was before the start of this work. In the following experimental campaigns, the permeation rates decrease until no superpermeation is observed anymore. Subsequently, one of the first aims of this work is the reproduction of the first experiment. The first pressure rise, measured in 2013, is shown as a black line in Figure 6.5. It was obtained with a membrane temperature of 200 ℃ and an upstream pressure of 2 Pa. The pressure rise stops at 2.6 Pa, as this is the upper pressure limit of the gauge used (PI03). It has been found that the degradation of the membrane can be attributed to the plasma source. The two grids in front of the plasma chamber are made from molybdenum. This material has been detected on the metal foil, on the stainless steel surfaces in the upstream chamber and on the inner surface of the ceramic cup in the plasma source. While the molybdenum on the foil surface can impede superpermeability, the molybdenum on the ceramic cup hinders plasma ignition by reflecting the RF radiation. This ceases the production of suprathermal hydrogen and thus prohibits superpermeation. After identifying this problem, the plasma source has been set back into operational state by sandblasting the inner surface of the ceramic cup. After performing this surface treatment, the experiment from 2013 has been reproduced.

Following the plasma source repair, three further pressure rise experiments with the same operation conditions are performed. Their data is plotted in Figure 6.5 in colour. While the original pressure rise is very smooth, the later ones are much less steady. This is due to unstable plasma operation. In all of the measurements, a flickering of the emitted light from the plasma is observed. Nevertheless, all of the experiments reveal an average permeation flux of around $2 \cdot 10^{-3}$ Pa $\mathrm{m}^3/(\mathrm{m}^2\ \mathrm{s})$ (with an assumed downstream gas temperature of 100 ℃).

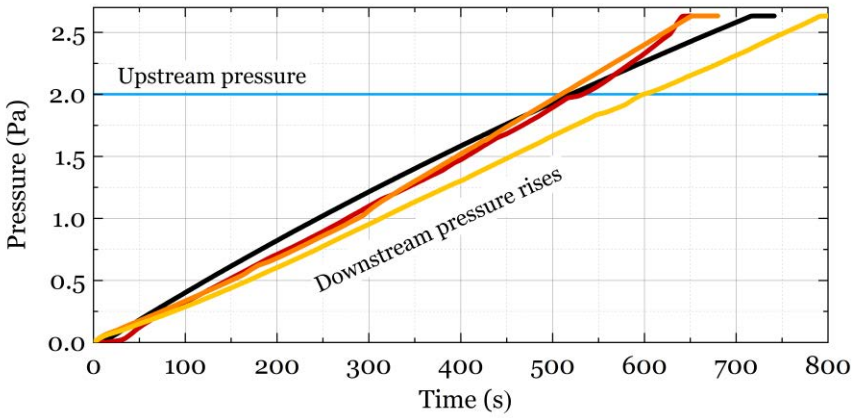

Figure 6.5: Several measured downstream pressure rises with H_2 due to PDP in HERMES. The upstream pressure is 2 Pa for each of the experiments; the vanadium foil temperature is 200 ℃.

While it has been possible to reproduce the 2013 result, it has not been possible to perform systematic measurements, as the results have varied significantly over time. The sequence of experiments has a higher influence on the results than the value that is varied. It is assumed that one main reason for this behaviour is the plasma source, which could only be used with an applied plasma potential in the order of $0.5 - 2$ keV. The sputtering of the molybdenum grids is one degradation mechanism. Another one is the removal of the non-metal surface layer on the foil. The binding energies of the surface layer particles are in the order of tens of eV. Therefore, they will be slowly removed by the incident plasma particles.

Although quantitative results have not been acquired, some important qualitative outcomes can be reported. One of these is derived from the previously shown measurements: superpermeation is demonstrated with H_2 and D_2. In Figure 6.1, a measurement with D_2 is shown, while in Figure 6.5, measurements with H_2 are shown. This is in line with the literature and confirms the current understanding of superpermeation.

Figure 6.6 shows the downstream pressure of a measurement taken with the pressure rise method. The same vanadium is used in two successive measurements, one with an upstream pressure of 2 Pa with H_2 gas, the other with an upstream pressure of 2.2 Pa with He gas. The foil is kept at 300 ℃ during the measurements. While the downstream pressure clearly exceeds the upstream pressure during the hydrogen experiment, the downstream pressure in the helium experiment merely increases by $4.4 \cdot 10^{-4}$ Pa.

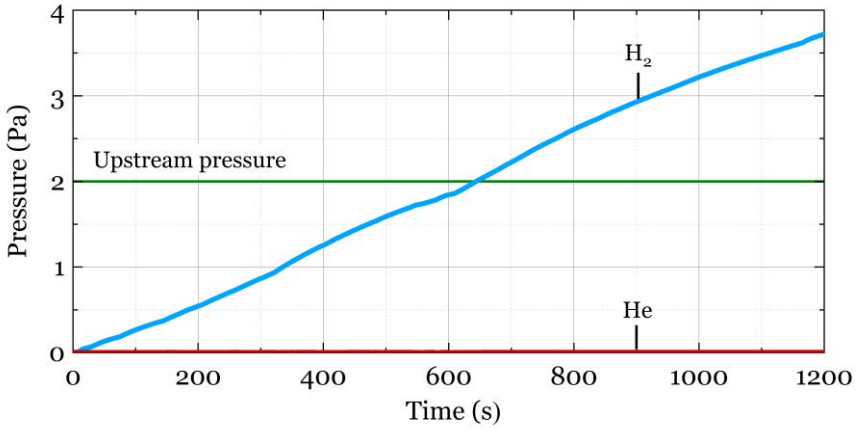

Figure 6.6: Pressure rises in the downstream chamber of HERMES while the ECR plasma is present. The same vanadium foil is used for both experiments at a temperature of 300 ℃; the upstream pressure is ~2 Pa.

Considering previous explanations and experiments, the pressure rise in the hydrogen experiment is very clear. It is caused by superpermeation. The pressure development in the helium experiment is also expected: plasma does not enhance the permeation of helium through metal foils. The small pressure rise that is observed can be easily explained by outgassing from the chamber wall or an imperfect sealing at any of the flanges. This result underlines previous

literature experiments and the theoretical prediction that helium permeation is insignificant for metal foil pumps and can be neglected.

In addition to vanadium, other materials can also be used as metal foils. In Figure 6.7, a PDP experiment with an iron foil is shown. Both the up- and downstream pressures are plotted. The iron foil temperature is set to 250 ℃, and the upstream pressure is 0.65 Pa during the first 450 s of the measurement. While the upstream pressure is very constant, the downstream pressure increases steadily. It exceeds the upstream value after 50 s. The pressure does not rise linearly but seems to approach an upper limit asymptotically in the first 450 s. At this point the plasma becomes unstable and starts to flicker, the upstream pressure is adjusted manually to a value of 0.8 Pa. After this adjustment the pressure rises again, but does not reach a convergent value within the time of the experiment.

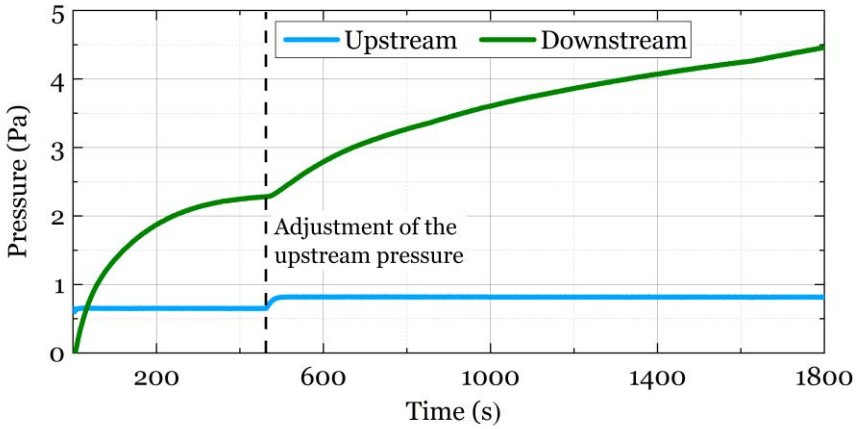

Figure 6.7: Plasma-driven permeation in HERMES with an iron membrane at a temperature of 250 °C.

The compression of hydrogen into the downstream chamber is a clear signal of superpermeation. The effects described in section 4.2 can explain the flattening of the pressure increase. The increased upstream pressure causes a more stable plasma operation and therefore a higher suprathermal hydrogen flux. This is supported by the downstream pressure increase after the upstream pressure adjustment.

A number of qualitative results have been extracted from the experiments in HERMES. The pressure rise method allows for gaining information on superpermeation. However, a reliable measurement of the average gas temperature is important in order to extract information with reasonable accuracy from it. The ECR plasma source used can be seen as suboptimal for reliable operation and investigation of superpermeability. Nevertheless, superpermeation with different materials has been demonstrated in this setup using iron and vanadium foils. The possibility of using different hydrogen isotopes for superpermeation has been shown by separate experiments with protium and deuterium. Furthermore, it has been proven that helium does not permeate vanadium in a significant amount. This underlines the possibility of separating hydrogen from helium in a metal foil pump.

In addition to these qualitative measurements with HERMES, quantitative results with HERMES*plus* can also be obtained as follows.

6.3.1 Influence of the metal foil temperature

There is only one possibility of demonstrating superpermeation in HERMES: namely, a permeation-driven increase of the downstream pressure beyond the value of the upstream pressure. In HERMES*plus*, another feature of superpermeability has been demonstrated. This is the temperature independence of superpermeability over a wide operational range. The dimensionless model predicts this feature, but it has also been reported in the literature, e.g. [166]. The permeation probability does not change significantly in the region of low permeation numbers (compare Figure 4.2). This translates to an unchanged permeation flux at different temperatures if the surface parameters and the upstream conditions remain constant.

In Figure 6.8, the measured hydrogen flows from three ADP experiments (two with the flux and one with the compression method) performed on different days are shown. The graph displays different values of permeated flow on the left axis as a function of the inverse temperature. The permeating flow is plotted logarithmically. On the right side, it is transposed to a hydrogen flux. The upper *x*-axis shows the foil temperature in [°C]. The spacing between the temperature steps on this upper axis is not equal, while the lower axis has equidistant spacing.

The results of the three experiments are shown in this graph. The filament is used as a suprathermal hydrogen source, with a temperature of around $2100\,\mathrm{K}$, for all of these experiments. The upstream pressure has been kept in the range between $6.3 \cdot 10^{-2}$ Pa and $7.0 \cdot 10^{-2}$ Pa for each of these measurements.

The measurements labelled 1st ADP and 2nd ADP show the combined flow of ADP and GDP based on the flux method. Both show a very constant permeating flow over a broad range of temperatures. These results have been obtained with steady state conditions. When the temperature is changed from one measurement point to the next, the flow changes temporarily, until the setup reaches equilibrium. The measured flows of the 1st ADP are about a factor of two higher than during the measurement of the 2nd ADP.

Additional to the two experiments undertaken with the flux method, the results of an experiment using the compression method are also displayed. This allows for distinguishing between the GDP and the ADP. The fully coloured circles are used to represent the ADP and the empty circles the GDP. One can see the temperature dependence for the GDP and ADP component. The GDP flow is more than two orders of magnitude smaller than the ADP. It exhibits a strong temperature dependence. The GDP flow increases with the temperature, while the ADP curve reveals only a small change with temperature.

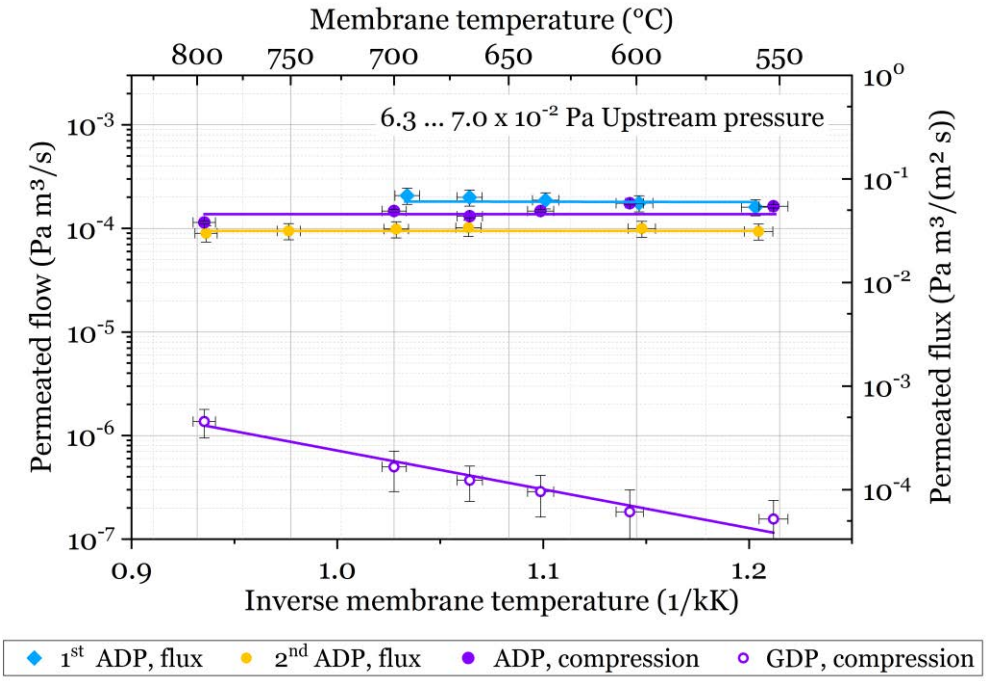

Figure 6.8: Experimentally determined ADP flows of H_2 at different membrane temperatures through a niobium foil in HERMES*plus* at a pressure of around $6.7 \cdot 10^{-2}$ Pa in the upstream chamber. Lines are shown to guide the eye.

The difference in flow between the 1st ADP and the 2nd ADP experiments can be caused by a number of reasons. One is a change of the incident atomic hydrogen flux. This can occur because the filament surface has to be clean for effective atomic hydrogen production and it is sensitive to impurities. Another reason for a change of incident atomic hydrogen flux is a change of the vacuum vessel wall. As the vessel consists of stainless steel, it will also have a natural oxide layer before filament operation. The atomic hydrogen degrades this oxide layer by forming water. The sticking coefficients of bare metal and oxide-covered metal are quite different, so this strongly affects the atomic hydrogen recombination. Another reason for the different flows between the two experiments can be attributed to the metal foil surface, which is influenced by the same effects as the filament and the vessel wall.

The change of the flow before the establishment of steady state at each temperature can be attributed to a different equilibrium hydrogen concentration in the metal foil needing to be established. When the temperature is decreased, the permeating flow decreases, as the hydrogen inventory needs to be raised to match the increased solubility. With time, the hydrogen inventory approaches equilibrium and the flow returns to the previous value. This change of the flow over time is also clear evidence that this effect cannot be caused by outgassing, as an outgassing flow does not increase over time at constant conditions.

The experiment with the compression method provides some additional input. First, it can be seen that the atomic hydrogen is the main driver for the permeation. Second, the ratio between the ADP and the GDP shifts: the GDP increases with temperature. This is a clear sign of surface-limited permeation for this material. The permeability of niobium decreases with

increasing temperature (compare Figure 3.16). Hence, a diffusion-limited permeation yields a decrease with temperature for GDP. The increased GDP flow in surface-limited permeation is caused by an increased sticking coefficient of molecular hydrogen on the niobium surface (compare Figure 3.10).

The temperature independence of the permeating flow is shown in these measurements. Surface-limited permeation is demonstrated, and a low permeation number is attributed to surface-limited setups. The prediction of the dimensionless model is thus proven to be correct.

6.3.2 Atomic hydrogen production

In the previously discussed experiments (1st ADP and 2nd ADP in Figure 6.8), the variation in incident hydrogen on the metal foil is presumably a reason for the different permeating flows. To demonstrate the significance of the incident flux, it is altered in the experiment shown in Figure 6.9. The graph uses the same axis and units as the previous graph and shows the results of two experiments performed with the compression method. The results marked by the violet circles have already been shown in the previous figure. Those presented by orange squares are obtained under the same experimental conditions, except for an increased upstream pressure. Both experiments have been performed at a high filament temperature of 2100 K to make the results comparable.

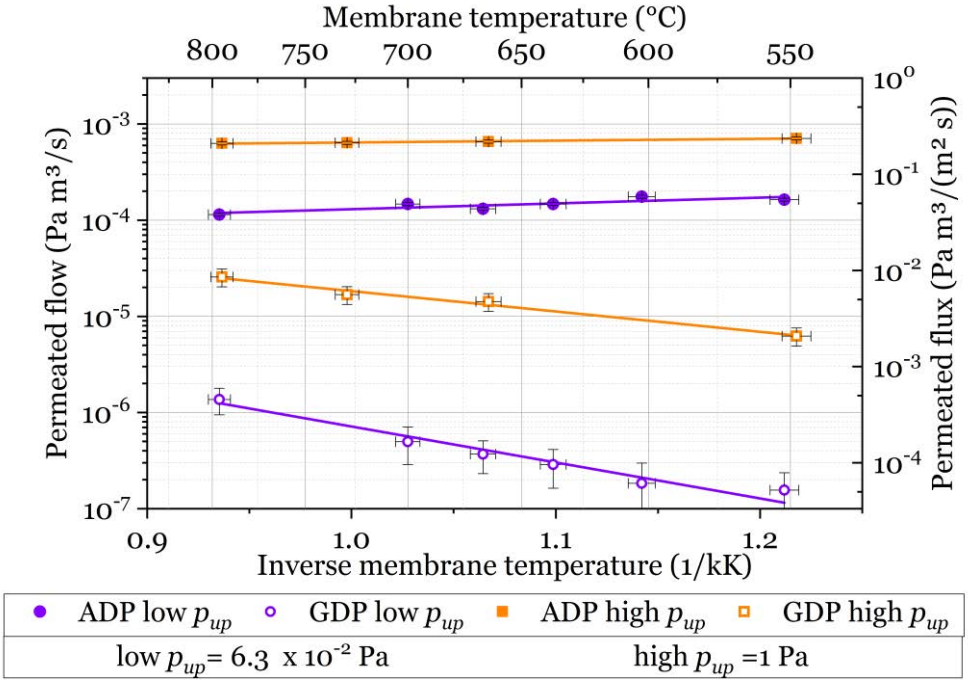

Figure 6.9: Experimentally determined ADP flows in HERMES*plus* at two different upstream pressures and several membrane temperatures. Lines are shown to guide the eye.

The results of the experiment with the upstream pressure of 1 Pa appear to be similar to those of the experiment with the upstream pressure of $6.3 \cdot 10^{-2}$ Pa, but the permeating flows are shifted towards higher values. The upstream pressure has been raised by a factor of 16, which results in

an average increase of permeating flow by a factor of 4.6. The ADP still dominates the flow, but the ratio is shifted towards the GDP. At the highest measured temperature, the GDP contributes 1.2 % of the flow in the low-pressure experiment and 3.9 % in the high-pressure experiment. The temperature dependence of the GDP flow has a different slope. The increase of the GDP from one experiment to the next is a factor of 39.9 at the lowest measured temperature and 18.8 at the highest temperature.

The main result of the comparison of these experiments is that a higher upstream pressure increases the production of atomic hydrogen and therefore causes a higher permeating flux. A quantitative comparison is not as simple, as the flow does not change proportionally with the upstream pressure applied. Two main factors have to be taken into account for this.

First, the likelihood of atomization on the filament decreases with increasing pressure. This behaviour has previously been described in section 3.2.1 and is one reason why suprathermal hydrogen sources other than filaments should be considered for metal foil pumps for the DIR concept.

Second, the surface property of the metal foil plays an essential role. The driving force for the GDP is the gas pressure. As it increases by a factor of 16, it is expected that the GDP increases by the same factor. In all cases, the GDP increases by a higher factor. This shows that another property in addition to the pressure also changes. Considering the equation (3.41) for molecular hydrogen absorption, it is most likely that the sticking coefficient changes. The other influencing factors can be excluded for several reasons. Changes in the surface roughness can be assumed to be permanent and have not been observed in subsequent measurements. While the higher gas pressure decreases the average gas temperature and therefore the pressure-to-surface flux conversion coefficient μ, it cannot explain the magnitude of the GDP change. Hence, only an increase in the molecular sticking coefficient provides a consistent reason. The sticking coefficient is lowered by non-metal species on the metal foil surface. These species are known to be effectively removed by atomic hydrogen. While they normally emerge from the bulk to the surface, this requires them to diffuse. The atomic hydrogen flux is strongly increased in comparison to the low upstream pressure experiment, so the sticking coefficient is englarged. At high temperatures, the diffusion of the non-metals from bulk to surface is quick, so the sticking coefficient is higher than at low temperatures. This matches the experimental observation. At 800 °C, the GDP increase is a factor of 18 larger than in the experiment with lower upstream pressure. This is quite close to the factor 16 of the pressure increase. At the lowest temperature, the GDP is a factor 39 higher than in the previous measurement. Another indication that this represents the influencing factor is that a straight, angled line in the log-inverse temperature plot can still represent the GDP flows. This is a clear sign that the underlying process must be temperature-activated, as with the diffusion process.

The experimental results and analysis underline the importance of the atomic hydrogen production for high permeating flows. Dynamic behaviour of the non-metal surface layer has been shown to occur, although this cannot be directly claimed as proven. The decrease of performance with the rising pressure of the filament as an atomic hydrogen source has been experimentally demonstrated. In this context, additional investigations on alternative production methods of suprathermal hydrogen are required.

6.3.3 Plasma-driven permeation

HERMES*plus* is equipped with a collisional plasma source in order to demonstrate the feasibility of suprathermal hydrogen production for metal foil pumps at higher pressures. The manufacturer of the DuoPlasmaline could not define an operating pressure range for the plasma source, as it has been custom made for this experimental setup. The usage of pure hydrogen gas is not very common for this type of plasma source and the surrounding geometry influences the operation. For stable operation, the manufacturer suggests a pressure of around 30 Pa. This is the reason for using this pressure in the following experiments.

In Figure 6.10, the measured PDP flows are shown in comparison to the previously shown ADP flows. The units and axis separation is the same as in the previous figures, but the *y*-axis shows a smaller range of values. This "zoom in" is selected to better compare the superpermeation measurements. The PDP flow measurements are acquired using the flux method. Their values are in the same range as the high upstream pressure ADP experiment. In contrast to the ADP results, the PDP flows are not temperature-independent; they increase with temperature. The PDP flow exceeds all previous measurements at high temperatures. The magnitude of the flow is higher than the most of the other superpermeation measurements. In contrast to the ADP, this measurement is temperature-dependent. It has the same slope as the GDP, so the GDP contributes much more to the measured flow than in the previous experiments. This is not surprising, as the upstream pressure is also much higher. This also shows that the suprathermal hydrogen production does not rise by the same extent. Further investigations are needed to obtain a clear interpretation of these results. This is especially the case because the plasma adds complexity to the topic. The plasma creates a potential to the membrane that can influence the suprathermal hydrogen flow to the membrane. The plasma also contains suprathermal hydrogen with much higher energies than the atomic hydrogen from a filament. Furthermore, it is important to note that the higher pressures can only be reached by throttling the pumping speed of the turbomolecular pump on the upstream chamber in the current setup. Due to the decreased pumping, any impurities will not be transported away as previously. These impurities can alter the surface of the metal foil.

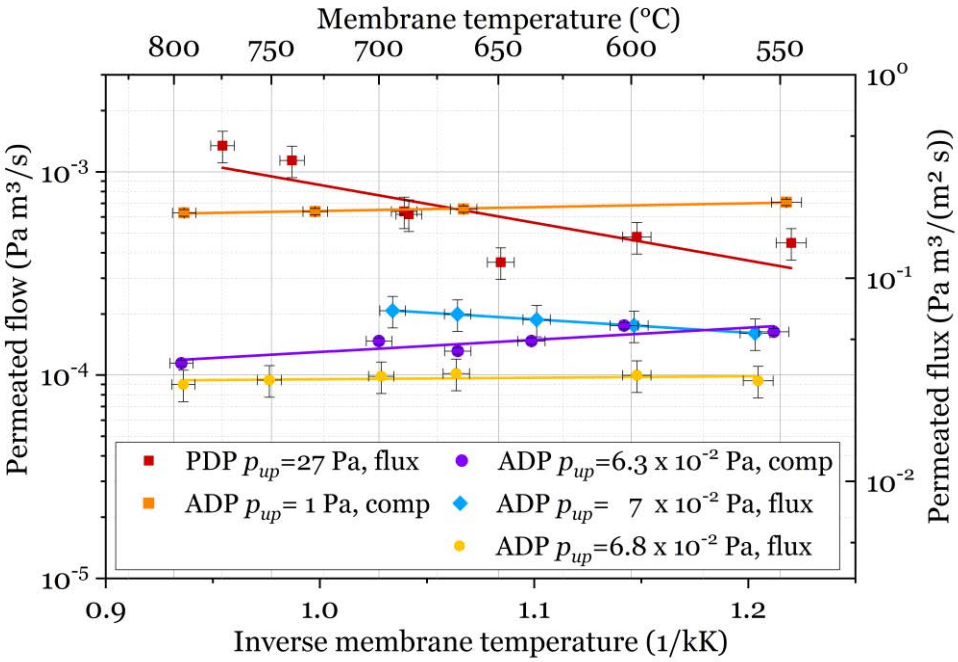

Figure 6.10: Comparison of PDP and ADP experiments with H_2 through niobium in HERMES*plus*. In the legend, the upstream pressures and the measurement method are given (flux=flux method, comp=compression method).

Following this experiment, an attempt has been made to evaluate the upstream pressure dependence of the permeating flow at a constant metal foil temperature. During the experiment, the central ceramic tube of the plasma source broke, which prevented further investigations. It is believed that the ceramic tube broke due to thermal stress. The breaking point is exactly at the end of the outer coaxial aluminium tube, and the temperature gradient is certainly quite high between the plasma-heated length of the tube in the vacuum chamber and the part protected by the aluminium tube. The design of the plasma source does not incorporate an element that ensures precise alignment of the ceramic tube; therefore, it is possible that the aluminium tube was locally in contact with the tube, causing local cooling. Despite the fast increase in upstream pressure following the breaking of the ceramic tube, the metal foil module has not been damaged in this process. This is shown in a series of measurements after resealing the vacuum chamber. No leak between up- and downstream chamber has been detected.

Plasma-driven permeation has been demonstrated in HERMES*plus*. Higher permeating flows than in the previous atom-driven permeation experiment have been shown for high temperatures. Further studies are needed to explain the observed processes in detail.

6.4 Analysis of metal foil surface conditions by gas-driven permeation

All previous experiments have been performed with a source for suprathermal hydrogen. The experiments with the compression method also allow for drawing conclusions regarding GDP occurring in parallel to ADP. Obviously, the GDP can also be studied independently by omitting the suprathermal hydrogen source from the experiment. This has been done multiple times in between the different experiments in order to ensure leak-tightness and to obtain information on the surface condition of the foil. Based on the observations during these routine tests, some relevant information on the relevance of the surface condition of the metal foils can also be derived.

In Figure 6.11, the pressure rises of four GDP measurements on a vanadium foil as a function of time are shown. The graph depicts the pressure in millipascal over the course of 1100 s. The GDP measurements are conducted consecutively. During all measurements, the upstream pressure is kept constant at 2 Pa and the metal foil temperature at 200 °C. After evacuating the downstream chamber, valve V5 is colsed. The resulting pressure increase is depicted with a line labelled "1st GDP". After the experiment, valve V5 is opened to allow the evacuation of the downstream chamber. All other conditions are kept constant. After the downstream pressure has decreased to a pressure below $2.5 \cdot 10^{-5}$ Pa, valve V5 is closed again to collect the next pressure increase. This procedure has been repeated four times. After these measurements, the plasma source is switched on (66% magnetron power, anode 1.4 kV) and a PDP pressure rise is observed, which causes a pressure rise to 4 Pa within 20 minutes.

The pressure increases follow a similar course. After a quick initial rise, which can probably be attributed to the increase of the downstream gas temperature, as previously described in 6.1, the pressure rises almost linearly during each experiment. When the pressure approaches 1 mPa, a step in the profile is observed. This can be attributed to the pressure gauge. The gauge internally switches its measurement principle from cold cathode to Pirani at this pressure [161]. The pressure rise is smallest in the first experiment and becomes increasingly larger in the course of the next three measurements.

For the interpretation of the results, it is first necessary to draw a conclusion about the state of the metal foil. In the PDP measurement after the 4th GDP, superpermeation is detected, because a higher pressure than in the upstream chamber is observed. This can only occur in the surface-limited regime. If a membrane is surface limited for a certain hydrogen flux, it remains in this regime for all smaller fluxes. This allows the conclusion that the surface state limits the permeation rate. The pressure rises become larger from the 1st GDP to the 4th GDP. This is equivalent to an increase in the molecular sticking coefficient on the surface. Although the permeation remains in the surface-limited regime and can therefore support superpermeation, the surfaces are constantly changing.

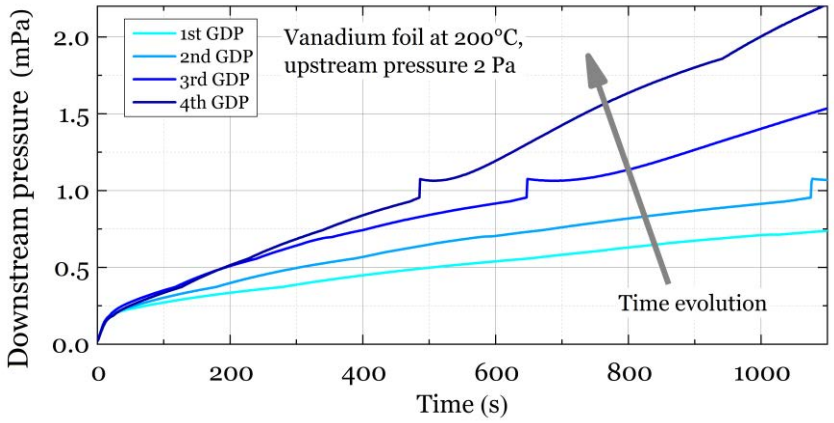

Figure 6.11: Downstream pressure rises of five consecutive gas-driven permeation (GDP) experiments in HERMES through a vanadium foil at 200 ℃ with an upstream pressure of 2 Pa.

This behaviour is not exclusive to the material vanadium; the behaviour has been also observed using an iron foil. Four consecutive GDP measurements have been conducted with an iron membrane. The foil temperature is 150 ℃ during the measurements and the driving pressure is 100 Pa. In Figure 6.12, the downstream pressure as a function of time is shown. While the quantitative pressure rises are significantly smaller than with vanadium, the qualitative behaviour of the pressure rises is similar. The conclusions are therefore the same.

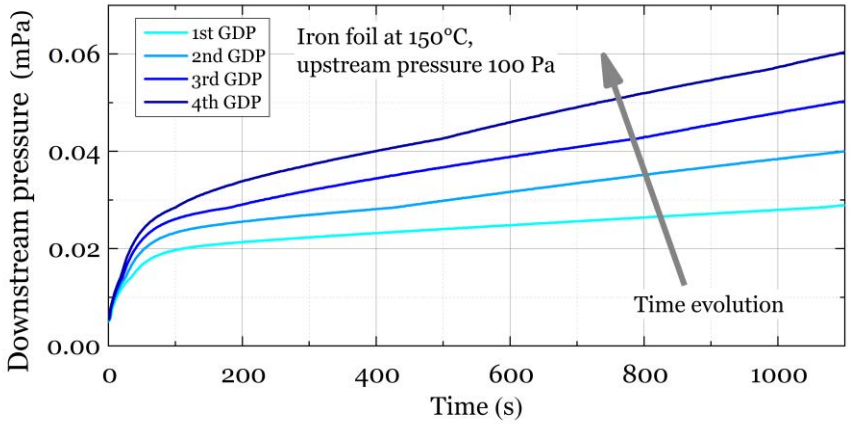

Figure 6.12: Downstream pressure rises of four consecutive gas-driven permeation (GDP) experiments in HERMES through an iron foil at 150 ℃ with an upstream pressure of 100 Pa.

To test the origin of this change in sticking coefficient, a number of dedicated measurements have been carried out in HERMES. In Figure 6.13, the pressure rises as a function of time are displayed. The red curve shows a GDP pressure rise, which is obtained to test the initial state of an iron membrane at 250 ℃ and an upstream pressure of 1 Pa. After this measurement, the gas in the upstream chamber is replaced by argon and the ECR source is operated for three hours. The subsequent GDP experiment exhibits a pressure rise, shown in

green. The pressure rises to a value about three times as high as the previous pressure rise. After this measurement, the upstream chamber is filled with 300 mbar of synthetic air (21 % oxygen, 79 % nitrogen). This condition is maintained overnight, while the downstream chamber is continuously evacuated. On the next day, the third pressure rise is measured, which is displayed in blue in the graph. Again, the same temperature and hydrogen upstream pressure are used. The downstream pressure reads about half the value of the previous measurement at each point in time.

The interpretation of the measurements shown in Figure 6.13 confirm the change in surface properties. The argon plasma causes the sticking coefficient to increase on the upstream surface. It is believed that this is caused by the removal of non-metals on the upstream surface of the metal foil. Argon is often used for such cleaning tasks, as it can be easily ionized and is heavy enough to transport the momentum necessary to cause sputtering. The treatment with synthetic air seems to have partly recovered the surface properties. This may have occurred by partial oxidation of the upstream surface of the metal foil. This provides a firm basis that non-metals significantly influence the hydrogen sticking coefficient on iron.

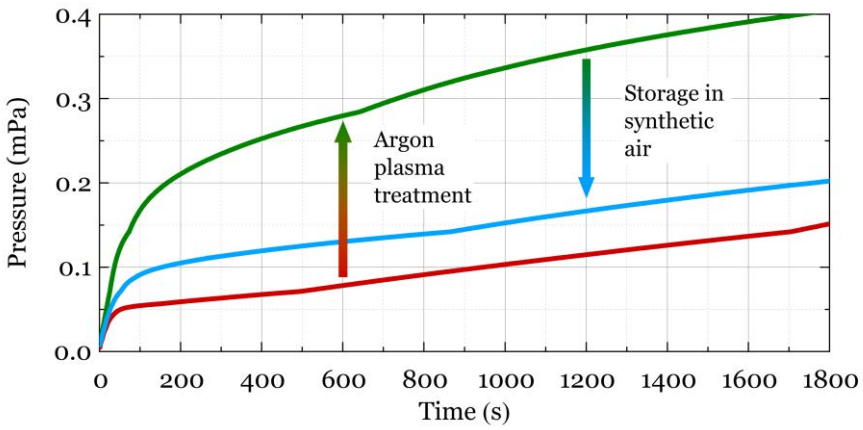

Figure 6.13: Comparison of three subsequent GDP measurements in HERMES with an iron foil at 250°C and an upstream pressure of 1 Pa.

The experimental campaign shows that the sticking coefficient of a vanadium foil and an iron foil increase over time in a hydrogen atmosphere. The iron foil tests demonstrate that this behaviour can be altered by plasma irradiation or an oxygen-containing atmosphere. Changes on the sticking coefficient do not interfere with superpermeability as long as the membrane stays in the surface-limited regime. Nevertheless, surfaces processes are very important for the permeation. Increasing sticking coefficients eventually limit the operation time of metal foil pumps. Therefore, more detailed metal-surface investigations are necessary for future superpermeation studies.

6.5 Material investigations of metal foils

While the study of the material aspects of superpermeability has not been the target of this work, the importance of material behaviour is undeniably high. In some cases, studying the metal foil itself has been found to be highly beneficial, as it provides some insight into the material aspects of superpermeation.

Shortly after the first PDP experiment shown (Figure 6.1), and during another PDP measurement in HERMES with the vanadium foil, the radiation heater broke. While hydrogen was constantly permeating the vanadium foil, the temperature suddenly decreased. The hydrogen flux was around $2.7 \cdot 10^{-2}$ Pa $m^3/(m^2\ s)$ (assumed downstream gas temperature is 150 °C), and the foil temperature was at 318 °C. The temperature did not decrease to ambient temperature immediately, as the hydrogen plasma was still heating it. When the plasma was switched off, the vanadium foil cooled down to ambient temperature. A case like this had always been avoided beforehand, as it means that a considerable amount of hydrogen remains trapped in the foil.

Normally, the plasma is turned off while both sides of the foil are evacuated. In this case, the foil temperature is kept constant or even slightly raised to remove the hydrogen from the foil. In the case of vanadium, the temperature rise is helpful in two ways. First, the higher temperature increases the diffusivity, so equilibrium establishes more quickly. Second, the solubility decreases, which increases the driving force for hydrogen to leave the metal.

The main reason for avoiding a high hydrogen concentration at low temperatures is hydrogen embrittlement. As the heater broke, it was impossible to get the hydrogen out via heating. As this was seen as highly valuable information, it was decided to attempt to determine the hydrogen concentration in the metal. The chosen method was an indirect measurement by X-ray diffractometry. The hydrogen itself cannot be detected via this method, but as it widens the metal lattice, the information of the metal structure can be used. Therefore, HERMES was opened and the foil was dismounted. Two samples of about 0.5 cm^2 were cut from it. One sample was taken from the edge of the foil, which was covered by the sealing surface. The second sample was taken from the middle of the foil, close to the spot where the thermocouple measured the membrane temperature. On both samples, X-ray diffractometry was performed with a 3kW Rigaku Smartlab with a sealed x-ray tube.

The sample from the edge is shown in black in Figure 6.14. The label “Vanadium” is given to this sample, as the XRD pattern exactly matches another sample, being the foil directly supplied by the manufacturer. In the same figure, the XRD pattern of the second sample is also shown. It is labelled “Vanadium with D_2”.

The graph shows the intensity of the X-ray reflection relative to the maximum value over the reflection angle. The intensity is plotted logarithmically in order to show all peaks within one graph. The five most important peaks are labelled according to their lattice orientation. Some information on the XRD method and the derivable information is presented in the appendix.

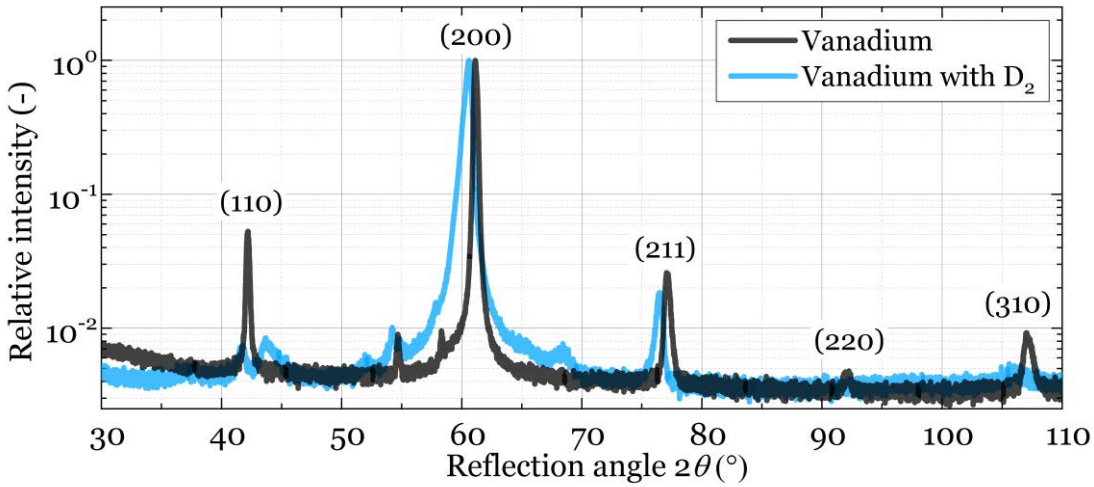

Figure 6.14: Measured XRD reflection pattern of two vanadium foils. One is a vanadium sample, as it is used for the presented experiments, and one is the same material after a D_2 superpermeation experiment. The family of plains is indicated close to the peaks.

Although several measurements have been performed with vanadium, only one of them is shown in Figure 6.14. The different measurements are so similar that this one can be seen as representative of all of them. All expected reflection peaks in the range of measured angles are visible. From each of the peaks, the lattice constant of vanadium can be determined. The average measured value is 0.302742 nm with an experimental standard deviation of 0.05 %. This value also matches the literature value [167]. The two unlabelled peaks, at 54.7° and at 58.32°, are identified as reflections of the (220) plane with other wavelengths from the X-ray source (λ(Cu Kb1), λ(W La1)).

The XRD pattern of the deuterium-loaded sample does not look as characteristic as the pure vanadium pattern. There are several unidentified peaks (37.00°, 43.71°, 52.09° and 68.43°). Two reasons can be suggested to explain the peaks. They can be attributed either to impurities on the foil surface or to another crystal structure of vanadium and deuterium. In the measurement, all peaks of the pure vanadium test can be found slightly shifted towards lower reflection angles. This shift corresponds with an increased lattice constant. Using the different identified peaks (except the (220) peak, which is too small to reliably identify a maximum), the lattice constant is calculated to be 0.30524 nm with an experimental standard deviation of 0.08 %.

To interpret this value, a relationship between deuterium content and lattice widening has to be known. This relationship is given by:

$$a_V(\text{nm}) = 0.3027 + 0.00017 c_D, \tag{6.1}$$

in [168] (incorporating the lattice constant of pure vanadium from [167]). The lattice constant of vanadium a_V is given in nm, while deuterium concentration c_D is described in at. %. Using this relationship, the deuterium content is calculated to be 14.85 at. %. This value is higher than the maximum deuterium concentration in the α–phase of vanadium in equilibrium. Thus, it is

expected that this supersaturated phase will decompose over time into an α–phase with maximum deuterium concentration at this temperature (∼4 at. %) and a β–phase with about 50 at. % vanadium. This separation between the phases is reported for the example in [8] for a vanadium sample with 10 at. % tritium.

A second XRD measurement is performed eight months after the previously shown one. In this test, the XRD pattern of the deuterium-loaded sample is the same as the pure vanadium sample. Therefore, it can be concluded that the hydrogen left the metal. In the previously described tritiated sample of [8], the tritium release is reported to be very slow, so that nearly all of the hydrogen should have still been in the sample. However, their sample was heated up to 200 °C in air, which might have passivated the surface.

As the unidentified peaks in the XRD measurement also disappear in the second measurement, it is likely that these are caused by β–phase vanadium hydride, which has a monoclinic structure. This crystal structure is not very well documented in the literature and is difficult to determine from an XRD measurement, as it has many more degrees of freedom than a bcc lattice.

For the metal foil pump development, the XRD measurement has two important results. Firstly, it confirms the prediction of the dimensionless theory that the hydrogen concentration can rise to very high values. This begs investigations that study the material properties of hydrogen-loaded samples in the further course of MFP development. Secondly, it demonstrates that hydrogen can be released from a vanadium sample even in atmospheric air. This information is valuable for the handling of hydrogen-loaded samples and is required for further material investigations.

The second material-related observation is made with a very different material. According to the literature, good superpermeability is obtained with copper-coated iron membranes, e.g. in [93]. In an attempt to replicate these results in HERMES, a pure iron foil of 0.1 mm thickness is coated with a 400 nm layer of copper. This is mounted in HERMES and tested. Although several tests with GDP and PDP are performed, the downstream pressure never exceeds the upstream pressure, hence superpermeation cannot be claimed for this foil.

When the metal foil is removed from the experiment, small blisters are found in several regions on the foil surface. A microscopic image of some of these blisters is shown in Figure 6.15. Consistent with the dimensionless model, the formation of blisters is expected in some superpermeable setups. Due to its low hydrogen solubility, copper is especially prone to this problem.

These two examples demonstrate the major impact of material behaviour on superpermeation for metal-hydrogen systems. Both are in line with the predictions made by the non-dimensional model. For further superpermeability studies, these aspects should be kept in mind and investigated in more detail.

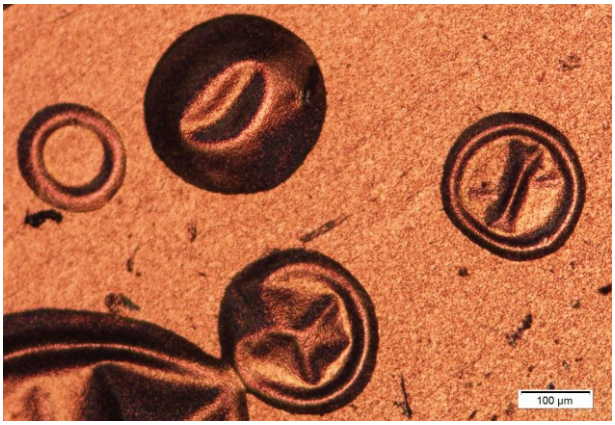

Figure 6.15: Photograph of blisters in a copper-coated iron foil (left). Multiple blisters of various sizes can be observed (~10 ... 500 µm) on the foil.

6.6 Options to improve superpermeability

Although the previous results are promising and demonstrate the potential of superpermeation, there are still a number of variables that can be improved.

The most important enhancement for future metal foil pumps is an increase of the incident suprathermal hydrogen flux onto the membrane. This improvement is potentially able to increase permeating fluxes by orders of magnitude.

The production of suprathermal hydrogen should also be increased. This can be done by optimizing the operating conditions of the plasma sources, e.g. the collisional and the ECR plasma. If the ECR plasma is superior in suprathermal hydrogen production, the extension of its operation regime to higher pressures is possible by pulsing RF power. The ignition of the ECR plasma is more rapid than the collisional plasma. At each pulse, the ECR leads to fast plasma ignition until the effects of collisional plasma take over. While it is certainly not the primary choice of operation, it is also possible to increase the suprathermal hydrogen production by adding certain gases to the plasma. The addition of water vapour in particular has been reported to assist the production of atomic hydrogen in plasma [169].

While this approach increases the production of suprathermal hydrogen, the minimization of unwanted recombination is certainly another valid approach. Suprathermal hydrogen can be lost upon contact with any surface. Thus, the metal foil should surround the suprathermal hydrogen source. An advisable geometry is a cylindrical membrane surrounding the source. This also provides an entrance for the gas mixture and an exit for the hydrogen-depleted gas. One should keep in mind that metal surfaces in particular lead to the loss of suprathermal hydrogen, so the use of glass or ceramic should be considered in these places. Instead of changing the construction material, a surface coating with enamel, for example, is also possible.

The metal foil itself can also be improved to obtain higher permeation fluxes. The permeation probability χ of absorbed hydrogen is about one-half in surface-limited metal foils with symmetric up- and downstream properties. This can be shifted towards higher probabilities by altering the surfaces. However, one should keep in mind that this can only increase the permeating flux by a factor of two (up to $\chi = 1$). This can be done, for example, by palladium-coating the downstream side of the foil. Depending on the materials, the diffusion of palladium into the bulk metal and vice versa will decrease the permeability and eventually stop the desired surface effect. To limit this detrimental diffusion, the operation temperature must stay below an upper limit. For a palladium-coated niobium membrane, this limit is in the region of $500\,°C$ [170]. The critical temperature for the formation of hydrides will still give a minimum operation temperature for the relevant materials.

The surface asymmetry can also be improved in a purely geometrical way. This is certainly not as effective as the coating with palladium, but it will not limit the operation conditions. It can be done by increasing the downstream roughness and/or decreasing the upstream roughness. The increase of downstream roughness can be done through sandblasting or other abrasive procedures. Certainly, lithographic structuring of the surface or the application of a porous cover layer (made of the base material or palladium) will emphasize the effect even better. The polishing of the front surface can also be advantageous, but this change can also decrease the implanted hydrogen flux, depending on the geometry of the pump. A large fraction of suprathermal hydrogen is reflected upon contact with the metal foil. If the likelihood of reaching another part of the metal foil surface after reflection is high, polishing is helpful. This is the case if the inner side of a cylindrical metal foil setup is the upstream surface. If, on the other hand, the membrane area is small and surrounded by other encompassing surfaces, as in HERMES*plus*, the polishing will decrease the implanted hydrogen flux and is therefore not advisable.

The previous suggestions target the increase of the pumped hydrogen flux. In addition, other parameters can be improved. The molecular sticking coefficient of hydrogen on the upstream side is tremendously important for several reasons. Keeping it constant is necessary for the stable and predictable operation of the MFP. The suggested downstream pressure during operation is also strongly dependent on this value. To allow higher backing pressures, the sticking coefficient should be kept as low as possible. The sticking coefficient can be influenced by refining the operation procedures. An example of this is the dissolution of oxygen in a niobium metal foil or increasing the oxygen diffusivity in niobium by removing carbon from it [116, 117]. The latter case can be reached by a very high temperature treatment, but it can prove worthwhile searching for alternative methods to obtain this state. Vanadium as an alternative to niobium should be reviewed with this relationship in mind. The addition of layer-forming gases to the pumped hydrogen stream is also an option if extreme surface degradation occurs or lower sticking coefficients are required [171]. In addition to the incident suprathermal hydrogen flow, the molecular sticking coefficient is the main factor determining the backing pressure in operation. This will decide whether the MFP needs to be backed by a high vacuum pump or if a roughing pump is sufficient.

The foil material can also be optimized to decrease the hydrogen (tritium) inventory in the membrane. This can be done by choosing or designing alloys that have decreased hydrogen

solubility but still a high diffusivity. These ideas are the design driver for palladium-alloyed vanadium in [172, 173]. Another promising material candidate is the alloy V-4Cr-4Ti, whose permeability is tested in [174]. Similar results are obtained for tungsten-alloyed niobium in [175].

The MFP is a complex device still in development. Its most important optimization parameters are addressed in this chapter. Nevertheless, this is not an exhaustive assessment of improvements, as the development of this pump is still ongoing.

6.7 Preliminary design considerations for implementation in a fusion reactor

The presented results justify the approach taken to developing a metal foil pump. The DIR has been shown to be essential for future power plants. Lowering the tritium inventory drastically enhances the inherent safety of such a power plant, but also eases the licensing process. The DIR also decreases the flow that needs to be treated by the tritium plant, therefore decreasing capital cost and space requirements.

Combining the information from the theoretical models and from the experiments presented in this thesis, a metal foil made from niobium is a good choice. Vanadium is a good alternative that is worth further investigation. As superpermeation requires surface-limited hydrogen transport, the thickness of the metal foil is of lesser importance in terms of transport capability. Nevertheless, the amount of tritium dissolved in the metal scales directly with the foil thickness. Therefore, a foil thickness of $0.1\,\mathrm{mm}$ is a good compromise between mechanical sturdiness and small tritium inventory. Taking the predictions of the internal hydrogen pressures and the maximum permeation fluxes, an operation temperature between 300 and $800\,℃$ is most desirable for metal foil pumps with niobium membranes. To be able to sustain a low sticking coefficient and a low tritium concentration in the metal foil, it is desirable to operate at the higher temperatures of the given range. Therefore, an operation temperature of $700\,℃$ is suggested.

Currently, the most limiting factor for the use of MFPs is the permeating flux, which gives an idea of the required metal foil area. The machine throughput of the EU-DEMO is expected to be in the range of $426\,\mathrm{Pa\,m^3/s}$ of hydrogen [89]. The MFPs have to pump $341\,\mathrm{Pa\,m^3/s}$ if the desired separation fraction lies at $80\,\%$. The pumps are expected to be connected to the 16 “divertor” pumping ports [176]. This equals a flow of $21.3\,\mathrm{Pa\,m^3/s}$ per port. With the experimentally demonstrated hydrogen flux of $0.449\,\mathrm{Pa\,m^3/(s\,m^2)}$, this corresponds to a necessary foil area of $47.4\,\mathrm{m^2}$ in each of the ports. As described in the previous chapter, the most promising design is a coaxial, cylindrical layout, with the metal foil being the outer tube. A diagram of this setup is shown in Figure 6.16.

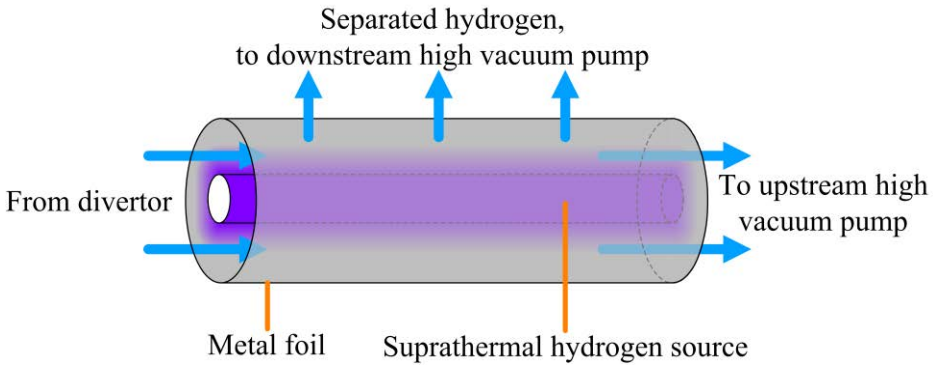

Figure 6.16: Diagram of a coaxial metal foil pump arrangement for future power reactor applications.

The desired operation pressure determines the diameter of these tubes, defining how thick the plasma volume around the inner cylinder is. The lower the pressure, the bigger the diameter of the metal foil has to be. For pressures in the region of $5 - 10$ Pa, a metal foil diameter of 0.5 m can be seen as an appropriate choice. To pump the previously derived hydrogen flow, around 30 m of tube has to be placed in each of these pumping ducts. Several parallel tubes might be the best option to fulfil this requirement. Six five-metres-long metal foil pumps are one option. A very similar design is suggested in [176, 177, 89]. A CAD drawing of this scheme is shown in Figure 6.17.

In the shown design, mercury diffusion pumps back the metal foil pumps on the up- and downstream side, as suggested by the KALPUREX process [24]. A common frame (in yellow) houses the assembly that hosts the system.

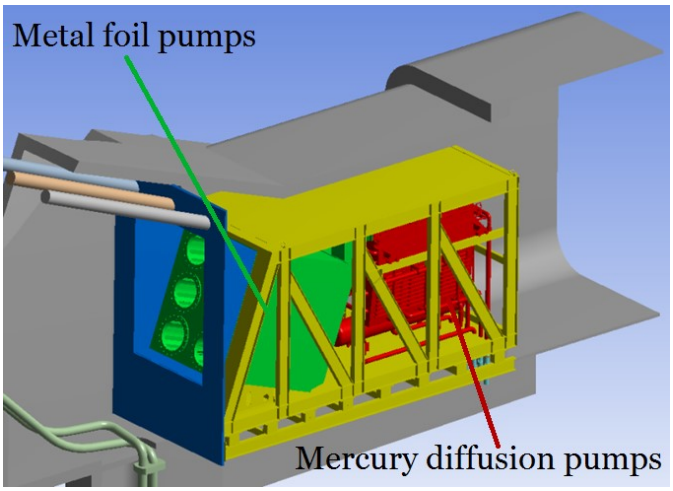

Figure 6.17: Conceptual design of an arrangement of six tubular metal foil pumps, backed by mercury diffusion pumps (up- and downstream); figure adapted from [89].

While it is possible to operate an MFP without a high vacuum pump as a backing pump on the downstream side, it seems currently unfeasible for this application based on the results demonstrated. With increasing downstream pressure, the pumped flow decreases. As described earlier, this is the most limiting design variable for the operation of the metal foil pump and thus should not be compromised. This limitation arises mainly from the amount of suprathermal hydrogen reaching the metal foil, but the reverse gas-driven permeation also decreases the effective pumped flow. With the tubular design, the losses of the suprathermal hydrogen due to wall interaction will be greatly decreased, but the production should also be increased. If this quest is successful, it might be still problematic to operate at higher downstream pressures due to the limitation from the internal hydrogen concentration. Other applications that require lower hydrogen fluxes can certainly be used with higher downstream pressures. To avoid decreasing the pumped flux too much, the downstream pressure should lie below the value of the p_1 as measured in the compression method (5.3.3). This value can also be computed by using the prediction method of section 4.2 to calculate the maximum compression pressure p_2, and using the relationship

$$p_1 = \frac{\varepsilon}{1+\varepsilon}\, p_2 \tag{6.2}$$

to obtain p_1. This correlation can be derived from equation (5.18).

The low technical readiness level of the MFP remains an important issue for the use of DIR. Nevertheless, the application of a MFP in DEMO is within reach. No fundamental problem has been found in this study, and the path towards a sound technical realization has been laid out. Further studies and investigations are needed before the MFP design for DEMO can be started. The external boundary conditions of operation pressure and maximum allowable protium content in the torus also need to be clarified before a design for DEMO can be created.

7 Next steps for the metal foil pump development

The next steps for the development of a metal foil pump for fusion should aim towards three aspects, which are:

- increase of suprathermal hydrogen production,
- optimization of the metal foil and its surface properties,
- prediction of the performance of an entire pump.

Studies on suprathermal hydrogen production should be performed via several paths. First, the HERMES*plus* setup should be employed to study the behaviour of the installed plasma source in more detail. The floating potential on the membrane is one factor that can be monitored, as well as the electron and ion temperature, which can be measured with the installed Langmuir probe. The membrane potential must be varied to gain knowledge on its influence. A desirable setting would certainly be to ground the membrane potential, as this greatly simplifies the design of a future pump. A method such as that described in [178] can be used to obtain information on the dissociation rates in the plasma. Adding a resonant magnetic field within the vacuum chamber is possible via permanent magnets, giving another degree of freedom for optimization. The influence of different gas species on the hydrogen plasma must be investigated to ensure a reliable suprathermal hydrogen production. In addition to the experimental work, modelling of the plasma composition is desirable to understand the limiting factors for the suprathermal hydrogen production and to improve the performance based on these. This work should aim for an experimental setup that has a larger membrane surface and can demonstrate reliable pumping over extended periods. Figure 7.1 depicts a CAD design suggestion for such a setup. This design has the advantage that it can be implemented in the HERMES*plus* test stand and can utilize all analytical equipment.

This design can also be used for experimental work concerning surface properties. Before this upgraded design is used, the current setup should be employed to study the sticking coefficient and the effects of operational procedures. This particularly includes the change of the sticking coefficient over time at different operational points. A series of compression experiments can help to monitor this. The amount of dissolved non-metals in the bulk of the metal foil is directly coupled to the formation of the surface barrier. Therefore, the bulk concentration of non-metals gives information on the surface state of the metal foil. As the electrical resistance of the group 5 metals changes significantly with the concentration of dissolved non-metals, this property should be monitored during these tests. As the setup is equipped with mass spectrometers and the foil temperature can easily be controlled, thermal desorption spectroscopy (TDS) measurements are feasible in order to measure surface species and their binding energies. The aim of these studies is the development of operational procedures allowing for a stable operation in all conditions.

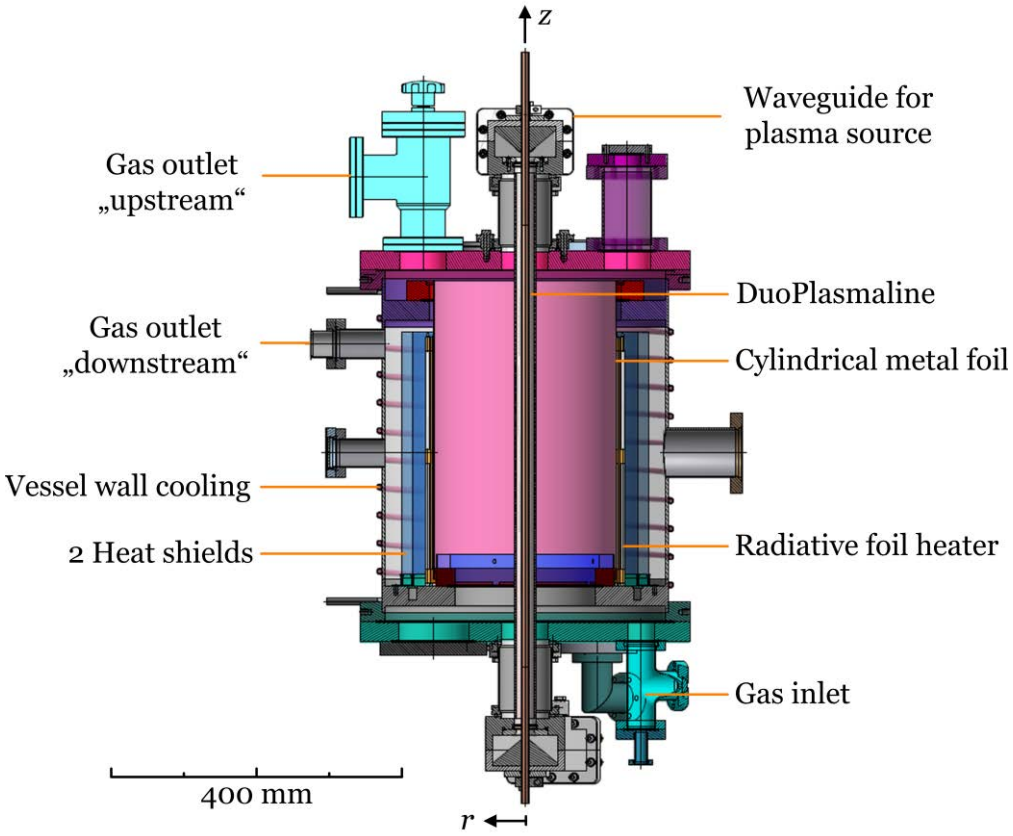

Figure 7.1: Design suggestion for a metal foil pump that is based on the current HERMES*plus* setup and is capable of reaching much higher permeation flows. The membrane surrounds the DuoPlasmaline cylindrically and is radiation-heated from the downstream side. Two heat shields keep heat loss low, and the chamber wall is cooled by water.

The third step for the metal foil pump development is the prediction of the pumping speed and separation probability. While these values can be easily predicted for incident suprathermal hydrogen, this is not yet sufficient for the prediction of the performance of a full pump. To obtain these values, vacuum flow calculations have to be performed. These require a plasma simulation as an input parameter. An even better prediction can be obtained if the two simulation methods are coupled.

Another development line should be directed towards the extrapolation to tritium operation. The slightly different binding energies of the tritium-containing species and the significantly different mass have a direct effect on the energetic hydrogen production and the vacuum flow. However, for the intended area of use, the influence of the isotope effect on the behaviour of the metal foil itself, including the surface properties, is minor according to current knowledge.

While these efforts all help in the development of a technical solution, there is one external factor that can limit the utilization of metal foil pumps in future fusion setups. This is the maximum allowable protium content in the torus. Metal foil pumps separate the hydrogen isotopes from other gases, but not the different isotopes of hydrogen. As small amounts of

protium are a common impurity in vacuum systems, these need to be removed by the tritium plant. Currently, there is no allowed protium content specified for the fusion plasma. This value needs to be determined before the requirements of the tritium plant and the metal foil pump separation fraction can be established. It seems unlikely that this boundary condition limits direct internal recycling, but strict requirements on the allowable protium content will increase the tritium plant significantly. Therefore, a case study based on the expected protium ingress and the fuel cycle layout is vital in order to assess the technically achievable protium content. This can be used to determine a reasonable requirement for the tritium plant systems.

Many of the aforementioned steps have already been initiated in order to continue the smooth development of a metal foil pump for future fusion power plants.

8 Summary of metal foil pump development

In this thesis, the fundamental development steps towards the realization of a metal foil pump are elaborated and proven through experiments. This work is motivated by the need for a process capable of separating hydrogen from other gases at low pressures for direct internal recycling. It has been demonstrated in this study that this concept is crucial for future fusion power plants. It increases the conversion rate, as seen from the tritium plant, and drastically decreases the processing time of the whole fuel cycle. This allows for operating with a much smaller tritium inventory and decreases the necessary size of the tritium plant.

The working principle of the metal foil pump is superpermeation. The basic physics and the relevant material data have been analysed comprehensively and consistently for the first time in literature. Based on this fundamental description, a dimensionless model has been developed that explains the governing principles and limiting domains. This enables making the correct choice of material, which resolves the literature disagreement on this matter. A metal foil pump that needs to process a high flux of hydrogen must be made from a material with high hydrogen solubility. The materials niobium and vanadium are currently the most promising candidates. For all other materials, the formation of hydrogen blisters has been identified as the main limitation for operation. For all materials, the increase of foil temperature has been shown to decrease the risk of blister formation.

The experimental results proving the above statements have been acquired by means of two setups. The first, HERMES, has been utilized for qualitative measurements. Its limitations have been identified in the course of this work and resulted in a second facility, HERMES*plus*. This setup has been designed, built and commissioned as part of the presented work. Several measurements confirm the capabilities of this setup and broaden the understanding of the field. For the first time in the literature, a collisional plasma source has been utilized to demonstrate superpermeation.

The variables for operational improvements have been analysed and critically discussed to formulate a development path for an advanced metal foil pump.

References

[1] C.A. Bertulani, Nuclear physics in a nutshell, Princeton University Press, Princeton, 2007.

[2] R. Herman, Fusion: The search for endless energy, Cambridge University Press, New York, 1990.

[3] J. Magill, G. Pfennig, R. Dreher, Z. Sóti, Karlsruher Nuklidkarte, 8. Auflage, Nucleonia GmbH, Eggenstein-Leopoldshafen, 2012.

[4] G. Audi, A.H. Wapstra, The 1995 update to the atomic mass evaluation, Nuclear Physics A 595 (1995) 409–480. doi: 10.1016/0375-9474(95)00445-9

[5] K.S. Krane, Introductory nuclear physics, John Wiley & Sons, Inc., Hoboken, 1988.

[6] H.-S. Bosch, G.M. Hale, Improved formulas for fusion cross-sections and thermal reactivities, Nuclear Fusion 32 (1992) 611–631. doi: 10.1088/0029-5515/32/4/I07

[7] M.H. Sikora, H.R. Weller, A new evaluation of the $^{11}B(p,\alpha)\alpha\alpha$ reaction rates, Journal of Fusion Energy 35 (2016) 538–543. doi: 10.1007/s10894-016-0069-y

[8] R. Lässer, Tritium and helium-3 in metals, Springer-Verlag, Berlin, 1989.

[9] A.M. Bradshaw, T. Hamacher, U. Fisher, Is nuclear fusion a sustainable energy form?, Fusion Engineering and Design 86 (2011) 2770–2773. doi: 10.1016/j.fusengdes.2010.11.040

[10] E. Serra, Hydrogen and tritium kinetics in fusion reactor materials. Report EUR 16471 EN, PhD-thesis, University of Salford, Joint Research Center-Institute for Advanced Materials, Ispra, 1996.

[11] Y. Xu, A general comparison between tokamak and stellarator plasmas, Matter and Radiation at Extremes 1 (2016) 192–200. doi: 10.1016/j.mre.2016.07.001

[12] F. Cismondi, L.V. Boccaccini, G. Aiello, J. Aubert, C. Bachmann, T. Barrett, L. Barucca, E. Bubelis, S. Ciattaglia, A. Del Nevo, E. Diegele, M. Gasparotto, G. Di Gironimo, P.A. Di Maio, F. Hernandez, G. Federici, I. Fernández-Berceruelo, T. Franke, A. Froio, C. Gliss, J. Keep, A. Loving, E. Martelli, F. Maviglia, I. Moscato, R. Mozzillo, Y. Poitevin, D. Rapisarda, L. Savoldi, A. Tarallo, M. Utili, L. Vala, G. Veres, R. Zanino, Progress in EU breeding blanket design and integration, Fusion Engineering and Design 136A (2018) 782–792. doi: 10.1016/j.fusengdes.2018.04.009

[13] Culham Centre for Fusion Energy, Photo gallery: JET vessel and plasma (2012) http://www.ccfe.ac.uk/images_detail.aspx?id=15 (Accessed 29th September 2019)

[14] T. Donné, W. Morris, X. Litaudon, C. Hidalgo, D. McDonald, H. Zohm, E. Diegele, A. Möslang, K. Nordlund, G. Federici, P. Sonato, C. Waldon, D. Borba, P. Helander, European research roadmap to the realisation of fusion energy, Report, Eurofusion, Garching, 2018.

[15] Y. Wan, J. Li, Y. Liu, X. Wang, V. Chan, C. Chen, X. Duan, P. Fu, X. Gao, K. Feng, S. Liu, Y. Song, P. Weng, B. Wan, F. Wan, H. Wang, S. Wu, M. Ye, Q. Yang, G. Zheng, G. Zhuang, Q. Li and CFETR team, Overview of the present progress and activities on the CFETR, Nuclear Fusion 57 (2017) 102009-1–17. doi: 10.1088/1741-4326/aa686a

[16] K. Tobita, N. Asakura, R. Hiwatari, Y. Someya, H. Utoh, K. Katayama, A. Nishimura, Y. Sakamoto, Y. Homma, H. Kudo, Y. Miyoshi, M. Nakamura, S. Tokunaga, A. Aoki, the J.S.D.T. for F. DEMO, Design strategy and recent design activity on Japan's DEMO, Fusion Science and Technology 72 (2017) 537–545. doi: 10.1080/15361055.2017.1364112

[17] K. Kim, K. Im, H.C. Kim, S. Oh, J.S. Park, S. Kwon, Y.S. Lee, J.H. Yeom, C. Lee, G.-S. Lee, G. Neilson, C. Kessel, T. Brown, P. Titus, D. Mikkelsen, Y. Zhai, Design concept of K-DEMO for near-term implementation, Nuclar Fusion 55 (2015) 053027-1–9. doi: 10.1088/0029-5515/55/5/053027

[18] B.V. Kuteev, Y.S. Shpanskiy and DEMO-FNS Team, Status of DEMO-FNS development, Nuclear Fusion 57 (2017) 076039-1–8. doi: 10.1088/1741-4326/aa6dcb

[19] R. Kemp, R. Wenninger, G. Federici, H. Reimerdes, R. Ambrosino, R. Brown, M. Coleman, Exploring a broad spectrum of design options for DEMO, Fusion Engineering and Design 136 B (2018) 970–974. doi: 10.1016/j.fusengdes.2018.04.049

[20] A.M. Garofalo, M.A. Abdou, J.M. Canik, V.S. Chan, A.W. Hyatt, D.N. Hill, N.B. Morley, G.A. Navratil, M.E. Sawan, T.S. Taylor, C.P.C. Wong, W. Wu, A. Ying, A fusion nuclear science facility for a fast-track path to DEMO, Fusion Engineering and Design 89 (2014) 876–881. doi: 10.1016/j.fusengdes.2014.03.055

[21] C. Day, T. Giegerich, The Direct Internal Recycling concept to simplify the fuel cycle of a fusion power plant, Fusion Engineering and Design 88 (2013) 616–620. doi: 10.1016/j.fusengdes.2013.05.026

[22] F. Romanelli, P. Barabaschi, D. Borba, G. Federici, L. Horton, R. Neu, D. Stork, H. Zohm, A roadmap to fusion energy, Report, European Fusion Development Agreement, Garching, 2012.

[23] C. Day, B. Butler, T. Giegerich, P.T. Lang, R. Lawless, B. Meszaros, Consequences of the technology survey and gap analysis on the EU DEMO R&D programme in tritium, matter injection and vacuum, Fusion Engineering and Design 109–111 (2016) 299–308. doi: 10.1016/j.fusengdes.2016.03.008

[24] T. Giegerich, C. Day, The KALPUREX-process – A new vacuum pumping process for exhaust gases in fusion power plants, Fusion Engineering and Design 89 (2014) 1476–1481. doi: 10.1016/j.fusengdes.2014.03.082

[25] C. Day, T. Giegerich, Development of advanced exhaust pumping technology for a DT fusion power plant, IEEE Transactions on Plasma Science 42 (2014) 1058–1071. doi: 10.1109/TPS.2014.2307435

[26] C. Day, D. Murdoch, R. Pearce, The vacuum systems of ITER, Vacuum 83 (2008) 773–778. doi: 10.1016/j.vacuum.2008.05.010

[27] R.C. Duckworth, L.R. Baylor, S.J. Meitner, S.K. Combs, D.A. Rasmussen, M. Hechler, T. Edgemon, C. Barbier, R. Pearce, R. Kersevan, M. Dremel, J.-C. Boissin, Development and demonstration of a supercritical helium-cooled cryogenic viscous compressor prototype for the ITER vacuum system, AIP Conference Proceedings 1434 (2012) 1234–1242. doi: 10.1063/1.4707046F

[28] R.J. Pearce, A. Antipenkov, B. Boussier, S. Bryan, M. Dremel, B. Levesy, C. Mayaux, M. Wykes, The ITER divertor pumping system, design evolution, simplification and performance, Fusion Engineering and Design 88 (2013) 809–813. doi: 10.1016/j.fusengdes.2013.01.050

[29] D. Latham, B.D. Power, N.T.M. Dennis, An assessment of some working fluids for diffusion pumps, Vacuum 2 (1952) 33–49. doi: 10.1016/0042-207X(52)90221-2

[30] D.O. Coffin, A tritium-compatible high-vacuum pumping system, Journal of Vacuum Science and Technology 20 (1982) 1126–1131. doi: 10.1116/1.571586

[31] H. Bannwarth, Liquid ring vacuum pumps, compressors and systems, Wiley-VCH, Weinheim, 2005.

[32] R.T. Tsugawa, J.S. Bowers, J.A. Emig, R.S. Hafner, J.L. Maienschein, A.S. Nicolosi, Determination of tritium in mercury from sprengel pumps, Journal of Nuclear Materials 172 (1990) 239–240. doi: 10.1016/0022-3115(90)90443-Q

[33] M. Abdou, N.B. Morley, S. Smolentsev, A. Ying, S. Malang, A. Rowcliffe, M. Ulrickson, Blanket/first wall challenges and required R&D on the pathway to DEMO, Fusion Engineering and Design 100 (2015) 2–43. doi: 10.1016/j.fusengdes.2015.07.021

[34] M.A. Abdou, E.L. Vold, C.Y. Gung, M.Z. Youssef, K. Shin, Deuterium-tritium fuel self-sufficiency in fusion reactors, Fusion Science and Technology 9 (1986) 250–285. doi: 10.13182/FST86-A24715

[35] M. Abdou, Overview of the tritium fuel cycle and conditions for tritium fuel self- sufficiency and other tritium issues, 4th IAEA DEMO Programme Workshop, Karlsruhe, Nov, 2016. https://nucleus.iaea.org/sites/fusionportal/Technical%20Meeting%20Proceedings/4th%20DEMO/website/talks/November%2015%20Sessions/Abdou.pdf (Accessed 9th November 2018)

[36] A.I. Livshits, M.E. Notkin, A.A. Samartsev, Physico-chemical origin of superpermeability — Large-scale effects of surface chemistry on “hot” hydrogen permeation and absorption in metals, Journal of Nuclear Materials 170 (1990) 79–94. doi: 10.1016/0022-3115(90)90329-L

[37] A.I. Livshits, Superpermeability in the atomic hydrogen-nickel system, Soviet Technical Physics Letters 3 (1977) 236–237.

[38] M. Taborelli, Cleaning and surface properties, in: D. Brandt (Ed.), Vacuum in accelerators, Proceedings of the CERN Accelerator School, Geneva, 2007. http://cds.cern.ch/record/923393/files/CERN-2007-003.pdf (Accessed 12th February 2019)

[39] A. Livshits, Y. Hatano, V. Alimov, M. Matsuyama, Probability of absorption/implantation of low-energy H_2^+ ions in O-covered vanadium, Journal of Nuclear Materials 363–365 (2007) 801–805. doi: 10.1016/j.jnucmat.2007.01.103

[40] A. Güntherschulze, H. Betz, H. Kleinwächter, Die Diffusion von Wasserstoff und Deuterium durch Eisen (in German), Zeitschrift für Physik 111 (1939) 657–679. doi: 10.1007/BF01330012

[41] H. Wichmann, W. Weizel, Der Einfluß einer Glimmentladung auf die Permeation von Gasen durch Metalle. Forschungsberichte des Landes Nordrhein-Westfalen Nr.1038 (in German), Report, Westdeutscher Verlag, Köln, 1961.

[42] J.R. Young, Palladium-diaphragm hydrogen pump, Review of Scientific Instruments 34 (1963) 374–377. doi: 10.1063/1.1718369

[43] I. Ali-Khan, K.J. Dietz, F.G. Waelbroeck, P. Wienhold, Embrittlement of stainless steels by low energy atomic hydrogen particles, Journal of Nuclear Materials 76–77 (1978) 263–264. doi: 10.1016/0022-3115(78)90155-1

[44] J. Winter, Carbonization in tokamaks, Journal of Nuclear Materials. 145–147 (1987) 131–144. doi: 10.1016/0022-3115(87)90318-7

[45] J. Park, T. Bennett, J. Schwarzmann, S.A. Cohen, Permeation of hydrogen through palladium, Journal of Nuclear Materials 220–222 (1995) 827–831. doi: 10.1016/0022-3115(94)00591-5

[46] M.L. Zheludkevich, A.G. Gusakov, A.G. Voropaev, E.N. Kozyrski, S.A. Raspopov, A.A. Vecher, “Superpermeability” and “pumping” of atomic hydrogen through palladium membranes, Journal of Membrane Science 320 (2008) 528–532. doi: 10.1016/j.memsci.2008.04.045

[47] A.I. Livshits, I.M. Meter, A.A. Samartsev, Interaction of a deuterium atomic beam with a palladium membrane, Soviet Technical Physics Letters 21 (1976) 848–854.

[48] A.I. Livshits, M.E. Notkin, S.V. Yakovlev, Superpermeability of atomic hydrogen in Armco iron, Soviet Technical Physics Letters 4 (1978) 192–193.

[49] F. Waelbroeck, I. Ali-Khan, K.J. Dietz, P. Wienhold, Hydrogen solubilisation into and permeation through wall materials, Journal of Nuclear Materials 85–86, Part 1 (1979) 345–349. doi: 10.1016/0022-3115(79)90514-2

[50] T. Tanabe, N. Saito, Y. Etoh, S. Imoto, Permeation and reemission of deuterium, implanted in first wall materials, Journal of Nuclear Materials 103 (1981) 483–487. doi: 10.1016/0022-3115(82)90644-4

[51] I. Takagi, K. Kodama, K. Shin, K. Higashi, H. Zushi, T. Mizuuchi, T. Senjyu, M. Wakatani, T. Obiki, Deuterium plasma-driven permeation in Heliotron E during discharge cleaning and in a small plasma device, Fusion Technology 25 (1994) 137–146. doi: 10.13182/FST94-A30263

[52] A.I. Livshits, F. Sube, M.N. Solovyev, M.E. Notkin, M. Bacal, Plasma driven superpermeation of hydrogen through group Va metals, Journal of Applied Physics 84 (1998) 2558–2564. doi: 10.1063/1.368418

[53] A.A. Skovoroda, Y.M. Pustovoit, V.S. Svishchov, V.S. Kulinauskas, Plasma driven permeation through the Nb membrane at low temperature, in: C.H. Wu (Ed.), Hydrogen recycling at plasma facing materials, Springer, Berlin, 2000, pp. 177–183.

[54] A.I. Livshits, M.E. Notkin, M. Bacal, Anomalous isotope effect in the permeation, retention and reemission at interaction of energetic hydrogen with niobium, Journal of Applied Physics 91 (2002) 4105–4109. doi: 10.1063/1.1455156

[55] W.T. Shmayda, F. Waelbroeck, J. Winter, P. Wienhold, T. Banno, N.P. Kherani, Tritium pumping based on asymmetric permeation, Fusion Technology 8 (1985) 2258–2289. doi: 10.13182/FST85-A24621

[56] P.L. Andrew, Hydrogen permeation through multilayer metallic membranes. UTIAS Report No. 342, PhD-thesis, University of Toronto, Toronto, 1991.

[57] A.I. Livshits, M.E. Notkin, Superpermeability of a niobium membrane with respect to hydrogen atoms and ions, Soviet Technical Physics Letters 7 (1981) 605–607.

[58] A.I. Livshits, M.E. Notkin, A.A. Samartsev, I.P. Grigoriadi, Large-scale effects of H_2O and O_2 on the absorption and permeation in Nb of energetic hydrogen particles, Journal of Nuclear Materials 178 (1991) 1–18. doi: 10.1016/0022-3115(91)90450-L

[59] V.R. Kapitanskii, A.I. Livshits, I.M. Metter, M.E. Notkin, Interaction of a palladium membrane with quasiequilibrium atomic hydrogen, Soviet Physics – Technical Physics 21 (1976) 602–609.

[60] H. Hackfort, K. Bösche, F. Waelbroeck, J. Winter, P. Wienhold, Hydrogen pumping and compression by superpermeation through iron, Journal of Nuclear Materials 144 (1987) 10–16. doi: 10.1016/0022-3115(87)90273-X

[61] H.K. Perkins, T. Noda, Deuterium transport through 304 and 304L stainless steel at low driving pressures and 15 keV deuteron bombardment, Journal of Nuclear Materials 71 (1978) 349–364. doi: 10.1016/0022-3115(78)90435-X

[62] A.I. Livshits, M.E. Notkin, A.A. Samartsev, A.O. Busnyuk, A.Y. Doroshin, V.I. Pistunovich, Superpermeability to fast and thermal hydrogen particles: applications to the pumping and recycling of hydrogen isotopes, Journal of Nuclear Materials 196 (1992) 159–163. doi: 10.1016/S0022-3115(06)80023-1

[63] A.V. Golubeva, M. Mayer, Y.M. Gasparyan, J. Roth, V.A. Kurnaev, The ion-driven permeation experiment PERMEX, Review of Scientific Instruments 80 (2009) 073501-1–7. doi: 10.1063/1.3154385

[64] A.I. Livshits, M.E. Notkin, Y. Pustovoit, A.A. Samartsev, Superpermeability of solid membranes and gas evacuation. Part II: Permeation of hydrogen through a palladium membrane under different gas and membrane boundary conditions, Vacuum 29 (1979) 113–124. doi: 10.1016/S0042-207X(79)80451-0

[65] A.A. Skovoroda, V.S. Svishchov, A.V. Spitsyn, V.L. Stolyarov, Y.M. Pustovoit, V.D. Borman, V.S. Kulikauskas, A.M. Shipilin, Plasma-driven superpermeation of hydrogen through Nb membranes: Bulk effects, Journal of Nuclear Materials 306 (2002) 232–240. doi: 10.1016/S0022-3115(02)01324-7

[66] A.M. Bruneteau, M.E. Notkin, A.I. Livshits, M. Bacal, Correlation between Balmer α emission and hydrogen flux through a superpermeable niobium membrane in a low-pressure multicusp plasma source, Nuclear Instruments and Methods in Physics Research Section B: Beam Interactions with Materials and Atoms 187 (2002) 393–400. doi: 10.1016/S0168-583X(01)01139-9

[67] W.T. Shmayda, N.P. Kherani, J. Winter, F. Waelbroeck, Atomic hydrogen radial flux dependence on plasma parameters in TEXTOR, Journal of Nuclear Materials 162–164 (1989) 582–586. doi: 10.1016/0022-3115(89)90331-0

[68] Y. Nakamura, S. Sengoku, Y. Nakahara, N. Suzuki, H. Suzuki, N. Ohyabu, A. Busnyuk, M. Notkin, A. Livshits, Deuterium pumping experiment with superpermeable Nb membrane in JFT-2M tokamak, Journal of Nuclear Materials 278 (2000) 312–319. doi: 10.1016/S0022-3115(99)00243-3

[69] R.K. Musyaev, B.S. Lebedev, S.K. Grishechkin, A.A. Yukhimchuk, A.A. Busnyuk, M.E. Notkin, A.A. Samartsev, A.I. Livshits, Tritium superpermeability: Experimental investigation and simulation of tritium recirculation in „prometheus“ setup, Fusion Science and Technology 48 (2005) 35–38. doi: 10.13182/FST05-A874

[70] A. Livshits, N. Ohyabu, M. Bacal, Y. Nakamura, A. Busnyuk, M. Notkin, V. Alimov, A. Samartsev, H. Suzuki, F. Sube, Fuel recycling and edge plasma control with membrane techniques: Plasma–membrane simulation experiments, Journal of Nuclear Materials 266–269 (1999) 1267–1272. doi: 10.1016/S0022-3115(98)00693-X

[71] A.I. Livshits, Interaction of membranes with nonequilibrium gases, Soviet Technical Physics Letters 20 (1976) 1207–1212.

[72] A.I. Livshits, Interaction of barriers with nonequilibrium gases in absorption with dissociation, Soviet Technical Physics Letters 21 (1976) 187–193.

[73] A.I. Livshits, M.E. Notkin, Y. Pustovoit, A.A. Samartsev, Superpermeability of solid membranes and gas evacuation Part I. Theory, Vacuum 29 (1979) 103–112. doi: 10.1016/S0042-207X(79)80450-9

[74] F. Waelbroeck, P. Wienhold, J. Winter, E. Rota, T. Banno, Influence of bulk and surface phenomena on the hydrogen permeation through metals. Jül-1966, Report, Kernforschungsanlage Jülich GmbH, Jülich, 1984.

[75] M. Profant, R. von Seggern, P. Wienhold, E. Horlitz, Die Berechnung der Wasserstoffdiffusion durch Metallmembranen bei quadratischen Randbedingungen dritter Art mit Hilfe einer Radialintegralmethode. Jül-2029 (in German), Report, Kernforschungsanlage Jülich GmbH, Jülich, 1985.

[76] P. Wienhold, M. Profant, F. Waelbroeck, J. Winter, Computer code PERI for the calculation of recycling, volume distribution, and permeation of hydrogen in first wall materials of tokamaks, Journal of Nuclear Materials 93–94, Part 2 (1980) 866–870. doi: 10.1016/0022-3115(80)90220-2

[77] P. Wienhold, M. Profant, F. Waelbroeck, J. Winter, Rechencode PERI: Permeation von Wasserstoff durch Metallmembranen. Freisetzung aus Metalloberflächen und Inventar in Metallwänden. Jül-1825 (in German), Report, Kernforschungsanlage Jülich GmbH, Jülich, 1983.

[78] A.I. Livshits, M.E. Notkin, V.I. Pistunovich, M. Bacal, A.O. Busnyuk, Superpermeability: Critical points for applications in fusion, Journal of Nuclear Materials 220–222 (1995) 259–263. doi: 10.1016/0022-3115(94)00424-2

[79] A. Livshits, N. Ohyabu, M. Notkin, V. Alimov, H. Suzuki, A. Samartsev, M. Solovyov, I. Grigoriadi, A. Glebovsky, A. Busnyuk, A. Doroshin, K. Komatsu, Applications of superpermeable membranes in fusion: The flux density problem and experimental progress, Journal of Nuclear Materials 241–243 (1997) 1203–1209. doi: 10.1016/S0022-3115(97)80221-8

[80] J.H. Ferziger, H.G. Kaper, Mathematical theory of transport processes in gases, North-Holland Publishing Company, Amsterdam, 1972.

[81] F. Sharipov, Analytical and numerical calculations of rarefied gas flows, in: K. Jousten (Ed.), Handbook of vacuum technology, Wiley-VCH Verlag GmbH & Co. KGaA, Weinheim, 2016.

[82] K. Huang, Statistical mechanics, 2nd edition, John Wiley & Sons, Inc., New York, 1963.

[83] A. Frohn, Einführung in die kinetische Gastheorie (in German), Akademische Verlagsgesellschaft, Wiesbaden, 1979.

[84] M. Gad-el-Hak (Ed.), The MEMS handbook, CRC press, Boca Raton, 2002.

[85] K. Jousten (Ed.), Wutz Handbuch Vakuumtechnik (in German), 10. Auflage, Vieweg+Teubner, Wiesbaden, 2010.

[86] S. Varoutis, S. Naris, V. Hauer, C. Day, D. Valougeorgis, Computational and experimental study of gas flows through long channels of various cross sections in the whole range of the Knudsen number, Journal of Vacuum Science & Technology A 27 (2009) 89–100. doi: 10.1116/1.3043463

[87] G.A. Bird, Molecular gas dynamics and the direct simulation of gas flows, Oxford University Press Inc., New York, 1994.

[88] L.T. Ho, Speed, Speed factor and power input of different designs of diffusion pumps, and Remarks on Measurements of Speed, Physics 2 (1932) 386–395. doi: 10.1063/1.1745064

[89] C. Day, B. Butler, T. Giegerich, B. Ploeckl, S. Varoutis, A smart three-loop fuel cycle architecture for DEMO, Fusion Engineering and Design 146B (2019) 2462–2468. doi: 10.1016/j.fusengdes.2019.04.019

[90] S.J. Blanksby, G.B. Ellison, Bond dissociation energies of organic molecules, Accounts of Chemical Research 36 (2003) 255–263. doi: 10.1021/ar020230d

[91] L. Latrasse, M. Radoiu, J. Lo, P. Guillot, 2.45-GHz microwave plasma sources using solid-state microwave generators. ECR-type plasma source, Journal of Microwave Power and Electromagnetic Energy 50 (2016) 308–321. doi: 10.1080/08327823.2016.1260880

[92] L. Latrasse, M. Radoiu, J. Lo, P. Guillot, 2.45-GHz microwave plasma sources using solid-state microwave generators. Collisional-type plasma source, Journal of Microwave Power and Electromagnetic Energy 51 (2017) 43–58. doi: 10.1080/08327823.2017.1293589

[93] W.T. Shmayda, N.P. Kherani, Application of hydrogen permeation through bilayer metal membranes, Proceedings of the 12th Symposium on Fusion Engineering (1987) 1247–1250.

[94] A.B. Antoniazzi, A.A. Haasz, P.C. Stangeby, The effect of adsorbed carbon and sulphur on hydrogen permeation through palladium, Journal of Nuclear Materials 162–164 (1989) 1065–1070. doi: 10.1016/0022-3115(89)90410-8

[95] A.I. Livshits, F.E. Balghiti, M. Bacal, Dissociation of hydrogen molecules on metal filaments in H^- ion sources, Plasma Sources Science and Technology 3 (1994) 465–472. doi: 10.1088/0963-0252/3/4/003

[96] Periodensystem der Elemente nach Fluck und Heumann (in German), 4. Auflage, Wiley-VCH Verlag GmbH & Co. KGaA, Weinheim, 2007.

[97] E.A. Brandes, G.B. Brook (Eds.), Smithells metals reference book, seventh edition, Butterworth-Heinemann, Oxford, 1992.

[98] A.B. Antoniazzi, A.A. Haasz, O. Auciello, P.C. Stangeby, Atomic, ionic and molecular hydrogen permeation facility with in situ Auger surface analysis, Journal of Nuclear Materials 128&129 (1984) 670–675. doi: 10.1016/0022-3115(84)90432-X

[99] W. Petasch, E. Räuchle, H. Muegge, K. Muegge, Duo-plasmaline — a linearly extended homogeneous low pressure plasma source, Surface and Coatings Technology 93 (1997) 112–118. doi: 10.1016/S0257-8972(97)00015-7

[100] E. Räuchele, Duo-plasmaline. A surface wave sustained linearly extended discharge, Journal de Physique IV 8 (1998) Pr7-99–Pr7-108. doi: 10.1051/jp4:1998708

[101] R. Geller, Electron cyclotron resonance ion sources and ECR plasmas, Institute of Physics Publishing, New York, 1996. doi: 10.1201/9780203758663

[102] A. Sieverts, Über Lösungen von Gasen in Metallen (in German), Zeitschrift für Elektrochemie und angewandte Physikalische Chemie 16 (1910) 707–713. doi: 10.1002/bbpc.19100161706

[103] J.-S. Wang, On the diffusion of gases through metals, Mathematical Proceedings of the Cambridge Philosophical Society 32 (1936) 657–662. doi: 10.1017/S030500410001940X

[104] M.A. Pick, K. Sonnenberg, A model for atomic hydrogen-metal interactions — application to recycling, recombination and permeation, Journal of Nuclear Materials 131 (1985) 208–220. doi: 10.1016/0022-3115(85)90459-3

[105] M.I. Baskes, A calculation of the surface recombination rate constant for hydrogen isotopes on metals, Journal of Nuclear Materials 92 (1980) 318–324.

[106] P.M. Richards, Surface-limited hydrogen release and uptake in metals, Journal of Nuclear Materials 152 (1988) 246–258. doi: 10.1016/0022-3115(88)90333-9

[107] A.A. Pisarev, O.V. Ogorodnikova, Elementary processes near the interface between hydrogen gas and solid, Journal of Nuclear Materials 248 (1997) 52–59. doi: 10.1016/S0022-3115(97)00201-8

[108] M. Dornheim, Thermodynamics of metal hydrides: Tailoring reaction enthalpies of hydrogen storage materials, in: J.C. Moreno-Piraján (Ed.), Thermodynamics. Interaction studies – solids, liquids and gases, IntechOpen Ltd., London, 2011.

[109] A. Staykov, J. Yamabe, B.P. Somerday, Effect of hydrogen gas impurities on the hydrogen dissociation on iron surface, International Journal of Quantum Chemistry 114 (2014) 626–635. doi: 10.1002/qua.24633

[110] L. Gong, Q. Su, H. Deng, S. Xiao, W. Hu, The stability and diffusion properties of foreign impurity atoms on the surface and in the bulk of vanadium: A first-principles study, Computational Materials Science 81 (2014) 191–198. doi: 10.1016/j.commatsci.2013.08.011

[111] Y. Hatano, A. Livshits, Y. Nakamura, A. Busnyuk, V. Alimov, C. Hiromi, N. Ohyabu, K. Watanabe, Influence of oxygen and carbon on performance of superpermeable membranes, Fusion Engineering and Design 81 (2006) 771–776. doi: 10.1016/j.fusengdes.2005.06.368

[112] I. Takagi, K. Moritani, H. Moriyama, Asymmetric surface recombination of hydrogen on palladium exposed to plasma, Journal of Nuclear Materials 313–316 (2003) 102–106. doi: 10.1016/S0022-3115(02)01370-3

[113] B. Dean, A.A. Haasz, P.C. Stangeby, Sticking coefficient of molecular and atomic hydrogen on palladium, Journal of Vacuum Science & Technology A 5 (1987) 2332–2335. doi: 10.1116/1.574446

[114] P.L. Andrew, A.A. Haasz, Effect of surface impurities on the permeation of hydrogen through iron, Journal of Vacuum Science & Technology A 8 (1990) 1807–1813. doi: 10.1116/1.576807

[115] Y. Hatano, K. Watanabe, A. Livshits, A. Busnyuk, V. Alimov, Y. Nakamura, K. Hashizume, Effects of bulk impurity concentration on the reactivity of metal surface: Sticking of hydrogen molecules and atoms to polycrystalline Nb containing oxygen, Journal of Chemical Physics 127 (2007) 204707-1–13. doi: 10.1063/1.2804874

[116] A.I. Livshits, V.N. Alimov, M.E. Notkin, M. Bacal, Hydrogen superpermeation resistant to ion sputtering, Applied Physics Letters 81 (2002) 2656–2659. doi: 10.1063/1.1510961

[117] A.I. Livshits, V.N. Alimov, M.E. Notkin, M. Bacal, Hydrogen superpermeation resistant to ion sputtering, Applied Physics A 80 (2005) 1661–1669. doi: 10.1007/s00339-004-2595-0

[118] H. Grabert, H.R. Schober, Theory of tunnelling and diffusion of light interstitials in metals, in: H. Wipf (Ed.) Hydrogen in metals III, Springer, Berlin, 1997, pp. 3–49.

[119] H. Wipf, Diffusion of hydrogen in metals, in: H. Wipf (Ed.), Hydrogen in metals III, Springer, Berlin, 1997, pp. 51–91.

[120] S. Hayashi, K. Hayamizu, O. Yamamoto, NMR study of the behavior of hydrogen in vanadium hydride. I. Superstructure and diffusion of hydrogen in β-$VH_{0.59}$, Journal of Chemical Physics 76 (1982) 4392–4397. doi: 10.1063/1.443553

[121] Y. Fukai, The metal-hydrogen system, Springer, Berlin, 1993.

[122] U. Wietelmann, M. Felderhoff, P. Rittmeyer, Hydrides, in: Ullmann's Ecyclopedia of Industrial Chemistry, Wiley-VCH Verlag GmbH & Co. KGaA, Weinheim, 2016.

[123] H.P. Bleichert, Thermodynamische Eigenschaften von Wasserstoff, Deuterium und Tritium in Vanadium, Jül-2005 (in German), Report, Kernforschungsanlage Jülich GmbH, Jülich, 1985.

[124] R. Lässer, K.-H. Klatt, P. Mecking, H. Wenzl, Tritium in Metallen: Präparationstechnik (Tritiumlabor). Jül-1800 (in German), Report, Kernforschungsanlage Jülich GmbH, Jülich, 1982.

[125] R. Lässer, T. Schober, The phase diagram of the vanadium tritium system, Journal of the Less-Common Metals 130 (1987) 453–458. doi: 10.1016/0022-5088(87)90140-8

[126] C. Schäfer, Diffusionseigenschaften bestimmter Metalle bei der Hochtemperatur-Wasserstoffabtrennung (in German), PhD-thesis, Technische Universität München, Fakultät für Maschinenwesen, München, 2010.

[127] M.V. Mundschau, Hydrogen separation using dense composite membranes: Part 1 fundamentals, In A.C. Bose (Ed.), Inorganic membranes for energy and environmental applications, Springer, New York, 2009, pp. 125–153. doi: 10.1007/978-0-387-34526-0

[128] G.M. Pressouyre, I.M. Bernstein, The role of trapping on hydrogen transport and embrittlement. Report number 036-099-7, PhD-thesis, Carnegie Mellon Unversity, 1977.

[129] J.M. Rowe, K. Sköld, H.E. Flotow, J.J. Rush, Quasielastic neutron scattering by hydrogen in the α and β phases of vanadium hydride, Journal of Physics and Chemistry of Solids 32 (1971) 41–54. doi: 10.1016/S0022-3697(71)80006-9

[130] M.D. Dolan, Non-Pd BCC alloy membranes for industrial hydrogen separation, Journal of membrane science 362 (2010) 12–28. doi: 10.1016/j.memsci.2010.06.068

[131] M. Sharpe, W.T. Shmayda, W.U. Schröder, Tritium migration to the surfaces of type 316 stainless steel; aluminium 6061; and oxygen-free, high-conductivity copper, Fusion Science and Technology 70 (2016) 97–11. doi: 10.13182/FST15-198

[132] C.J. Kershner, Helium permeation through tantalum metal. MLM-1846, AEC Research and Development Report, Mound Laboratory, Miamisburg, 1972.

[133] T. Shiraishi, M. Nishikawa, T. Fukumatsu, Permeation of multi-component hydrogen isotopes through nickel, Journal of Nuclear Materials 254 (1998) 205–214. doi: 10.1016/S0022-3115(97)00362-0

[134] C. San Marchi, B.P. Somerday, R.S. Larson, S.F. Rice, Solubility of hydrogen and its isotopes in metal from mixed gases, Journal of Nuclear Materials 372 (2008) 421–425. doi: 10.1016/j.jnucmat.2007.02.016

[135] M.W. Chase (Ed.), NIST-JANAF thermochemical tables, Fourth edition, American Institute of Physics, Woodbury, 1998.

[136] W.M. Jones, Thermodynamic functions for tritium and tritium hydride. The equilibrium of tritium and hydrogen with tritium hydride. The dissociation of tritium and tritium hydride, Journal of Chemical Physics 16 (1948) 1077–1081. doi: 10.1063/1.1746727

[137] W.M. Jones, Thermodynamic functions for tritium deuteride. The dissociation of tritium deuteride. Equilibria among the isotopic hydrogen molecules, Journal of Chemical Physics 17 (1949) 1062–1064. doi: 10.1063/1.1747113

[138] W.M. Jones, Equilibria in hydrogen-tritium mixtures. Steady states and initial reaction rates at 76.7°K, Journal of Chemical Physics 47 (1967) 4675–4679. doi: 10.1063/1.1701683

[139] J.W. Pyper, P.C. Souers, The chemical equilibria relating the isotopic hydrogens at low temperatures. UCRL-52104, Report, Lawrence Livermore Laboratory, Livermore (1976).

[140] J.W. Pyper, P.C. Souers, Equilibrium constants for the hydrogen isotopic self-exchange reactions in the 4.2- to 50-K temperature range, Advances in Cryogenic Engineering 23 (1978) 705–711. doi: 10.1007/978-1-4613-4039-3_88

[141] P.C. Souers, Hydrogen properties for fusion energy, University of California Press, Berkeley, Los Angeles, 1986.

[142] O.V. Ogorodnikova, Comparison of hydrogen gas–, atom– and ion–metal interactions, Journal of Nuclear Materials 277 (2000) 130–142. doi: 10.1016/S0022-3115(99)00206-8

[143] O.V. Ogorodnikova, Surface effects on plasma-driven tritium permeation through metals, Journal of Nuclear Materials 290–293 (2001) 459–463. doi: 10.1016/S0022-3115(00)00642-5

[144] O.V. Ogorodnikova, A model for the steady state plasma- and gas driven hydrogen isotope permeation through multi-layer metal, in: A. Hassanein (Ed.) Hydrogen and helium recycling at plasma facing materials, Kluwer Academic Publishers, 2002, pp. 95–103.

[145] T. Nagasaki, R. Yamada, M. Saidoh, H. Katsuta, Simultaneous ion and gas driven permeation of deuterium through nickel, Journal of Nuclear Materials 151 (1988) 189–201. doi: 10.1016/0022-3115(88)90071-2

[146] H. Hackfort, A selective pump for hydrogen isotopes based on the superpermeation effect in iron, Fusion Engineering and Design 10 (1989) 293–297. doi: 10.1016/0920-3796(89)90066-5

[147] P.L. Andrew, A.A. Haasz, Models for hydrogen permeation in metals, Journal of Applied Physics 72 (1992) 2749–2757. doi: 10.1063/1.351526

[148] J.H. Spurk, Dimensionsanalyse in der Strömungslehre, Springer-Verlag, Berlin, 1992.

[149] I. Ali-Khan, K.J. Dietz, F.G. Waelbroeck, P. Wienhold, The rate of hydrogen release out of clean metallic surfaces, Journal of Nuclear Materials 76 &77 (1978) 337–343. doi: 10.1016/0022-3115(78)90167-8

[150] E. Rota, F. Waelbroeck, P. Wienhold, J. Winter, Measurements of surface and bulk properties for the interaction of hydrogen with inconel 600, Journal of Nuclear Materials 111–112 (1982) 233–239. doi: 10.1016/0022-3115(82)90214-8

[151] P. Wienhold, E. Rota, F. Waelbroeck, J. Winter, T. Banno, Permeation von Wasserstoff durch Metallmembranen. Jül-2079 (in German), Report, Kernforschungsanlage Jülich GmbH, Jülich, 1986.

[152] B.L. Doyle, A simple theory for maximum H inventory and release: A new transport parameter, Journal of Nuclear Materials 111 (1982) 628–635. doi: 10.1016/0022-3115(82)90277-X

[153] R. Anton, T. Wiegner, W. Naumann, M. Liebmann, C. Klein, C. Bradley, Design and performance of a versatile, cost-effective microwave electron cyclotron resonance plasma source for surface and thin film processing, Review of Scientific Instruments 71 (2000) 1177–1180. doi: 10.1063/1.1150420

[154] F. Bernhard, Handbuch der Technischen Temperaturmessung. 2.Auflage (in German), Springer, Berlin, 2014.

[155] MKS Instruments, Inc., MKS Baratron® type 627D absolute pressure transducer, Manual, 2013.

[156] MKS Instruments, Inc., Type 390/590 absolute type 398/598 differential high accuracy pressure transducers, instruction manual, 1985.

[157] J.F. O'Hanlon, A user's guide to vacuum technology, 3rd ed., John Wiley & Sons, Hoboken, 2003.

[158] A.S. Berman, Free molecule transmission probabilities, Journal of Applied Physics 36 (1965) 3356. doi: 10.1063/1.1702984

[159] Pfeiffer Vacuum, HiPace 80 Turbopumpe. Betriebsanleitung (in German), https://www.pfeiffer-vacuum.com/de/produkte/vakuumerzeugung/turbopumpen/hybridgelagert/hipace-80/?detailPdoId=5429. (Accessed 17th December 2018).

[160] JCGM, JCGM 100:2008. Evaluation of measurement data – Guide to the expression of uncertainty in measurement, Joint Committee for Guides in Metrology (2008). https://www.bipm.org/utils/common/documents/jcgm/JCGM_100_2008_E.pdf (Accessed 15th January 2019)

[161] MKS Instruments, Inc., 972B DualMag™ vacuum pressure transducer, Operation and installation manual, 2018.

[162] Sensortherm, Datenblatt Metis M311/M322 (in German), 2018. https://www.sensortherm.de/userfiles/file/datenblaetter/de/Sensortherm-Datenblatt_Metis_M311_M322.pdf (Accessed 17th January 2019)

[163] D. van Essen, W.C. Heerens, On the transmission probability for molecular gas flow through a tube, Journal of Vacuum Science & Technology 13 (1976) 1183. doi: 10.1116/1.569064

[164] P. Szwemin, M. Niewiński, Comparison of transmission probabilities calculated by Monte Carlo simulation and analytical methods, Vacuum 67 (2002) 359–362. doi: 10.1016/S0042-207X(02)00225-7

[165] H. Shinagawa, H. Setyawan, T. Asai, Y. Sugiyama, K. Okuyama, An experimental and theoretical investigation of rarefied gas flow through circular tube of finite length, Chemical Engineering Science 67 (2002) 4027-4036. doi: 10.1016/S0009-2509(02)00318-4

[166] A.I. Livshits, A.A. Samartsev, Attaining the extreme values of the adhesion and penetration probabilities in the system of hydrogen and palladium membrane, Soviet Technical Physics Letters 49 (1979) 1365–1366.

[167] E. Fromm, E. Gebhardt (Eds.), Gase und Kohlenstoff in Metallen (in German), Springer, Berlin, 1976.

[168] W. Pesch, Strukturen und Phasenumwandlungen im Vanadium-Wasserstoff und Vanadium-Deuterium-System. Jül-1737 (in German), Report, Kernforschungsanlage Jülich GmbH, Jülich, 1981.

[169] J. Kikuchi, M. Suzuki, H. Yano, S. Fujimura, Effects of H_2O on atomic hydrogen generation in hydrogen plasma, Advanced Techniques for Integrated Circuit Processing II 1803 (1993) 70–76. doi: 10.1117/12.142937

[170] V.N. Alimov, Y. Hatano, A.O. Busnyuk, D.A. Livshits, M.E. Notkin, A.I. Livshits, Hydrogen permeation through the Pd–Nb–Pd composite membrane: Surface effects and thermal degradation, International Journal of Hydrogen Energy 36 (2011) 7737–7746. doi: 10.1016/j.ijhydene.2011.04.016

[171] A.I. Livshits, M.E. Notkin, A.A. Samartsev, M.N. Solovyov, Interactions of low energy ions with niobium: effects of non-metallic overlayers on reemission, retention and permeation, Journal of Nuclear Materials 233–237 (1996) 1113–1117. doi: 10.1016/S0022-3115(96)00084-0

[172] V.N. Alimov, A.O. Busnyuk, M.E. Notkin, E.Y. Peredistov, A.I. Livshits, Hydrogen transport through V–Pd alloy membranes: Hydrogen solution, permeation and diffusion, Journal of Membrane Science 481 (2015) 54–62. doi: 10.1016/j.memsci.2015.01.058

[173] V.N. Alimov, I.V. Bobylev, A.O. Busnyuk, M.E. Notkin, E.Y. Peredistov, A.I. Livshits, Hydrogen transport through the tubular membranes of V–Pd alloys: Permeation, diffusion, surface processes and WGS mixture test of membrane assembly, Journal of Membrane Science 549 (2018) 428–437. doi: 10.1016/j.memsci.2017.12.017

[174] R.E. Buxbaum, R. Subramanian, J.H. Park, D.L. Smith, Hydrogen transport and embrittlement for palladium coated vanadium—chromium—titanium alloys, Journal of Nuclear Materials 233–237 (1996) 510–512. doi: 10.1016/S0022-3115(96)00239-5

[175] N. Watanabe, H. Yukawa, T. Nambu, Y. Matsumoto, G.X. Zhang, M. Morinaga, Alloying effects of Ru and W on the resistance to hydrogen embrittlement and hydrogen permeability of niobium, Journal of Alloys and Compounds 477 (2009) 851–854. doi: 10.1016/j.jallcom.2008.10.164

[176] C. Gliss, R. Ambrosino, C. Bachmann, S. Ciattaglia, D. Flammini, T. Giegerich, S. Jimenez, A. Wild, Initial integration concept of the DEMO lower horizontal port, Fusion Engineering and Design 146B (2019) 2667–2670. doi: 10.1016/j.fusengdes.2019.04.078

[177] T. Giegerich, C. Day, C. Gliss, X. Luo, H. Strobel, A. Wilde, S. Jimenez, Preliminary configuration of the torus vacuum pumping system installed in the DEMO lower port, Fusion Engineering and Design 146B (2019) 2180–2183. doi: 10.1016/j.fusengdes.2019.03.147

[178] A. Cotter, A. Stowell, J. Carlson, J.R. Doyle, Mass spectrometric method for estimating dissociation rates in hydrogen discharge plasmas, Journal of Vacuum Science & Technology A 36 (2018) 031304. doi: 10.1116/1.5020723

[179] J. Völkl, G. Alefeld, Diffusion of hydrogen in metals, in: J. Völkl, G. Alefeld (Eds.), Hydrogen in metals I. Basic properties, Springer Berlin Heidelberg, 1978, pp. 321–348.

[180] A. Tahara, Y. Hayashi, Measurements of permeation of hydrogen isotopes through α-iron by pressure modulation and ion bombarding, Transactions of the Japan Institute of Metals 26 (1985) 869–875. doi: 10.2320/matertrans1960.26.869

[181] F. Reiter, K.S. Forcey, G. Gervasini, A compilation of tritium-material interaction parameters in fusion reactor materials. EUR 15217 EN, Report, Commission of the European Communities, Ispra, 1993.

[182] R. Lässer, P. Meuffels, R. Feenstra, Datenbank der Löslichkeit der Waserstoffisotope Protium (H), Deuterium (D) und Tritium (T) in den Metallen V, Nb, Ta, Pd und den Legierungen V_{1-x} Nb_x, $V_{1-x}Ta_x$, Nb_{1-x} Mo_x, $Pd_{1-x}Ag_x$. Jül-2183 (in German), Report, Kernforschungsanlage Jülich GmbH, Jülich, 1988.

[183] H. Bleichert, H. Wenzl, Die unterschiedliche Löslichkeit der Wasserstoffisotope Protium, Deuterium und Tritium in Vanadium, physica status solidi (b) 144 (1987) 361–373. doi: 10.1002/pssb.2221440132Kof59

[184] P. Kofstad, W.E. Wallace, L.J. Hyvönen, Thermodynamics of formation of tantalum-hydrogen solid solutions from vapor pressure data, Journal of the American Chemical Society 81 (1959) 5015–5019. doi: 10.1021/ja01528a001

[185] E. Veleckis, R.K. Edwards, Thermodynamic properties in the systems vanadium-hydrogen, niobium-hydrogen, and tantalum-hydrogen, Journal of Physical Chemistry 73 (1969) 683–692. doi: 10.1021/j100723a033

[186] Z. Qi, J. Völkl, R. Lässer, H. Wenzl, Tritium diffusion in V, Nb and Ta, Journal of Physics F: Metal Physics 13 (1983) 2053–2062. doi: 10.1088/0305-4608/13/10/015

[187] T. Kuji, W.A. Oates, Thermodynamic properties of Nb-H alloys I: The α phase, Journal of the Less Common Metals 102 (1984) 251–260. doi: 10.1016/0022-5088(84)90321-7

[188] J.F. Smith, The H-Nb (hydrogen-niobium) and D-Nb (deuterium-niobium) systems, Bulletin of Alloy Phase Diagrams 4 (1983) 39–46. doi: 10.1007/BF02880318

[189] G. Matusiewicz. H.K. Birnbaum, The isotope effect for the diffusion of hydrogen in niobium, Journal of Physics F: Metal Physics 7 (1977) 2285–2289. doi: 10.1088/0305-4608/7/11/009

[190] H.F. Franzen, A.S. Khan, D.T. Peterson, The solubility of hydrogen in tantalum at high temperatures, Journal of the Less-Common Metals 55 (1977) 143–147.

[191] E. Wicke, G.H. Nernst, Zustandsdiagramm und thermodynamisches Verhalten der Systeme Pd/H_2 und Pd/D_2 bei normalen Temperaturen; H/D-Trenneffekte (in German), Berichte der Bunsengesellschaft 68 (1964) 224–235. doi: 10.1002/bbpc.19640680303

[192] H. Brodowsky, Das System Palladium/Wasserstoff (in German), Zeitschrift für Physikalische Chemie 44 (1965) 129–142. doi: 10.1524/zpch.1965.44.3_4.129

[193] W. Jost, A. Widmann, Über die Diffusion von Wasserstoff und von Deuterium in Palladium (in German), Zeitschrift für Physikalische Chemie B 29 (1935) 247–255. doi: 10.1515/zpch-1935-2926

[194] E. Wicke, H. Brodowsky, Hydrogen in palladium and palladium alloys, in: G. Alefeld, J. Völkl (Eds.), Hydrogen in metals II – application-oriented properties, Springer, Berlin, 1978, pp. 73–156.

[195] W. Kley, W. Drexel, The diffusion of hydrogen in α-palladium-hydride. EUR-5466, Report, Commission of the European Communities, Kirchberg, 1976.

[196] J. Völkl, G. Wollenweber, K.-H. Klatt, G. Alefeld, Reversed isotope dependence for hydrogen diffusion in palladium, Zeitschrift für Naturforschung A 26 (1971) 922–923. doi: 10.1515/zna-1971-0522

[197] R.A. Oriani, The Physical and Metallurgical Aspects of Hydrogen in Metals, Proceedings of the fourth International Conference on Cold Fusion 1 (1993) 18-1–52. Report ID: EPRI TR-104188-V1, Electric Power Research Institute, Palo Alto, 1994.

[198] W. M. Robertson, Hydrogen permeation, diffusion and solution in nickel, Zeitschrift für Metallkunde 64 (1973) 436–443.

[199] L. Katz, M. Guinan, R.J. Borg, Diffusion of H_2, D_2, and T_2 in single-crystal Ni and Cu, Physical Review B 4 (1971) 330–341. doi: 10.1103/PhysRevB.4.330

[200] Y. Ebisuzaki, W.J. Kass, M. O'Keeffe, Isotope effects in the diffusion and solubility of hydrogen in nickel, Journal of Chemical Physics 46 (1967) 1373–1378. doi: 10.1063/1.1840859

[201] W. Eichenauer, W. Löser, H. Witte, Löslichkeit und Diffusionsgeschwindigkeit von Wasserstoff und Deuterium in Einkristallen aus Nickel und Kupfer (in German), Zeitschrift für Metallkunde 56 (1965) 287–293.

[202] K. Kuehn, A student's guide through the great physics texts. Volume IV: Heat, atoms and quanta, Springer, Heidelberg, 2016, p. 342.

[203] G. Hölzer, M. Fritsch, M. Deutschmann, J. Härtwig, E. Förster, $K\alpha_{1,2}$ and $K\beta_{1,3}$ x-ray emission lines of the 3d transition metals, Physical Review A 56 (1997) 4554–4568. doi: 10.1103/PhysRevA.56.4554

[204] B.D. Cullity, Elements of X-ray diffraction, second edition, Addison-Wesley, Reading, 1978.

Appendix

Equation of the Gaussian distribution

A Gaussian or normal distribution is generally described by the equation:

$$f^G(x, {\sigma_{sd}}^2) = \frac{1}{\sqrt{2\,\pi\,{\sigma_{sd}}^2}}\,\exp\left\{-\frac{x^2}{2\,{\sigma_{sd}}^2}\right\}. \tag{0.1}$$

It is used in Chapter 3 to derive the Maxwell-Boltzmann distribution.

Calculating the mean molecular speed

The mean molecular speed $\bar{u}$ is an often-used parameter. The derivation via the integration of the Maxwell-Boltzmann distribution is shown below. This is put into context in section 3.1. The mean velocity $\bar{u}$ is given by:

$$\bar{u} = \int_0^\infty u\, f^M(m, T, u)\, du. \tag{0.2}$$

With the constant

$$c_1 = \frac{m}{2\,\mathrm{k}\,T} \tag{0.3}$$

as a simplification and equation (3.5), one obtains:

$$\begin{aligned}\bar{u} &= \int_0^\infty u\;\, 4\,\pi\,u^2 \left(\frac{c_1}{\pi}\right)^{3/2} \exp\{-c_1 u^2\}\; du = 4\,\pi\,\left(\frac{c_1}{\pi}\right)^{3/2} \int_0^\infty u^3\,\exp\{-c_1 u^2\}\, du, \\ &= 4\,\pi \left(\frac{c_1}{\pi}\right)^{3/2} \left[\frac{c_1 u^2 + 1}{2\,{c_1}^2} \exp\{-c_1 u^2\}\right]_0^\infty \quad = 4\pi \left(\frac{c_1}{\pi}\right)^{3/2} \left[0 - \left(-\frac{1}{2\,{c_1}^2}\right)\right] \\ &= \frac{2}{\sqrt{\pi\, c_1}}\end{aligned} \tag{0.4}$$

By reinserting equation (0.3), the final expression is obtained:

$$\bar{u} = \sqrt{\frac{8\,\mathrm{k}\,T}{\pi\, m}}. \tag{0.5}$$

Calculating the surface flux

The surface flux is another parameter used in this work. Its derivation, based on the Maxwell-Boltzmann distribution, is given below. The full context can be found in section 3.1.

$$j_{n,x} = \int_0^\infty \varrho_n \, f^M(m,T,\xi_x)\, d\xi_x \qquad = \varrho_n \sqrt{\frac{m}{2\,\pi\,\mathrm{k}\,T}} \int_0^\infty \xi_x \, \exp\left\{\frac{-m\,{\xi_x}^2}{\mathrm{k}\,T}\right\} \, d\xi_x$$

$$= \varrho_n \sqrt{\frac{m}{2\,\pi\,\mathrm{k}\,T}} \left[\frac{-\mathrm{k}\,T}{m} \exp\left\{\frac{-m\,{\xi_x}^2}{\mathrm{k}\,T}\right\}\right]_0^\infty = \varrho_n \sqrt{\frac{m}{2\,\pi\,\mathrm{k}\,T}} \frac{\mathrm{k}\,T}{m} = \varrho_n \sqrt{\frac{\mathrm{k}\,T}{2\,\pi\,m}}. \tag{0.6}$$

By inserting equation (3.9), one obtains:

$$j_{n,x} = \varrho_n \frac{\bar{u}}{4}. \tag{0.7}$$

Particle collisions

In section 3.1, the transport of gas in vacuum is described. The collision cross-section is a value that is often needed for vacuum calculations. Information from [84] on the cross-sections of the relevant gas species for metal foil pumps is given in Table 11. The values for the temperature correction via equation (3.18) are also shown.

Table 11: Diameters of collisions for H_2 and He with Sutherland correction for temperature dependence, from [85].

Gas	$D(273.15\ \mathrm{K})$ (nm)	D_∞(nm)	T_S (K)	Temperature range (K)
H_2	27.2	22 … 24	75 … 235	75 … 1000
He	21.8	18.2 … 19.4	22 … 175	20 … 1000

To get a feeling for the likelihood of interactions, the mean free paths and Knudsen numbers for an example case are given in Table 12.

Table 12: Mean free path of pure H_2 gas at 298 K and Knudsen number in a tube with 100 mm inner diameter.

Pressure	1013 hPa	100 Pa	1 Pa	0.01 Pa
Mean free path $\bar{l}$	126 nm	128 µm	12.8 mm	1.28 m
Knudsen number $Kn\,(-)$	$1.3 \cdot 10^{-6}$	$1.3 \cdot 10^{-3}$	$1.3 \cdot 10^{-1}$	13

Calculation of thermionic emission

In Table 1 in section 3.2.1, the thermionic emission temperature for an emission of $1\ \mathrm{A/cm^2}$ for several metals is listed. The thermionic emission current can be calculated via the Richardson-Dushman equation. This is given by [97]:

$$i_{te} = c_R\, {T_f}^2 \exp\left\{-\frac{\Phi}{\mathrm{k}\,T}\right\}. \tag{0.8}$$

The current density of thermionic emission i_{te} in this equation is dependent on the metal (filament) temperature T_f, the material-related values of the Richardson's constant c_R and the work function Φ. The values used for the calculation are collected in Table 13.

Table 13: Material data for the calculation of thermionic emissions [97]. The temperature for the emission of $1\ \mathrm{A/cm^2}$ is calculated via the Richardson-Dushman equation.

Material	c_R $(\mathrm{A/(cm^2K^2)})$	Φ (eV)	$T(i_{te} = 1\ \mathrm{A/cm^2})$ (K)
W	60	4.54	2400
Pt	32	5.32	2849
Nb	120	4.19	2166
Ta	120	4.25	2195
Mo	55	4.15	2218
Th on W	3	2.63	1673

Sticking coefficients of hydrogen on real metal surfaces

The molecular sticking coefficients of hydrogen on metal surfaces are very important for superpermeability. The surface processes are discussed in section 3.3.1. Only a small number of sticking coefficients are reported in literature. For this collection, the target has been to identify very high and low reported values to cover the possible range of occurrence. Often this data is reported as recombination coefficients. The sticking coefficients are calculated from these via equation (3.40), using the solubility values given in Table 15.

Table 14: Molecular hydrogen sticking coefficient data.

No		State	α_{m0} $(-)$	E_{α_m} (eV)	T. range (K)	Source
(8.9)	Pd	Under plasma irradiation	$1.53 \cdot 10^{-3}$	-0.192	~ 340–530	[112]
(8.10)	Pd	~19% S and 2% O on surface	$1.64 \cdot 10^{-4}$	0.049	~ 330–670	[113]
(8.11)	Nb	0.03% O dissolved in bulk	$2.20 \cdot 10^{-2}$	0.16	~ 450–1220	[115]
(8.12)	Nb	0.13% O dissolved in bulk	$1 \cdot 10^{-3}$	0.14	~ 450–935	[115]
(8.13)	Nb	0.13% O dissolved in bulk	$3 \cdot 10^{-1}$	0.6	~ 935–1300	[115]
(8.14)	Nb	1.53% O dissolved in bulk	$2 \cdot 10^{-5}$	0.115	~ 450–660	[115]
(8.15)	Nb	1.53% O dissolved in bulk	$1.5 \cdot 10^{-4}$	0.23	~ 660–1470	[115]
(8.16)	Nb	1.53% O dissolved in bulk	$2 \cdot 10^{-1}$	1.14	~1470–1970	[115]
(8.17)	Ni	Highest α_m literature value	$5.83 \cdot 10^{-2}$	0.094	~ 560–840	[51]
(8.18)	Ni	Lowest α_m literature value	$3.21 \cdot 10^{-8}$	-0.106	~ 500–840	[51]
(8.19)	Fe	Highest α_m literature value	$3.29 \cdot 10^{-4}$	0.09	~ 420–710	[114]
(8.20)	Fe	Intermediate α_m literature value	$1.02 \cdot 10^{-5}$	0.195	~ 310–710	[114]
(8.21)	Fe	Lowest α_m literature value	$1.32 \cdot 10^{-5}$	0.313	~ 280–710	[114]

Hydride structures

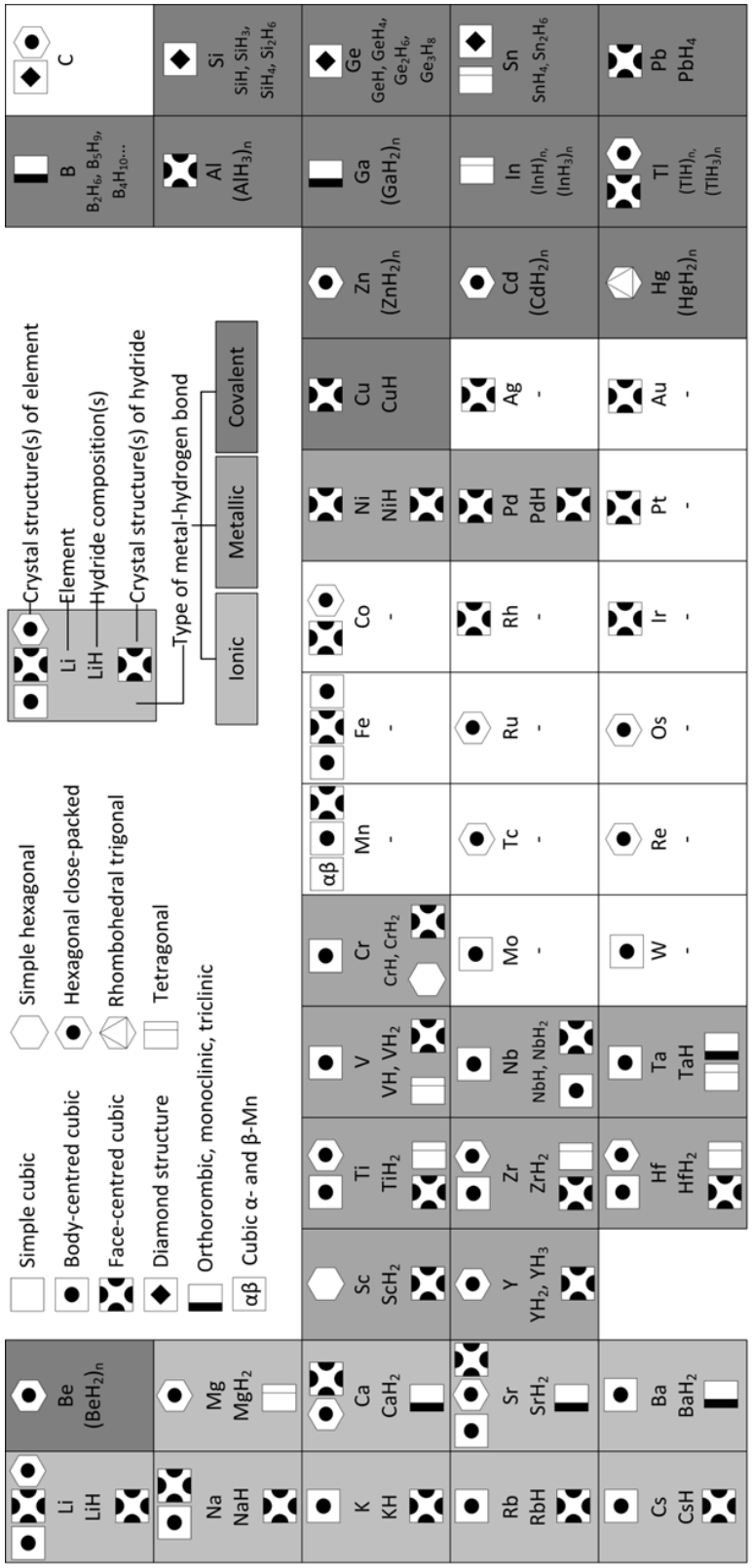

Figure 0.1: Excerpt of the periodic table, including the formed hydrides and crystal structures.

Diffusivity, solubility and permeability of hydrogen in metals

The topic of section 3.3.2 is the interaction between hydrogen and metals. Unfortunately, data on the diffusivity, solubility and permeability of the different hydrogen isotopes in and through metals is not easy to find. While some sources can be found in the literature, some measurements significantly deviate from other results. As this information is still important for the presented work, a literature study was initiated as part of a bachelor thesis. As this thesis, "Literature Study and Analysis of Metal-Hydrogen Properties for Separation and Storage" by Daniel Bitter, has not been published, the results are reprinted here. In Table 15, the suggested values are shown. For some materials, the measurements show a large spread. This is especially the case for copper and iron. To increase the validity of the values, an attempt is made to create an average fit of the available data. The sources used are shown in Table 16. If more than a single source is given, the value is calculated by averaging the literature data. Some sources themselves are already averaged values from the literature, e.g. [179]. Only two of the three functions are needed to calculate the third one. Values obtained via this route are marked by "Calc".

Table 15: Diffusivity, solubility and permeability values for the different hydrogen isotopes in selected metals. Crystal structure data is from [167] and the sources for the individual values are given in the next table (Table 16).

Metal	Q	$D_0 \cdot 10^7$ (m^2/s)	E_D (eV)	K_0 $\left(\frac{mol}{m^3\sqrt{Pa}}\right)$	ΔH_0 (eV)	$P_0 \cdot 10^7$ $\left(\frac{mol}{m\ s\ \sqrt{Pa}}\right)$	E_P (eV)
α-Fe (bcc)	H	0.75	0.105	0.418	0.283	0.31	0.388
	D	0.428	0.067	0.245	0.269	0.105	0.336
	T	0.256	0.055	0.691	0.252	0.102	0.328
V (bcc)	H	0.31	0.045	0.26	– 0.330	0.08	– 0.285
	D	0.38	0.073	0.26	– 0.333	0.10	– 0.260
	T	0.56	0.094	0.24	– 0.349	0.14	– 0.246
Nb (bcc)	H	0.50	0.106	0.27	– 0.366	0.13	– 0.260
	D	0.52	0.127	0.27	– 0.403	0.14	– 0.276
	T	0.44	0.134	0.33	– 0.351	0.15	– 0.217
Ta(bcc)	H	0.44	0.140	0.23	– 0.363	0.10	– 0.223
	D	0.46	0.160	0.16	– 0.385	0.075	– 0.225
	T	0.37	0.162	0.09	– 0.371	0.034	– 0.209
Pd (fcc)	H	2.90	0.23	0.655	– 0.097	1.90	0.133
	D	2.50	0.219	0.666	– 0.078	1.67	0.141
	T	8.05	0.257	0.771	– 0.066	6.21	0.191
$Pd_{0.9}Ag_{0.1}$	H	3.5	0.232	0.57	– 0.138	2.5	0.094
	D	2.3	0.225	0.66	– 0.111	1.5	0.115
	T	6.3	0.247	0.71	– 0.1	4.5	0.147
$Pd_{0.8}Ag_{0.2}$	H	2.8	0.232	0.45	– 0.175	1.5	0.057
	D	1.6	0.206	0.49	– 0.153	0.8	0.053
	T	5.6	0.247	0.58	– 0.134	3.2	0.113
$Pd_{0.7}Ag_{0.3}$	H	1.9	0.243	0.39	– 0.199	0.9	0.043
	D	1.1	0.225	0.36	– 0.187	0.4	0.038
	T	6.5	0.269	0.44	– 0.167	2.9	0.102
Ni (fcc)	H	6.44	0.417	0.525	0.129	3.38	0.565
	D	4.87	0.396	0.782	0.147	3.81	0.543
	T	3.90	0.402	0.838	0.130	3.26	0.532
Cu (fcc)	H	11.3	0.400	0.71	0.37	7.81	0.770
	D	7.3	0.381	8.64	0.448	63.1	0.829
	T	6.3	0.383	5.19	0.572	32.9	0.955

Table 16: Sources for the data given in the previous table (Table 15). Calc = Values were calculated by the other two parameters.

Metal	Q	Diffusivity	Solubility	Permeability
α-Fe (bcc)	H	[179]	[8] [180]	Calc
	D	[180]	Calc	[180]
	T	[181]	Calc	[181]
V (bcc)	H	[179]	[182] [183] [184] [185]	Calc
	D	[179]	[182] [183] [181]	Calc
	T	[186]	[183] [181]	Calc
Nb (bcc)	H	[179]	[185] [187] [182]	Calc
	D	[179]	[188] [1]	Calc
	T	[189] [186]	[181]	Calc
Ta(bcc)	H	[179]	[182] [185] [190]	Calc
	D	[179]	[182]	Calc
	T	[186]	Calc	[181]
Pd (fcc)	H	[179]	[191] [182] [192]	Calc
	D	[193] [194] [195] [196]	[191] [182] [192]	Calc
	T	[194] [195]	[182] [197]	Calc
$Pd_{0.9}Ag_{0.1}$	H	[194]	[182]	Calc
	D	[194]	[182]	Calc
	T	[194]	[182]	Calc
$Pd_{0.8}Ag_{0.2}$	H	[194]	[182]	Calc
	D	[194]	[182]	Calc
	T	[194]	[182]	Calc
$Pd_{0.7}Ag_{0.3}$	H	[194]	[182]	Calc
	D	[194]	[182]	Calc
	T	[194]	[182]	Calc
Ni (fcc)	H	[198]	[198]	[198]
	D	[199] [200] [201]	[201]	Calc
	T	[199] [181]	[181]	Calc
Cu (fcc)	H	[199]	[201]	Calc
	D	[199]	[201]	Calc
	T	[199] [181]	[181]	Calc

[1] K_0 is assumed to be the same as for H

Equilibrium constants for the hydrogen isotopologues

In Table 11, values for the different functions describing the equilibrium constants between the hydrogen isotopologues are given. Detailed information on these is given in section 3.3.3.

Table 17: Collection of literature data and presented results to calculate the equilibrium constants. Recommended values for the different temperatures are marked with *.

No		Temperature range (K)	K_0 (-)	C_h (K)	Uncertainty	Reference
1*	K_{HD}	4.2 ... 50	6.785	-78.70	+5.2 ...3.0 % [139] ±3 % [141]	[139], [141]
2*	K_{HD}	50 ... 250	3.804	-51.178		This work, data: [141]
3	K_{HD}	50 ... 300	3.850	-53.22		[139]
4*	K_{HD}	250 ... 1250	4.207	-75.316		This work, data: [137]
5	K_{HD}	Around 298.15	4.21	-76.98		[134]
6*	K_{HT}	4.2 ... 50	10.22	-171.1	+36.5...33.7 % [139] ±35 % [141]	[139], [141]
7*	K_{HT}	50 ... 250	4.082	-143.064		This work, data: [141]
8	K_{HT}	50 ... 300	3.995	-140.86		[139]
9*	K_{HT}	250 ... 1250	4.518	-166.588		This work, data [136]
10*	K_{DT}	4.2 ... 12.5	5.924	-20.24	+2.6 ...2.1 % [139], ±2 % [141]	[139], [141]
11*	K_{DT}	16.7 ... 33.3	2.995	-10.82	±0.9 % [139], ±1 % [141]	[139], [141]
12*	K_{DT}	50 ... 250	4.149	-23.708		This work, data: [141]
13*	K_{DT}	250 ... 1250	4.075	-19.456		This work, data: [137]
14	K_{DT}	50 ... 300	4.141	-22.72	+1.1 ...1.3 %	[139]

Additional information on the measurement accuracy

For the flux method, an uncertainty of the effective pumping speed through the orifice has to be determined. The orifice is precision-drilled into a sheet of copper. The hole has a radius of $2.15\,\mathrm{mm}$, and the thickness of the copper is $2.1\,\mathrm{mm}$. The uncertainty for both values is estimated to be smaller than $0.05\,\mathrm{mm}$, as this is the smallest value that can be reliably measured with the callipers.

To be able to calculate the uncertainty of the conductance, the derivative of equation (5.4) has to be determined. It is found to be:

$$\frac{d\Omega}{dL_C} = \frac{1}{4}\left(-\frac{{L_C}^2}{\sqrt{4+{L_C}^2}} - \sqrt{4+{L_C}^2} + \frac{\left(\sqrt{4+{L_C}^2}-L_C\right)\left({L_C}^3-{L_C}^2\sqrt{4+{L_C}^2}+8\sqrt{4+{L_C}^2}-16\right){L_C}^2}{3\sqrt{4+{L_C}^2}\left(L_C\sqrt{4+{L_C}^2}-4\ln\left(\sqrt{4+{L_C}^2}+L_C\right)+\ln(16)\right)} \right.$$
$$\left. + \frac{\left({L_C}^4+8\,L_C\left(\sqrt{4+{L_C}^2}-2\right)-{L_C}^3\sqrt{4+{L_C}^2}\right)^2}{9\sqrt{4+{L_C}^2}\left(L_C\sqrt{4+{L_C}^2}-4\ln\left(\sqrt{4+{L_C}^2}+L_C\right)+\ln(16)\right)^2} + 2L_C \right). \tag{0.22}$$

The uncertainty of the pumping speed of the turbomolecular pump for hydrogen ($48\,\mathrm{l/s}$) is not given by the manufacturer, thus it is estimated to be $\pm 2\ \mathrm{l/s}$. The effective pumping speed at the orifice is determined to be $3.99\,\mathrm{l/s}$ with standard deviation of $3.6\,\%$.

X-ray diffraction

It is not straightforward to measure the hydrogen concentration within metals. Instead of measuring the hydrogen itself, one can also measure the effect of the hydrogen on the metal. The formation of hydrides is often connected to a change in the crystal structure. Even hydrogen in interstitial solution changes the lattice constant by widening the unit cell. Both effects – the change of the crystal structure and the widening of the lattice constant – can be identified by X-ray diffractometry (XDR).

For carrying out XRD a parallel, monochromatic X-ray beam is directed onto a probe surface. Dependent on the crystal structure, constructive and destructive interference at different reflection angles cause a reflection pattern, which can be used to determine the crystal structure as well as the lattice constant. In Figure 0.2 b), an example of a constructive interference – and thus intensity peak – in an XRD pattern at a reflection angle of $2\,\theta$ is shown. Within a regular lattice, several planes can cause such a (Bragg) reflection. In Figure 0.2, these are marked with A to D.

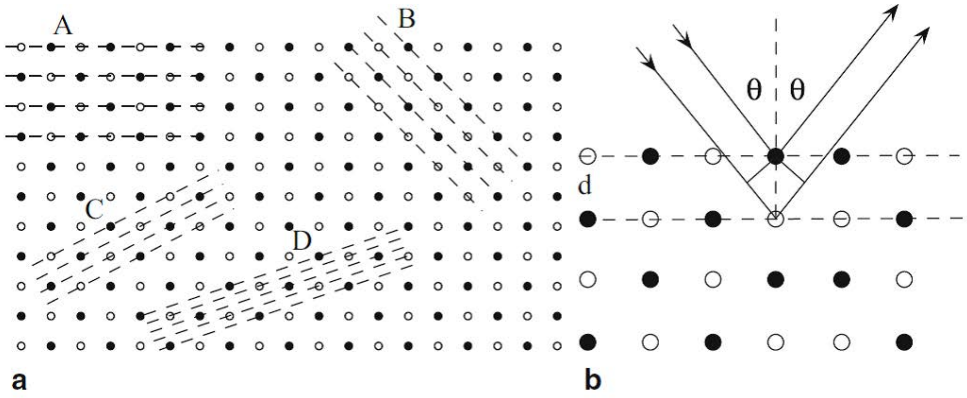

Figure 0.2: a) Four sets of planes constructed in different regions of a crystal lattice. b) Incident X-rays reflecting from adjacent planes, which are separated by distance d and a scattering angle of 2θ. Taken from [202].

The spacing between the planes can be determined by the simple equation

$$d = \frac{\lambda}{2 \sin \theta}. \tag{0.23}$$

The wavelength λ of the X-ray is needed to calculate this. It is dependent on the cathode material of the X-ray tube. In the presented measurements, a copper cathode is used with the main wavelength of [203]:

$$\lambda_{\mathrm{Cu\,Ka1}} = 0.154060\ \mathrm{nm}. \tag{0.24}$$

Dependent on the crystal structure of the material and the plane that causes the reflection, the spacing between the planes d can be used to calculate the lattice constant. The material in question, vanadium, has a body-centred cubic (bcc) lattice. In this crystal structure, the lattice constant can be easily calculated by using the law of Pythagoras. For this, the planes have to be known and the Miller indices $(h\ k\ l)$ can be used to calculate the constant with

$$a = d\sqrt{h^2 + k^2 + l^2} = d\sqrt{i_M}. \tag{0.25}$$

In a primitive cubic lattice, all planes will cause a reflection, while for face-centred cubic and body-centred cubic lattices, only some planes can be seen. Table 18 shows which planes will cause a reflection for which lattices.

Table 18: Allowed list of $i_M = h^2 + k^2 + l^2$ and the corresponding Miller indices (hkl) for the different planes in cubic crystals. Note that $i_M = 7$ and 15 are missing, as there are no integer values for h, k, l that give these numbers. pc = primitive cubic, fcc = face-centred cubic, bcc = body-centred cubic [204].

i_M	1	2	3	4	5	6	8	9	10	11	12	13	14	16
pc	x	x	x	x	x	x	x	x	x	x	x	x	x	x
fcc			x	x			x			x	x			x
bcc		x		x		x	x		x		x		x	x
(hkl)	100	110	111	200	210	211	220	221 300	310	311	222	320	321	400

P&ID of HERMES

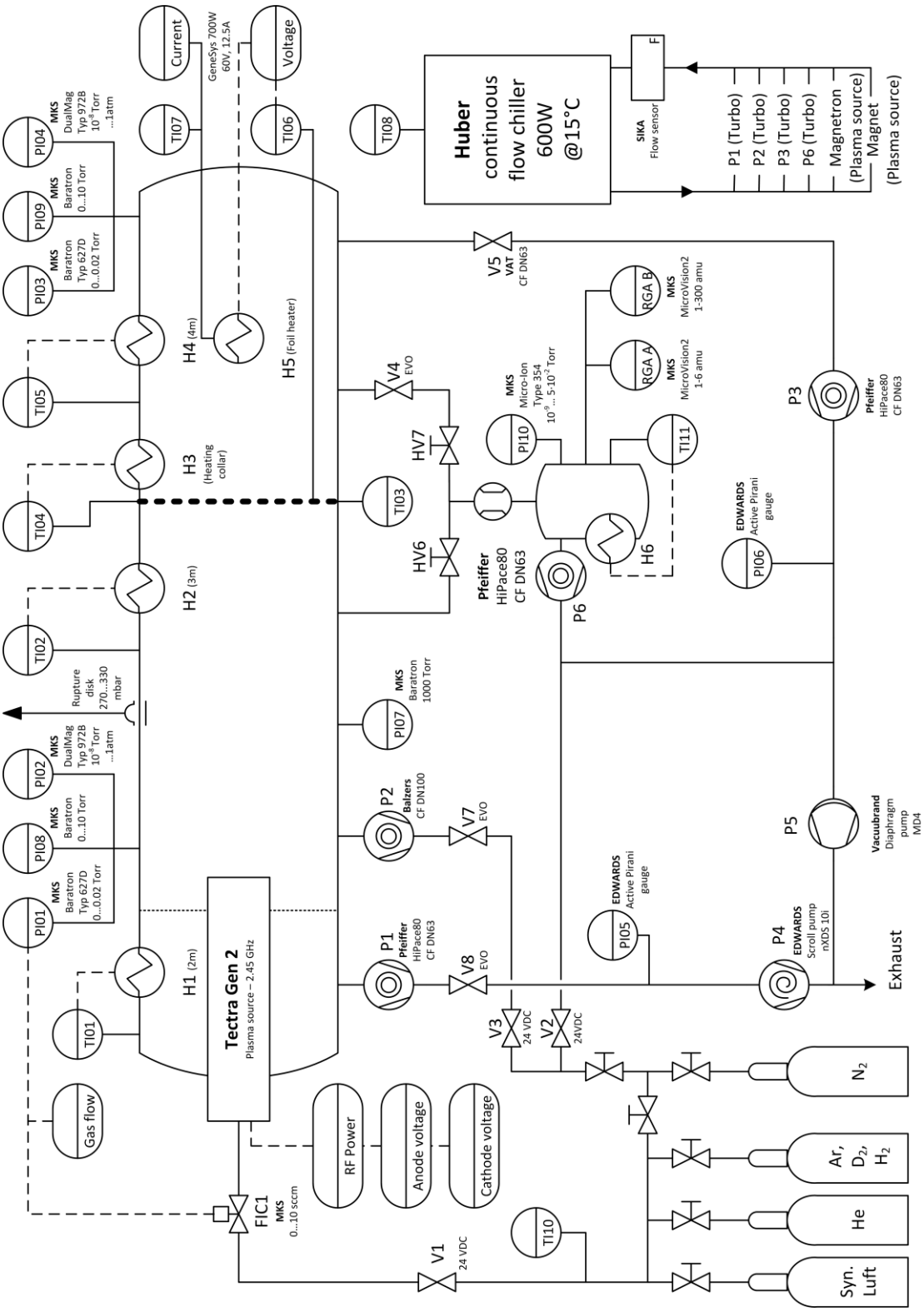

Figure 0.3: Piping and instrumentation diagram of HERMES.

P&ID of HERMES*plus*

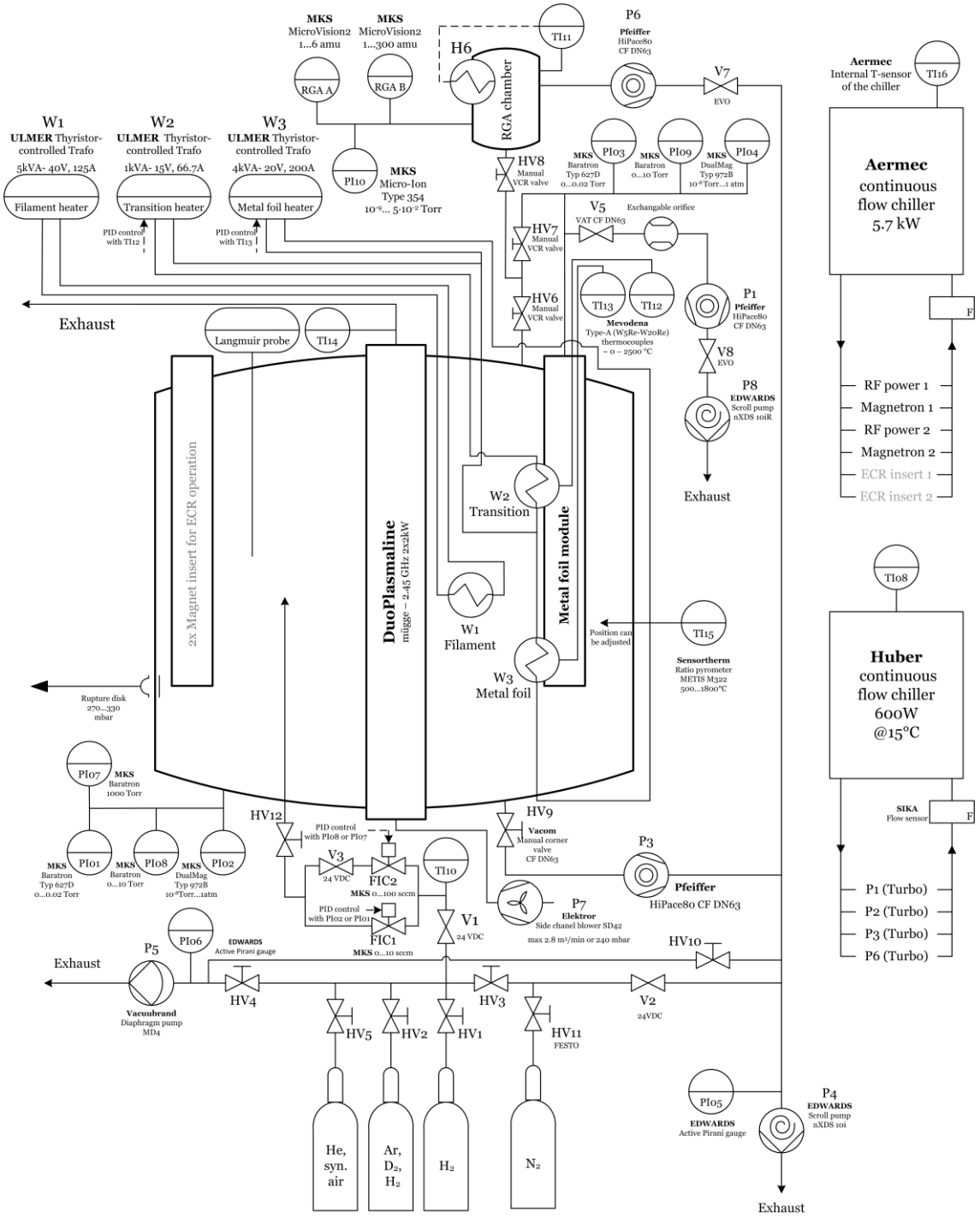

Figure 0.4: Piping and instrumentation diagram of HERMES*plus*. The elements of the planned ECR insert are shown in grey.